

Design Tools for Zero-Net Mass-Flux Separation Control Devices

**DISTRIBUTION STATEMENT A**  
Approved for Public Release  
Distribution Unlimited

AFOSR Grant # F49620-03-1-0135

By  
Quentin Gallas, Ryan Holman, and Lou Cattafesta

Department of Mechanical and Aerospace Engineering  
University of Florida

20050715 007

**REPORT DOCUMENTATION PAGE**

AFRL-SR-AR-TR-05-

0266

Public reporting burden for this collection of information is estimated to average 1 hour per response, including the time for reviewing instructions, data needed, and completing and reviewing this collection of information. Send comments regarding this burden estimate or any other aspect of this burden to Department of Defense, Washington Headquarters Services, Directorate for Information Operations and Reports (0704-0188), 121 4302. Respondents should be aware that notwithstanding any other provision of law, no person shall be subject to any penalty for failing to comply with a collection of information if it does not have a valid OMB control number. PLEASE DO NOT RETURN YOUR FORM TO THE ABOVE ADDRESS.

<b>1. REPORT DATE (DD-MM-YYYY)</b> 05-05-2005		<b>2. REPORT TYPE</b> Final		<b>3. DATES COVERED (From - To)</b> 01-03-2003-31-12-2004	
<b>4. TITLE AND SUBTITLE</b> Design Tools For Zero Net Mass Flux Separation Control Devices Modeling and Experimental Effort.				<b>5a. CONTRACT NUMBER</b>	
				<b>5b. GRANT NUMBER</b> F49620-03-1-0135	
				<b>5c. PROGRAM ELEMENT NUMBER</b>	
<b>6. AUTHOR(S)</b> Quentin Gallas, Ryan Holman, and Lou Cattafesta				<b>5d. PROJECT NUMBER</b>	
				<b>5e. TASK NUMBER</b>	
				<b>5f. WORK UNIT NUMBER</b>	
<b>7. PERFORMING ORGANIZATION NAME(S) AND ADDRESS(ES)</b> University of Florida Mechanical and Aerospace Engineering 231 Aerospace Building Gainesville FL 32611-6250				<b>8. PERFORMING ORGANIZATION REPORT NUMBER</b>	
<b>9. SPONSORING / MONITORING AGENCY NAME(S) AND ADDRESS(ES)</b> AFOSR/AFRL AF Office of Scientific Research 4015 Wilson Boulevard Rm. 713 Arlington VA 22203				<b>10. SPONSOR/MONITOR'S ACRONYM(S)</b>	
				<b>11. SPONSOR/MONITOR'S REPORT NUMBER(S)</b>	
<b>12. DISTRIBUTION / AVAILABILITY STATEMENT</b>  Approved for Public Release; distribution is unlimited					
<b>13. SUPPLEMENTARY NOTES</b>					
<b>14. ABSTRACT</b>  This report discusses the fundamental dynamics of zero-net mass flux (ZNMF) actuators commonly used in active flow-control applications. The present work addresses unresolved technical issues by providing a clear physical understanding of how these devices behave in a quiescent medium and interact with an external boundary layer by developing and validating reduced-order models. The results are expected to ultimately aid in the analysis and development of design tools for ZNMF actuators in flow-control applications.					
<b>15. SUBJECT TERMS</b>					
<b>16. SECURITY CLASSIFICATION OF:</b>			<b>17. LIMITATION OF ABSTRACT</b>  UL	<b>18. NUMBER OF PAGES</b>  191	<b>19a. NAME OF RESPONSIBLE PERSON</b> Lou Cattafesta
<b>a. REPORT</b> Unclassified	<b>b. ABSTRACT</b> Unclassified	<b>c. THIS PAGE</b> Unclassified			<b>19b. TELEPHONE NUMBER (include area code)</b> (352) 392-0961

7-7-05

## TABLE OF CONTENTS

	<u>page</u>
Abstract .....	4
1. Introduction.....	5
1.1 Motivation.....	5
1.2 Overview of a Zero-Net Mass Flux Actuator .....	6
1.3 Technical Issues .....	9
1.4 Objectives .....	10
1.5 Approach and Outline of Report.....	10
2. Dynamics of Isolated Zero-Net Mass-Flux Actuators.....	11
2.1 Characterization and Parameter Definitions .....	11
2.2 Dimensional Analysis .....	14
2.2.1 Definition and Discussion.....	14
2.2.2 Dimensionless Linear Transfer Function for a Generic Driver .....	15
2.3 Test Matrix.....	18
3. Experimental Setup.....	21
3.1 Experimental Setup.....	21
3.1.1 Cavity Pressure .....	24
3.1.2 Diaphragm Deflection.....	25
3.1.3 Velocity Measurement .....	27
3.1.4 Data-Acquisition System .....	29
3.2 Data Processing.....	32
3.3 Fourier Series Decomposition.....	37
3.4 Flow Visualization .....	41
4. Results: Orifice Flow Physics.....	42
4.1 Local Flow Field .....	43
4.1.1 Velocity Profile through the Orifice: Numerical Results .....	43
4.1.2 Exit Velocity Profile: Experimental Results.....	50
4.1.3 Jet Formation .....	57
4.2 Influence of Governing Parameters .....	58
4.2.1 Empirical Nonlinear Threshold.....	59
4.2.2 Strouhal, Reynolds, and Stokes Numbers versus Pressure Loss .....	60
4.3 Nonlinear Mechanisms in a ZNMF Actuator .....	67
5. Results: Cavity Investigation.....	73
5.1 Cavity Pressure Field .....	73
5.1.1 Experimental Results .....	74

5.1.2	Numerical Simulation Results .....	77
5.2	Compressibility of the Cavity .....	82
5.2.1	LEM-Based Analysis .....	82
5.2.2	Experimental Results .....	86
5.3	Driver, Cavity, and Orifice Volume Velocities .....	91
6.	Reduced-Order Model of Isolated ZNMF Actuator .....	98
6.1	Orifice Pressure Drop .....	98
6.1.1	Control Volume Analysis .....	99
6.1.2	Validation through Numerical Results.....	101
6.1.3	Discussion: Orifice Flow Physics .....	107
6.1.4	Development of Approximate Scaling Laws .....	112
6.2	Refined Lumped Element Model.....	120
6.2.1	Implementation .....	120
6.2.2	Comparison with Experimental Data.....	123
7.	Zero-Net Mass-Flux Actuator Interacting with an External Boundary Layer.....	130
7.1	On the Influence of Grazing Flow .....	130
7.2	Dimensional Analysis .....	134
7.3	Reduced-Order Models .....	138
7.3.1	Lumped Element Modeling-Based Semi-Empirical Model of the External Boundary Layer.....	138
7.3.2	Velocity Profile Scaling Laws .....	151
8.	Conclusions and Future Work .....	178
8.1	Conclusions.....	178
8.2	Recommendations for Future Research .....	180
9.	List of References .....	181



## Abstract

This report discusses the fundamental dynamics of zero-net mass flux (ZNMF) actuators commonly used in active flow-control applications. The present work addresses unresolved technical issues by providing a clear physical understanding of how these devices behave in a quiescent medium and interact with an external boundary layer by developing and validating reduced-order models. The results are expected to ultimately aid in the analysis and development of design tools for ZNMF actuators in flow-control applications.

The case of an isolated ZNMF actuator is first documented. A dimensional analysis identifies the key governing parameters of such a device, and a rigorous investigation of the device physics is conducted based on various theoretical analyses, phase-locked measurements of orifice velocity, diaphragm displacement, and cavity pressure fluctuations, and available numerical simulations. The symmetric, sharp orifice exit velocity profile is shown to be primarily a function of the Strouhal and Reynolds numbers and orifice aspect ratio. The equivalence between Strouhal number and dimensionless stoke length is also demonstrated. A criterion is developed and validated, namely that the actuation-to-Helmholtz frequency ratio is less than 0.5, for the flow in the actuator cavity to be approximately incompressible. An improved lumped element modeling technique developed from the available data is developed and is in reasonable agreement with experimental results.

Next, the case in which a ZNMF actuator interacts with an external grazing boundary layer is examined. Again, dimensional analysis is used to identify the dimensionless parameters, and the interaction mechanisms are discussed in detail for different applications. An acoustic impedance model (based on the NASA "ZKTL model") of the grazing flow influence is then obtained from a critical survey of previous work and implemented in the lumped element model. Two scaling laws are then developed to model the jet velocity profile resulting from the interaction - the profiles are predicted as a function of local actuator and flow condition and can serve as approximate boundary conditions for numerical simulations. Finally, extensive discussion is provided to guide future modeling efforts.

## 1. Introduction

### 1.1 Motivation

The past decade has seen numerous studies concerning an exciting type of active flow control actuator. Zero-net mass flux (ZNMF) devices, also known as synthetic jets, have emerged as versatile actuators with potential applications such as thrust vectoring of jets (Smith and Glezer 1997), heat transfer augmentation (Campbell et al. 1998; Guarino and Manno 2001), active control of separation for low Mach and Reynolds numbers (Wynanski 1997; Smith et al. 1998; Amitay et al. 1999; Crook et al. 1999; Holman et al. 2003) or transonic Mach numbers and moderate Reynolds numbers (Seifert and Pack 1999, 2000a), and drag reduction in turbulent boundary layers (Rathnasingham and Breuer 1997; Lee and Goldstein 2001). This versatility is primarily due to several reasons. First, these devices provide unsteady forcing, which has proven to be more effective than its steady counterpart (Seifert et al. 1993).

Second, since the jet is synthesized from the working fluid, complex fluid circuits are not required. Finally the actuation frequency and waveform can usually be customized for a particular flow configuration. Synthetic jets exhausting into a quiescent medium have been studied extensively both experimentally and numerically. Additionally, other studies have focused on the interaction with an external boundary layer for the diverse applications mentioned above. However, many questions remain unanswered regarding the fundamental physics that govern such complex devices.

Practically, because of the presence of rich flow physics and multiple flow mechanisms, proper implementation of these actuators in realistic applications requires design tools. In turn, simple design tools benefit significantly from low-order dynamical models. However, no suitable models or design tools exist because of insufficient understanding as to how the performance of ZNMF actuator devices scales with the governing nondimensional parameters. Numerous parametric studies provide a glimpse of how the performance characteristics of ZNMF actuators and their control effectiveness depend on a number of geometrical, structural, and flow parameters (Rathnasingham and Breuer 1997; Crook and Wood 2001; He et al. 2001; Gallas et al. 2003a). However, *nondimensional* scaling laws are required since they form an essential component in the design and deployment of ZNMF actuators in practical flow control applications.

For instance, scaling laws are expected to play an important role in the aerodynamic design of wings that, in the future, may use ZNMF devices for separation control. The current design paradigm in the aerospace industry relies heavily on steady Reynolds Averaged Navier Stokes (RANS) computations. A validated *unsteady* RANS (URANS) design tool is required for separation control applications at transonic Mach numbers and flight Reynolds number. However, these computations can be quite expensive and time-consuming. Direct modeling of ZNMF devices in these computations is expected to considerably increase this expense, since the simulations must resolve the flow details in the vicinity of the actuator while also capturing the global flow characteristics. A viable alternative to minimize this cost is to simply model the effect of the ZNMF device as a time- and flow-dependant boundary condition in the URANS calculation. Such an approach requires that the device be characterized by a small set of nondimensional parameters, and the behavior of the actuator must be well understood over a wide range of conditions.

Furthermore, successful implementation of robust closed-loop control methodologies for this class of actuators calls for simple (yet effective) mathematical models, thereby emphasizing the need to develop a reduced-order model of the flow. Such low-order models will clearly aid in the analysis and development of design tools for sizing, design and deployment of these actuators. Below, an overview of the basic operating principles of a ZNMF actuator is provided.

## 1.2 Overview of a Zero-Net Mass Flux Actuator

Typically, ZNMF devices are used to inject unsteady disturbances into a shear flow, which is known to be a useful tool for active flow control. Most flow control techniques require a fluid source or sink, such as steady or pulsed suction (or blowing), vortex-generator jets (Sondergaard et al. 2002; Eldredge and Bons 2004), etc., which introduces additional constraints in the design of the actuator and sometimes results in complicated hardware. This motivates the development of ZNMF actuators, which introduce flow perturbations with zero-net mass injection, the large coherent structures being synthesized from the surrounding working fluid (hence the name “synthetic jet”).

A typical ZNMF device with different transducers is shown in Figure 1-1. In general, a ZNMF actuator contains three components: an oscillatory driver (examples of which are discussed below), a cavity, and an orifice or slot. The oscillating driver compresses and expands the fluid in the cavity by altering the cavity volume  $\nabla$  at the excitation frequency  $f$  to create pressure oscillations. As the cavity volume is decreased, the fluid is compressed in the cavity and expels some fluid through the orifice. The time and spatial averaged ejection velocity during this portion of the cycle is denoted  $\overline{V}_j$ . Similarly, as the cavity volume is increased, the fluid expands in the cavity and ingests some fluid through the orifice. Common orifice geometries include simple axisymmetric hole (height  $h$ , diameter  $d$ ) and rectangular slot (height  $h$ , depth  $d$  and width  $w$ ), as schematically shown in Figure 1-2. Downstream from the orifice, a jet (laminar or turbulent, depending on the jet Reynolds number  $Re = \overline{V}_j d / \nu$ ) is then synthesized from the entrained fluid and sheds vortices when the driver oscillations exceed a critical amplitude (Utturkar et al. 2003).

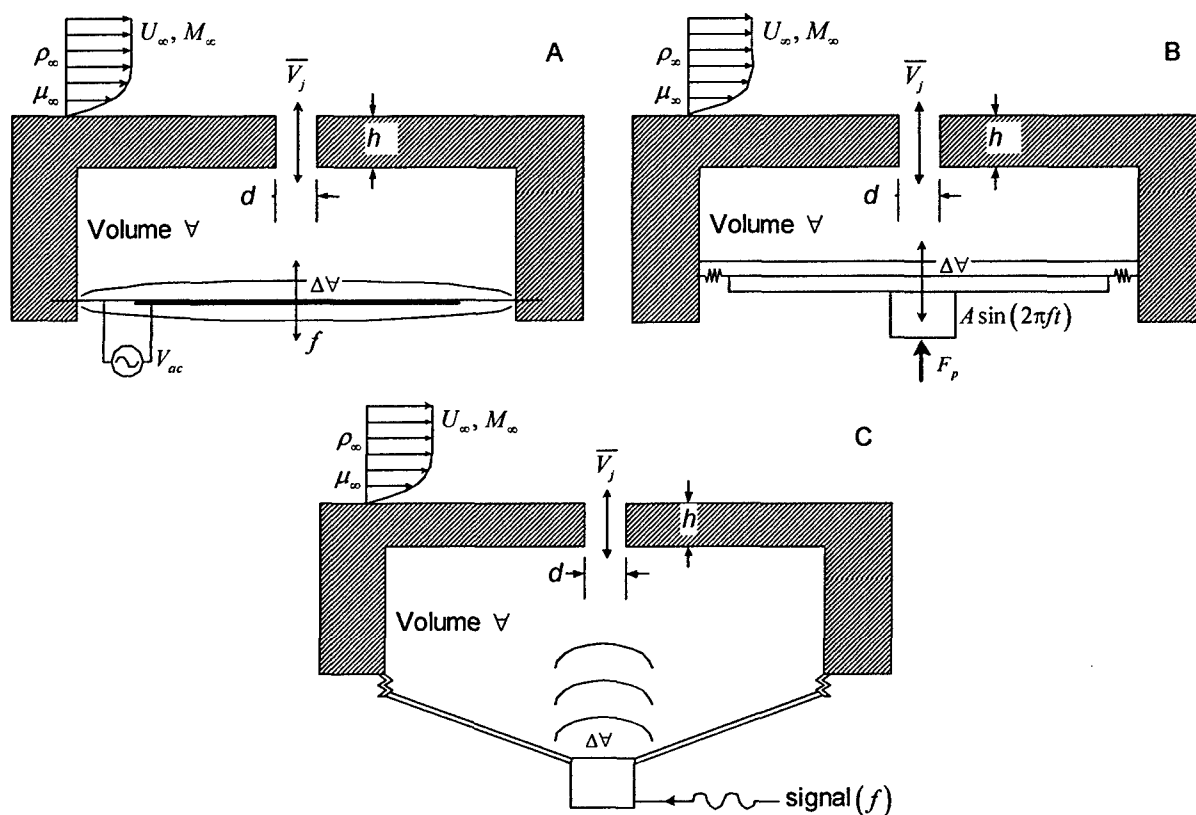


Figure 1-1: Schematic of typical zero-net mass flux devices interacting with a boundary layer, showing three different types of excitation mechanisms. A) Piezoelectric diaphragm. B) Oscillating piston. C) Acoustic excitation.

Even though no net mass is injected into the embedded flow during a cycle, a non-zero transfer of momentum is established with the surrounding flow. The exterior flow, if present, usually consists of a turbulent boundary layer (since most practical applications deal with such a turbulent flow) and is characterized by the freestream velocity  $U_\infty$  and acoustic speed  $c_\infty$ , pressure gradient  $dP/dx$ , radius of curvature  $R$ , thermal diffusivity  $\alpha_\infty$ , and displacement  $\delta^*$  and momentum  $\theta$  thicknesses. Finally, the ambient fluid is characterized by its density  $\rho_\infty$  and dynamic viscosity  $\mu_\infty$ .

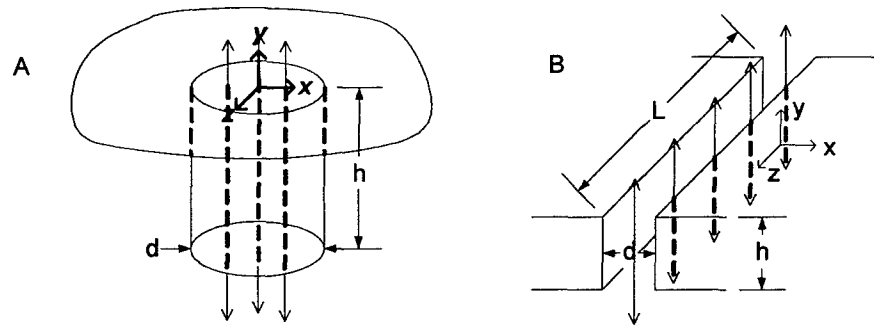


Figure 1-2: Orifice geometry. A) Axisymmetric. B) Rectangular.

Figure 1-1 shows three kinds of drivers commonly used to generate a synthetic jet:

- An oscillating membrane (usually a piezoelectric patch mounted on one side of a metallic shim and driven by an ac voltage).
- A piston mounted in the cavity (using an electromagnetic shaker, a camshaft, etc.).
- A loudspeaker enclosed in the cavity (an electrodynamic voice-coil transducer).

For each of them, we are interested mainly in the volume displacement generated by the driver that will eject and ingest the fluid through the orifice. Although each driver will obviously have its own characteristics, common parameters of a generic driver are its frequency of excitation  $f$ , the corresponding volume  $\Delta V$  that it displaces, and the dynamic modal characteristics of the driver.

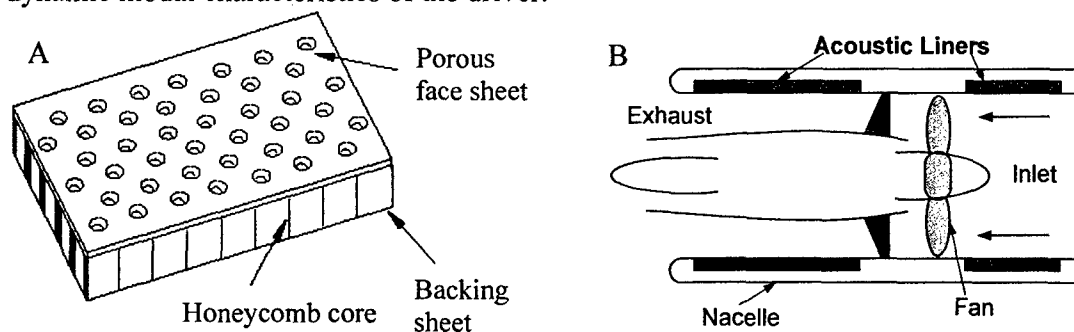


Figure 1-3: Helmholtz resonators arrays. A) Schematic. B) Application in engine nacelle acoustic liners.

Although noticeable differences exist, it is worthwhile to compare synthetic jets with the phenomenon of acoustic flow generation, the *acoustic streaming*, extensively studied by aeroacousticians in the past (e.g., Lighthill 1978). *Acoustic streaming* is the result of a steady flow produced by an acoustic field and is the evidence of the generation of vorticity by the sound, which occurs for example when sound impinges on solid boundaries. Quoting Howe (1998, p. 410),

When a sound wave impinges on a solid surface in the absence of mean flow, the dissipated energy is usually converted directly into heat through viscous action. At

very high acoustic amplitudes, however, free vorticity may still be formed at edges, and dissipation may take place, as in the presence of mean flow, by the generation of vortical kinetic energy which escapes from the interaction zone by self-induction. This nonlinear mechanism can be important in small perforates or apertures.

This type of flow generation could be relevant in the application of ZNMF devices where similar nonlinear flow through the orifice is expected. In particular, ZNMF devices are similar to flow-induced resonators, such as Helmholtz resonators used in acoustic liners as sound-absorber devices. As Figure 1-3 shows, a simple single degree-of-freedom (SDOF) liner consists of a perforate sheet backed with honeycomb cavities and interacting with a grazing flow. Similar liners with a second cavity (or more) are commonly used in engine nacelles to attenuate the sound noise level. More recently, Flynn et al. (1990) and Urzynick and Fernholz (2002) used Helmholtz resonators for flow control applications. More details will be given in subsequent sections.

### **1.3 Technical Issues**

By surveying the literature, i.e. looking at the flow mechanism of isolated ZNMF actuators to more complex behavior when the actuator is interacting with an incoming boundary layer, along with examples of sound absorber technology, several key issues can be highlighted that still remain to be addressed. This subsection lists the principal ones.

**Fundamental flow physics.** Clearly, there still exists a lack in the fundamental understanding of the flow mechanisms that govern the dynamics of ZNMF actuators. While the cavity design is well understood, the orifice modeling and especially the effect of the interaction with an external boundary layer requires more in-depth consideration. Also, whether performing experimental studies or numerical simulations, researchers are confronted with a huge parameter space that is time consuming and requires expensive experiments or simulations. Hence the development of simple physics-based reduced-order models is primordial.

**2D vs. 3D.** While most of the numerical simulations are performed for two-dimensional problems, three-dimensionality effects clearly can be important, especially to model the flow coming out of a circular orifice as shown in Rizzetta et al. (1998) or Ravi et al. (2004) that also found distinct and non negligible three-dimensional effects of the flow.

**Compressibility effects.** Usually, the entire flow field is numerically solved using an incompressible solver. However, such an assumption, although valid outside the actuator, may be violated inside the orifice at high jet velocity and, more generally, inside the cavity due to the acoustic compliance of the cavity. Indeed, the cavity acts like a spring that stores the potential energy produced by the driver motion.

**Lack of high-resolution experimental data.** Most of the experimental studies employed either Hot Wire Anemometry (HWA), Particle Image Velocimetry (PIV) or Laser Doppler Velocimetry (LDV) to measure the flow. However, each of these techniques has shortcomings, as briefly enumerated below.

In the case of HWA, since the flow is highly unsteady and by definition oscillatory, its deployment must be carefully envisaged, especially considering the de-rectification procedure used to obtain the reversal flow. Since it is an intrusive technique that may perturb the flow, other issues are that it is a single point measurement (hence the need to

traverse the whole flow field), problems arise with measurements near zero velocity (transition from free to forced convection), and the accuracy may be affected by the calibration (sensitivity), the local temperature, or some conductive heat loss.

With regards to PIV, although the main advantage resides in the fact that it is a non-intrusive flow visualization technique that captures instantaneous snapshots of the flow field, the micro/meso scale of ZNMF devices requires very high resolution in the vicinity of the actuator orifice in order to obtain reasonable accuracy in the data. This is difficult to achieve using a standard digital PIV system.

Finally, a large number of samples are required in order to get proper accuracy in the data from LDV measurement, and excellent spatial resolution is difficult to achieve due to the finite length of the probe volume. Also, since LDV is a single point measurement, a traversing probe is required in order to map the entire flow field.

**Lack of accurate low-order models.** Clearly, the few reduced-order models that are present so far are not sufficient to be able to capture the essential dynamics of the flow generated by a ZNMF actuator. Better models must be constructed to account for the slot geometry and the impact of the crossflow on the jet velocity profile. Clearly, the task of extracting a validated semi-empirical model is far from trivial. But leveraging past experience is critical to yielding accurate low-order models for implementation of a ZNMF actuator.

#### **1.4 Objectives**

Currently, it is difficult for a prospective user to successfully choose and use the appropriate actuator that will satisfy specific requirements. Even though many designs have been used in the literature, no studies have systematically studied the optimal design of these devices. For instance, how large should the cavity be? What type of driver is most appropriate to a specific application? Possibilities include a low cost, low power piezoelectric-diaphragm, an electromagnetic or mechanical piston that will provide large flow rate but may require significant power, or a voice-coil speaker typically used in audio applications? What orifice geometry should be chosen? Options include sharp versus rounded edges, large versus short thickness, an axisymmetric versus a rectangular slot? Clearly, no validated tools are currently available for end users to address these questions. Generally, a trial and error method using expensive experimental studies and/or time consuming numerical simulations have been employed.

The present work seeks to address these issues by providing a clear physical understanding of how these devices behave and interact with and without an external flow, and by developing and validating reduced-order dynamical models and scaling laws. Successful completion of these objectives will ultimately aid in the analysis and development of design tools for sizing, design and deployment of ZNMF actuators in flow control applications.

#### **1.5 Approach and Outline of Report**

To reach the stated objectives, the following technical approach has been employed. First, the identification of outstanding key issues and the formulation of the problem have been addressed in this section by surveying the literature concerning the modeling in diverse applications of ZNMF actuators and acoustic liner technology. The relevant information about the key device parameters and flow conditions (like the driver configuration, cavity, orifice shape, or the external boundary layer parameters) are thus extracted. Before investigating how a ZNMF device interacts with an external boundary

layer, the case of an isolated ZNMF actuator must be fully understood and documented. This is the subject of Section 2. An isolated ZNMF device is first characterized and the relevant parameters are defined. Then, the previous work done by the author in Gallas et al. (2003a) is summarized. Their work discusses a lumped element model of a piezoelectric-driven ZNMF actuator. One goal of the present work is to extend their model to more general devices and to remove, as far as possible, some restricting limitations, especially on the orifice loss coefficient. Consequently, a thorough nondimensional analysis is first carried out to extract the physics behind such a device.

Also, some relevant modeling issues are discussed and reviewed, for instance on the orifice geometry effects and the driving transducer dynamics. Then, to study in great details the dynamics of isolated ZNMF actuators, an extensive experimental investigation is proposed where various test actuator configurations are examined over a wide range of operating conditions. The experimental setup is described in Section 3.

## **2. Dynamics of Isolated Zero-Net Mass-Flux Actuators**

Several key issues were highlighted in the introduction section that will be addressed in this report. This Section is first devoted to familiarize the reader with the dynamics of ZNMF actuators, their behavior and inherent challenges in developing tools to accurately model them. One goal, before addressing the general case of the interaction with an external boundary layer, is to understand the nonlinear dynamics of an isolated ZNMF actuator. This section is therefore entirely dedicated to the analysis of isolated ZNMF actuators issuing into a quiescent medium, as outlined below.

The device is first characterized and the relevant parameters defined in order to clearly define the scope of the present investigation. The previous work performed by the author in Gallas et al. (2003a) is next summarized. Their work discusses a lumped element model of a piezoelectric-driven ZNMF actuator that relates the output volume flow rate to the input voltage in terms of a transfer function. Their model is extended to more general devices and solutions to remove some restricting limitations are explored. Based on this knowledge, a thorough dimensional analysis is then carried out to extract the physics behind an isolated ZNMF actuator. A dimensionless linear transfer function is also derived for a generic driver configuration, which is thought to be relevant as a design tool. It is shown that a compact expression can be obtained regardless of the orifice geometry and regardless of the driver configuration. Finally, relevant modeling issues pointed out in the first section are discussed and reviewed. Some issues are then addressed, more particularly on the modeling of the orifice flow where a temporal analysis of the existing lumped element model is proposed along with a physically-based discussion on the orifice loss mechanism. Issues on the dynamics of the driving transducer are discussed as well. Finally, a test matrix constructed to study the ZNMF actuator dynamics is presented.

### **2.1 Characterization and Parameter Definitions**

Figure 1-1 shows a typical ZNMF actuator, where the geometric parameters are shown. First of all, it is worthwhile to define some precise quantities of interest that have been used in the published literature and try to unify them into a generalized form. For instance, people have used the impulse stroke length, some spatially or time averaged exit velocities, or Reynolds numbers based either on the circulation of vortex rings or on an



averaged jet velocity to characterize the oscillating orifice jet flow. Here, an attempt to unify them is made.

The inherent nature of the jet is both a function of time (oscillatory motion) and of space (velocity distribution across the orifice exit area). It is also valuable to distinguish the ejection from the ingestion portion of a cycle. Many researchers (Smith and Glezer 1998, Glezer and Amitay 2002) characterize a synthetic jet based on a simple “slug velocity profile” model that includes a dimensionless stroke length  $L_0/d$  and a Reynolds number  $Re_{v_{cl}} = V_{CL}d/\nu$  based on the velocity scale (average orifice velocity) such that

$$V_{CL} = fL_0 = f \int_0^{T/2} v_{CL}(t) dt, \quad (1-1)$$

where  $v_{CL}(t)$  is the centerline velocity,  $T = 1/f$  is the period, thereby  $T/2$  representing half the period or the time of discharge for a sinusoidal signal, and  $L_0$  is the distance that a “slug” of fluid travels away from the orifice during the ejection portion of the cycle or period.

In addition, Smith and Glezer (1998) have employed a Reynolds number based on the impulse per unit length (i.e., the momentum associated with the ejection per unit width),  $Re_{I_0} = I_0/\mu d$ , where the impulse per unit width is defined as

$$I_0 = \rho d \int_0^{T/2} v_{CL}^2(t) dt. \quad (1-2)$$

Or similarly, following the physics of vortex ring formation (Glezer 1988), a Reynolds number,  $Re_\Gamma = \Gamma_0/\nu$ , is used based on the initial circulation associated with the vortex generation process, with  $\Gamma_0$  defined by

$$\Gamma_0 = \frac{1}{2} \int_0^{T/2} v_{CL}^2(t) dt = \frac{1}{2} \frac{T}{2} \overline{V_{CL}^2}. \quad (1-3)$$

Alternatively (Utturkar et al. 2003), a spatial and time-averaged exit velocity during the expulsion stroke is used to define the Reynolds number  $Re = \overline{V_j}d/\nu$ , where the time-averaged exit velocity  $\overline{V_j}$  is defined as

$$\overline{V_j} = \frac{2}{T} \frac{1}{S_n} \int_{S_n} \int_0^{T/2} v(t, x) dt dS_n = \frac{2}{T} \int_0^{T/2} \hat{v}(t) dt, \quad (1-4)$$

where  $\hat{v}(t)$  is the spatial averaged velocity,  $S_n$  is the exit area of the orifice neck, and  $x$  is the cross-stream coordinate (see Figure 1-2 for coordinates definition). For general purposes, instead of limiting ourselves to a simple uniform “slug” profile, the latter definition is considered throughout this report.

Notice that for a “slug” profile, it can be shown that the average orifice velocity scale defined above in Eq. 1-1 and Eq. 1-4 is related by  $V_{CL} = 2\bar{V}_j$ . Similarly,  $L_0/d = V_{CL}/(fd)$  is closely related to the inverse of the Strouhal number  $St$  since

$$\frac{L_0}{d} = \frac{V_{CL}}{fd} = \frac{2\bar{V}_j}{\omega d/2\pi} = \pi \frac{\bar{V}_j}{\omega d} = \pi \frac{1}{St}, \quad (1-5)$$

and since

$$\frac{1}{St} = \frac{\bar{V}_j}{\omega d} = \frac{\bar{V}_j d}{\nu} \frac{\nu}{d^2 \omega} = \frac{Re}{S^2}, \quad (1-6)$$

the following relationship always holds

$$\frac{1}{St} = \frac{Re}{S^2} = \frac{L_0/d}{\omega \tau}, \quad (1-7)$$

where  $\tau$  is the time of discharge ( $= T/2$  for a sinusoidal signal) and  $S = \sqrt{\omega d^2/\nu}$  is the Stokes number. The use of the Stokes number to characterize a synthetic jet and the relationship to the Strouhal number were previously mentioned in Utturkar et al. (2003) and Rathnasingham and Breuer (1997). The corresponding relations between the different definitions are summarized in Table 2-1.

Correspondingly, the volume flow rate coming out of the orifice during the ejection part of the cycle can be defined as

$$\bar{Q}_j = \frac{1}{\tau} \int_{S_n} \int_0^\tau v(t, x) dt dS_n = \bar{V}_j S_n. \quad (1-8)$$

And clearly, since we are dealing with a zero-net mass flux actuator, the following relationship always holds

$$\bar{Q}_{j,\text{total}} = \bar{Q}_{j,\text{ex}} + \bar{Q}_{j,\text{in}} = 0, \quad (1-9)$$

where the suffices ‘ex’ and ‘in’ stand for ‘expulsion’ and ‘ingestion’, respectively.

Table 2-1: Correspondence between synthetic jet parameter definitions

$\frac{L_0}{d}$	$\rightarrow \left( \times \frac{1}{\omega \tau} \right) \rightarrow$	$\frac{1}{St} = \frac{Re}{S^2}$
$Re_{l_0}, Re_{\Gamma_0}$	$\rightarrow$	$Re$

As seen from the above definitions, once a velocity or time scale has been chosen, a length scale must be similarly selected for the orifice or slot. Figure 1-3 show two typical orifice geometries encountered in a ZNMF actuator, and give the geometric parameters

and coordinates definition. Notice that the orifice is straight in both cases. No beveled, rounded or other shapes are taken into account, although other geometries have been investigated (Bridges and Smith 2001; Smith and Swift 2003b; Milanovic & Zaman 2005; Shuster and Smith 2004). Throughout this report, the primary length scale used is the diameter or depth of the orifice  $d$ . The spanwise orifice width  $w$  is used as needed for discussions related to a rectangular slot, and the height  $h$  is a third characteristic dimension. Clearly, if  $d$  is chosen as the characteristic length scale, then  $w/d$  and  $h/d$  are key nondimensional parameters.

## 2.2 Dimensional Analysis

### 2.2.1 Definition and Discussion

In the first part of this section, the primary output variables of interest have been defined, and specifically the spatial and time-averaged ejection velocity of the jet  $\overline{V}_j$  defined in Eq. 1-4. It is then interesting to rewrite them in terms of pertinent dimensionless parameters. Using the Buckingham-Pi theorem (Buckingham 1914), the dependence of the jet output velocity can be written in terms of nondimensional parameters.

$$\left. \begin{array}{c} |Q_j/Q_d| \\ St \\ Re \end{array} \right\} = fn \left( \frac{\omega}{\omega_H}, \frac{h}{d}, \frac{w}{d}, \frac{\omega}{\omega_d}, \frac{\Delta \nabla}{d^3}, kd, S \right). \quad (1-10)$$

The quantities in the left hand side of the functional are possible choices that the dependent variable  $\overline{V}_j$  can take.  $Q_j/Q_d$  represents the ratio of the volume flow rate of the driver ( $|Q_d| = \omega_d \Delta \nabla$ ) to the jet volume flow rate of the ejection part.  $St$  is the Strouhal number and  $Re$  is the jet Reynolds number defined earlier. Notice the close relationship between the jet Reynolds number, the Stokes number and the Strouhal number that were given by Eq. 1-7 and found again here by manipulation of the  $\Pi$ -groups. Therefore, for a given geometric configuration, either the Strouhal or the Reynolds numbers along with the Stokes number could suffice to characterize the jet exit behavior. It is also interesting to view Eq. 1-7 as the basis for the jet formation criterion defined by Utturkar et al. (2003). Actually, it is intrusive to look at the different physical interpretations that the Strouhal number can take. In the fluid dynamics community, it is usually defined as the ratio of the unsteady to the steady inertia. However, it can also be interpreted as the ratio of 2 length scales or 2 time scales, such that

$$\left\{ \begin{array}{l} St = \frac{\omega d}{\overline{V}_j} = \frac{d}{\overline{V}_j / \omega} \approx \frac{d}{L_0} \\ St = \frac{\omega d}{\overline{V}_j} = \frac{\omega}{\overline{V}_j / d} \approx \frac{t_{\text{oscillation}}}{t_{\text{convection}}} \end{array} \right. \quad (1-11)$$

where  $d/L_0$  is the ratio of a typical length scale  $d$  of the orifice to the particle excursion  $L_0$  through the orifice. The Strouhal number can also be the ratio of the oscillation time scale to the convective time scale.

The physical significance of each term in the RHS of Eq. 1-10 is described below:

- $\omega/\omega_H$  is the ratio of the driving frequency to the Helmholtz frequency  $\omega_H = c_0 \sqrt{S_n/h'\nabla}$ , a measure of the compressibility of the flow inside the cavity.
- $h/d$  is the orifice/slot height to diameter aspect ratio.
- $w/d$  is the orifice/slot width to diameter aspect ratio.
- $\omega/\omega_d$  is the ratio of the operating frequency to the natural frequency of the driver.
- $\Delta\nabla/d^3$  is the ratio of the displaced volume by the driver to the orifice diameter cubed.
- $kd = d/\lambda$  is the ratio of the orifice diameter to the acoustic wavelength.
- $S = \sqrt{\omega d^2/\nu}$  is the Stokes number, the ratio of the orifice diameter to the unsteady boundary layer thickness in the orifice  $\sqrt{\nu/\omega}$ .

It is evident that in the case of an isolated ZNMF actuator, the response is strongly dependant on the geometric parameters  $\{\omega/\omega_H, h/d, w/d, kd\}$  and the operating conditions  $\{\omega/\omega_d, \Delta\nabla/d^3, S\}$ . In fact, from the functional form described by Eq. 1-10 and for a given device with fixed dimensions and a given fluid, the actuator output is only dependent on the driver dynamics  $(\omega_d, \Delta\nabla)$  and the actuation frequency  $\omega$ .

Although compressibility effects in the orifice are neglected in this report, it warrants a few lines. Compressibility will occur in the orifice for high Mach number flows and/or for high density flows. If the compressibility of the fluid has to be taken into account, it follows by definition that density must be considered as a new variable. For instance, the pressure is now coupled to the temperature and density through the equation of state. Similarly, the continuity equation is no longer trivial. Also, temperature is important, and one has to reminder that the variation of the thermal conductivity  $k$  and dynamic viscosity  $\mu$  - that are transport quantities - with temperature may be important.

### 2.2.2 Dimensionless Linear Transfer Function for a Generic Driver

Valuable physical insight into the dependence of the device behavior on geometry and material properties is provided by the frequency response of the ZNMF actuator device. In order to obtain an expression of the linear transfer function of the jet output to the input signal to the actuator, the compact nonlinear analytical model given by LEM is used in a similar manner as described and introduced in the previous section, since it was shown to be a valuable design tool. Notice however that the nonlinear part of the model in its present form -only confined in the orifice- is neglected for simplicity in this analysis. Figure 2-1 shows a schematic representation of a ZNMF actuator having a generic driver using LEM. This representation enables us to bypass the need of an

expression for the acoustic impedance  $Z_{aD}$  of the driving transducer, although it lacks its dynamics modeling.

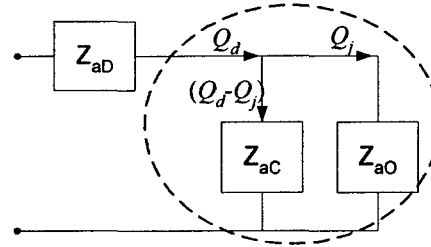


Figure 2-1: Schematic representation of a generic-driver ZNMF actuator.

In this case, a convenient representation of the transfer function is to normalize the jet volume flow rate by the driver volume flow rate,  $Q_j/Q_d$ , and obtain an expression via the current/flow divider shown in Figure 2-1,

$$\begin{aligned} \frac{Q_j(s)}{Q_d(s)} &= \frac{Z_{aC}}{Z_{aC} + Z_{aO}} = \frac{1/sC_{aC}}{1/sC_{aC} + R_{aO} + sM_{aO}} \\ &= \frac{1}{\frac{1}{C_{aC}M_{aO}} + \frac{R_{aO}}{M_{aO}}s + s^2} \end{aligned} \quad (1-12)$$

assuming that the acoustic orifice impedance  $Z_{aO} = R_{aO} + M_{aO}$  only contains the linear resistance  $R_{aN}$  and the radiation mass  $M_{aRad}$  is neglected or added to  $M_{aO}$ .

Knowing that the Helmholtz resonator frequency of the actuator is defined by

$$\omega_H = \sqrt{\frac{1}{C_{aC}M_{aO}}}, \quad (1-13)$$

and the damping ratio of the system by

$$\zeta = \frac{1}{2} R_{aN} \sqrt{\frac{C_{aC}}{M_{aO}}}, \quad (1-14)$$

by substituting in Eqs. 1-13 and 1-14, Eq. 1-12 can then be rewritten as

$$\frac{Q_j(s)}{Q_d(s)} = \frac{\omega_H^2}{s^2 + 2\zeta\omega_H s + \omega_H^2}. \quad (1-15)$$

This is a second-order system whose performance is set by the resonator Helmholtz frequency. Figure 2-2 below shows the effect of the damping coefficient  $\zeta$  on the

frequency response of  $Q_j/Q_d$ , where for  $\zeta < 1$  the system is said to be underdamped, and for  $\zeta > 1$  the system is overdamped. The damping coefficient controls the amplitude of the resonance peak, allowing the system to yield more or less response at the Helmholtz frequency.

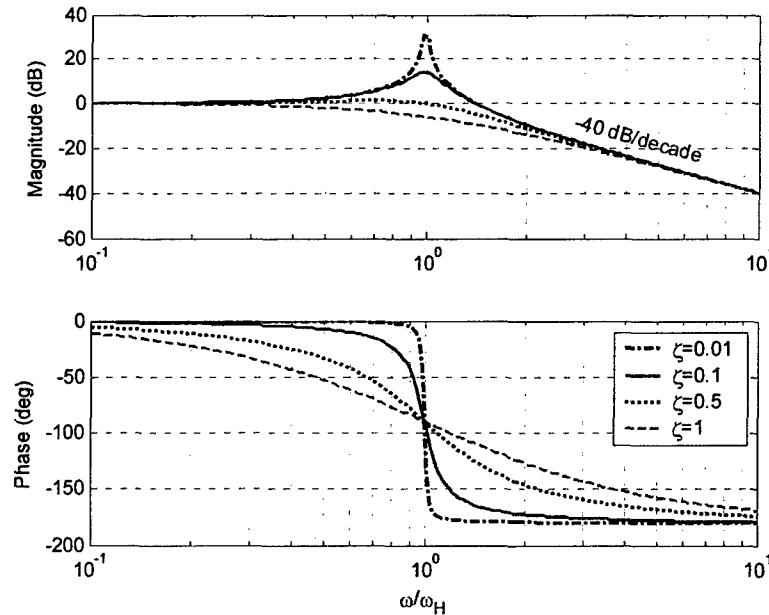


Figure 2-2: Bode diagram of the second order system given by Eq. 1-15, for different damping ratio.

Since the expression of  $\omega_H$  differs from the orifice geometry, two different cases are examined and summarized in

Table 2-2. The damping coefficient is found from the following arrangement (shown for the case of a circular orifice, but one can similarly arrive at the same result for a rectangular slot)

$$\begin{aligned}\zeta &= \frac{1}{2} \left( \frac{8\mu h}{\pi (d/2)^4} \right) \sqrt{\frac{\nabla / (\rho c_0^2)}{(4\rho h) / (3\pi (d/2)^2)}} = \sqrt{\frac{64^2 \mu^2 h^2 \nabla}{\pi^2 d^8 (6) \rho c_0^2} \frac{3\pi d^2}{16\rho h}} \\ &= \sqrt{768 \frac{\nabla h}{\pi d^2 c_0^2} \frac{\nu^2}{d^4} \left( \frac{\omega}{\omega} \right)^2} = \sqrt{144 \frac{16\nabla h}{3\pi d^2 c_0^2} \frac{\nu^2}{d^4 \omega^2} \omega^2} \quad (1-16)\end{aligned}$$

that is,

$$\zeta = 12 \frac{\omega}{\omega_H} \frac{1}{S^2} \quad (1-17)$$

Table 2-2: Dimensional parameters for circular and rectangular orifices

	Circular orifice	Rectangular slot
$Q_d$ (m <sup>3</sup> /s)	$j\omega_d\Delta\forall$	$j\omega_d\Delta\forall$
$\omega_H$ (rad/s)	$\sqrt{\frac{3\pi(d/2)^2 c_0^2}{4h\forall}}$	$\sqrt{\frac{5w(d/2)c_0^2}{3h\forall}}$
$C_{aC}$ (s <sup>2</sup> m <sup>4</sup> /kg)	$\frac{\forall}{\rho c_0^2}$	$\frac{\forall}{\rho c_0^2}$
$R_{aN}$ (kg/m <sup>4</sup> ·s)	$\frac{8\mu h}{\pi(d/2)^4}$	$\frac{3\mu h}{2w(d/2)^3}$
$M_{aN}$ (kg/m <sup>4</sup> )	$\frac{4\rho h}{3\pi(d/2)^2}$	$\frac{3\rho h}{5w(d/2)}$
$\zeta = \frac{1}{2}R_{aN}\sqrt{\frac{C_{aC}}{M_{aN}}}$	$12\frac{\omega}{\omega_H}\frac{1}{S^2}$	$5\frac{\omega}{\omega_H}\frac{1}{S^2}$

Notice that the damping coefficient has the same fundamental expression whether the orifice is circular or rectangular, the difference being incorporated in a multiplicative constant. Substituting these results into Eq. 1-15 and replacing the Laplace variable  $s = j\omega$  yields the final form for a *generic* driver and a *generic* orifice

$$\frac{Q_j}{Q_d} = \frac{Q_j(\omega)}{j\omega\Delta\forall} \approx \frac{1}{\left[1 - \left(\frac{\omega}{\omega_H}\right)^2\right] + j\left[\frac{1}{S}\left(\frac{\omega}{\omega_H}\right)\right]^2}. \quad (1-18)$$

Clearly, the advantage of non-dimensionalizing the jet volume flow rate by the driver flow rate allows us to isolate the driver dynamics from the main response, thereby decoupling the effect of the various device components from each other. Eq. 1-18 is an important result in predicting the linear system response in terms of the nondimensional parameters  $\omega/\omega_d$ ,  $\omega/\omega_H$ , and  $S$  as a function of the driver performance. It yields such interesting results that actually a thorough analysis of Eq. 1-18 is provided in details in Section 5 where the reader is referred to for completeness.

To summarize, this section has provided a dimensional analysis of an isolated ZNMF actuator. A compact expression, in terms of the principal dimensionless parameters, has been found for the nondimensional transfer function that relates the output to the input of the actuator. Most importantly, such an expression was derived regardless of the orifice geometry and regardless of the driver configuration. Next, with this knowledge gained, the modeling issues presented earlier in the introduction section and at the beginning of this section are further considered.

### 2.3 Test Matrix

A significant database forms the basis of a test matrix that includes direct numerical simulations and experimental results. The test matrix is comprised of various test

actuator configurations that are examined to ultimately assess the accuracy of the developed reduced-order models over a wide range of operating conditions.

The goal is to test various actuator configurations in order to cover a wide range of operating conditions, in a quiescent medium, by varying the key dimensionless parameters extracted in the above dimensional analysis. Available numerical simulations are used along with experimental data performed in the Fluid Mechanics Laboratory at the University of Florida on a single piezoelectric-driven ZNMF device exhausting in still air. Table 2-3 describes the test matrix. The first six cases are direct numerical simulations (DNS) from the George Washington University under the supervision of Prof. Mittal. They use a 2D DNS simulation. Case 8 comes from the first test case of the NASA LaRC workshop (CFDVal 2004). Then, Case 9 to Case 72 are experimental test cases performed at the University of Florida for axisymmetric piezoelectric-driven ZNMF actuators. The experimental setup is described in details in Section 3, and the results are systematically analyzed and studied in Section 4, Section 5, and Section 6.

Table 2-3: Test matrix for ZNMF actuator in quiescent medium

Case	Type	$f$ (Hz)	$d$ (mm)	$h$ (mm)	$w/d$	$\nabla$ (mm <sup>3</sup> )	$S$	Re	$St$	$f/f_H$	$f/f_a$	Jet
1	CFD	0.38	1	1	$\infty$	800	25.0	262	2.4	0.13	—	X
2	CFD	0.38	1	2	$\infty$	800	25.0	262	2.4	0.15	—	X
3	CFD	0.06	1	0.68	$\infty$	360	10.0	262	0.4	0.01	—	J
4	CFD	0.20	0.1	0.1	$\infty$	800	5.0	63.6	0.4	0.00	—	J
5	CFD	0.80	0.1	0.1	$\infty$	800	10.0	255	0.4	0.01	—	J
6	CFD	1.99	0.1	0.1	$\infty$	800	15.8	477	0.5	0.03	—	J
7	CFD	1.99	0.1	0.1	$\infty$	800	15.8	636	0.4	0.03	—	J
8	exp/cfd	446	1.27	13.5	28	7549	17.1	861	0.3	2.65	0.99	J
9	exp.	39	1.9	1.8	—	7109	7.6	8.79	6.6	0.06	0.06	X
Case	Type	$f$ (Hz)	$d$ (mm)	$h$ (mm)	$w/d$	$\nabla$ (mm <sup>3</sup> )	$S$	Re	$St$	$f/f_H$	$f/f_a$	Jet
10	exp.	39	1.9	1.8	—	7109	7.6	12.0	4.8	0.06	0.06	J
11	exp.	39	1.9	1.8	—	7109	7.6	22.6	2.5	0.06	0.06	J
12	exp.	39	1.9	1.8	—	7109	7.6	33.2	1.7	0.06	0.06	J
13	exp.	39	1.9	1.8	—	7109	7.6	39.8	1.4	0.06	0.06	J
14	exp.	39	1.9	1.8	—	7109	7.6	46.5	1.2	0.06	0.06	J
15	exp.	39	1.9	1.8	—	7109	7.6	52.5	1.1	0.06	0.06	J
16	exp.	39	1.9	1.8	—	7109	7.6	59.7	1.0	0.06	0.06	J
17	exp.	39	1.9	1.8	—	7109	7.6	66.0	0.9	0.06	0.06	J
18	exp.	39	1.9	1.8	—	7109	7.6	73.7	0.8	0.06	0.06	J
19	exp.	39	1.9	1.8	—	7109	7.6	81.6	0.7	0.06	0.06	J
20	exp.	39	1.9	1.8	—	7109	7.6	88.2	0.6	0.06	0.06	J
21	exp.	780	1.9	1.8	—	7109	34.0	192	6.0	1.24	1.23	X
22	exp.	780	1.9	1.8	—	7109	34.0	242	4.8	1.24	1.23	J
23	exp.	780	1.9	1.8	—	7109	34.0	374	3.1	1.24	1.23	J
24	exp.	780	1.9	1.8	—	7109	34.0	513	2.2	1.24	1.23	J
25	exp.	780	1.9	1.8	—	7109	34.0	637	1.8	1.24	1.23	J
26	exp.	780	1.9	1.8	—	7109	34.0	750	1.5	1.24	1.23	J
27	exp.	780	1.9	1.8	—	7109	34.0	825	1.4	1.24	1.23	J
28	exp.	780	1.9	1.8	—	7109	34.0	930	1.2	1.24	1.23	J
29	exp.	780	1.9	1.8	—	7109	34.0	1131	1.1	1.24	1.23	J
30	exp.	780	1.9	1.8	—	7109	34.0	1120	1.0	1.24	1.23	J
31	exp.	780	1.9	1.8	—	7109	34.0	1200	1.0	1.24	1.23	J



32	exp.	780	1.9	1.8	—	7109	34.0	1264	0.9	1.24	1.23	J
33	exp.	780	1.9	1.8	—	7109	34.0	1510	0.8	1.24	1.23	J
34	exp.	780	1.9	1.8	—	7109	34.0	1589	0.7	1.24	1.23	J
35	exp.	780	1.9	1.8	—	7109	34.0	1683	0.7	1.24	1.23	J
36	exp.	780	1.9	1.8	—	7109	34.0	1774	0.6	1.24	1.23	J
37	exp.	780	1.9	1.8	—	7109	34.0	1842	0.6	1.24	1.23	J
38	exp.	780	1.9	1.8	—	7109	34.0	1876	0.6	1.24	1.23	J
39	exp.	780	1.9	1.8	—	7109	34.0	2755	0.4	1.24	1.23	J
40	exp.	1200	1.9	1.8	—	7109	42.1	90.8	19.5	1.91	1.90	X
41	exp.	39	2.98	1.05	—	7109	11.9	40.6	3.49	0.04	0.06	J
42	exp.	39	2.98	1.05	—	7109	11.9	47.3	2.99	0.04	0.06	J
43	exp.	39	2.98	1.05	—	7109	11.9	63.4	2.23	0.04	0.06	J
44	exp.	500	2.98	1.05	—	7109	42.6	1959	0.93	0.55	0.79	J
45	exp.	500	2.98	1.05	—	7109	42.6	2615	0.69	0.55	0.79	J
46	exp.	780	2.98	1.05	—	7109	53.2	109	26.0	0.86	1.23	X
47	exp.	780	2.98	1.05	—	7109	53.2	254	11.2	0.86	1.23	X
48	exp.	780	2.98	1.05	—	7109	53.2	571	4.96	0.86	1.23	J
49	exp.	780	2.98	1.05	—	7109	53.2	1439	1.97	0.86	1.23	J
50	exp.	780	2.98	1.05	—	7109	53.2	2022	1.40	0.86	1.23	J
51	exp.	39	2.96	4.99	—	7109	11.8	29.8	4.69	0.06	0.06	J
52	exp.	39	2.96	4.99	—	7109	11.8	43.0	3.25	0.06	0.06	J
53	exp.	39	2.96	4.99	—	7109	11.8	55.7	2.51	0.06	0.06	J
54	exp.	39	2.96	4.99	—	7109	11.8	71.9	1.94	0.06	0.06	J
55	exp.	780	2.96	4.99	—	7109	52.9	125	22.3	1.25	1.23	X
56	exp.	780	2.96	4.99	—	7109	52.9	318	8.79	1.25	1.23	X
57	exp.	780	2.96	4.99	—	7109	52.9	867	3.22	1.25	1.23	J
58	exp.	780	2.96	4.99	—	7109	52.9	2059	1.36	1.25	1.23	J
59	exp.	780	2.96	4.99	—	7109	52.9	3039	0.92	1.25	1.23	J

Case	Type	$f$ (Hz)	$d$ (mm)	$h$ (mm)	$w/d$	$\nabla$ (mm <sup>3</sup> )	$S$	$Re$	$St$	$f/f_H$	$f/f_a$	$Jet$
60	exp.	39	1.0	5.0	—	7109	4.0	132	0.12	0.16	0.06	J
61	exp.	39	1.0	5.0	—	7109	4.0	157	0.10	0.16	0.06	J
62	exp.	39	1.0	5.0	—	7109	4.0	205	0.08	0.16	0.06	J
63	exp.	500	1.0	5.0	—	7109	14.3	286	0.72	2.10	0.79	J
64	exp.	500	1.0	5.0	—	7109	14.3	461	0.44	2.10	0.79	J
65	exp.	730	1.0	5.0	—	7109	17.3	269	1.11	3.07	1.16	J
66	exp.	730	1.0	5.0	—	7109	17.3	611	0.49	3.07	1.16	J
67	exp.	730	1.0	5.0	—	7109	17.3	893	0.33	3.07	1.16	J
68	exp.	730	1.0	5.0	—	7109	17.3	1081	0.28	3.07	1.16	J
69	exp.	730	1.0	5.0	—	7109	17.3	1361	0.22	3.07	1.16	J
70	exp.	39	0.98	0.92	—	7109	3.9	49.6	0.31	0.09	0.06	J
71	exp.	39	0.98	0.92	—	7109	3.9	112	0.14	0.09	0.06	J
72	exp.	39	0.98	0.92	—	7109	3.9	179	0.09	0.09	0.06	J

To conclude this section, a dimensional analysis of an isolated ZNMF actuator was performed. A compact expression, in terms of the principal dimensionless parameters, was found for the nondimensional linear transfer function that relates the output to the input of the actuator, regardless of the orifice geometry and of the driver configuration. Next, some modeling issues have been investigated for the different components of a ZNMF actuator. Specifically, the LEM technique has been used in the time domain to

yield some insight on the orifice shape effect, and a physical description on the associated orifice losses has been provided. Finally, since one of the goals of this research is to develop a refined low-order model, which is presented in Section 6 and that builds on the results presented in the subsequent sections, a significant database forms the basis of a test matrix that is comprised of direct numerical simulations and experimental results.

### **3. Experimental Setup**

This section provides the details on the design and the specifications of the ZNMF devices used in the experimental study. Descriptions of the cavity pressure, driver deflection, and actuator exit velocity measurements are provided, along with the dynamic data acquisition system employed. Then, the data reduction process is presented with some general results. A description of the Fourier series decomposition applied to the phase-locked, ensemble average time signals is presented next. Finally, a description of the flow visualization technique employed to determine if a synthetic jet is formed is then provided.

#### **3.1 Experimental Setup**

In this report, two different experiments are performed. The first one, referred to as Test 1, is used in the orifice flow analysis presented in Section 4 and the corresponding test cases are listed in Table 2-3. The second test, Test 2, is used in the cavity compressibility analysis (presented in Section 5). Test 1 consists of phase-locked measurements of the velocity profile at the orifice, cavity pressure, and diaphragm deflection, and the device uses a large diaphragm and has an axisymmetric straight orifice. On the other hand, in Test 2 only the frequency response of the centerline velocity and driver displacement are acquired, and the device uses a small diaphragm and the orifice is a rectangular slot. However, since the two tests share the same equipment and basic setup and Test 1 requires additional equipment, only Test 1 is detailed below.

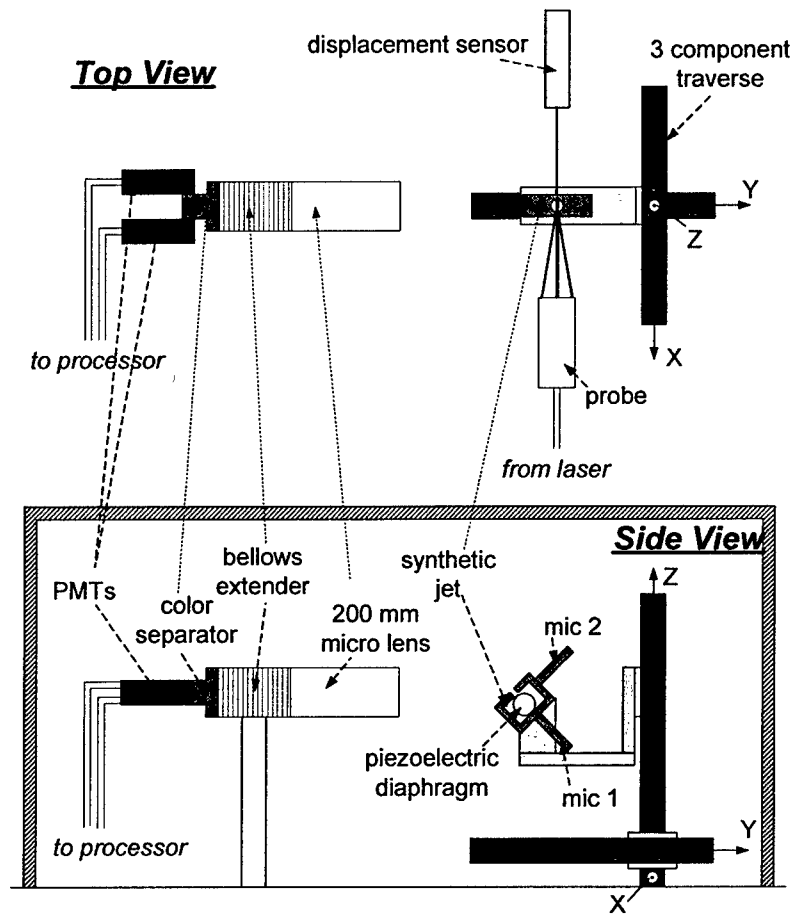


Figure 3-1: Schematic of the experimental setup for phase-locked cavity pressure, diaphragm deflection and off-axis, two-component LDV measurements.

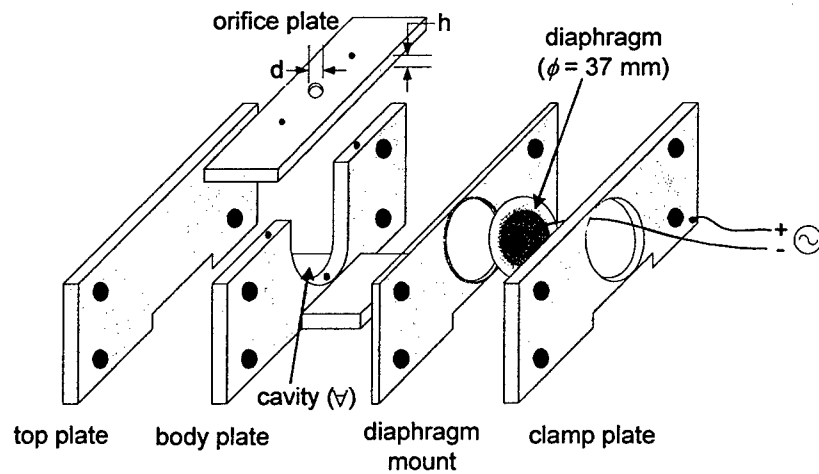


Figure 3-2: Exploded view of the modular piezoelectric-driven ZNMF actuator used in the experimental test.

Figure 3-1 shows a schematic of the complete experimental setup, where a large enclosure ( $2m \times 1m \times 1m$ ) is constructed with a tarp to house the ZNMF actuator device, the LDV transmitting and receiving optics, and the displacement sensor. The ZNMF actuator consists of a piezoelectric diaphragm driver mounted on the side of the cavity, and has an axisymmetric straight orifice. The commercially available diaphragm (APC International Ltd. Model APC 850) consists of a piezoelectric patch (PZT 5A) which is bonded to a metallic shim (made of brass). The diaphragm is clamped between two plates and have an effective diameter equals to 37 mm. Figure 3-2 gives an exploded view of the device and Table 3-1 summarizes the geometric dimensions.

Only the orifice top plate is changed to allow five orifice aspect ratio configurations, and the input voltage and actuation frequency are also varied to yield a large parameter space investigation in terms of the following dimensional parameters:  $\{h/d; S; Re; \omega/\omega_H; \omega/\omega_d; kd; \Delta\forall/d^3\}$ . An emphasis is made in the orifice aspect ratio variation, hence the five different orifices used, and the input sinusoidal voltage applied to the driver varies from 4 V<sub>pp</sub> to 60 V<sub>pp</sub>, the frequencies being set to 39, 500, 730 and 780 Hz. This device is constructed specifically to operate in the low-to-moderate Stokes number range,  $S < 60$ . The signal source is provided by an Agilent model 33120A function generator. The signal from the function generator is applied to a Trek amplifier (model 50/750), and the amplified sinusoidal input voltage signal is then applied to the driver via a small wire soldered to the piezoceramic patch, which converts the voltage into a mechanical deflection.

Since the two variable input parameters are the frequency of oscillation, the amplitude of the forcing signal, and the different orifice plates, the change in these dimensional parameters can be converted into a change in dimensionless numbers like the Stokes number  $S$ , the actuation-to-Helmholtz frequency ratio  $f/f_H$ , the driving-to-diaphragm natural frequency  $f/f_d$ , the dimensionless wavenumber  $kd$ , and the dimensionless driver amplitude  $\Delta\forall/d^3$ .

Table 3-1: ZNMF device characteristic dimensions used in Test 1

<b>Cavity</b>					
Volume $\nabla$ (m <sup>3</sup> )	7.11×10 <sup>-6</sup>				
<b>Orifice</b>					
Diameter $d$ (mm)	1.0	2.0	3.0	1.0	1.0
Height $h$ (mm)	5.0	1.8	1.0	0.9	5.0
<b>Piezoelectric diaphragm</b>					
<b>Shim (Brass)</b>					
Elastic modulus (Pa)	8.963×10 <sup>10</sup>				
Poisson's ratio	0.324				
Density (kg/m <sup>3</sup> )	8700				
Thickness (mm)	0.10				
Diameter (mm)	37				
<b>Piezoceramic (PZT-5A)</b>					
Elastic modulus (Pa)	6.3×10 <sup>10</sup>				
Poisson's ratio	0.31				
Density (kg/m <sup>3</sup> )	7700				
Thickness (mm)	0.11				
Diameter (mm)	25				
Relative dielectric constant	1750				
$d_{31}$ (m/V)	-1.75×10 <sup>-10</sup>				
$C_{ef}$ (nF)	76				

### 3.1.1 Cavity Pressure

The pressure fluctuations inside the cavity are measured simultaneously at two locations using flush-mounted Brüel and Kjær (B&K) 1/8" diameter condenser type microphones (Model 4138) powered by B&K 2670 pre-amplifiers and a B&K 2804 power supply. Before each test, the microphones are calibrated using a B&K pistonphone type 4228. The operational frequencies of the ZNMF device are usually from about 30 Hz to 1 kHz in this test, which is well within the frequency range of the microphone, from 6.5 Hz to 140 kHz ( $\pm 2$  dB). The nominal sensitivity of the B&K 4138 type microphones is  $-60 \pm 1.5$  dB (ref. 1V/Pa), or 1.0 mV/Pa. When assembling the device parts together, all leaks are carefully minimized by sealing the parts with RTV, and the pressure ports are properly sealed. Figure 3-3 shows a schematic of the two microphone measurement locations inside the cavity. Notice that for the highest frequency of operation (780 Hz), the ratio of the wavelength ( $\lambda = c_0/f = 2\pi/k$ ) to the distance ( $l = 28.7\text{mm}$ ) separating the two microphones in the cavity is less than unity ( $kl < 0.41$ ), implying that the acoustic pressure waves inside the cavity change very little because the distance between microphones is small compared with the acoustic wavelength.

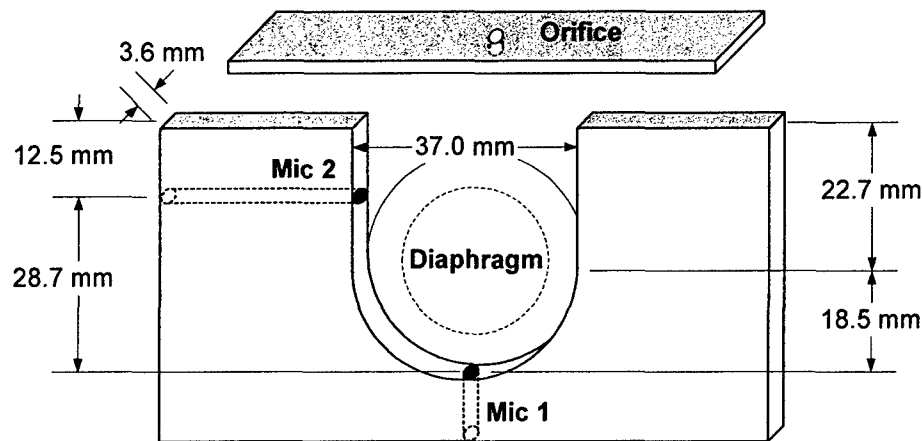


Figure 3-3: Schematic (to scale) of the location of the two 1/8" microphones inside the ZNMF actuator cavity.

### 3.1.2 Diaphragm Deflection

The deflection of the diaphragm is measured using a laser displacement sensor Micro-Epsilon Model ILD2000-10. The sensitivity is 1 V/mm, with a full-scale range of 10 mm and a resolution of  $\sim 0.1 \mu\text{m}$ . The sensor bandwidth is 10 kHz, and the spot size of the laser is  $40 \mu\text{m}$ . Figure 3-4 gives the displacement sensor sign convention between the measured deflection of the diaphragm and the measured voltage. As the diaphragm moves inside the actuator cavity, the distance  $d$  increases and the measured voltage increases as well. Conversely, as the diaphragm deflects away from the cavity, the distance  $d$  measured by the laser sensor decreases and the corresponding voltage decreases. Therefore, a positive diaphragm displacement implies the driver deflects to decrease the cavity volume, leading to compression of the fluid in the cavity and hence an increase in cavity pressure. On the contrary, a negative diaphragm displacement implies the diaphragm deflects to increase the cavity volume, thus expanding the fluid inside the cavity and causing a decrease in the pressure in the cavity.

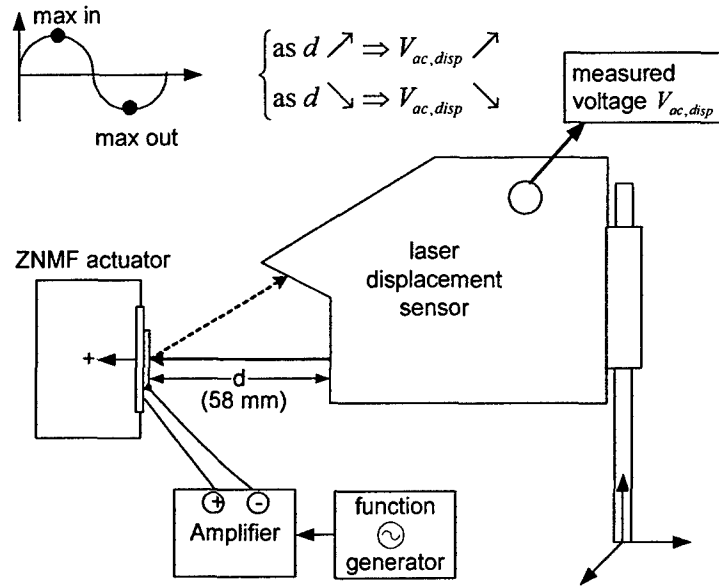


Figure 3-4: Laser displacement sensor apparatus to measure the diaphragm deflection with sign convention. *Not to scale.*

This measurement is used to determine the volume velocity ( $\text{m}^3/\text{s}$ )  $Q_d$  of the diaphragm. We actually use two techniques, depending on the ratio  $f/f_d$ . Recall that, assuming a sinusoidal steady state operating condition,  $Q_d$  is given by

$$Q_d = j\omega\Delta V = j\omega \int_{S_d} w^*(r) W_0 2\pi r dr \quad (2-1)$$

where  $w^*(r) = w(r)/W_0$  is the transverse displacement of the diaphragm normalized by the centerline amplitude  $W_0$ . Therefore, if one knows the diaphragm mode shape, then only  $W_0$  is required via measurement to calculate  $Q_d$  by virtue of Eq. 2-1. If the mode shape is not known, then it must also be measured. The former technique is thus a single-point measurement, where only the centerline displacement of the oscillating diaphragm is acquired phased-locked to the drive signal. The mode shape is computed using the static linear composite plate theory described in Prasad et al. (2002). This model is only valid from frequencies ranging from DC up to the first natural frequency  $f_d$ , hence the importance of the frequency ratio  $f/f_d$ . This piezoelectric diaphragm has its first natural frequency at about  $f_d \approx 632 \text{ Hz}$ . Then from Eq. 2-1, the diaphragm volume flow rate can be determined by simply integrating the mode shape of the circular piezoelectric diaphragm.

In the case where the frequency ratio  $f/f_d$  is greater than one, the static mode shape is no longer valid, so a second measurement technique is employed to experimentally acquire the mode shape by systematically traversing the laser displacement sensor across the diaphragm radius. The root-mean-square value of the

diaphragm deflection is computed for each position, and assuming a sinusoidal signal the amplitude is obtained by multiplying the rms value by a factor  $\sqrt{2}$ . This sinusoidal assumption was visually checked during the time of acquisition for all signals, and on some test cases a Fourier series decomposition was performed that validated this assumption, as described at the end of this Section. Figure 3-5 shows the measured and computed mode shape of the piezoelectric diaphragm at several forcing frequencies. In the case where  $f/f_d \leq 1$ , the comparison between the experimentally determined mode shape and the linear model shows good agreement. Similarly, the figure shows the diaphragm deflection along versus radius for the highest frequency used in this experimental test,  $f = 780 \text{ Hz}$ , which clearly indicates the breakdown of the static model. The slope discontinuity in the experimental data near the position  $r/a = 0.65$  corresponds to the edge of the piezoelectric patch that is bonded via epoxy on the metallic shim and is a result of optical diffraction of the laser beam at this location.

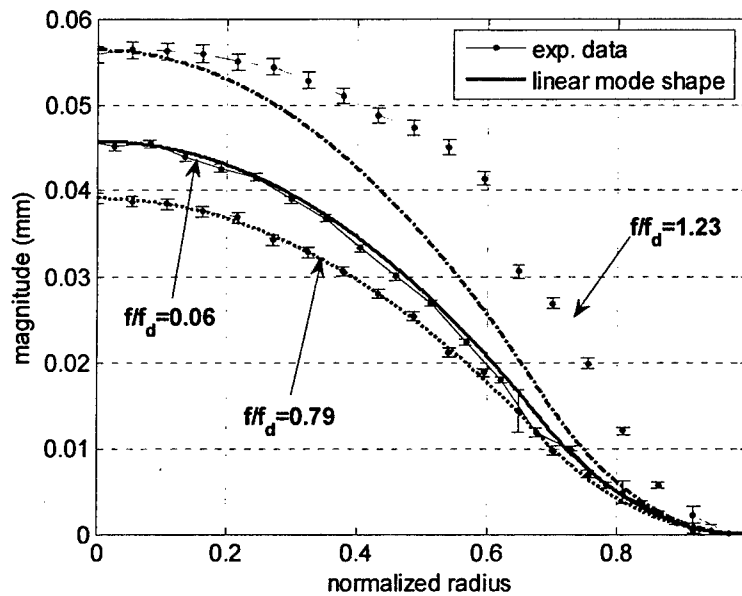


Figure 3-5: Diaphragm mode shape comparison between linear model and experimental data at three test conditions:  $f/f_d = 0.06$  and  $V_{ac} = 60 \text{ V}_{pp}$ ,  $f/f_d = 0.79$  and  $V_{ac} = 50 \text{ V}_{pp}$ , and  $f/f_d = 1.23$  and  $V_{ac} = 20 \text{ V}_{pp}$ .

### 3.1.3 Velocity Measurement

Velocity measurements of the flowfield emanating from the ZNMF orifice are obtained using Laser Doppler Velocimetry (LDV), the details of which are listed in Table 3-2. The synthetic jet actuator is mounted to a three-axis traverse with sub-micron spatial resolution to move the orifice with respect to the fixed laser probe volume location. The traverse is traversed in either 0.1 mm or 0.05 mm steps across the orifice, yielding a total of 31 to 41 positions at which the phase-locked velocities are measured, depending on the orifice diameter.

The enclosure shown in Figure 3-1 is seeded with LeMaitre haze fluid using a LeMaitre Neutron XS haze machine, where the haze particles have a mean diameter



small enough that it does not influence on the measured flow field (this is verified by computing the time constant  $\tau$  of the particle and then by showing that the particle response, which is like a 1<sup>st</sup>-order system, faithfully tracks velocity fluctuations at frequencies well below  $1/\tau$ . The reader is referred to Holman (2005) for the details and analysis on the seed particle dynamics).

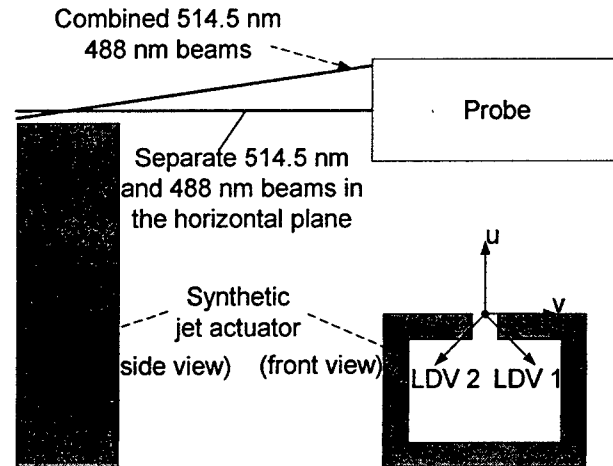


Figure 3-6: LDV 3-beam optical configuration.

The 488 and 514.5 nm wavelengths of a Spectra-Physics 2020 argon-ion laser are used to obtain coincident, two-component velocity measurements using a Dantec FiberFlow system. Typically, the beam strength is approximately 30 ~ 50 mW for the green (514.5 nm) and 15 ~ 20 mW for the blue (488 nm). As shown in Figure 3-6, a three-beam optical combiner configuration is used to facilitate velocity measurements at the exit plane surface of the synthetic jet actuator. Due to mounting constraints, the actuator is mounted at a 45° angle with respect to the horizontal such that the scattered light from the probe volume may reach the receiving optics. A direction cosine transformation is then applied to the acquired velocity components LDV 1 and LDV 2 to extract the axial and radial velocity components.

A 200 mm micro lens and bellows extender collects lights at 90° off-axis in order to improve the spatial resolution since only a slice of the probe volume is “seen” by the optics. Scattered light from the probe volume is focused and passed through a 100  $\mu\text{m}$  diameter pinhole aperture. The resulting field of view was imaged using a micro-ruler and found to be approximately 10  $\mu\text{m}$ , indicating that the effective length of the probe volume  $dz$  has been reduced by over an order of magnitude from that listed in Table 3-2. After the pinhole, a color separator splits the 514.5 nm and 488 nm wavelengths and transmits the light to two separate photomultiplier tubes (PMTs), which convert the Doppler signal to a voltage, and it is then passed through a high-pass filter to remove the Doppler pedestal. An additional band-pass filter is then applied to remove noise in the signal outside of the expected velocity range. Next, the FFT of the signals is computed, and the velocity is then computed from the measured Doppler frequency and the fringe spacing. Finally, since two components of velocity are measured, a coincidence filter is applied to ensure that a Doppler signal is present on both channels at the same instant in

time. At each radial measurement position, 8192 samples are acquired in both LDV1 and LDV2, which yields approximately 200 velocity values at each phase bin. Note that each data point has a time of arrival relative to the trigger signal that denotes the zero phase angle. The LDV data are then divided into phase bins with  $15^\circ$  spacing, as explained in more details in the data processing section.

Table 3-2: LDV measurement details

Property	LDV 1	LDV 2
Wavelength (nm)	514.5	488
Focal length (mm)	120	120
Beam diameter (mm)	1.35	1.35
Beam spacing (mm)	26.9	26.9
Number of fringes	25	25
Fringe spacing ( $\mu\text{m}$ )	2.31	2.19
Beam half-angle (deg)	6.39	6.39
Probe volume – $dx$ (mm)	0.058	0.056
Probe volume – $dy$ (mm)	0.058	0.055
Probe volume – $dz$ (mm)	0.523	0.496

### 3.1.4 Data-Acquisition System

Figure 3-7 shows a flow chart of the experimental setup. The piezoelectric diaphragm is actuated using an Agilent 33120A function generator with a Trek amplifier (Model 50/750). Using the sync signal of the function generator, the measured quantities are acquired in a phase-locked mode. A National Instruments model NI-4552 dynamic signal analyzer (DSA) PCI card is used for data acquisition (DAQ). It is a 16-bit, sigma-delta DAQ card that can sample up to 4 channels of analog input simultaneously and has a bandwidth of approximately 200 kHz. In addition, a built-in analog and digital anti-aliasing filter is used. The low-pass analog filter has a fixed cutoff frequency of 4 MHz, which is well above the frequencies considered here and may be considered to have zero phase offset in the passband. The digital filter removes all frequency components above the desired Nyquist frequency in the oversampled signal and then decimates the resulting signal to achieve the desired sampling rate.

Similarly, since the signals are ac coupled to remove any dc offset and to increase the resolution in the signal measurements, any slight amplitude attenuation and phase shift occurring at low frequencies due to the ac coupling high pass filter are accounted for. This ac coupling high pass filter has a  $-3$  dB cutoff frequency at approximately 3.4 Hz, and the  $-0.01$  dB cutoff frequency is approximately 70.5 Hz. Finally, to guarantee statistical accuracy in the results, for each signal 100 samples per period are used and at least 500 blocks of data are acquired. For signals having very low amplitude, up to 5000 blocks were taken to minimize noise in the acquired phase-locked data.

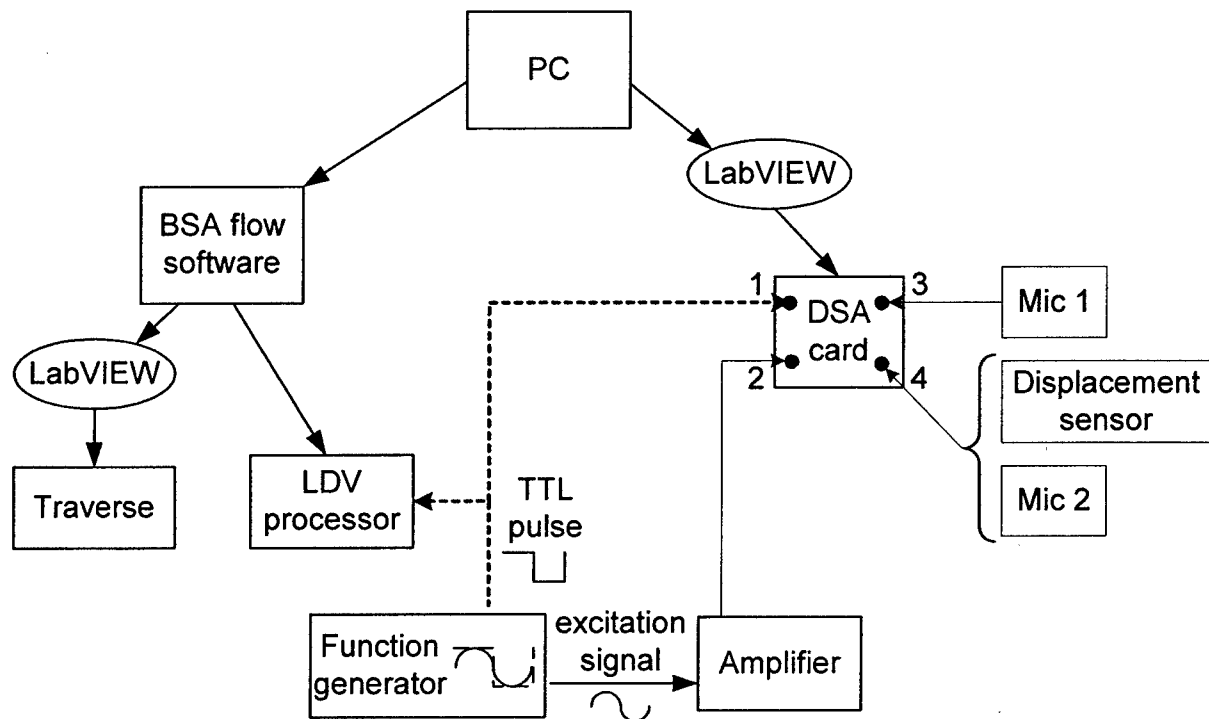


Figure 3-7: Flow chart of measurement setup.

As showed in Figure 3-7, the DAQ card interfaces with a standard PC through National Instruments' LabVIEW software. LabVIEW is also used to control the traverse for LDV velocity measurements and interface with the Dantec BSA Flow software that controls the LDV system. Of the 4 channels of the DSA card, the sync signal coming from the function generator is recorded in the first channel, the second channel acquires the input voltage to the piezoelectric diaphragm after amplification, the third channel monitors the pressure fluctuations from microphone 1 situated at the bottom of the cavity, and the fourth channel acquires either the signal from the displacement sensor or from the second microphone located in the side of the cavity.

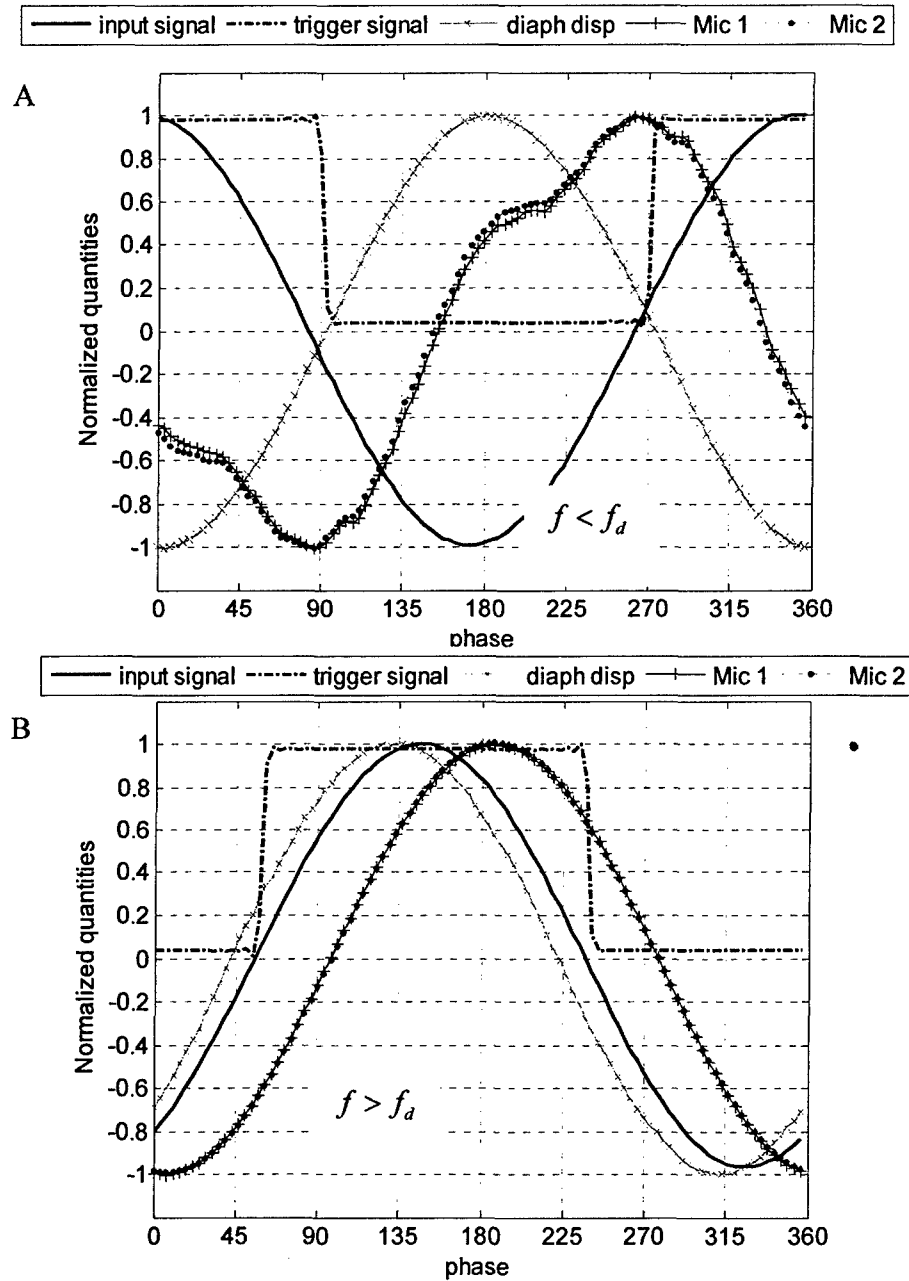


Figure 3-8: Phase-locked signals acquired from the DSA card, showing the normalized trigger signal, displacement signal, pressure signals and excitation signal. A) Case 70,  $f = 39$  Hz. B) Case 65,  $f = 730$  Hz.

Two sample graphs of the trigger signal, displacement signal, pressure signals and excitation waveform coming from the DSA card during one cycle are shown in Figure 3-8. Figure 3-8A is representative of a test case in which the driving signal frequency is below the resonance frequency of the diaphragm  $f_d$ , and it can be seen that the diaphragm displacement is out of phase with the input voltage. On the other hand, when the device is actuated beyond  $f_d$ , a  $180^\circ$  phase shift occurs in the diaphragm frequency

response, hence the input signal and the displacement signal are nearly in phase, as shown in Figure 3-8B. Similarly, this means that a positive voltage from the function generator results in a diaphragm deflection out from the cavity. Note that this is a relevant observation when comparing the experimental results with the low-dimensional model discussed in later sections. The dynamics of the diaphragm can also be seen from Figure 3-8 as it deflects in and out of the cavity. An increase in the diaphragm deflection results in a rise in cavity pressure (with a phase lag), and vice versa, which confirms the sign convention shown previously in Figure 3-4.

### 3.2 Data Processing

Once the data have been simultaneously acquired for the cavity pressures, diaphragm displacement, and the velocity profile from the setup described above, it then needs to be carefully processed in order to have great confidence in using the results. First, the pressure and diaphragm signals are averaged using a vector spectral averaging technique to eliminate noise from the synchronous signals. This averaging technique, in contrast with the more common RMS averaging technique that reduces signal fluctuations but not the noise floor, computes the average of complex quantities directly, separating the real from the imaginary part, which then reduces the noise floor since random signals are not phase-coherent from one data block to the next. For instance, using the vector averaging technique, the power spectrum is computed such that (National Instruments 2000)

$$G = \langle X^* \rangle \cdot \langle X \rangle, \quad (2-2)$$

where  $X$  is the complex FFT of a signal  $x$ ,  $X^*$  is the complex conjugate of  $X$ , and  $\langle X \rangle$  is the average of  $X$ , real and imaginary parts being averaged separately. In contrast, the RMS averaging technique used the following equation for the power spectrum,

$$G = \langle X^* \cdot X \rangle. \quad (2-3)$$

Then, once the velocity data is acquired with the LDV system, the velocity profiles must be integrated spatially and temporally to determine the average volume flow rate  $\overline{Q_j}$  and hence  $\overline{V_j}$ , via

$$\overline{Q_j} = \frac{1}{\tau} \int_{S_n} \int_0^\tau v(t, x) dt dS_n = \overline{V_j} S_n, \quad (2-4)$$

where  $0 < t < \tau$  is the time of expulsion portion of the cycle. However, an important issue is statistical analysis of the LDV data. Velocity measurements "arrive" at random points during a cycle, and like all experimental measurements, random noise also exists.

Therefore, the velocity data points must be sorted into phase bins to generate a phase-locked velocity profile. Each bin is a representation of the mean and uncertainty for all of the velocity points that fall within that bin. Therefore, to know the optimum bin width to minimize the combined random and bias errors in the LDV measurements, Figure 3-9 illustrates the percent error in the computed quantity  $\overline{V_j}$  from simulated LDA data, for several simulated signal-to-noise ratios (SNR) and where 8192 samples are

acquired. As expected, for very large bin widths – on the order of  $45^\circ$  – the error in  $\overline{V_j}$  is quite large. However, in the bin width range  $5\text{-}20^\circ$ , the error appears to be minimized. In this plot, the mean value of the error is indicative of the bias error due to the size of the bin width, while the error bars indicate the random error component. Not surprisingly, as the SNR is increased, this random error decreases. Most notably, however, the optimum phase bin width does not appear to be a function of the SNR. Based on this plot, an acceptable trade-off in the experimental test is found by choosing a bin width of  $15^\circ$ , which is equivalent to sampling 24 points per period.

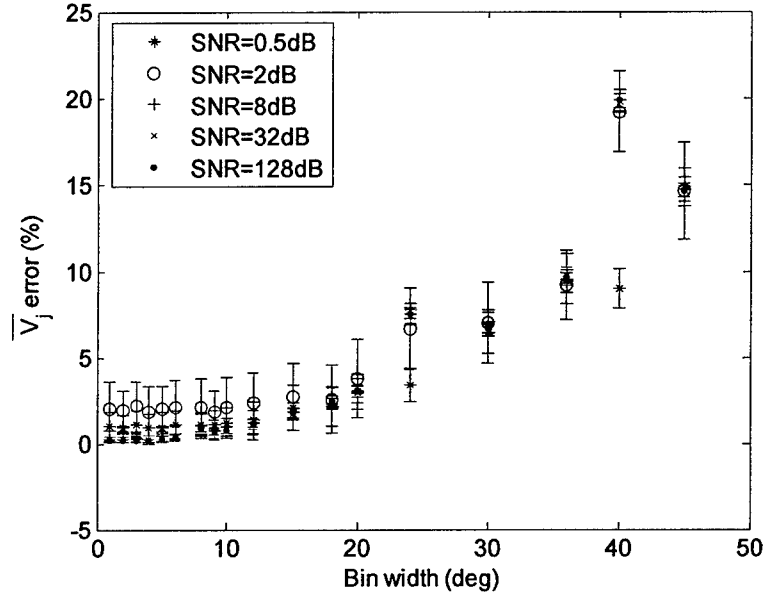


Figure 3-9: Percentage error in  $\overline{V_j}$  from simulated LDV data at different signal to noise ratio, using 8192 samples.

Next, an outlier rejection technique is applied on the raw velocity data to ensure high quality experimental data. The modified Tau-Thomson outlier rejection criterion is extended for two joint probability distribution function (pdf) distributions, corresponding to the two set of data from LDV1 and LDV2, and a 99.9% confidence interval is retained. Basically, the value of the joint pdf is computed for each data pair and is compared to a look-up table that is generated depending on the percentage confidence interval from a joint Gaussian pdf. This table gives the locus of points on the bounding ellipse and if a point falls outside the ellipse, it is considered as an outlier. The details of this outlier rejection criterion can be found in Holman (2005).

Another source of uncertainty comes from the phase resolution in each of the signals. As seen above, the volume flow rate at the exit has a phase resolution of  $\phi = 15^\circ \pm \Delta\phi$ , where  $\Delta\phi$  corresponds to half the bin width, i.e.  $7.5^\circ$ . Similarly, the data acquired by the DSA card (trigger signal, diaphragm displacement and pressure fluctuations) are acquired with 100 samples per period. That yields a phase uncertainty of  $\pm 1.8^\circ$  in these signals. Thus, the net uncertainty in the phase between the pressure and the volume flow rate at the orifice is then estimated to be

$$\phi(Q, \Delta P) = \Delta\phi \pm \delta\phi, \quad (2-5)$$

where  $\Delta\phi$  is the phase difference in  $Q_j$  and  $\Delta P$ , and  $\delta\phi = 7.5 + 1.8 = 9.4^\circ$ .

Next, the phase-locked profiles are spatially integrated to determine the periodic volume flow rate since

$$Q_j(t) = \int_{S_n} v(t, x) dS_n. \quad (2-6)$$

The spatial integration is numerically performed using a trapezoidal integration scheme. Figure 3-10 illustrates a set of typical phase-locked axial velocity profiles during four different phases separated by  $90^\circ$  in the cycle, corresponding approximately to maximum expulsion, maximum ingestion, and the two phases half way between. Figure 3-10A plots the vertical velocity component, while the radial component is plotted in Figure 3-10B, and Figure 3-10C gives the corresponding volume flow rate after integration across the orifice. The error bars represent an estimate of the 95% confidence interval for each velocity measurement and are obtained using a perturbation technique (Schultz et al. 2005) that yields the same nominal values of uncertainty as a standard Monte Carlo technique but with significantly less computational time.

This method is employed to estimate the uncertainty in the averaged volume flow rate. The 95% confidence interval estimate of  $\overline{Q_j}$ , in turn, is used to estimate the uncertainty in the Reynolds number, which is in the range of 2-10%, via the following relationship

$$\overline{Q_j} = \overline{V_j} S_n, \quad (2-7)$$

so the Reynolds number can be defined as,

$$\text{Re} = \frac{\overline{Q_j} d}{\nu S_n}, \quad (2-8)$$

and similarly to compute the stroke length  $L_0$  based on the phase-locked velocity profile,

$$L_0 = \frac{1}{S_n} \int_0^\tau \int_{S_n} v(r, t) dS_n dt = \tau \overline{V_j}. \quad (2-9)$$

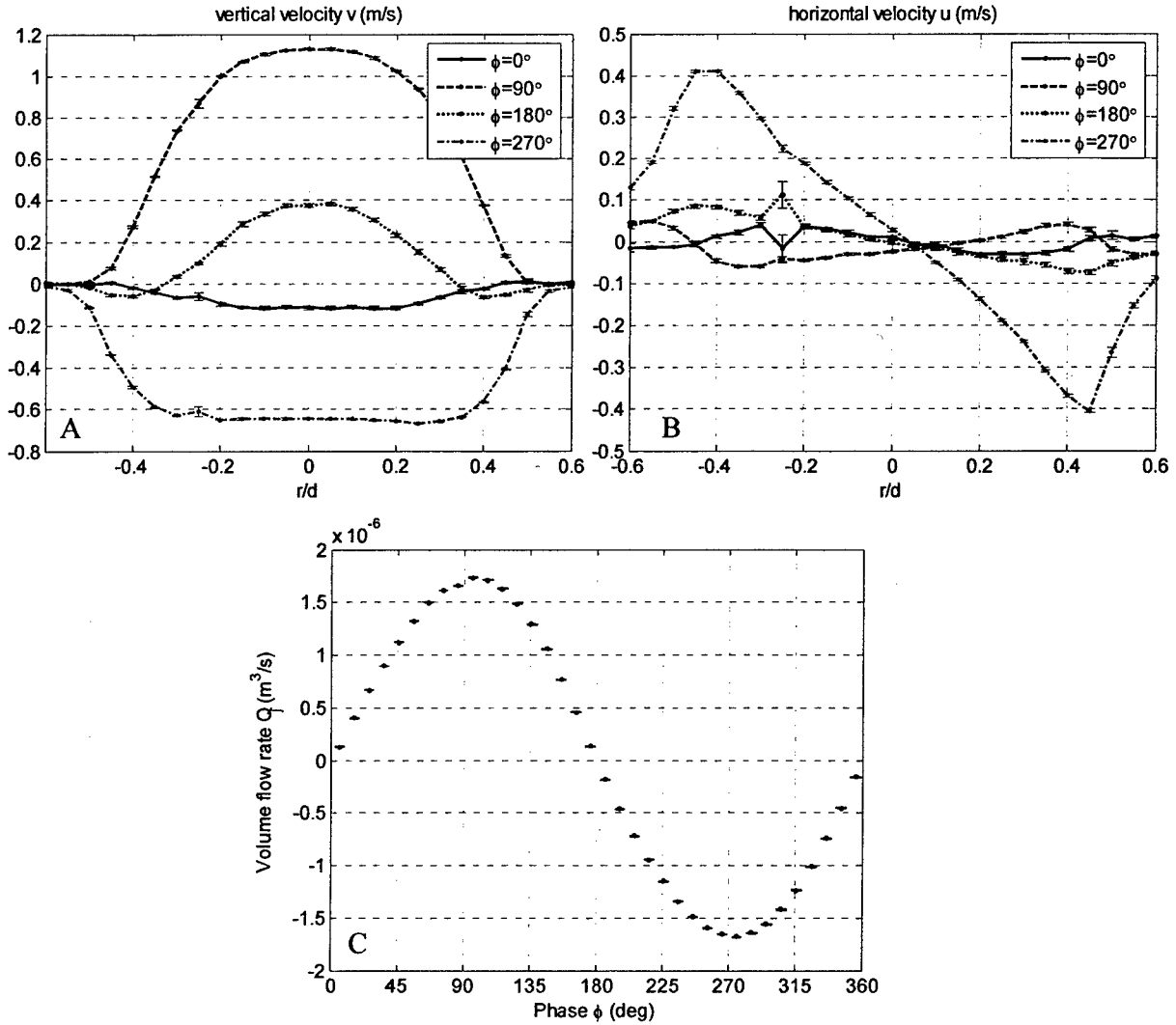


Figure 3-10: Phase-locked velocity profiles and corresponding volume flow rate acquired with LDV for Case 14 ( $S=8$ ,  $V_{ac}=28 V_{pp}$ ,  $Re=46.5\pm3\%$ ), acquired at  $y/d=0.05$ . A) Vertical velocity component. B) Horizontal velocity component. C) Volume flow rate.

The locus of the positive values of the volume flow rate are integrated to give the average volume flow rate during the expulsion part of the cycle,  $\overline{Q_j}$ , which is related to the average velocity by Eq. 2-7. In this experimental work, zero phase angle corresponds to the volume flow rate  $Q_j$  equal to zero with positive slope, meaning at the beginning of the expulsion phase of the cycle. Then, since all signals are phase-locked to the trigger signal of the input voltage, a corresponding phase shift is applied to each signal. Also, since the phase resolution is only  $15^\circ$  in the LDV data, the two points bracketing the data point where  $Q_j(t)=0$  are picked and a linear interpolation is then performed between them with a phase resolution of  $1^\circ$ , as illustrated in Figure 3-10C.



Furthermore, in order to gain more confidence in the experimental data, some features of the device behavior are checked. First, the integration of the volume flow rate over a complete cycle, while never exactly equal to zero, is found to be typically less than 1% of the amplitude of  $\overline{Q}_j(t)$ , even though the acquired velocity profiles are always at about 0.1 mm above the surface of the orifice (so for  $y/d = [0.033; 0.05; 0.1]$ ), hence entraining some mass flow that could affect the volume flow rate. But this is not surprising since a previous study has shown that a synthetic jet appears to remain zero-net mass-flux even up to  $y/d = 0.4$  (Smith and Glezer 1998); or actually as long as the distance above the orifice is small compared to the stroke length ( $y/L_0$ ).

Similarly for the cavity pressure measurements, the pressure signal sometimes is “noisy” at the low frequency and low amplitude (or Reynolds number) cases, which is principally due to 60 Hz line noise contamination. However, the signal is at least an order of magnitude higher than the microphone noise floor, as shown in Figure 3-11 for Case 52, and the Fourier series decomposition to the vector-averaged signal described next still provides a good fit to the time signal, while rejecting contaminated noise.

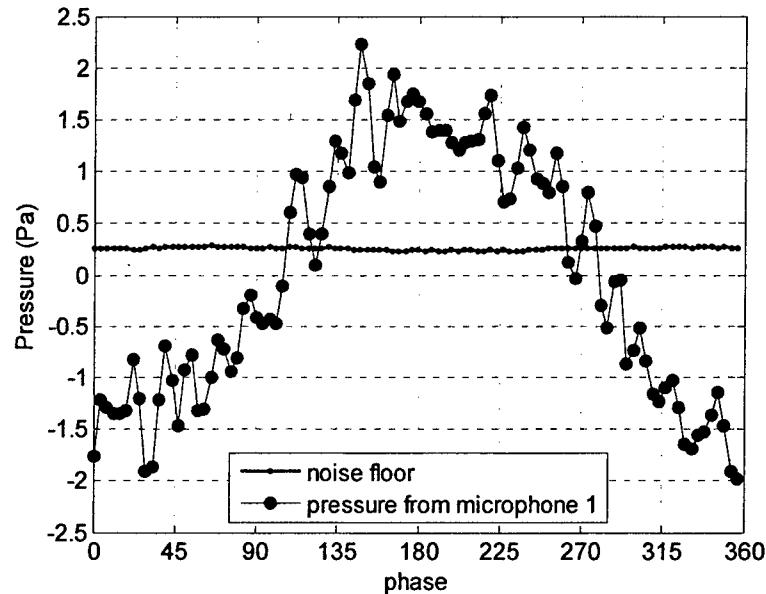


Figure 3-11: Noise floor in the microphone measurements compared with Case 52.

Finally, repeatability in the extracted experimental data is an important issue to be considered. Thus, to ensure fidelity in this experimental setup, several cases were retaken at different periods in time. For instance, Case 20 and Case 29 have been experimentally tested twice four months apart, while Case 62 and Case 69 have also been taken twice within a time frame of weeks. Table 3-3 compares the results between these cases for the principal governing parameters. As can be seen, the results are within the estimated confidence interval. It should be pointed out though that for Case 20 and Case 29, the velocity measurements were acquired at a slightly different distance from the surface ( $y/d = 0.07$  and  $y/d = 0.05$ , respectively) that could explain the larger difference seen in  $\overline{Q}_j$  in these cases.

Table 3-3: Repeatability in the experimental results

Case #	S	Re	$\Delta P_c$ (Pa)		$Q_d$ (m <sup>3</sup> /s)
			Mic 1	Mic 2	
20	7.6	88.2 ± 4%	3.59 ± 13%	3.2 ± 14%	3.48 × 10 <sup>-6</sup> ± 7%
	7.6	85.0 ± 4%	3.26 ± 10%	-	3.79 × 10 <sup>-6</sup> ± 7%
29	33.9	1131 ± 10%	414.9 ± 16%	365.6 ± 16%	6.41 × 10 <sup>-5</sup> ± 11%
	33.9	968.8 ± 6%	331.5 ± 10%	-	6.27 × 10 <sup>-5</sup> ± 10%
62	3.9	204.9 ± 4%	39.9 ± 11%	43.0 ± 12%	4.09 × 10 <sup>-6</sup> ± 6%
	3.9	192.9 ± 3%	45.1 ± 3%	49.3 ± 3%	4.18 × 10 <sup>-6</sup> ± 1% t
69	17.3	1361 ± 5%	1610 ± 4%	1957 ± 3%	4.48 × 10 <sup>-4</sup> ± 2%
	17.3	-	1685 ± 4%	1974 ± 3%	4.59 × 10 <sup>-4</sup> ± 2%

### 3.3 Fourier Series Decomposition

Typical results of the phase-locked measurements are shown in Figure 3-12 for four test cases, where the jet volume flow rate and the pressure fluctuations from microphone 1 and microphone 2 are plotted as a function of phase during one full cycle of operation. Clearly, while the jet volume flow rate is nearly sinusoidal, the cavity pressure fluctuations deviate significantly from a sinusoid for Cases 44 and 72 in this example, indicating significant nonlinearities. Therefore, a Fourier series decomposition via least squares estimation is performed to determine the number of significant harmonic components for all the trace signals.

To determine the number of relevant harmonics that capture the principal features of the signal, a vector averaged power spectrum analysis is performed for each individual case, as shown for four cases in Figure 3-13. Clearly, although more than 90% of the total power in the signal is present at the fundamental, the contribution from subsequent harmonics may not be negligible, especially from the 2<sup>nd</sup> harmonic (at  $3f_0$ ). There exist several criteria to determine the degree of confidence in the relevant harmonics to keep in the Fourier series reconstruction. Here, we use the residual of the least squares fit, where the signal is decomposed into  $k$  components until the least square estimation of the  $(k+1)^{\text{th}}$  harmonic only fits noise, hence reaching a negligible residual value. This can be seen from Figure 3-13. Once the number of significant harmonics retained in the signal has been validated for each case, the Fourier series fit to the waveforms for the volume flow rate and the two pressure signals are plotted on top of the data points as a function of phase, as shown in Figure 3-12 for selected cases. In these cases, only the first 3 harmonics in the signals are kept.

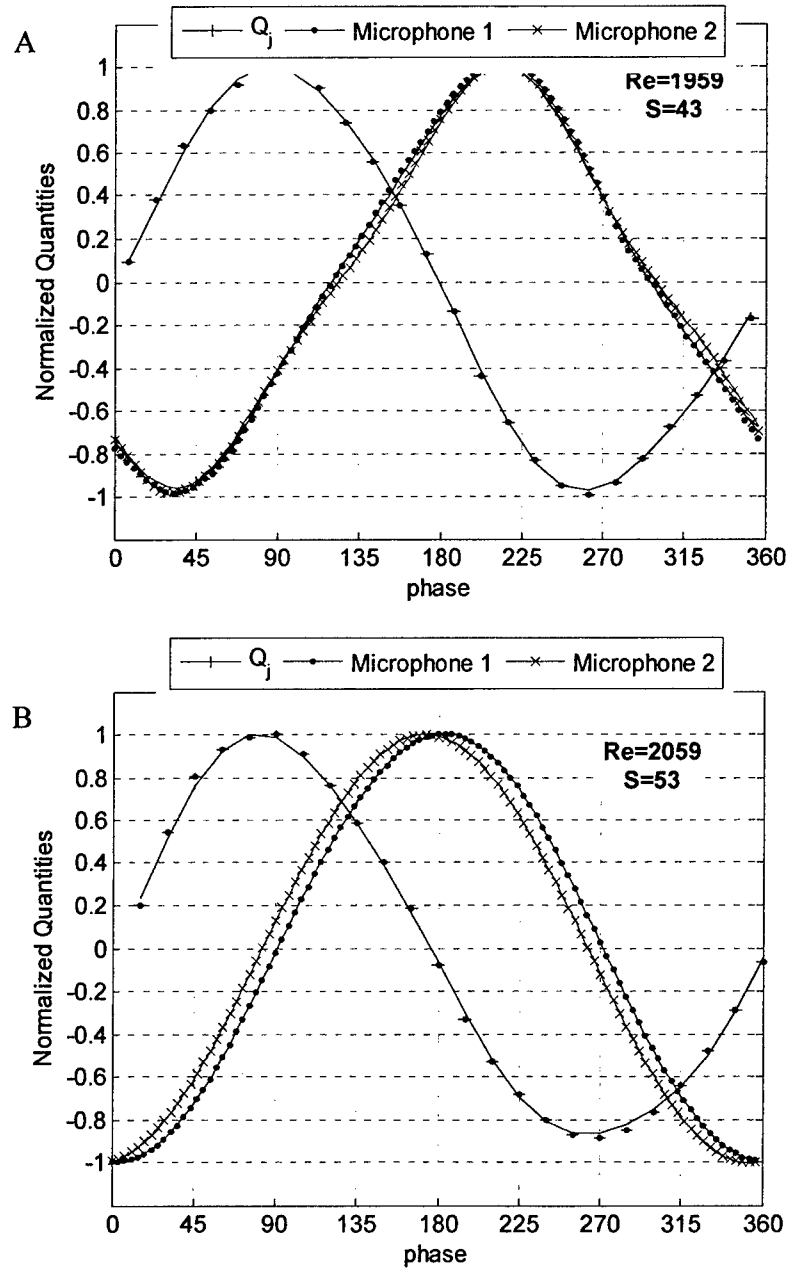


Figure 3-12: Normalized quantities vs. phase angle. A) Case 44 ( $h/d = 0.35$ ,  $St = 0.93$ ). B) Case 58 ( $h/d = 1.68$ ,  $St = 1.36$ ). C) Case 63 ( $h/d = 5.0$ ,  $St = 0.72$ ). D) Case 72 ( $h/d = 0.94$ ,  $St = 0.31$ ). The symbols represents the experimental data, the lines are the Fourier series fit on the data using only 3 terms, and errorbars are omitted in the pressure signal for clarity.

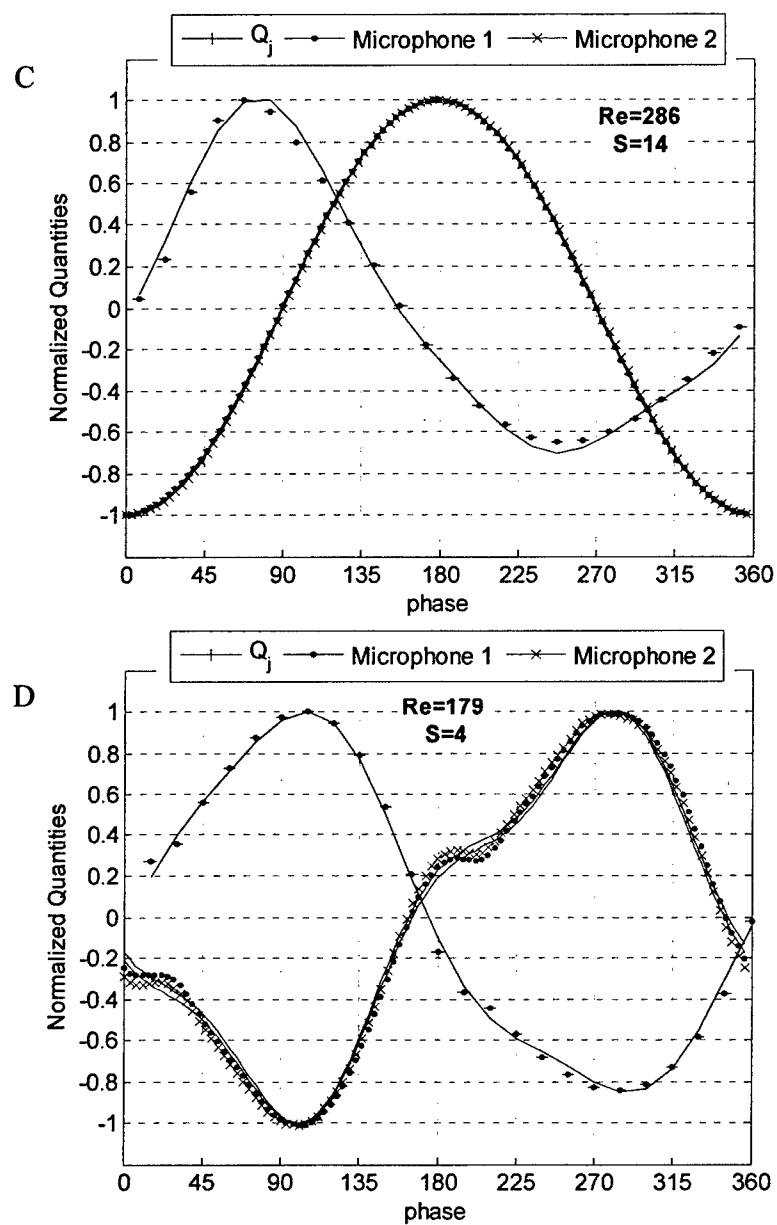


Figure 3-12: Continued.

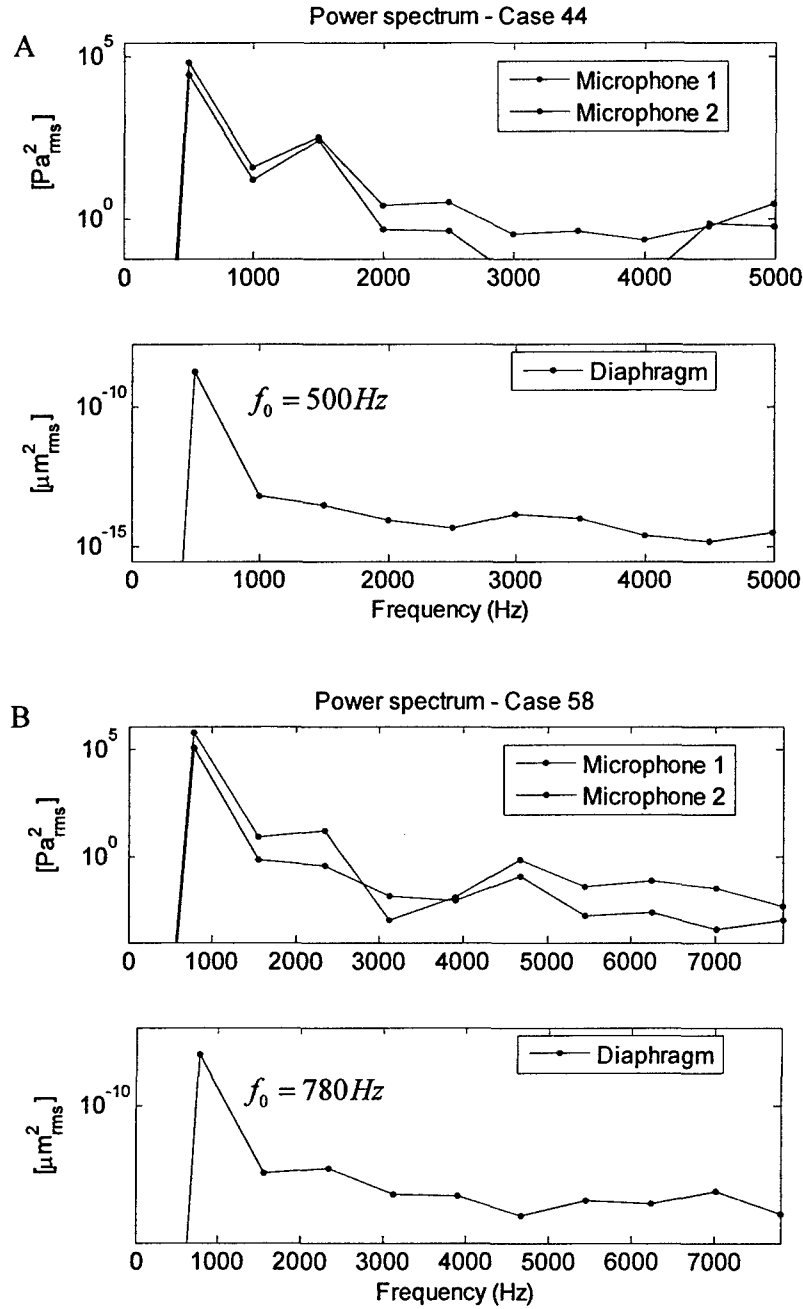


Figure 3-13: Power spectrum of the two pressure recorded and the diaphragm displacement. A) Case 44 ( $h/d = 0.35$ ,  $St = 0.93$ ). B) Case 58 ( $h/d = 1.68$ ,  $St = 1.36$ ). C) Case 63 ( $h/d = 5.0$ ,  $St = 0.72$ ). D) Case 72 ( $h/d = 0.94$ ,  $St = 0.31$ ). The symbols are exactly at the harmonics locations.

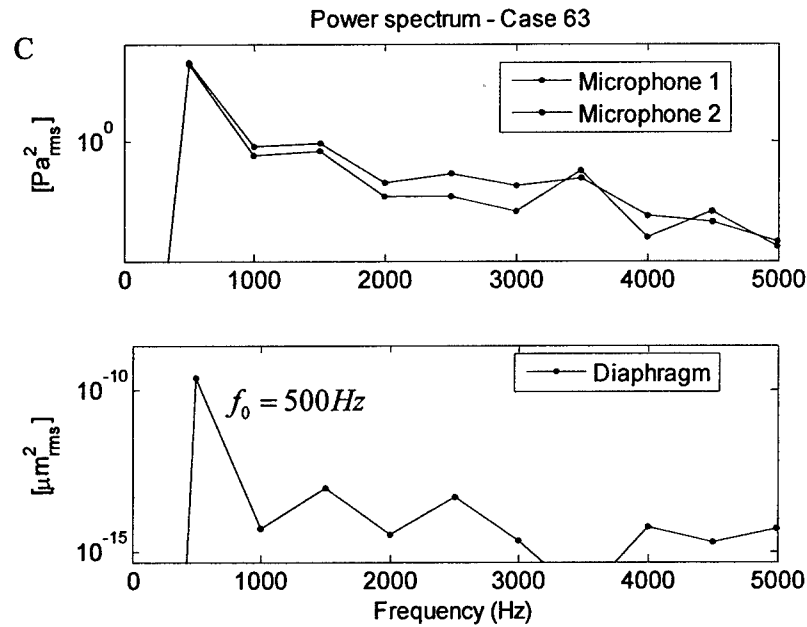


Figure 3-13: Continued.

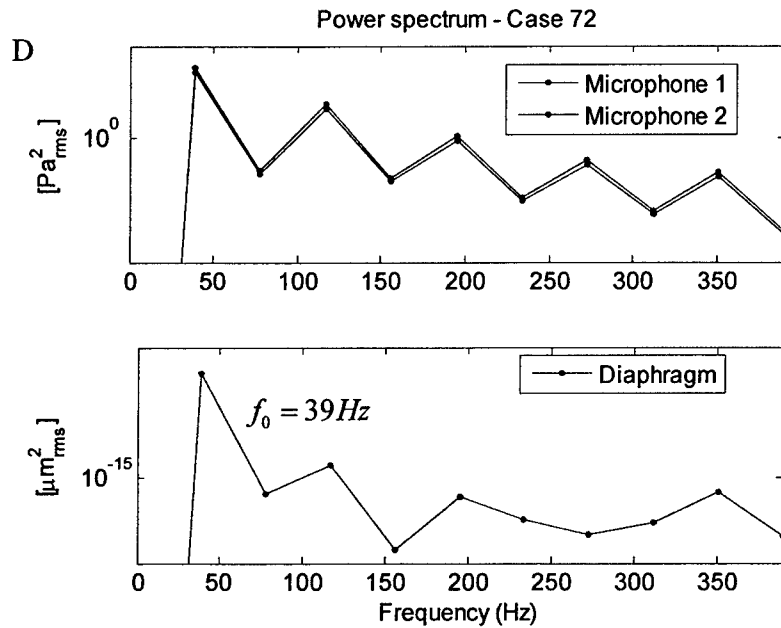


Figure 3-13: Continued.

### 3.4 Flow Visualization

In addition to the above experimental setup that provides quantitative results on the ZNMF actuator device under a wide range of operating conditions, a qualitative visualization of the flow behavior emanating from the orifice is performed, mainly to ascertain whether a jet is formed or not, and if indeed a jet is formed, under which flow region it can fall within.

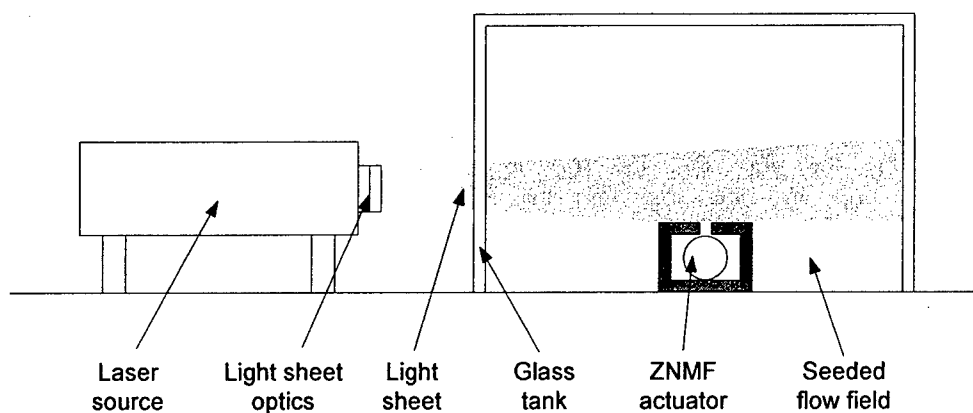


Figure 3-14: Schematic of the flow visualization setup.

Figure 3-14 shows a schematic of the flow visualization setup, where a continuous-watt argon-ion laser is used in conjunction with optical lenses to form a thin light sheet centered on the orifice axis, and atomized haze fluid is introduced into the tank to seed the flow. The topology of the orifice flow behavior is simply noted and Table 2-3 in Section 2 lists the results for most of the cases. The nomenclature presented in this report is crude and far from exhaustive. The reader is referred to the detailed work preformed by Holman (2005) for a complete qualitative and quantitative study on the different topological regimes of ZNMF actuators exhausting into a quiescent medium. The topological regimes identified through this test matrix only include the no flow regime or a distinct flow pattern present at the orifice exit. In Table 2-3, it is referred to as follows:

- X: no jet formed
- J: jet formed

To conclude this section, an extensive experimental investigation has been described, the results of which are used throughout this report. In particular, Section 4 focuses on orifice flow physics, hence presenting the results of the LDV measurements and the flow visualization. The cavity pressure and diaphragm deflection measurements are presented in Section 5 where the cavity behavior is thoroughly investigated. Finally, Section 6 leverages all the information gathered and uses all these results for the development of a refined reduced-order model.

#### 4. Results: Orifice Flow Physics

This section presents the results of the experimental and numerical investigation described in Section 3. It focuses on the rich and complex flow physics of a ZNMF actuator exhausting into a quiescent medium. The local flow field at the orifice exit is first examined via the numerical simulations that provide useful information on the flow pattern inside the actuator, followed by the results of the experimentally acquired velocity profiles. Some results on the jet formation are presented next. A detailed investigation is then performed on the influence of the governing parameters on the orifice flow field and more generally on the actuator performance. Finally, the diverse mechanisms that can generate non-negligible nonlinearities in the actuator behavior are reviewed and the related limitations addressed. Ultimately, this investigation on the orifice flow behavior

will help in developing physics-based reduced-order models of ZNMF actuators exhausting into quiescent air for both modeling and design purposes, as detailed in Section 6.

The test matrix tabulated in Table 2-3 is designed to cover a significant parameter space, in terms of nondimensional parameters, where a total of 8 numerical simulations and 62 different experimental cases are considered. The dimensional parameters varied in this study are the orifice diameter  $d$  and height  $h$ , the actuation frequency  $\omega$ , and the input voltage amplitude (i.e., driver amplitude). Hence, in terms of dimensionless parameters, this corresponds to varying the orifice aspect ratio  $h/d$ , the jet Reynolds number  $Re = \bar{V}_j d / \nu$ , the Stokes number  $S = \sqrt{\omega d^2 / \nu}$ , the dimensionless volume displaced by the driver  $\Delta V / d^3$ , the actuation-to-Helmholtz frequency ratio  $\omega / \omega_H$ , the actuation-to-diaphragm frequency ratio  $\omega / \omega_d$ , and the dimensionless wavenumber  $kd$ . Recall that the Reynolds, Stokes, and Strouhal numbers are related via  $St = S^2 / Re$  so that knowledge of any two dictates the remaining quantity. The available numerical simulations are from the George Washington University (lead by Prof. Mittal) in a collaborative joint effort between our two groups. Next, the experimental setup is presented in detail in Section 3, and this investigation provides information on the velocity profile across the orifice – hence jet volume flow rate, cavity pressure oscillations, and driver volume flow rate as a function of phase angle and in terms of the above dimensionless parameters.

#### 4.1 Local Flow Field

##### 4.1.1 Velocity Profile through the Orifice: Numerical Results

The major limitation in the experimental setup is that it is spatially limited, in the sense that data cannot be acquired inside the orifice. Therefore, the role of numerical simulations that can provide information anywhere inside the computed domain is relevant in this study. The test cases of interest correspond to Case 1, 2 & 3 in Table 2-3. They have the same Reynolds number  $Re = 262$ , but have different Stokes number ( $S = 25$  or  $S = 10$ ) and orifice aspect ratio  $h/d$  (1, 2, and 0.68, for Cases 1, 2, and 3, respectively). Note also that they share a straight rectangular slot for the orifice and that the simulations are two-dimensional.



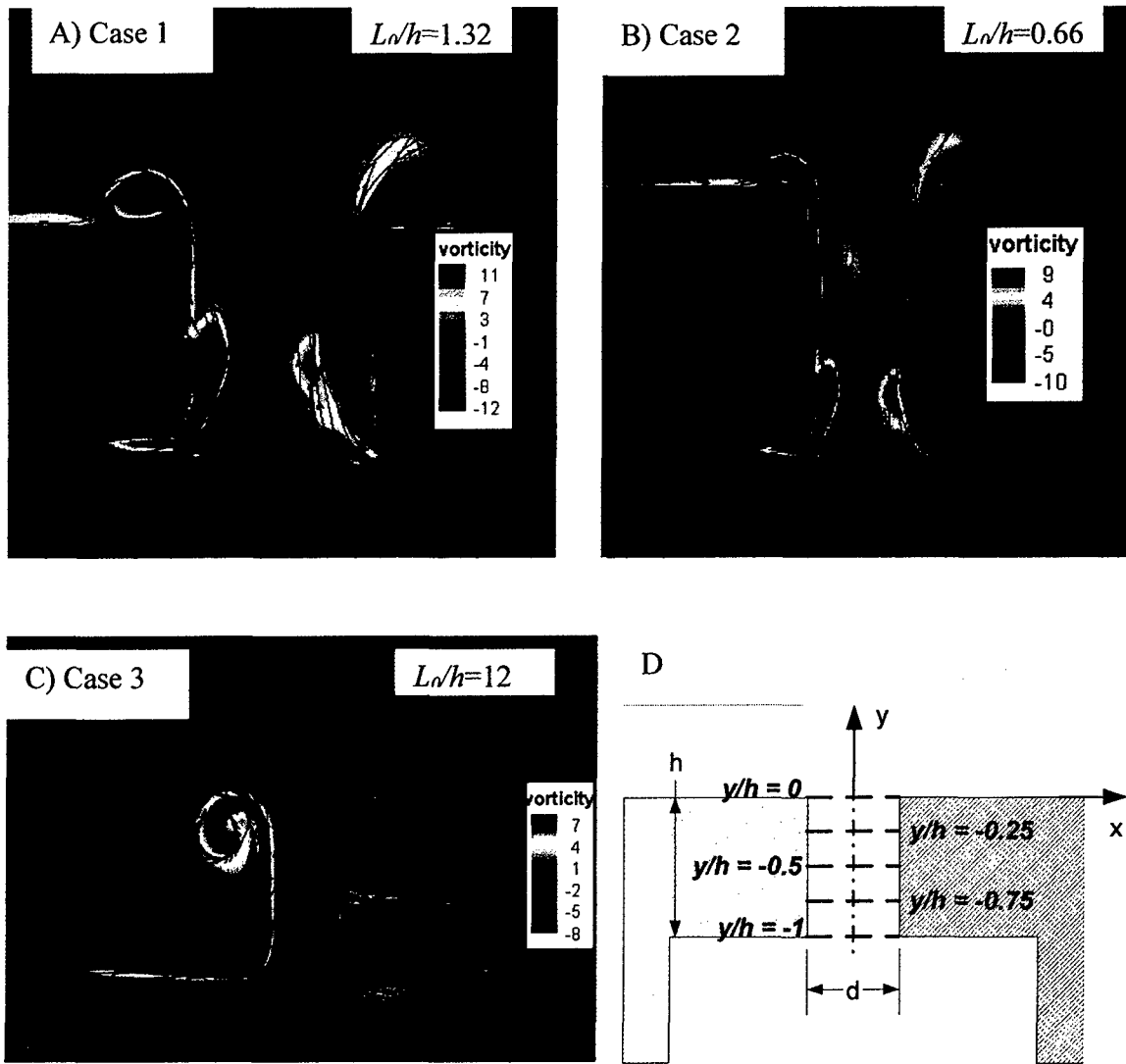


Figure 4-1: Numerical results of the orifice flow pattern showing axial and longitudinal velocities, azimuthal vorticity contours, and instantaneous streamlines at the time of maximum expulsion. A) Case 1 ( $h/d = 1$ ,  $St = 2.38$ ,  $S = 25$ ). B) Case 2 ( $h/d = 2$ ,  $St = 2.38$ ,  $S = 25$ ). C) Case 3 ( $h/d = 0.68$ ,  $St = 0.38$ ,  $S = 10$ ). D) Actuator schematic with coordinate definition.

Figure 4-1 shows the flow pattern inside the orifice for A) Case 1, B) Case 2 and C) Case 3. The azimuthal vorticity contours are plotted along with the axial and longitudinal velocities and some instantaneous streamlines, during the time of maximum expulsion. Also, Figure 4-1D shows a schematic of the actuator configuration and provides the coordinate definition and labels used. Notice the recirculation zones inside the orifice for the cases of low stroke length  $L_0$  (Case 1 and Case 2). Clearly, the orifice flow undergoes significant changes as a function of the geometry and actuation conditions. Therefore,

the vertical velocity profile is probed at five different locations along the orifice height from  $y/h = 0$  to  $y/h = -1$  and at different phases during one cycle, as schematized in Figure 4-1D.

Figure 4-2, Figure 4-3, and Figure 4-4 show the computed vertical velocity profiles at various locations in the orifice and corresponding at four different times during the cycle, for Case 1, Case 2, and Case 3, respectively. Also for clarification, the azimuthal vorticity contours are shown in each figure. First of all, it can be seen that Case 1 and Case 2 are qualitatively similar, although the three cases show that the velocity profile undergoes significant development along the orifice length. In particular, Figure 4-2 and Figure 4-3 show a strong phase dependence in the velocity profile inside the orifice, which is not the case for Case 3. Similarly, the Stokes number dependency in the shape of the velocity profile is clearly denoted. In particular, the velocity profiles at the exit ( $y/h = 0$ ) during the time of maximum expulsion are nearly identical for Case 1 and Case 2 that have the same Stokes number, as shown in Figure 4-2B and Figure 4-3B, respectively.

For the low stroke length – or high Strouhal number - cases at the maximum expulsion time (Cases 1 and 2 in Figure 4-2B and Figure 4-3B, respectively), the variation in the boundary layer thickness at the walls (from thin to thick as the fluid moves toward the orifice exit), along with the variation of the core region is indicative of the flow acceleration inside the orifice. This tangential acceleration of fluid at the boundary wall generates vorticity (Morton 1984). Also, notice the smoother profiles near the walls along the orifice length for the time of beginning of the expulsion stroke (Figure 4-2A and Figure 4-3A) and beginning of the ingestion stroke (Figure 4-2C and Figure 4-3C), compared when the cycle reaches its maximum expulsion and ingestion (Figure 4-2B and Figure 4-2D, and Figure 4-3B and Figure 4-3D). At the time of maximum expulsion velocity ( $\phi = 90^\circ$ ), for these two cases of high Strouhal number where no jet is formed, the velocity profiles are influenced by the vorticity that is not expelled at the exit (or inlet during maximum ingestion) and is trapped inside the orifice, leading to secondary vortices.

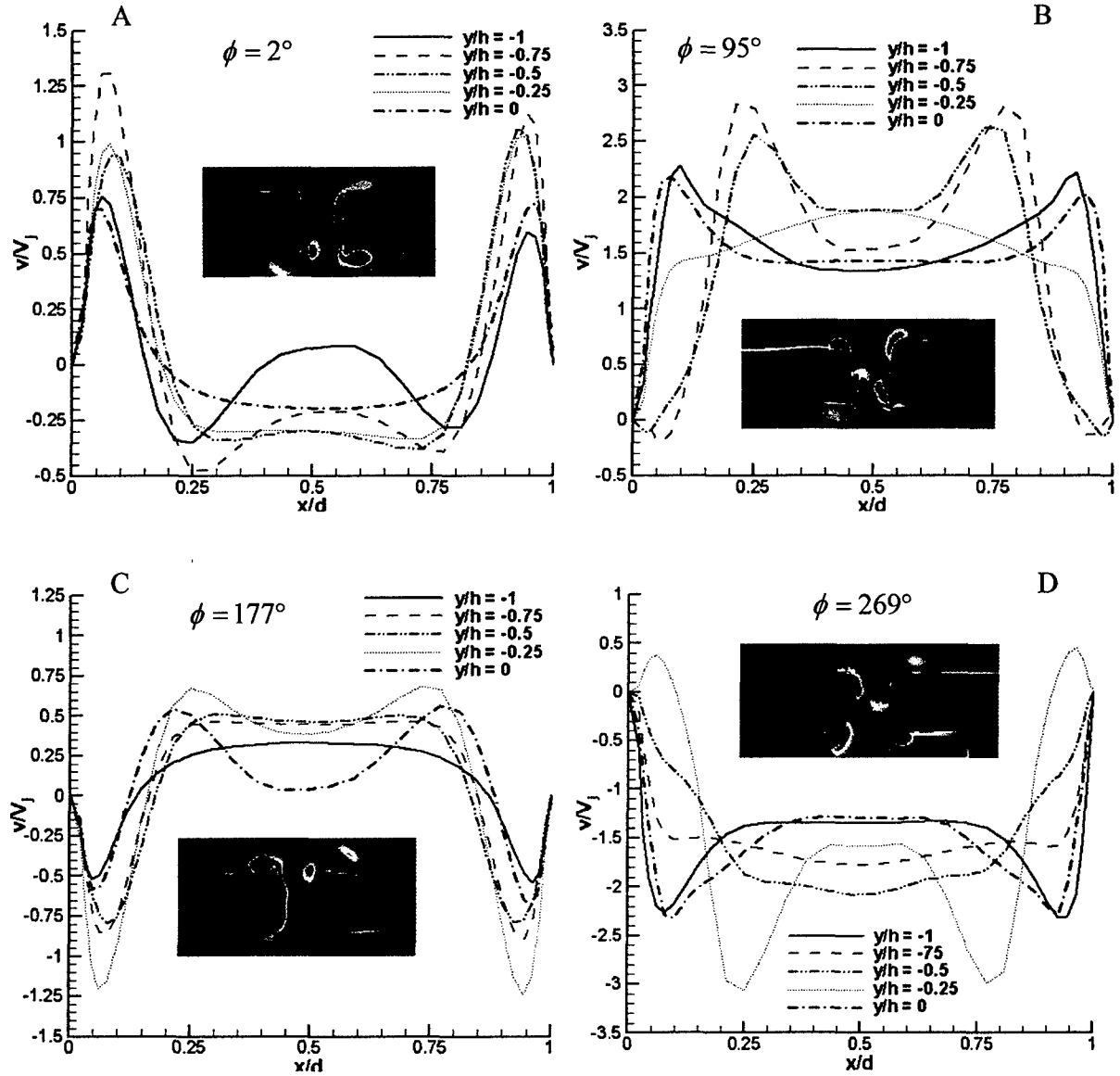


Figure 4-2: Velocity profile at different locations inside the orifice for Case 1 ( $h/d = 1$ ,  $St = 2.38$ ,  $S = 25$ ). A) Beginning of expulsion ( $2^\circ$ ). B) Maximum expulsion ( $95^\circ$ ). C) Beginning of ingestion ( $177^\circ$ ). D) Maximum ingestion ( $269^\circ$ ). The vertical velocity is normalized by  $\bar{V}_j$ . Also shown are the azimuthal vorticity contours for each phase.

In the case of a larger stroke length ( $L_0/h = 12$ ), as seen in Figure 4-4, the flow is always reversed near the walls. Interestingly, in Case 3 the flow is “similar” along the orifice height – roughly independent of  $y$ , but is still dependant of the phase angle, hence of time. Notice that in this case where the stroke length is much larger than the orifice

height, the flow is dominated by entrance and exit losses, where viscous effects are confined at the walls and the core region is moving in phase at each  $y$  location along the orifice. In this case, the flow never reaches a fully developed stage, as shown in Figure 4-4C.

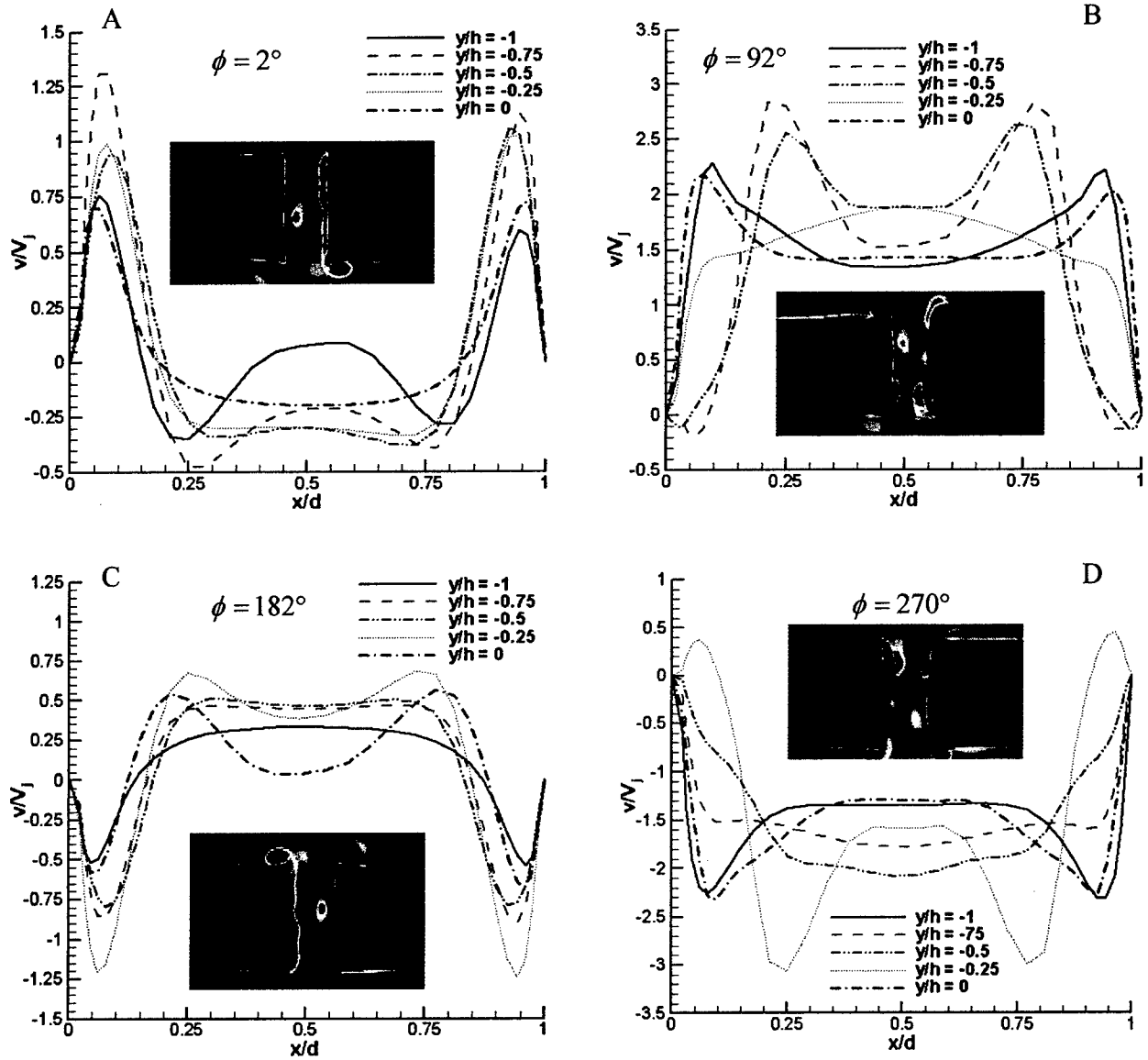


Figure 4-3: Velocity profile at different locations inside the orifice for Case 2 ( $h/d = 2$ ,  $St = 2.38$ ,  $S = 25$ ). A) Beginning of expulsion ( $2^\circ$ ). B) Maximum expulsion ( $92^\circ$ ). C) Beginning of ingestion ( $182^\circ$ ). D) Maximum ingestion ( $270^\circ$ ). The vertical velocity is normalized by  $\bar{V}_j$ . Also shown are the azimuthal vorticity contours for each phase.

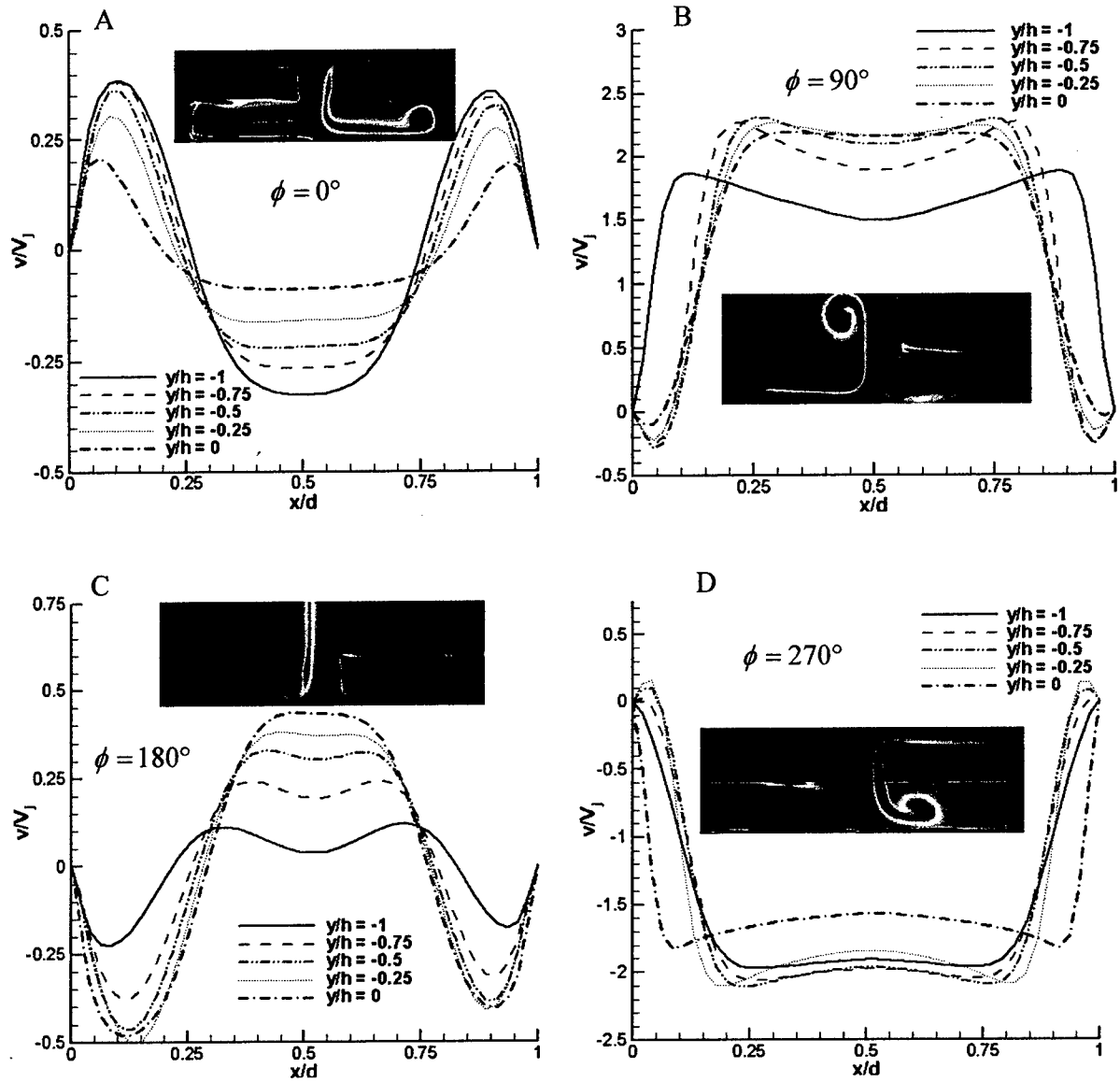


Figure 4-4: Velocity profile at different locations inside the orifice for Case 3 ( $h/d = 0.68$ ,  $St = 0.38$ ,  $S = 10$ ). A) Beginning of expulsion ( $0^\circ$ ). B) Maximum expulsion ( $90^\circ$ ). C) Beginning of ingestion ( $180^\circ$ ). D) Maximum ingestion ( $270^\circ$ ). The vertical velocity is normalized by  $\bar{V}_j$ . Also shown are the azimuthal vorticity contours for each phase.

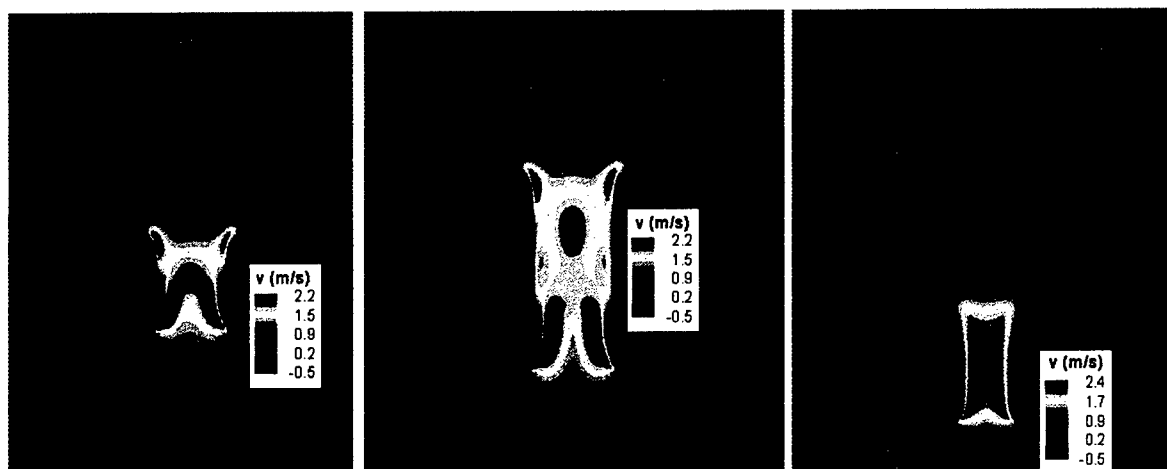


Figure 4-5: Vertical velocity contours inside the orifice during the time of maximum expulsion. A) Case 1, ( $h/d = 1$ ,  $St = 2.38$ ). B) Case 2 ( $h/d = 2$ ,  $St = 2.38$ ). C) Case 3 ( $h/d = 1$ ,  $St = 0.38$ ).

Figure 4-5 shows the vertical velocity contours inside the orifice for the three numerical cases, at the time of maximum expulsion in Figure 4-5A, Figure 4-5B, and Figure 4-5C, respectively. As noted above, Case 3 that has a large stroke length shows a flow inside the orifice that is never fully-developed, still in its development stage while it is exhausting into the quiescent medium. The growing boundary layer at the orifice walls are clearly seen and never merge. This is not the case for lower stroke lengths (Cases 1 and 2). Indeed, Case 1 in Figure 4-5A is a case where the flow seems to be on the onset of reaching a fully-developed stage. And this is more clearly seen in Figure 4-5B where for Case 2 the boundary layers merge somewhere past the middle of the orifice height. However, as already seen in Figure 4-1B and Figure 4-3B, the fact that some of the non-ejected vortices are trapped inside the orifice visibly perturb the flow pattern from the expected exact solution where the fully-developed region should be represented by uniform velocity contours.

On the other hand, one can interpret the flow pattern shown in Figure 4-5 with a different point of view. For instance, a vena contracta can be seen in Case 1 and Case 2 (Figure 4-5A and Figure 4-5B, respectively), but a core flow moving in phase in Case 3 (Figure 4-5C). None of these three cases are “fully-developed” in the strict sense (velocity profile invariant of position  $y$ ). Clearly, Cases 1 and 2 are affected by the trapped  $z$ -vorticity that is generated at the wall and at the orifice leaps; and in the absence of this  $z$ -vorticity, the flow would appear to be fully-developed. Contrarily, for Case 3 (Figure 4-5C) the vena contracta extends the full height of the orifice and the flow never reaches a fully-developed stage.

On the vorticity dynamics inside the orifice, the generation of the azimuthal or  $z$ -vorticity comes from the pressure gradient present at the sharp edges of the orifice exit (and inlet), and of the fluid tangential acceleration at the wall boundary inside the orifice. This generation process is instantaneous and inviscid (Morton 1984). However, the “decay” or “destruction” of vorticity only results from the cross-diffusion of the two

vorticity fluxes that are of opposite sense and that occurs at the center line. Here, the diffusion time scale for vorticity to diffuse across the slot is

$$t_{vis} \sim d^2/\nu, \quad (3-1)$$

and the convective time scale for a fluid particle to travel the orifice height is given by

$$t_{conv} \sim h/\overline{V}_j. \quad (3-2)$$

Therefore, the ratio of the time scales,

$$\frac{t_{vis}}{t_{conv}} \sim \frac{d^2}{\nu} \frac{\overline{V}_j}{h} \sim \frac{d}{h} \text{Re}, \quad (3-3)$$

provides an indication of the establishment of fully-developed flow as a function of Reynolds number. Table 4-1 summarizes this ratio of the time scales for the 3 numerical test cases investigated above. As discussed above, the flow is more willing to appear as fully-developed for Case 2 than for Case 3 that has the largest stroke length.

Table 4-1: Ratio of the diffusive to convective time scales

Case	1	2	3
$\frac{t_{vis}}{t_{conv}} \sim \frac{d}{h} \text{Re}$	262	131	385

#### 4.1.2 Exit Velocity Profile: Experimental Results

The flow field at the vicinity of the orifice exit surface is examined by extracting the velocity profiles. Four cases are considered that represent four typical flow regimes. They are shown in Figure 4-6, Figure 4-7, Figure 4-8, and Figure 4-9, corresponding in Table 2-3 to Case 71, Case 43, Case 69, and Case 55, respectively. The first common parameter of interest is the Stokes number, ranging from  $S = 4$  to  $S = 53$ , that clearly dictates the shape of the velocity profile, as a function of phase angle, as expected from the theoretical pressure-driven pipe flow solution. This is actually shown in the upper left plot in each test case figure, where the exact solution of the pressure-driven oscillatory pipe flow is plotted versus radius of the orifice diameter during the time of maximum expulsion. Note that the amplitude of the exact solution is normalized by the corresponding experimental centerline velocity at maximum expulsion. At a low Stokes number ( $S = 4$ ), Figure 4-6 shows a parabolic profile in the orifice velocity for each phase angle, representative of the steady state Poiseuille pipe flow solution. Next, as the Stokes number increases ( $S = 12$ ), as seen in Figure 4-7, an overshoot takes place near the edges known as the Richardson effect. For this case of low Reynolds number ( $\text{Re} = 63$ ), the

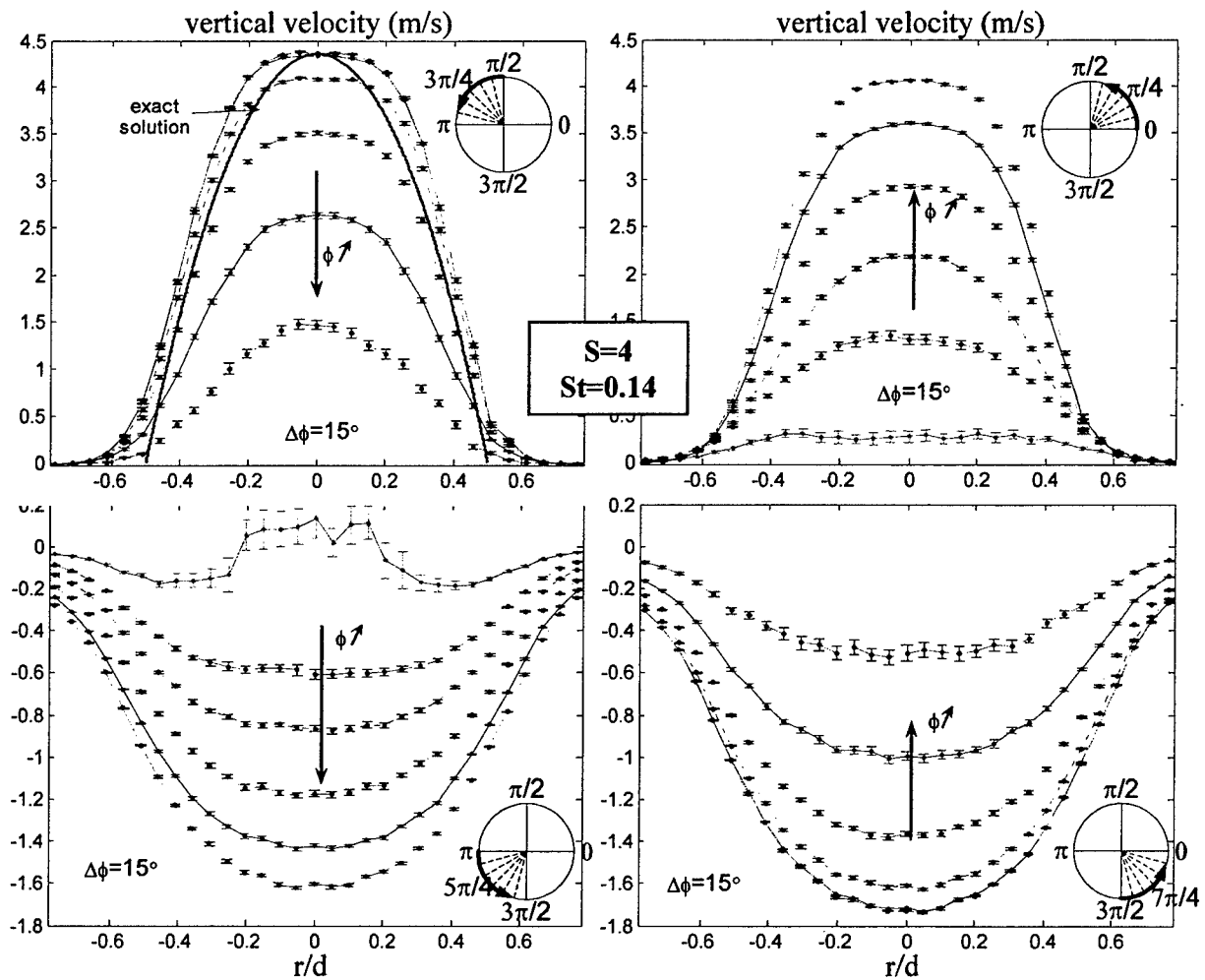


Figure 4-6: Experimental vertical velocity profiles across the orifice for a ZNMF actuator in quiescent medium at different instant in time for Case 71:  $Re = 112$ ,  $h/d = 0.94$ ,  $y/d = 0.1$ . The solid line in the upper left plot is the exact solution of oscillatory pipe flow, normalized by the experimental centerline velocity, at maximum expulsion. The zero phase corresponds to the start of the expulsion cycle.

velocity profile seems to be slightly different from expulsion to ingestion times in the cycle. As the Stokes number increases further, as in Figure 4-8 where  $S = 17$ , the overshoot is less pronounced, but the Reynolds number is much higher ( $Re = 1361$ ) and now the ingestion and expulsion profiles exhibit less variation in their profiles. Notice also that in this case, the orifice aspect ratio is  $h/d = 5$  and  $L_0/h = 0.9$  is less than unity so the flow is expected to reach a fully-developed state, compared with Case 43 in Figure 4-7 where for a similar Stokes number ( $S = 12$ ), the orifice aspect ratio is less than unity and the stroke length is greater than the orifice height ( $L_0/h = 1.3$ ), meaning that the flow may not reach a fully-developed state and is dominated by entrance and exit region



effects. Finally, the case of highest Stokes number ( $S = 53$ ) shows a nearly slug velocity profile, as seen in Figure 4-9. Note that in this case, no jet is formed at the orifice lip.

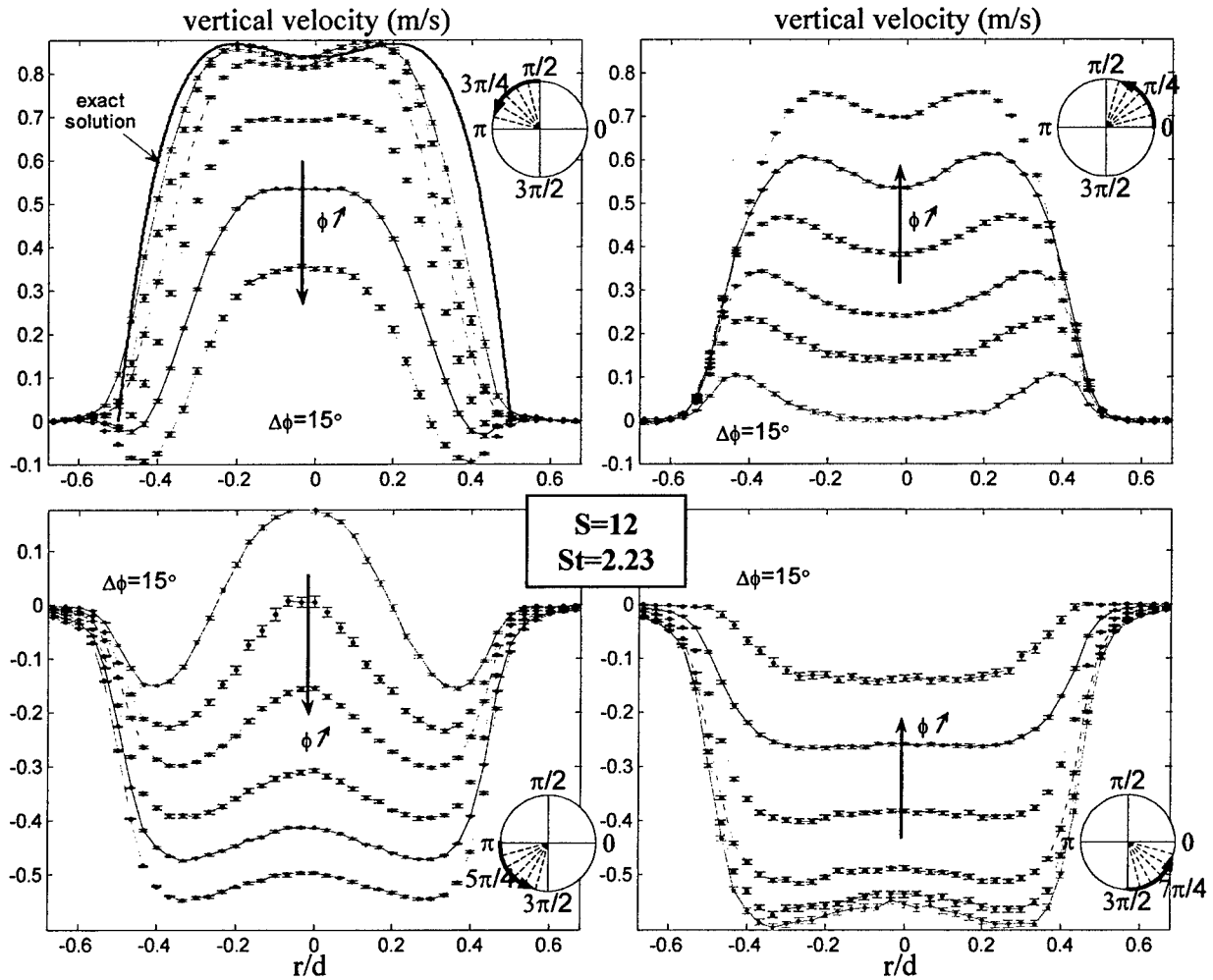


Figure 4-7: Experimental vertical velocity profiles across the orifice for a ZNMF actuator in quiescent medium at different instant in time for Case 43:  $Re = 63$ ,  $h/d = 0.35$ ,  $y/d = 0.03$ . The solid line in the upper left plot is the exact solution of oscillatory pipe flow, normalized by the experimental centerline velocity, at maximum expulsion. The zero phase corresponds to the start of the expulsion cycle.

Another interesting result comes from a comparison of these experimental velocity profiles with the theoretical ones, as shown in each figure in the upper left plot. Notice that the overall profile, particularly the overshoot near the wall if present, is well represented. However, because of the finite distance off the orifice surface at which the LDV data have been acquired ( $y/d = 0.1, 0.03, 0.1$ , and  $0.03$  for Case 71, 43, 69, and 55, respectively), the profiles cannot exactly match at the orifice edge. An additional reason for the difference noticed between the exact solution and the experimental results is that

the flow may not be fully-developed by the time it reaches the orifice exit. Recall that the theoretical solution assumes a fully-developed flow inside the orifice, meaning the boundary layer forming at the orifice entrance has finally merged. If not, the flow is still evolving along the length of the orifice. Hence, it would be like having an effective diameter -less than the actual one- for which the exact solution should be valid (a change in the diameter  $d$  will change the Stokes number  $S$  and the shape of the velocity profile). This remark is important for modeling purposes.

For the four cases represented here, and actually for all the experimental test cases considered in this study, notice the large velocity gradients near the edge of the orifice that the LDV experimental setup is able to accurately capture. Especially for the large Reynolds number case (Case 69) in Figure 4-8, where the vertical velocity jumps from about zero to 40 m/s over a length scale of 0.3 mm. Similarly, it can be seen from these plots that, although the edges of the orifice are at  $r/d = \pm 0.5$ , the velocity tends to a zero value beyond the orifice lip. This is due to the fact that the LDV data have been acquired at a finite distance  $y/d$  above the orifice surface, and that fluid entrainment is significant near the edge of the axisymmetric orifice. Indeed, although not shown here for these cases, but Figure 3-10 in the experimental setup section is representative of a typical case, the radial velocity component assumes its maximum near the edge of the orifice. This is observed for the expulsion part of the cycle as well as for the ingestion part. Notice though that it is more the ratio  $y/L_0$  rather than that the finite distance  $y/d$  that does matter in this scenario (Smith and Swift 2003b).

Next, in terms of phase angle during an entire cycle, as seen in all these plots, the velocity profiles are clearly phase dependent. Notice also that the profiles are not symmetric from the expulsion to the ingestion periods, especially in magnitude, the ingestion part having usually a broader velocity profile with decreased amplitude. Clearly, during the expulsion phase the flow is ejected into quiescent medium similar to a steady jet, whereas during the ingestion phase, the flow is similar to that in the entrance region of a steady pipe flow. This observation corroborates our global approach outlined in Section 2 in making a clear distinction between the expulsion and the ingestion portion of the cycle. Also, it is worthwhile to note that all the test cases considered in this report are close to zero-net mass flux. For instance, for the four experimental cases discussed above, the ratio between  $\overline{Q_{tot}}$ , the total volume flow rate during one cycle, and  $\overline{Q_e}$ , the volume flow rate during the expulsion part of the cycle, is equal to 0.17, 0.01, 0.39, and 0.09, for Cases 71, 43, 69, and 55, respectively. The total volume flow rate being at least an order of magnitude lower than that during the expulsion part, the zero-net mass flux condition is indeed verified.

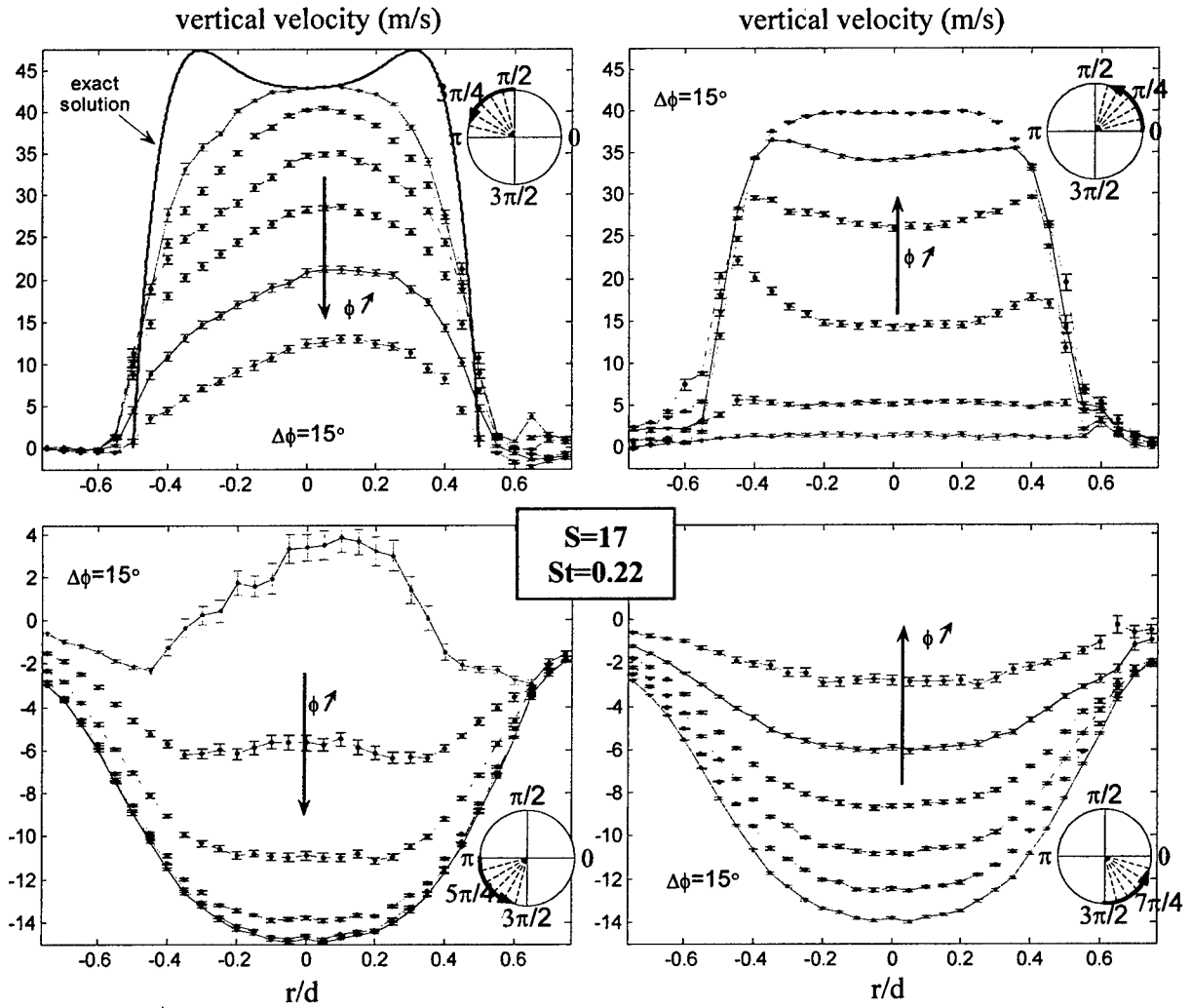


Figure 4-8: Experimental vertical velocity profiles across the orifice for a ZNMF actuator in quiescent medium at different instant in time for Case 69:  $Re = 1361$ ,  $h/d = 5$ ,  $y/d = 0.1$ . The solid line in the upper left plot is the exact solution of oscillatory pipe flow, normalized by the experimental centerline velocity, at maximum expulsion. The zero phase corresponds to the start of the expulsion cycle.

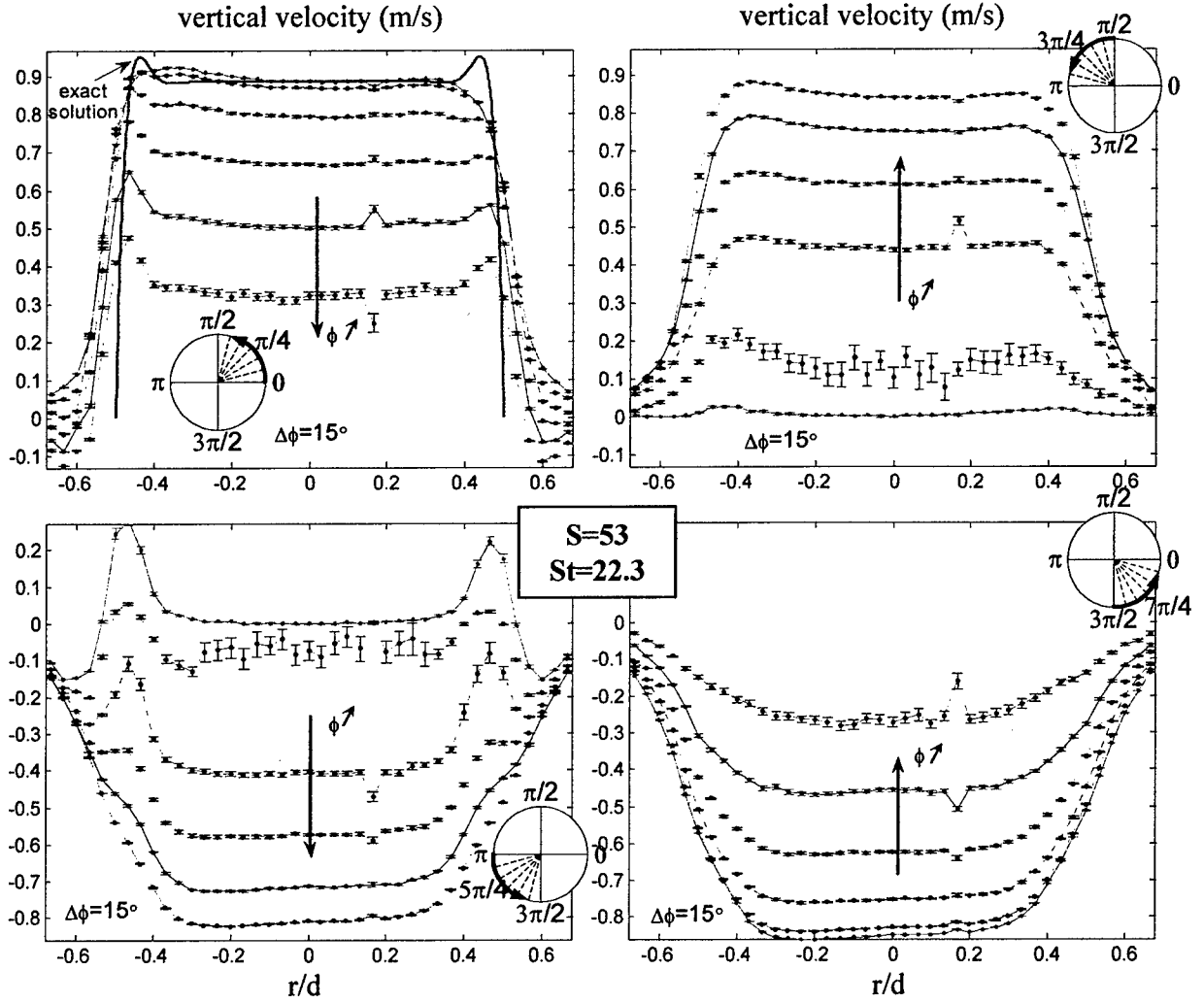


Figure 4-9: Experimental vertical velocity profiles across the orifice for a ZNMF actuator in quiescent medium at different instant in time for Case 55:  $Re = 125$ ,  $h/d = 1.68$ ,  $y/d = 0.03$ . The solid line in the upper left plot is the exact solution of oscillatory pipe flow, normalized by the experimental centerline velocity, at maximum expulsion. The zero phase corresponds to the start of the expulsion cycle.

Finally, another interesting observation is found in the relationship between the centerline velocity  $V_{CL}(t)$  at the exit and the corresponding mean – or spatially averaged – velocity  $\widehat{V}_j(t) = (\pi/2)\overline{V}_j$ . This is shown in Figure 4-10A and Figure 4-10B where the ratio of the two time-averaged velocities is plotted versus Stokes number and Reynolds number, respectively. For instance, it is expected that  $V_{CL} = 2\widehat{V}_j = 2\overline{V}_j$  for the steady Poiseuille flow, which is seen in Figure 4-10A, while for high Stokes number where the velocity profile is expected to be slug-like, it should asymptotes to unity. Recall the

analytical solution for an oscillatory pipe flow plotted again in Figure 4-10A. However, there is no such well-defined behavior for all the cases studied here that will dictate a scaling law for this velocity ratio.

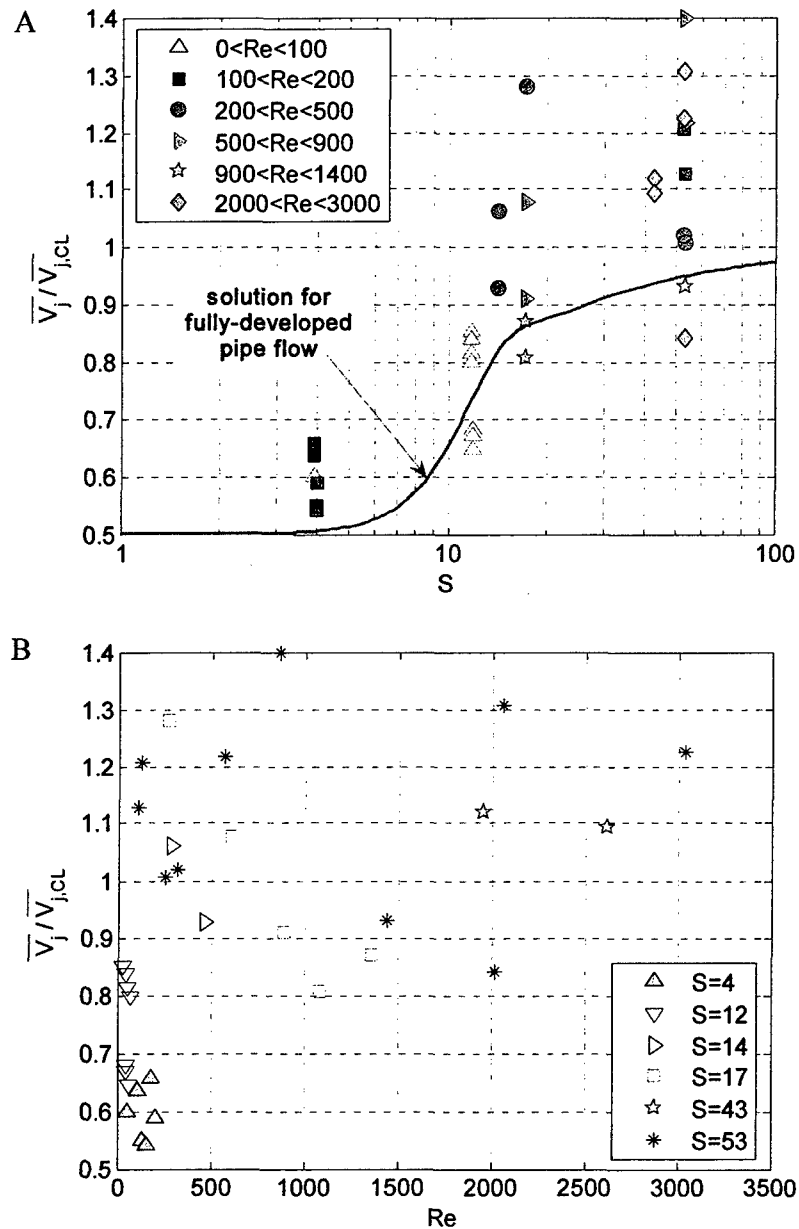


Figure 4-10: Experimental results of the ratio between the time- and spatial-averaged velocity  $\overline{V_j}$  and time-averaged centerline velocity  $\overline{V_{j,CL}}$ . A) Versus Stokes number  $S$ . B) Versus Reynolds number  $Re$ .

#### 4.1.3 Jet Formation

Next, the question whether a jet is formed or not at the orifice exit is investigated, since it has been shown in the previous sections that this criterion may influence on the orifice flow dynamics. Past simulations and experiments have shown that the vorticity flux is the key aspect that determines the “formation” of synthetic jets in quiescent flow (Utturkar et al. 2003, Holman et al. 2005). This flux of vorticity,  $\Omega_v$ , during the expulsion can be defined as

$$\Omega_v = \frac{1}{d/2} \int_0^\tau \int_0^{d/2} \xi_z(x,t) v(x,t) d\left(\frac{x}{d/2}\right) dt, \quad (3-4)$$

where  $\xi_z(x,t)$  is the azimuthal vorticity component of interest for an axisymmetric orifice, and  $\tau$  is the time of expulsion. Simple scaling arguments lead to the conclusion that the nondimensional vorticity flux is proportional to the Strouhal number via

$$\frac{\Omega}{V_j d} \sim \frac{1}{St} > K, \quad (3-5)$$

where  $K$  was a constant determined to be 2.0 and 0.16 for two-dimensional and axisymmetric orifice, respectively, and that predicts whether or not a jet would be formed at the orifice. Only two topological regimes are identified in this report: jet formed or no jet formed, as summarized in Table 2-3 for all the test cases. Again, the reader is referred to Holman (2005) for a more complete and thorough qualitative and quantitative analysis on this topic. Figure 4-11 shows how this jet formation criterion defined in Utturkar et al. (2003) compares with the experimental data. Clearly, for the range of Stokes and Reynolds numbers investigated in the present experiments, the jet formation criterion defined in Eq. 3-5 for a circular orifice is in good agreement with the flow visualization results. The cases having a clear jet formed are well above the line  $1/St = 0.16$ , while the ones well below this line do not create a jet. And around this criterion line, the flow regions are more in a transitional regime in terms of jet formation. Notice that although only the experimental results on the circular orifice are presented here, the numerical simulations featuring a rectangular slot and shown in Table 2-3 do satisfy the jet formation criterion as well. Consequently, this investigation on the jet formation criterion, validated through the flow visualization results, gives confidence in using this criterion for the description of the orifice flow behavior.

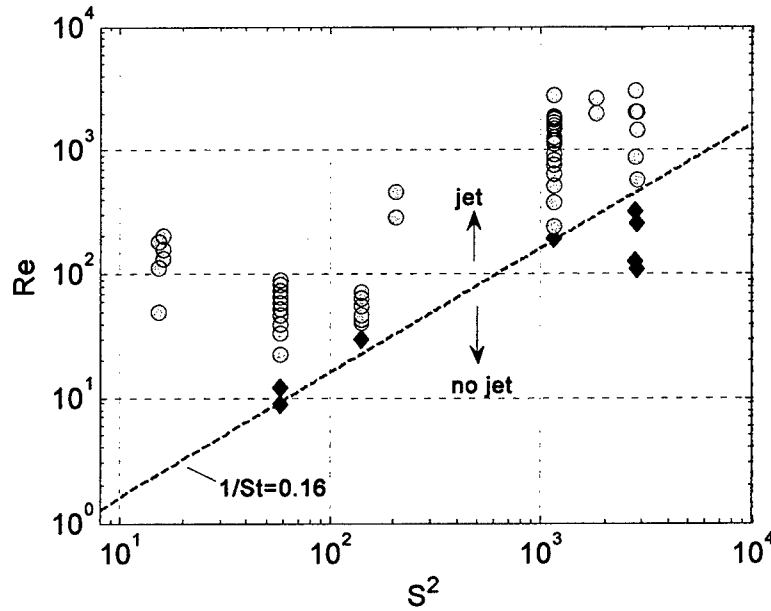


Figure 4-11: Experimental results on the jet formation criterion.

#### 4.2 Influence of Governing Parameters

In this section, the governing parameters extracted from the dimensional analysis and described in Section 2 are applied in this experimental investigation in order to confirm their validity and also investigate their respective influence on the ZNMF actuator behavior. The functional form (Eq. 1-10) is reproduced for illustration,

$$\left. \begin{array}{c} |Q_j/Q_d| \\ St \\ Re \end{array} \right\} = fn \left( \frac{h}{d}, \frac{w}{d}, \frac{\Delta \nabla}{d^3}, \frac{\omega}{\omega_H}, \frac{\omega}{\omega_d}, kd, S \right). \quad (3-6)$$

Note that the role of the Helmholtz frequency and of the cavity size and driver characteristics  $(\omega/\omega_H; \Delta \nabla/d^3; \omega/\omega_d; kd)$  is not addressed in this section, the next section being entirely dedicated to them. Since the experimental test only uses axisymmetric orifices, the functional form for fixed driver/cavity parameters can be recast as

$$\left. \begin{array}{c} St \\ Re \end{array} \right\} = fn \left( \frac{h}{d}, S \right). \quad (3-7)$$

So any two parameters between the Strouhal number, Reynolds number and Stokes number, plus the orifice aspect ratio should suffice in describing the ZNMF actuator flow characteristics. For completeness, as mentioned at the end of Section 2 in the description of the different regimes of the orifice flow, recall the dimensionless stroke length that is simply related to the above parameters by

$$\frac{L_0}{h} = \left( \pi \frac{d}{h} \right) \frac{\text{Re}}{S^2} = \left( \pi \frac{d}{h} \right) \frac{1}{St}, \quad (3-8)$$

where the constant  $\pi = \omega\tau$  comes from the assumption of a sinusoidal jet velocity.

Before presenting some results on the experimental data, a remark should be made concerning their interpretation. As explained previously, the cavity pressure fluctuations are used in lieu of the pressure drop across the orifice since experimentally, it is rather difficult to acquire the dynamic pressure drop across the orifice for such small devices. However, the acquired cavity pressure may deviate from the actual pressure drop through the orifice. This will be discussed further in Section 5.

#### 4.2.1 Empirical Nonlinear Threshold

First of all, the “current” approach to characterize or “calibrate” an oscillatory fluidic actuator that was first indirectly addressed by Ingard and Labate (1950) and more recently by Seifert and Pack (1999) is applied here, which uses the simple empirical observation that the cavity pressure fluctuation  $\Delta p$  is linearly proportional to the centerline exit velocity fluctuation  $v_{CL}$  at low forcing levels, and to  $v_{CL}^2$  (i.e., nonlinear) at sufficiently high forcing levels. Figure 4-12 shows the variation of the averaged jet velocity  $\bar{V}_j$  to the cavity fluctuating pressure  $\Delta P_c$  for a specific Stokes number. Notice that two scaling regions can be extracted from this plot, i.e. as the pressure amplitude increases the jet velocity varies from a linear to a nonlinear scaling dependence.

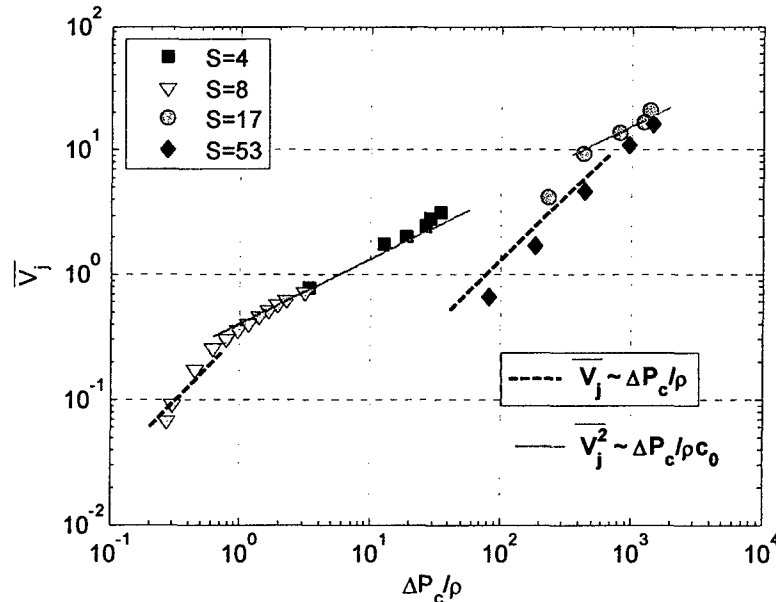


Figure 4-12: Averaged jet velocity vs. pressure fluctuation for different Stokes number.

However, the threshold level from which the linear proportionality can be distinguished from the nonlinear one varies as a function of the Stokes number. Clearly, this “calibration” curve is Stokes number dependant and practically useless. This analysis is based only on the velocity and pressure information and thus lacks crucial



nondimensional parameters to be taken into account to capture more physics. This motivates the dimensional analysis performed in Section 2, and the dependency of the actuator behavior on those parameters is investigated next.

#### 4.2.2 Strouhal, Reynolds, and Stokes Numbers versus Pressure Loss

Consider the loss mechanisms inside the orifice, especially the minor nonlinear losses. Nonlinear losses are known to be dependant on the flow parameters and, in the case of steady flow, empirical laws already exist (White 1991). However, for an oscillatory pipe or channel flow, this topic is still the focus of current research. Here, a physics-based qualitative description on the nonlinear loss mechanism is attempted. The nonlinear loss coefficient can be written as

$$K_d = \frac{\Delta P_c}{0.5 \rho \bar{V}_j^2}, \quad (3-9)$$

where  $\Delta P_c$  represents the cavity pressure fluctuations which is equivalent to the pressure drop across the orifice for a ZNMF actuator (see Section 5 for more details on the pressure equivalence), and  $0.5 \rho \bar{V}_j^2$  is the dynamic pressure based on the time and spatial-averaged expulsion velocity at the orifice exit  $\bar{V}_j$ .

The experimentally determined loss coefficient  $K_d$  is plotted versus  $St \cdot h/d$ , which is equivalent to the ratio of the stroke length to the orifice height, is shown in Figure 4-13A and Figure 4-13B using linear and logarithmic scales, respectively. Notice that the 3 numerical simulation results discussed above are also included for comparison. From the linear scale, Figure 4-13A, the pressure loss data asymptote to a constant value of order of magnitude  $O(1)$  as  $(St \cdot h/d \propto h/L_0)$  decreases beyond a certain value. This suggests that when the fluid particle excursion or stroke length is much larger than the orifice height  $h$ , minor “nonlinear” losses due to entrance and exit effects dominate the flow. However, the magnitude of these losses and the degree of nonlinear distortion is likely to be strongly dependent on Reynolds number, in a similar manner as for the steady state case where tabulated semi-empirical laws, which are exclusively a function of  $Re$ , are able to accurately predict such pressure loss (White 1991). The logarithmic plot in Figure 4-13B confirms that  $K_d$  is not only a function of the Reynolds number but also of the Stokes number, hence Strouhal number, the ratio of unsteady to steady inertia.

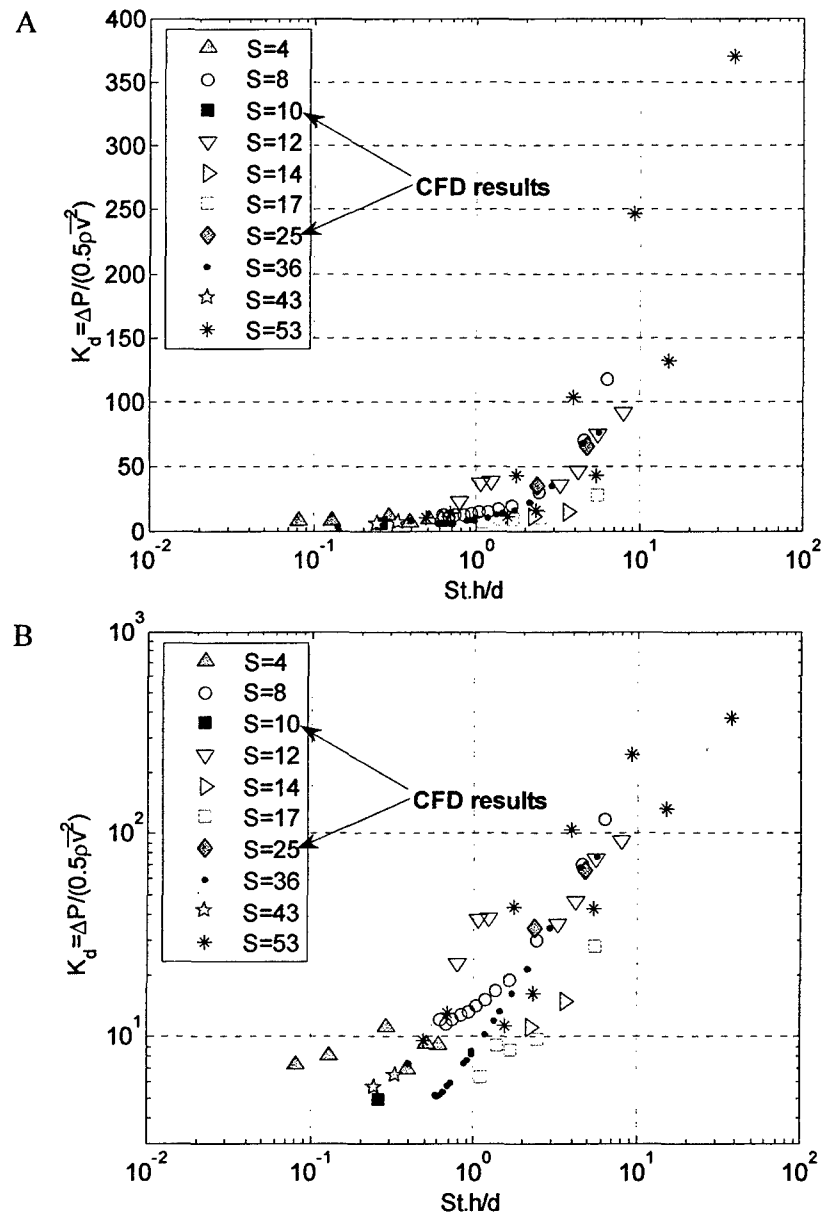


Figure 4-13: Pressure fluctuation normalized by the dynamic pressure based on averaged velocity  $\bar{V}_j$  vs.  $St \cdot h/d$ . A) Linear scale. B) Logarithmic scale.

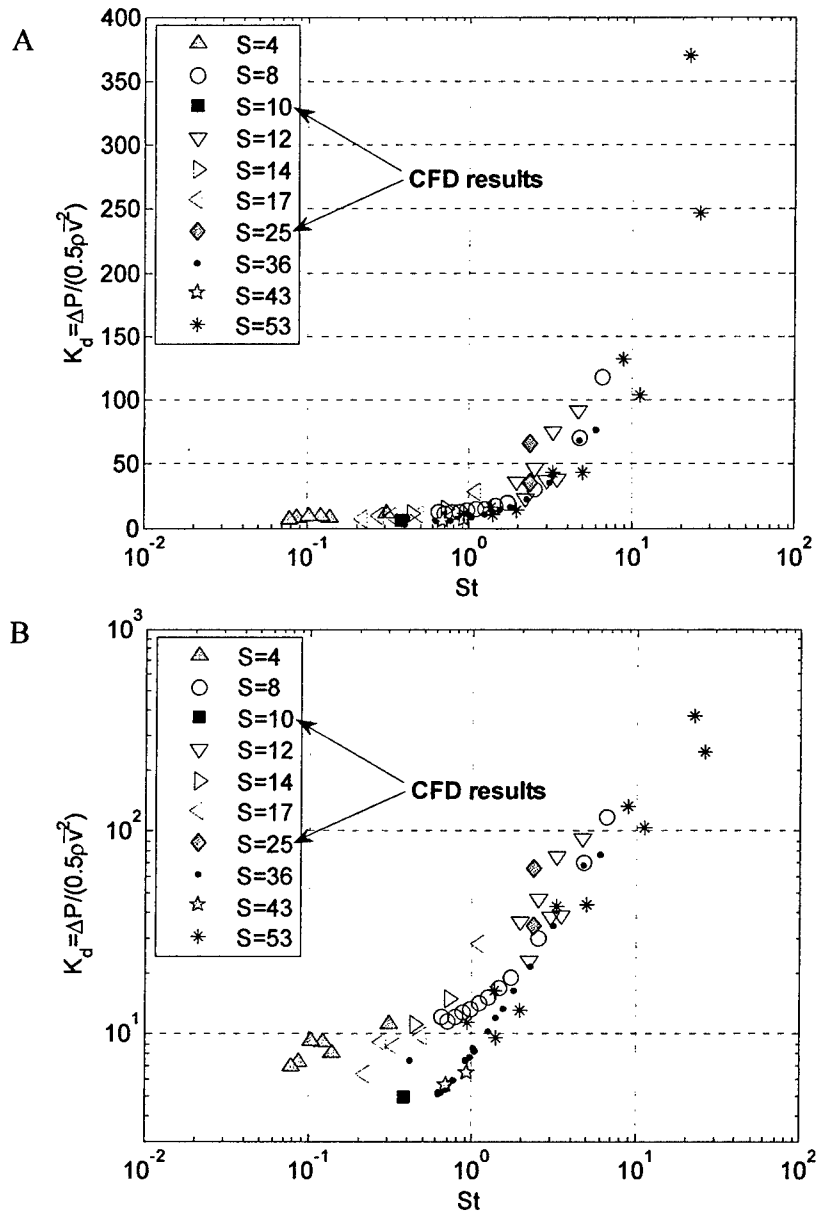


Figure 4-14: Pressure fluctuation normalized by the dynamic pressure based on averaged velocity  $\bar{V}_j$  vs. Strouhal number. A) Linear scale. B) Logarithmic scale.

Interestingly, the loss coefficient is again shown in Figure 4-14 in a linear and logarithmic scale, but this time as a function of the Strouhal number only. Notice the linear plot shows better collapse in the data for high Strouhal number, i.e. for unsteady inertia greater than steady inertia, while for low Strouhal numbers, not much difference is noticed. This suggests that there exists 2 distinct regimes in which the loss coefficient  $K_d$  is primarily a function of the Strouhal number for high  $St$ , while for low  $St$ , a dimensionless stroke length may be more appropriate in describing the variations in  $K_d$ .

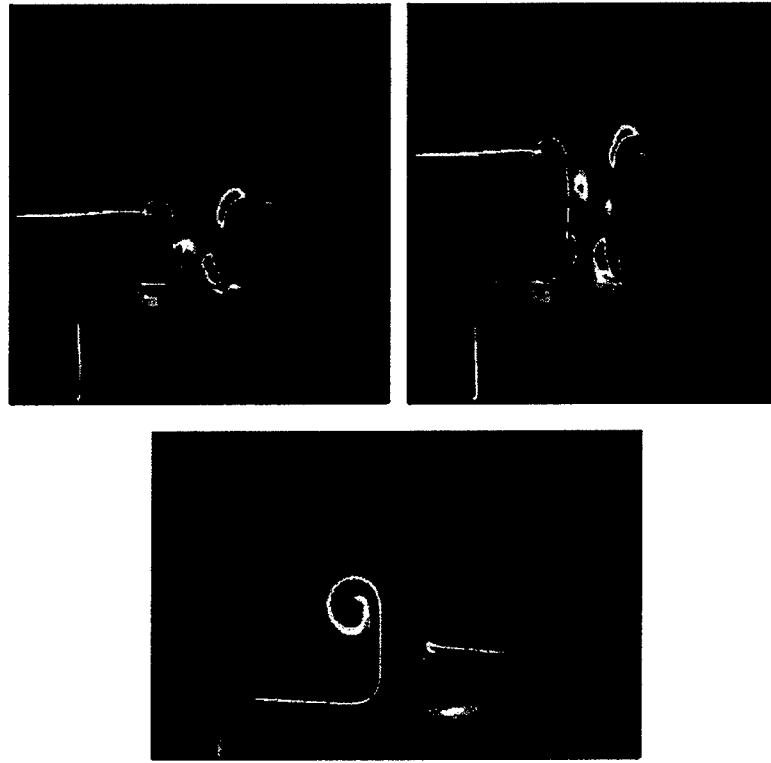


Figure 4-15: Vorticity contours during the maximum expulsion portion of the cycle from numerical simulations. A) Case 1 ( $h/d = 1$ ,  $St = 2.38$ ). B) Case 2 ( $h/d = 2$ ,  $St = 2.38$ ). C) Case 3 ( $h/d = 1$ ,  $St = 0.38$ ).

As previously discussed in Gallas et al. (2004), the results of numerical simulations allow detailed investigation of these issues. Again, CFD simulations have the capability to provide information everywhere in the computed domain. Figure 4-15 shows the variation of the spanwise vorticity for the three computational cases (Case 1, 2 and 3) at the time of maximum expulsion. As already shown in Figure 4-11 on the jet formation criterion, for Cases 1 and 2 no jet is formed (Figure 4-15A and Figure 4-15B), whereas for Case 3 a clear jet is formed (Figure 4-15C). The spanwise vorticity contours show that the vortices formed during the expulsion cycle for Case 1 and 2 are ingested back during the suction cycle, leading to the trapping of vortices inside the orifice, which is in contrast when clear jet formation occurs as for Case 3.

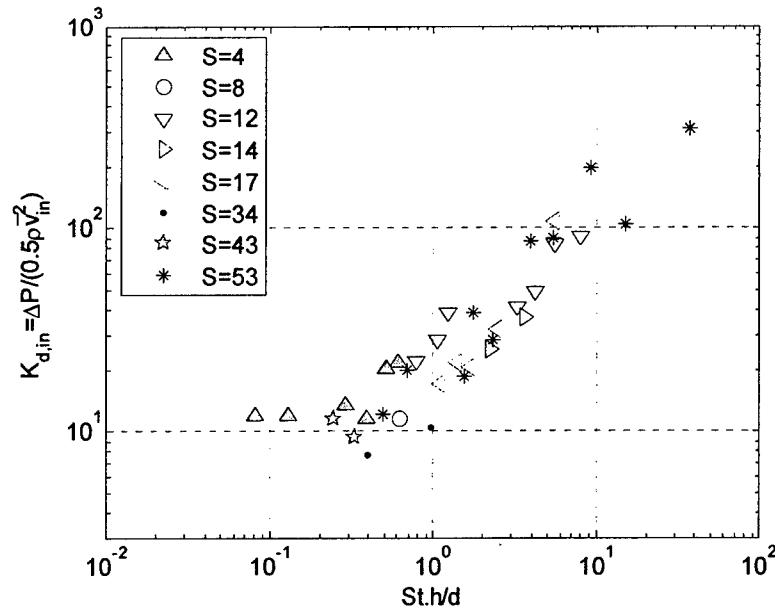


Figure 4-16: Pressure fluctuation normalized by the dynamic pressure based on ingestion time averaged velocity vs.  $St \cdot h/d$ .

Finally, it is interesting to compare the results from the expulsion to the ingestion phases during a cycle. Usually, only the expulsion part is considered since it is the most important and relevant in terms of practical applications. However, momentum flux occurs for both expulsion and ingestion, and for modeling purposes the ingestion part should not be disregarded. Especially from the experimental and numerical results shown in the first section of this section on the velocity profiles inside and at the exit of the orifice, which noticeably identify a clear distinction between the ingestion and expulsion profiles in time. Hence, similarly to Figure 4-13, the nondimensional pressure loss coefficient  $K_{d,in}$  based on the spatial and time averaged exit velocity during the ingestion phase is shown in Figure 4-16 as a function of  $St \cdot h/d$  for several Stokes numbers. Interestingly, a similar trend is observed between the ingestion and expulsion time of the cycle. This observation is further validated via the analysis of the numerical data, where similarly to the data presented in Figure 4-15, the spanwise vorticity contours occurring during the maximum ingestion are shown for Cases 1, 2 and 3 in Figure 4-17.

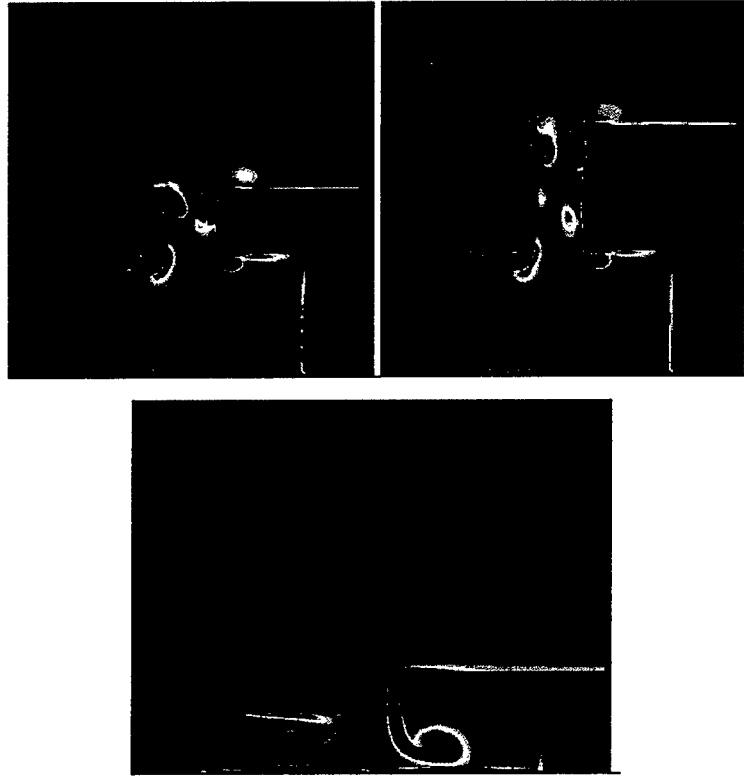


Figure 4-17: Vorticity contours during the maximum ingestion portion of the cycle from numerical simulations. A) Case 1 ( $h/d = 1$ ,  $St = 2.38$ ). B) Case 2 ( $h/d = 2$ ,  $St = 2.38$ ). C) Case 3 ( $h/d = 1$ ,  $St = 0.38$ ).

This is an important result that will be used later on when developing the reduced-order models of ZNMF actuators in Section 6. Indeed, the analysis of the oscillatory flow through a symmetric orifice (i.e., same geometry on both ends) can be simplified as follows: whatever is true during the expulsion stroke will be valid for the ingestion stroke as well. The experimental setup only permits measurement of the exhaust flow during expulsion and inlet flow during ingestion. During the expulsion phase, the flow at the orifice exit sees a baffled open medium where the flow exhausts, while during the ingestion phase, the flow sees the orifice exit as an entrance region. Again, this simplification is possible for *symmetric* orifices only, so no asymmetric orifice can be considered in this analysis.

To confirm this, the CFD results are again used. Indeed, to be true the velocity profile at the orifice exit ( $y/h = 0$ ) during maximum ingestion should match the velocity profile at the orifice inlet ( $y/h = -1$ ) during maximum expulsion. This is shown in Figure 4-18, Figure 4-19, and Figure 4-20 for Case 1, Case 2, and Case 3, respectively. The left hand plot compares the vertical velocity (normalized by  $\bar{V}_j$ ) at the start of expulsion versus the start of ingestion, at both orifice ends (inlet:  $y/h = -1$ , and exit:  $y/h = 0$ ). The right hand plot is similar but for the times of maximum expulsion and ingestion during a cycle. Notice how the velocity profiles are close to each other, especially for Case 2 (Figure 4-19), which confirms the argument stated above: whatever is true during the

expulsion stroke at the orifice exit will be valid for the ingestion stroke at the orifice inlet as well, and vice-versa.

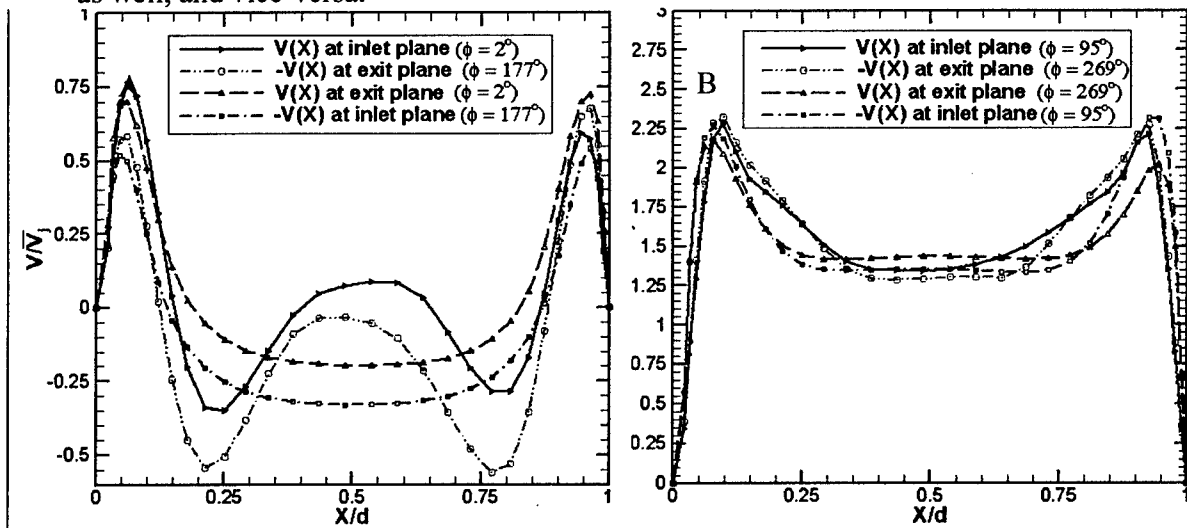


Figure 4-18: Comparison between Case 1 vertical velocity profiles at the orifice ends. A) At start of expulsion and start of ingestion. B) At maximum expulsion and maximum ingestion.

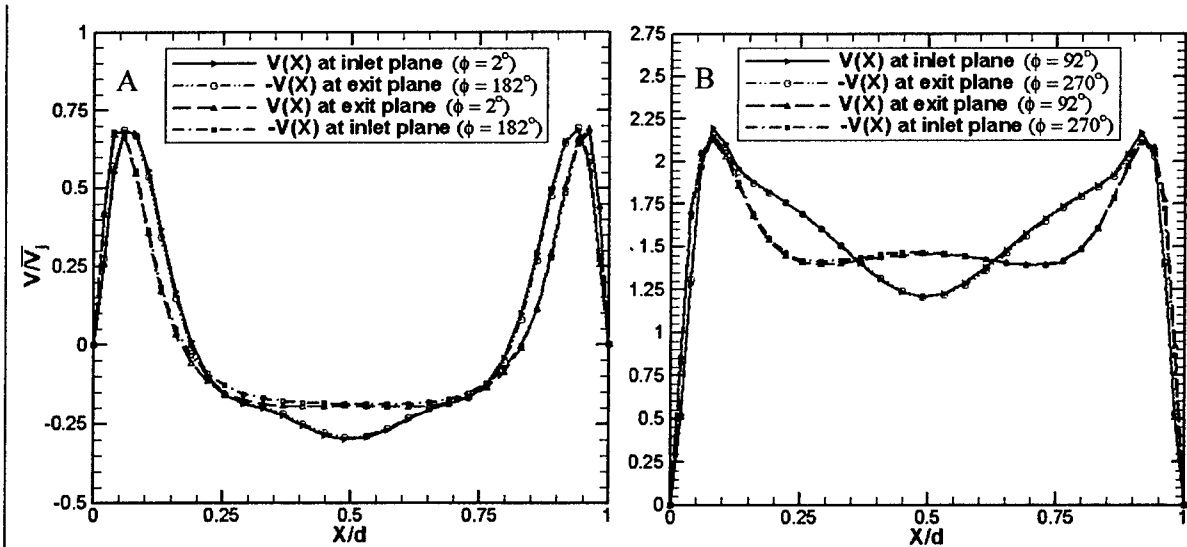


Figure 4-19: Comparison between Case 2 vertical velocity profiles at the orifice ends. A) At start of expulsion and start of ingestion. B) At maximum expulsion and maximum ingestion.

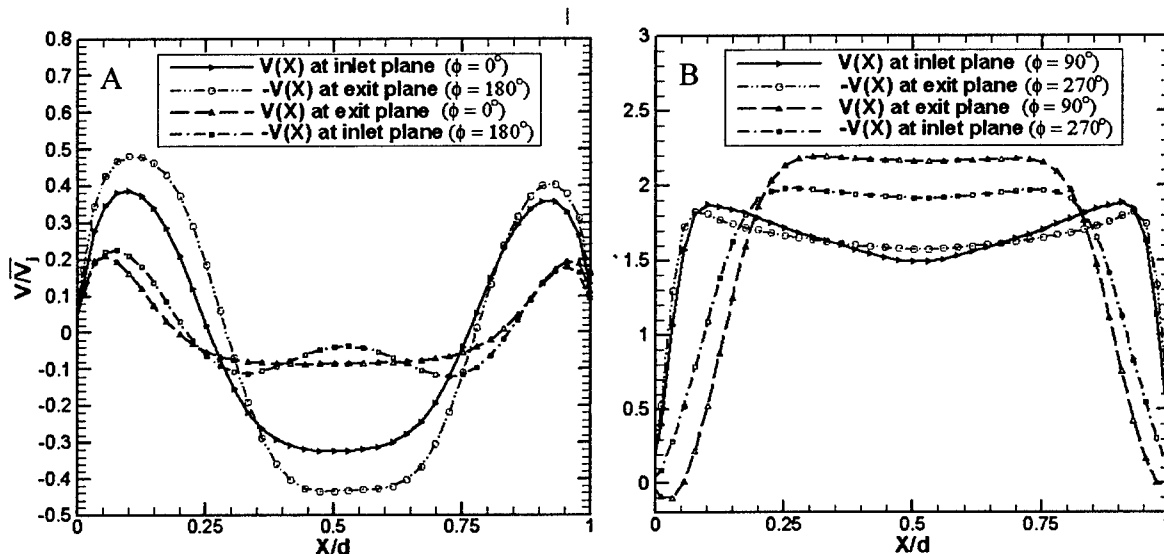


Figure 4-20: Comparison between Case 3 vertical velocity profiles at the orifice ends. A) At start of expulsion and start of ingestion. B) At maximum expulsion and maximum ingestion.

#### 4.3 Nonlinear Mechanisms in a ZNMF Actuator

In view of the experimental results, the effect of the different nonlinear mechanisms present in the system may be a critical issue that needs to be addressed if one wants to gain confidence in the interpretation and the use of the experimental data. If one “takes a ZNMF actuator apart,” it is basically comprised of the driver (a piezoelectric diaphragm in the case of the current experimental tests), the cavity, and the orifice. Hence, by considering the pressure fluctuation signal as the output signal of interest, nonlinearities in this signal can arise due to:

1. orifice nonlinearities
2. cavity nonlinearities
3. driver nonlinearities

First, the oscillatory nature of the flow through the orifice can generate nonlinearities in the pressure signal due to the entrance and exit regions. These nonlinearities are the focus of this report, the goal being to isolate them in order to develop a suitable reduced-order model that accounts for these types of nonlinearities in the pressure signal. Before proceeding down this path, we first need to understand how nonlinearities due to the cavity pressure fluctuations and the driver scale with operating conditions.

Starting with the cavity pressure fluctuations, nonlinearities in the signal can arise due to deviations of the sound speed from the isentropic small-signal sound speed (Blackstock 2000, pp. 34-35). The general isentropic equation of state  $p = p(\rho) = p' + p_0$  can be expressed in terms of a Taylor series expansion, such that



$$p' = \underbrace{\frac{\gamma p_0}{\rho_0}}_{c_0^2} \rho' \left[ 1 + \frac{(\gamma-1)}{2!} \frac{\rho'}{\rho_0} + \frac{(\gamma-1)(\gamma-2)}{3!} \left( \frac{\rho'}{\rho_0} \right)^2 + \dots \right], \quad (3-10)$$

where  $\gamma$  is the ratio of specific heats, and the superscript  $'$  denotes fluctuating quantities and the subscript 0 denotes nominal values. Here, the small-signal isentropic sound speed is defined as  $c_0 = \sqrt{\gamma p_0 / \rho_0}$  that is strictly speaking only valid in the limit as  $\rho \rightarrow \rho_0$ . It is therefore of interest to apply Eq. 3-10 in the case of the ZNMF actuator having a closed cavity to isolate its effect. For a closed cavity, the conservation of mass can be directly written as

$$\frac{\partial}{\partial t}(\rho \nabla) = 0, \quad (3-11)$$

or,

$$\nabla \frac{d\rho}{dt} + \rho \frac{d\nabla}{dt} = 0, \quad (3-12)$$

which is simply equivalent to

$$\frac{\rho'}{\rho} = \frac{d\rho}{\rho} = -\frac{d\nabla}{\nabla}. \quad (3-13)$$

By then substituting Eq. 3-13 in Eq. 3-10, and for an adiabatic gas, Figure 4-21 can be generated that shows the variation between the linear small-signal approximation and the exact nonlinear solution, as a function of the change of volume inside the cavity. Hence, significant nonlinearities due to the departure of the cavity small-signal approximation will not arise for pressures below  $\sim 160$  dB, and/or for change in the cavity volume  $d\nabla/\nabla < 0.02$ . Notice that the change in volume is dictated by the driver volume flow rate  $Q_d = j\omega\Delta\nabla$ , where here  $\Delta\nabla = d\nabla$ . The maximum change in cavity volume and pressure seen in our experiments is for Case 69, where  $d\nabla/\nabla = 0.014$  and the pressure is equal to 64 dB, which is well below the departure of the small-signal approximation. This effect is therefore not an issue in our experiments.

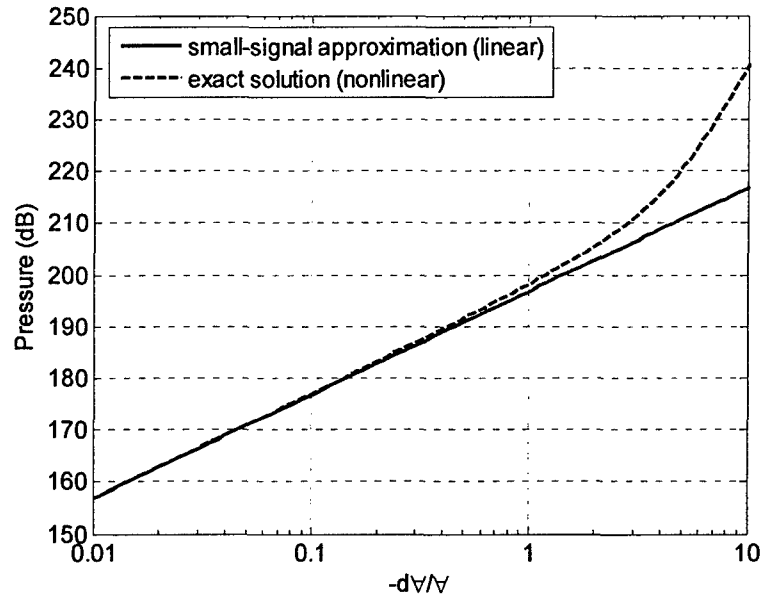


Figure 4-21: Determination of the validity of the small-signal assumption in a closed cavity.

Next, the driver nonlinearities are considered. Obviously, by driving the piezoelectric diaphragm at frequencies much higher than the first natural frequency  $f_d$ , some nonlinearity can result in the driver signal. Hence, most of the test cases are operating at frequencies below  $f_d = 632$  Hz, and only two frequencies above  $f_d$  (at  $f = 730$  Hz and  $f = 780$  Hz) are considered in the experimental investigation, for which the distortion of the driver signal is closely monitored. Similarly, nonlinear behavior can occur at dc, coming from the distortion in the measured displacement signal for a pure tone input. Note that nonlinearities can also arise from the power amplifier. As detailed in Section 3, the input signal is amplified before arriving to the piezoelectric driver, and the amplifier has intrinsic dynamics.

After being identified, these nonlinearities must also be extracted and quantified to determine their effect on the actuator behavior. A useful tool in the investigation of nonlinear effects is found in the study of the total harmonic distortion (THD). The THD is defined as the ratio of the sum of the powers of all harmonic frequencies above the fundamental frequency to the power of the fundamental one (National Instruments 2000):

$$\text{THD (\%)} = \frac{\sum_{k=1}^N G(\omega_k)}{G(\omega_0)} \times (100), \quad (3-14)$$

where  $k = 1 \dots N$  is the number of harmonics and  $k = 0$  represents the fundamental frequency. The results of the spectral analysis of the time signal presented in Section 3 are used in this investigation. Note that in this analysis the THD contains the measured total harmonic distortion up to and including the highest harmonic at  $10\omega$  ( $N = 10$ ), hence is not limited to the first few harmonics. First, Figure 4-22 shows the THD present in the cavity pressure (taken with microphone 1, see Section 3 for definition) as a function of

the change in the cavity volume  $dV/V$  and function of the ratio of the Helmholtz to actuation frequency  $\omega/\omega_H$ . Clearly, the distortions in the cavity pressure signal are not affected by the change in cavity volume, as shown in Figure 4-22A and described above. Similarly, compressibility effects appear to not play a role in the cavity pressure signal distortion, as seen from Figure 4-22B. The next section (Section 5) discusses the cavity compressibility effect in more details.

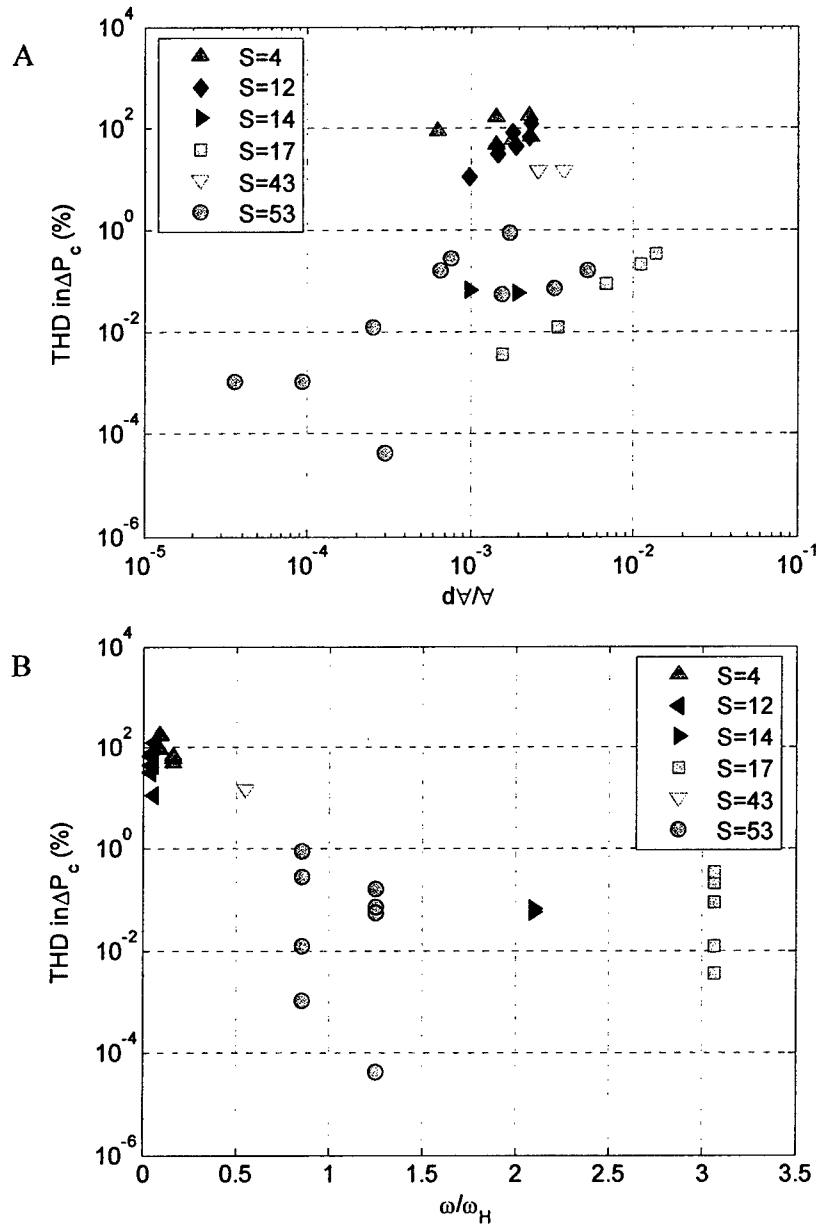


Figure 4-22: Log-log plot of the cavity pressure total harmonic distortion in the experimental time signals. A) Versus  $dV/V$ . B) Versus  $\omega/\omega_H$ .

Next, Figure 4-23 shows the THD variation in the time signals as a function of the Strouhal number for different Stokes numbers. From the pressure signal (acquired by microphone 1, see Figure 3-3 in Section 3 for definition) plotted in Figure 4-23A, significant nonlinearities are present especially at the low Strouhal number cases. This is in accordance with the time traces already seen in Figure 3-12: Continued. . Figure 4-23B shows the THD in the jet volume velocity which, besides a few cases at low Strouhal numbers, is less than 1%. This means that the majority of the cases can have  $Q_j$  accurately represented by a pure sinusoidal signal. Finally, the THD present in the diaphragm signal is shown in Figure 4-23C. Clearly, the motion of the diaphragm displacement in time can be correctly assumed to be sinusoidal for all the cases considered, a negligible percent of nonlinearities in the signal being present. Therefore, practically the nonlinearities present in the experimental signal mostly come from the orifice, no cases are found to be strongly affected by nonlinearities that are not due just to the orifice.

To summarize this section, a joint experimental and numerical investigation of the velocity profiles, at the orifice exit as well as inside the orifice, has been performed. Numerical simulations are a useful tool to elucidate the orifice flow physics in ZNMF actuators and complement the experimental results. Clearly, the orifice flow is far from trivial, especially for such small orifices and flow conditions, and it exhibits a rich and complex behavior that is a function of the location inside the orifice and a function of phase angle during the cycle.

Next, the influence of the governing parameters, such as the orifice aspect ratio  $h/d$ , Stokes number  $S$ , Reynolds number  $Re$ , Strouhal number  $St$ , or stroke length  $L_0$ , has been experimentally and numerically investigated. It has been found that a dimensionless stroke length – equivalent to the Strouhal number times  $h/d$  - is the main parameter in describing the losses associated with the pressure drop across the orifice.

Finally, a survey of the possible sources of nonlinearities present in the time signals of interest (pressure, jet volume flow rate) has been performed. Potential nonlinear sources were identified and evaluated; their overall influence on the actuator performance has been quantified through a total harmonic distortion analysis. The information gathered through this study on the orifice flow results will aid in the understanding and the development of a physics-based reduced-order model of such actuators in subsequent sections.

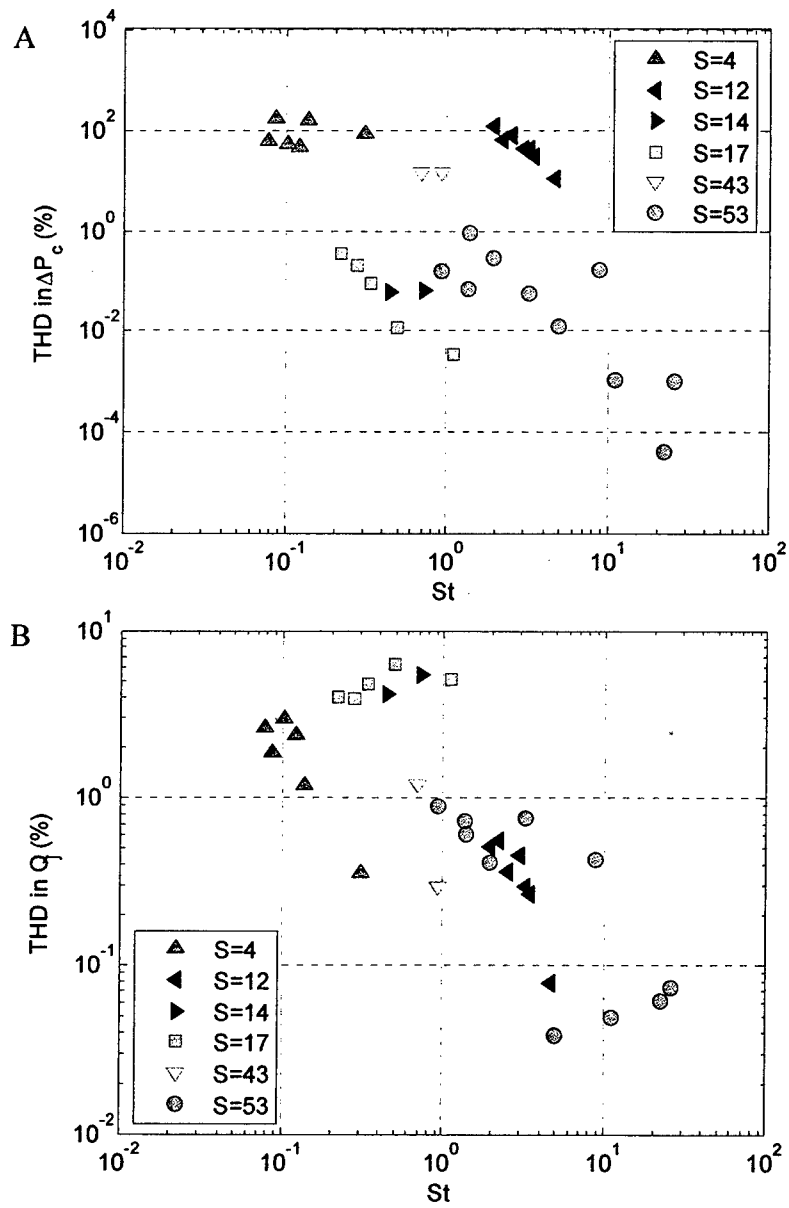


Figure 4-23: Log-log plot of the total harmonic distortion in the experimental time signals vs. Strouhal number as a function of Stokes number. A) Cavity pressure. B) Jet volume flow rate. C) Driver volume flow rate.

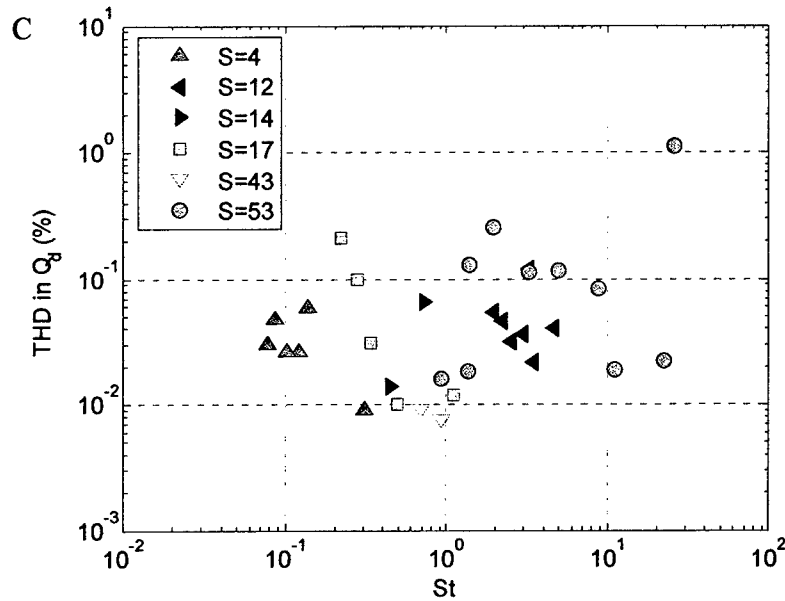


Figure 4-23: Continued.

## 5. Results: Cavity Investigation

This section discusses the cavity behavior of a ZNMF actuator device, based on the experimental results presented in the previous section and using available numerical simulation results. A discussion is first provided on the measured and computed cavity pressure field, based on experimental and numerical results. Then follows a careful analysis of the compressibility effects occurring inside the cavity where it is shown that the Helmholtz frequency is the critical parameter to be considered. Finally, the driver, cavity and jet volume velocities are considered, specifically their respective roles and how they interact and couple with each other. Ultimately, this investigation on the cavity will give valuable insight and help in the understanding of the physical behavior of ZNMF actuators in quiescent air for both modeling and design purposes.

### 5.1 Cavity Pressure Field

The knowledge of the pressure inside the cavity is of great interest since it dictates the orifice flow behavior, which is naturally a pressure-driven oscillatory flow. In fact, the cavity pressure fluctuations are approximately equivalent to the pressure drop across the orifice; hence it plays a central role in the overall actuator response. Specifically, the magnitude and the phase of the pressure signal are of interest, and comparing the data from two separate microphones placed at different locations inside the cavity, as shown in Figure 3-3, provide some answers. Moreover, since a characteristic feature of the reduced-lumped element model presented in Section 2 is to assume that the pressure drop across the orifice is equivalent to the cavity pressure, it is of great importance to know whether or not this assertion is valid. This is detailed below, based on both experimental and numerical results.

### 5.1.1 Experimental Results

First of all, a spectrum analysis has been performed on the pressure traces to characterize the dominant features of the time signals. Figure 5-1 shows the coherent power spectrum of Cases 9 to 20 (all with the same Stokes number of 8) recorded via Microphone 1, that clearly indicates non negligible harmonic components present in almost all cases, with the fundamental component  $f_0$  always capturing most of the total power and the 2<sup>nd</sup> harmonic at  $3f_0$  having the next most contribution. Notice however the presence of the 60 Hz and 120 Hz line noise from the noise floor measurement shown on the front face. Also, it is found that only super-harmonics are present, no sub-harmonics, which shows that using a Fourier series decomposition of the phase-locked pressure signal is a valid approach.

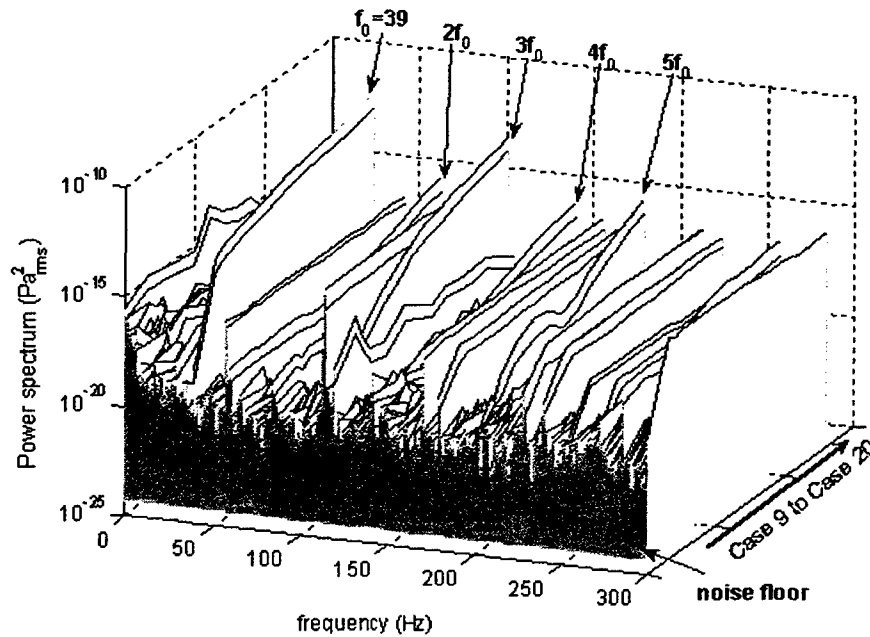


Figure 5-1: Coherent power spectrum of the pressure signal for Cases 9 to 20,  $S = 8$  and  $Re = 9 \rightarrow 88$ .

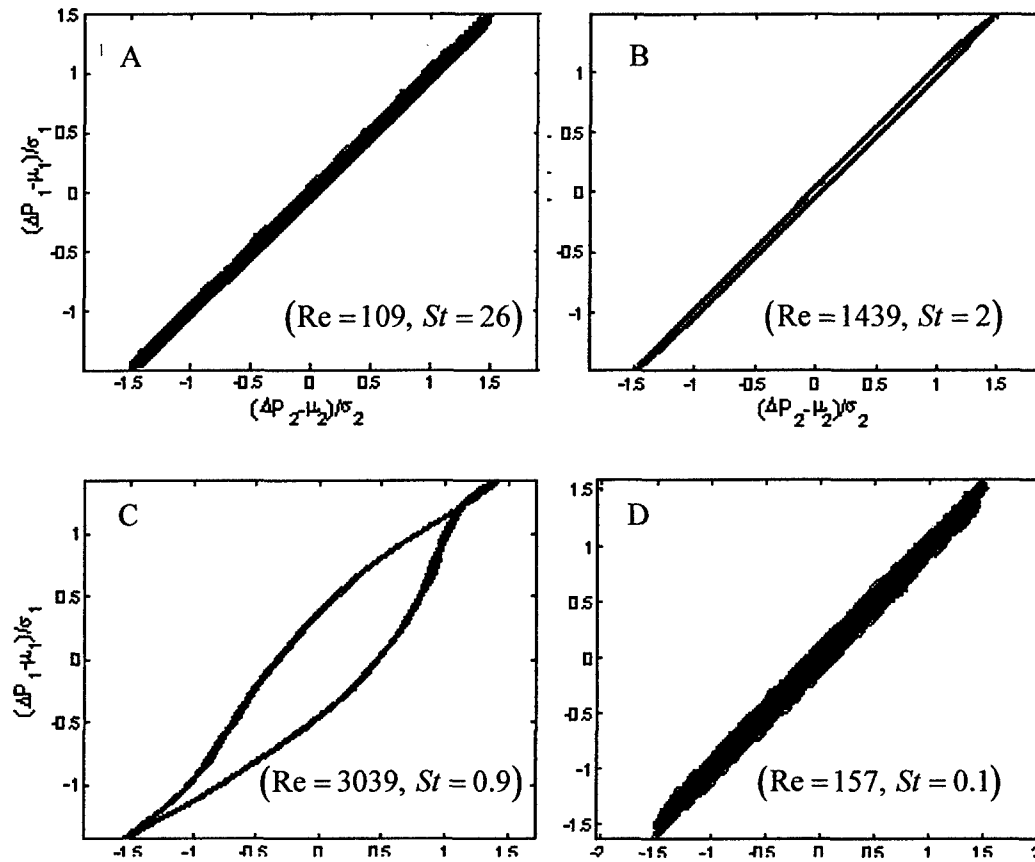


Figure 5-2: Phase plot of the normalized pressures taken by microphone 1 versus microphone 2. A) Case 46. B) Case 49. C) Case 59. D) Case 62.

Next, the phase difference between the two microphones is analyzed. Four different cases are examined, one when the two pressure signals appear quite sinusoidal and similar in shape as in Case 46 ( $Re = 109$ ,  $St = 26$ ) and Case 49 ( $Re = 1439$ ,  $St = 2$ ), another one (Case 59,  $Re = 3039$ ,  $St = 0.9$ ) when one microphone exhibits some distortion while the other is rather sinusoidal, and finally the scenario when both signals are clearly nonlinear, as in Case 62 ( $Re = 157$ ,  $St = 0.1$ ). Figure 5-2 shows the phase plots of these four cases, where the pressure data is normalized by subtracting the mean  $\mu$  and dividing by the standard deviation  $\sigma$ . Clearly, in each scenario the phase between the two microphones is surprisingly invariant, with the exception of Case 59. And although only four cases are reported here, this behavior is typical for all cases. As for Case 59, Figure 5-3 plots the phase locked pressure signals during one cycle, and the phase difference observed from the phase plot is clearly seen here when crossing the zero axis, but the peak amplitudes occur at the same phase for each signal, i.e. at the maximum expulsion and maximum ingestion time of the cycle.



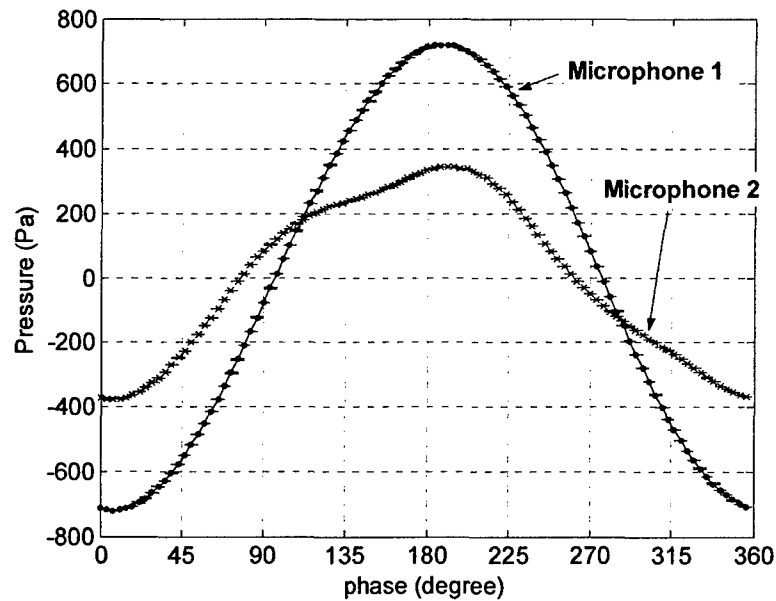


Figure 5-3: Pressure signals experimentally recorded by microphone 1 and microphone 2 as a function of phase in Case 59 ( $S = 53$ ,  $Re = 3039$ ,  $St = 0.9$ ).

The amplitude of the pressure inside the cavity is investigated next. While the phase seems spatially invariant inside the cavity, a change in amplitude is noted. This is already seen in Figure 5-3 for Case 59, but is also represented for all cases in Figure 5-4 that plots the ratio of the total amplitude between microphone 2 and 1, as a function of the inverse of the Strouhal number. Noticeably, referring to Figure 3-3 for the microphone locations, whether the pressure amplitude is recorded on the side or on the bottom of the cavity does matter. Notice that by plotting  $\Delta P_{c,2}/\Delta P_{c,1}$  against  $1/St$ , one can also infer the influence of the jet formation criterion on the pressure data. Certainly, whether a jet is formed or not may affect the pressure amplitude variation inside the cavity. Moreover, when looking at the value of  $kH$  - the wavenumber times the largest cavity dimension - for these cases, and indicated in the legend of Figure 5-4, it is clear that for the high Stokes number cases, the compact acoustic source approximation may not be valid anymore, meaning that the cavity does not act like a pure compliance and some mass, or inertia, terms may come into play.

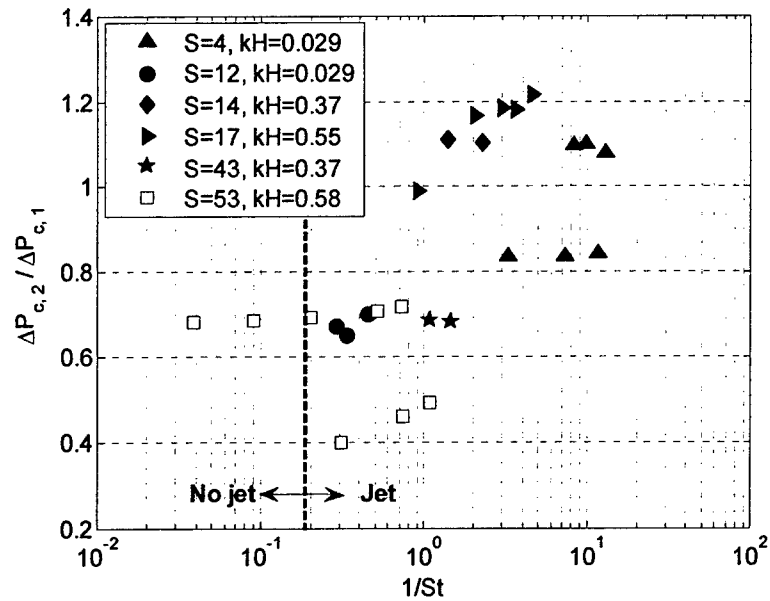


Figure 5-4: Ratio of microphone amplitude (Pa) vs. the inverse of the Strouhal number, for different Stokes number. The vertical line indicates the jet formation criterion.

### 5.1.2 Numerical Simulation Results

Numerical simulations are a useful tool, especially when experiments fail. Indeed, in the present context it is really difficult, if not impossible, to measure the actual pressure drop across the orifice - hence the two microphones placed inside the cavity. Therefore, the importance of the CFD results takes its entire place for cavity flows.

To confirm the experimental observations, available numerical simulation data is thus analyzed. These data have been previously reported in Gallas et al. (2004), and Case 2 ( $Re = 262$ ,  $St = 2.4$ ) and Case 3 ( $Re = 262$ ,  $St = 0.4$ ) in the test matrix (Table 2-3) are considered here. Notice however that this simulation uses an incompressible solver for the cavity where the pressure field is computed by solving the Poisson equation, and that it assumes a 2D sinusoidal vibrating membrane at the bottom of the cavity, thereby neglecting any three-dimensional effects. Yet the solution can be considered valid since the actuation frequency is far below the Helmholtz frequency (the next section describes this compressibility effect in great detail), and since the cavity size is much smaller than the wavelength. Also, previous work (Utturkar et al. 2002) showed that the ZNMF actuator performance was rather insensitive to the driver placement inside the cavity.

The pressure distribution at one instant in time is first given for Case 2, where Figure 5-5A corresponds to  $45^\circ$  during the expulsion portion of the cycle ( $0^\circ$  corresponding to the onset of jet expulsion), and Figure 5-5B is at the beginning of the ingestion cycle. In this case where no jet is formed, the pressure is fairly uniform inside the cavity away from the orifice entrance. On the other hand, in the case where a clear jet is formed, as for Case 3, the pressure inside the cavity has a more disturbed pattern, as it can be seen in Figure 5-6 where contours of the pressure field is shown at different phases during the ingestion portion of the cycle. Nodes are present inside the cavity as a function of phase, which is mainly due to the high stroke length that is characteristic of

this case. During the ingestion process, fluid particles reach and impinge on the bottom of the cavity, hence generating some circulation at the corners that quickly dissipates as the driver starts a new cycle.

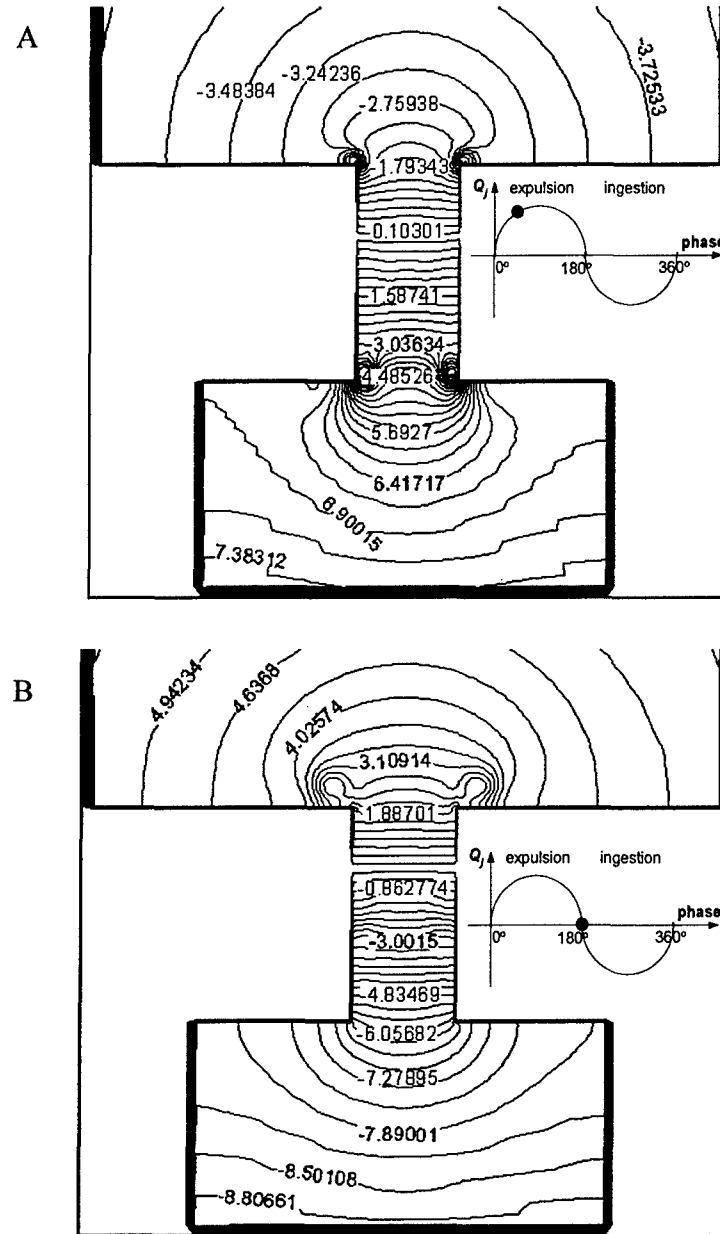


Figure 5-5: Pressure contours in the cavity and orifice for  $Re = 262$  and  $St = 2.4$  (Case 2) from numerical simulations. A) 45° during expulsion. B) Beginning of the suction cycle, referenced to  $Q_j$ .

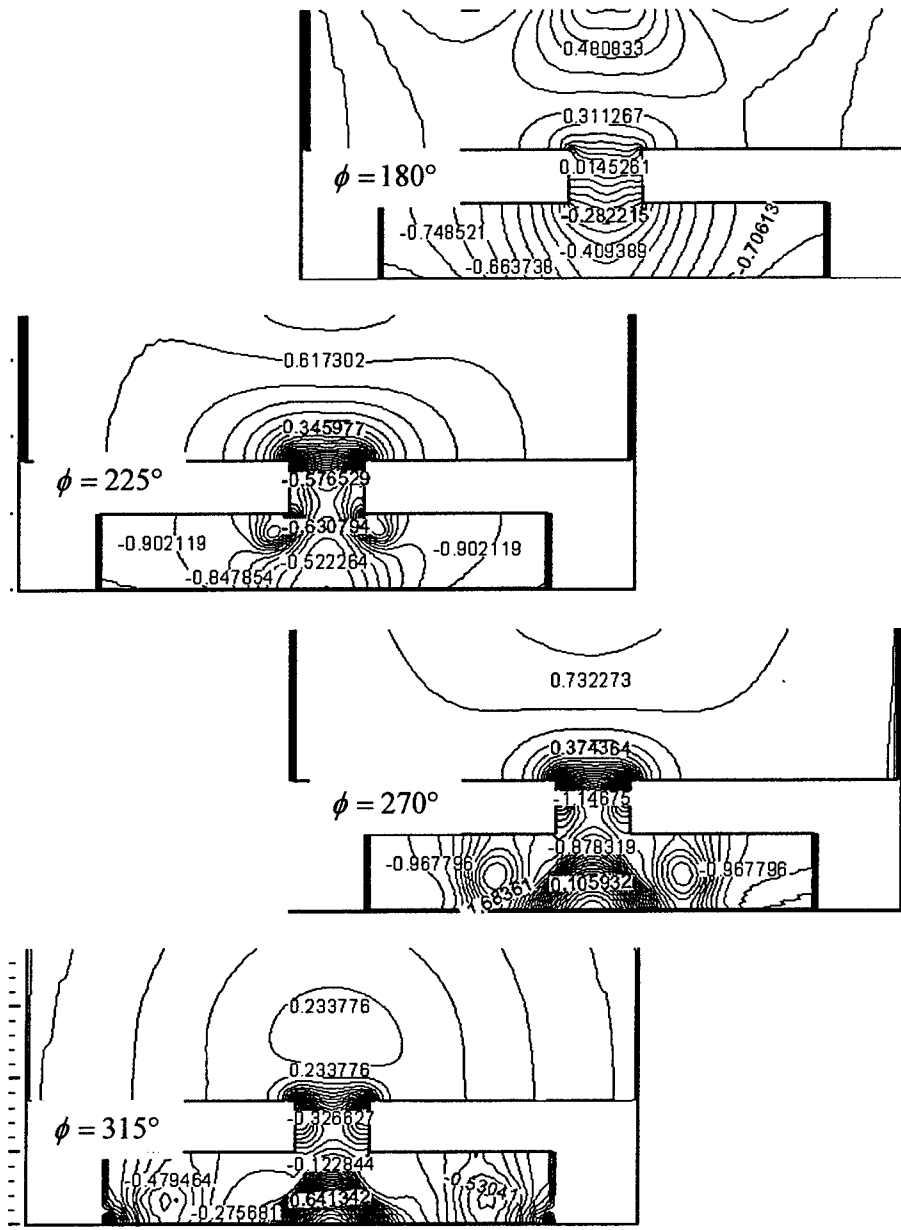


Figure 5-6: Pressure contours in the cavity and orifice for  $Re = 262$  and  $St = 0.4$  (Case 3) from numerical simulations at four different phases during the ingestion part of the cycle.

To complete this picture of the pressure field, the cavity is probed at fifteen locations, as schematized in Figure 5-7, and the instantaneous pressure is recorded as a function of time during one cycle. The results for Case 2 (no jet) are plotted in Figure 5-8A and for Case 3 (strong jet) in Figure 5-8B. The vertical axis shows the magnitude of the pressure normalized by  $\rho \bar{V}_j^2$ , on one of the horizontal axes is the phase angle and on the other one the five slices corresponding to the five cuts made parallel to the driver up to the orifice inlet, as schematized in Figure 5-7. For each slice, the side, middle and

center probes are plotted on top of each other. In these two examples, the effect of a jet being formed at the orifice exit, and hence at the orifice inlet as well, does appear to influence the pressure field inside the cavity.

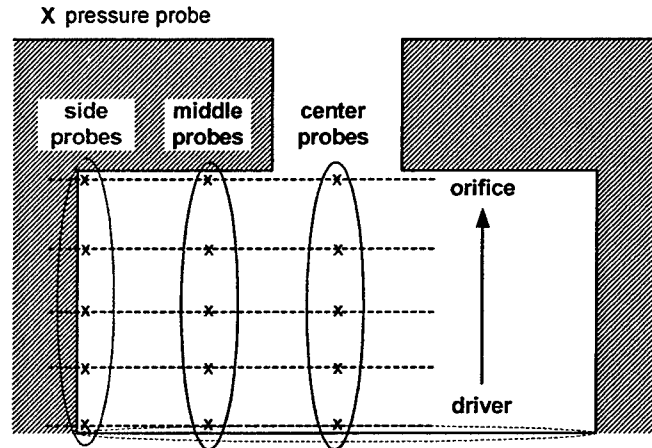


Figure 5-7: Cavity pressure probe locations in a ZNMF actuator from numerical simulations.

Actually, to try comparing the CFD data with the experimental results, although the driver is not on the same side of the cavity and is modeled as a 2D vibrating membrane, the three locations corresponding to the positions of the two microphones in the experimental setup plus just at the orifice entrance are extracted from the above figures and are shown in Figure 5-9. Clearly, as one move towards the orifice, the pressure decreases and increasing distortion in the time signals are noted for the large stroke length case. Also, the pressure is much larger in amplitude for the higher Stokes number case, although the two cases have the same jet Reynolds number. Note that the phase between the different pressure probes is again spatially invariant.

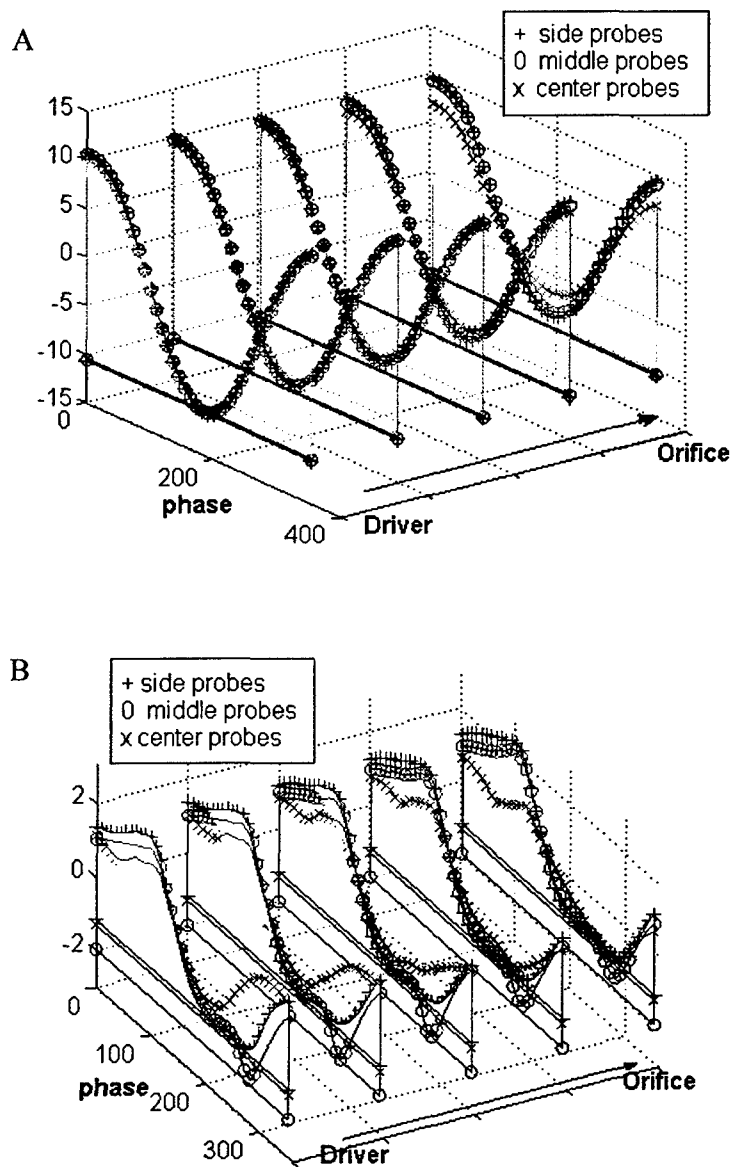


Figure 5-8: Normalized pressure inside the cavity during one cycle at 15 different probe locations from numerical simulation results. A) Case 2 (no jet formed). B) Case 3 (jet formed).

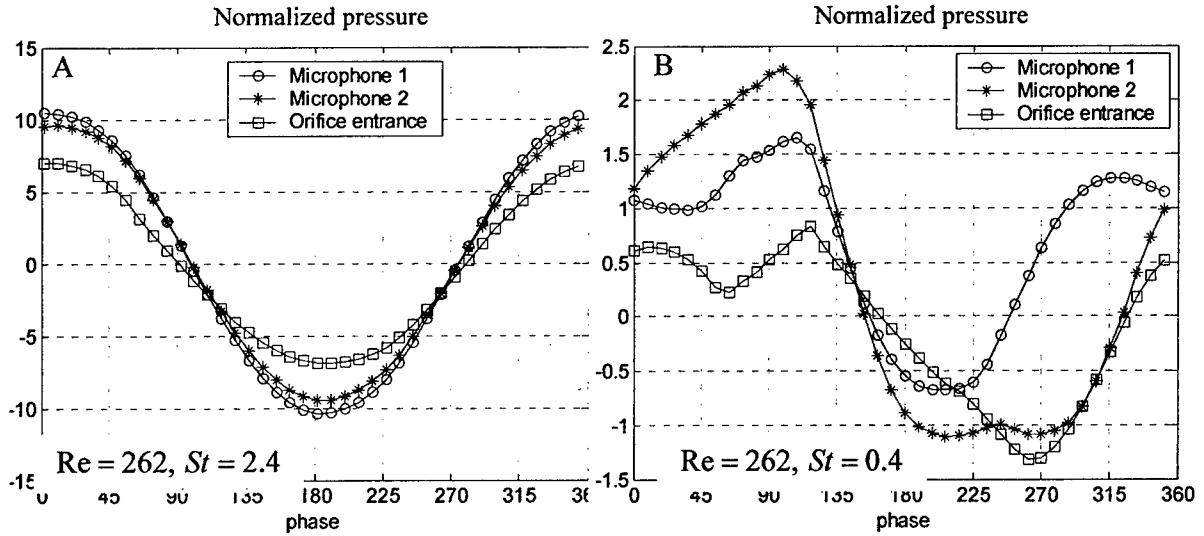


Figure 5-9: Cavity pressure normalized by  $\rho \bar{V}_j^2$  vs. phase from numerical simulations corresponding to the experimental probing locations. A) Case 2 (no jet formed). B) Case 3 (jet formed).

## 5.2 Compressibility of the Cavity

The question of the validity of an incompressible assumption for modeling the cavity is of great interest and practical importance. First, from a computational point of view, it is rather essential to know whether the flow inside the cavity can be considered as incompressible, the computational approach being quite different for a compressible and an incompressible solver. Second, from the equivalent circuit perspective of the lumped element model presented in Section 2, a high cavity impedance (which occurs for a “stiff” or incompressible cavity) will prevent the flow from going into the cavity branch. On the other hand, a “compliant” or compressible cavity will draw fluid flow hence reducing the output response. The compressibility behavior is explored via illustrative cases, both analytically and experimentally. The LEM prediction serves in providing the general trend and behavior in the frequency domain, while experimental data are used here to validate these findings.

### 5.2.1 LEM-Based Analysis

First, consider some analytical examples. They are Case 1 described in Gallas et al. (2003a) and Case 1 of the NASA Langley workshop CFDVal2004 (2004). Both examples have a piezoelectric-diaphragm driver and are thus expected to exhibit two resonant frequencies. The acoustic impedance of the cavity  $Z_{ac}$  is systematically varied through the cavity volume variable  $\nabla$  since, assuming an isentropic ideal gas, they are directly related via

$$Z_{ac} = \frac{1}{j\omega C_{ac}} = \frac{\rho c_0^2}{j\omega \nabla}, \quad (4-1)$$

and the frequencies that govern the system response are recorded and compared. From Eq. 4-1, it is expected that as the cavity volume decreases and tends to zero, the acoustic

compliance  $C_{ac}$  also tends to zero, and the cavity becomes “stiff”. These frequencies are defined as follows. In particular,  $f_1$  and  $f_2$  are the first and second resonance frequencies, respectively, in the synthetic jet frequency response and are defined in Gallas et al. (2003a)

$$\psi^2 - [f_d^2(1 + \mathfrak{C}) + f_H^2]\psi + f_d^2 f_H^2 = 0, \quad (4-2)$$

where  $\mathfrak{C} = C_{ad}/C_{ac}$  is the compliance ratio, and  $\psi = f_i^2$ . The two roots of the quadratic equation Eq. 4-2 are the square of the natural frequencies of the synthetic jet, i.e.  $f_1^2$  and  $f_2^2$ . Here,  $f_H = \omega_H/2\pi$  is the Helmholtz frequency of the synthetic jet resonator and since

$$\omega_H = \sqrt{\frac{1}{M_{ao}C_{ac}}}, \quad (4-3)$$

is directly proportional to the cavity and orifice geometrical dimensions via both the acoustic mass of the orifice  $M_{ao}$  and the acoustic compliance of the cavity  $C_{ac} \propto V$  (see Eq. 4-1). Similarly,  $f_d = \omega_d/2\pi$  is the natural frequency of the actuator diaphragm. In general  $f_1 \neq f_H$  or  $f_d$  and  $f_2 \neq f_d$  or  $f_H$ , and only for the limiting cases when  $f_1$  and  $f_2$  are widely separated in frequency do the two peaks approach the driver and Helmholtz frequencies. Nevertheless, these two frequencies are always constrained via  $f_1 f_2 = f_d f_H$ .

With this information as background, consider Case 1 from Gallas et al. (2003a), in which all parameters are fixed to their respective nominal values and the cavity volume is progressively decreased. The baseline case is such that  $f_H < f_d$ , and the natural frequency of the diaphragm along with the orifice dimensions are held constant. Table 5-1 shows the impact of the decrease of the cavity volume on the frequency response of the system, and is illustrated in the log-log plot in Figure 5-10. The first frequency  $f_1$  is clearly governed by the diaphragm natural frequency and tends to a fixed value equal to  $f_d$  as the volume decreases, while the second frequency  $f_2$  is influenced by the Helmholtz frequency  $f_H$  that tends to infinity as the volume is decreased. Notice however that LEM breaks down for high frequencies since the assumption of  $kd \ll 1$  is no longer valid.



Table 5-1: Cavity volume effect on the device frequency response for Case 1 (Gallas et al. 2003a) from the LEM prediction.

$f_d = 2114 \text{ (Hz)}$	$f_H \text{ (Hz)}$	$f_1 \text{ (Hz)}$	$f_2 \text{ (Hz)}$
Baseline: $\nabla_0 = 2.5 \times 10^{-6} \text{ (m}^3\text{)}$	941	918	2,167
$\nabla = \nabla_0/2$	1,331	1,254	2,243
$\nabla = \nabla_0/5$	2,104	1,685	2,640
$\nabla = \nabla_0/10$	2,976	1,832	3,434
$\nabla = \nabla_0/20$	4,208	1,885	4,719
$\nabla = \nabla_0/50$	6,654	1,911	7,363
$\nabla = \nabla_0/100$	9,410	1,918	10,372
$\nabla = \nabla_0/500$	21,042	1,924	23,123
$\nabla = \nabla_0/1000$	29,757	1,924	32,690

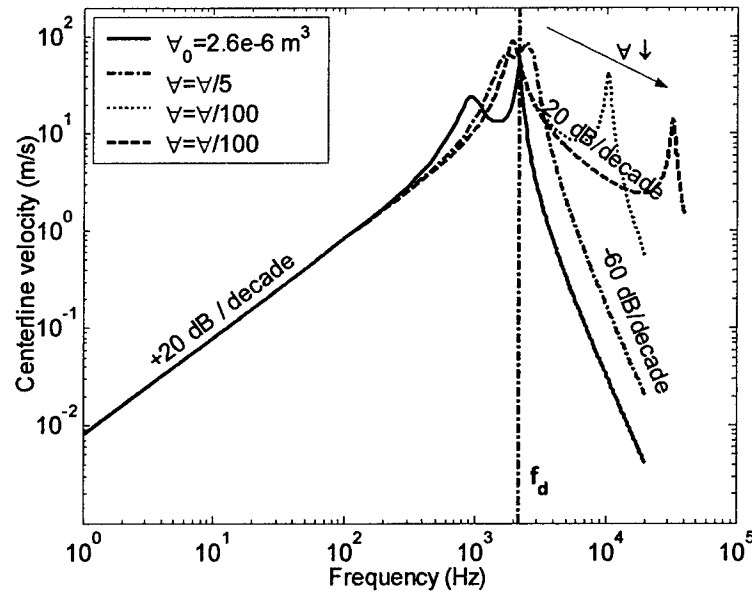


Figure 5-10: Log-log frequency response plot of Case 1 (Gallas et al. 2003a) as the cavity volume is decreased from the LEM prediction.

Table 5-2: Cavity volume effect on the device frequency response for Case 1 (CFDVal 2004) from the LEM prediction.

$f_d = 460 \text{ (Hz)}$	$f_H \text{ (Hz)}$	$f_1 \text{ (Hz)}$	$f_2 \text{ (Hz)}$
Baseline: $\nabla_0 = 7.4 \times 10^{-6} \text{ (m}^3\text{)}$	1,985	446.2	2,048
$\nabla = \nabla_0/2$	2,808	446.5	2,894
$\nabla = \nabla_0/5$	4,440	446.7	4,574
$\nabla = \nabla_0/10$	6,279	446.8	6,468
$\nabla = \nabla_0/20$	8,880	446.8	9,146
$\nabla = \nabla_0/50$	14,044	446.9	14,461
$\nabla = \nabla_0/100$	19,856	446.8	20,451
$\nabla = \nabla_0/500$	44,400	446.8	45,729
$\nabla = \nabla_0/1000$	62,791	446.8	64,671

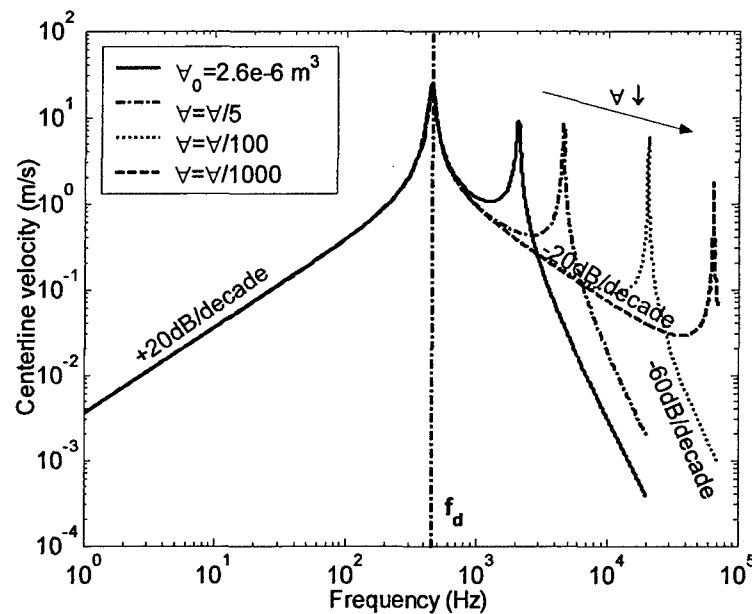


Figure 5-11: Log-log frequency response plot of Case 1 (CFDVal 2004) as the cavity volume is decreased from the LEM prediction.

Similarly, as a second example, all parameters are based on Case 1 of the NASA workshop CFDVal2004 (2004), and the cavity volume is again progressively decreased from its nominal value. This time, the baseline case is such that  $f_H > f_d$ , and Table 5-2 and Figure 5-11 are generated to illustrate the behavior of the actuator frequency response. In this case, the first resonant frequency is governed by the cavity resonant

frequency  $f_H$  that tends to infinity as the cavity volume is decreased, while the second frequency is limited by the natural frequency of the diaphragm  $f_d$ . This case is actually the continuation of the previous example but starting with  $f_H$  already greater than  $f_d$ , hence starting with a smaller cavity.

Interestingly, in both cases the system exhibits a 20 dB/decade rise at low frequencies, and has a -60 dB/decade roll off at high frequencies representative of a system with a pole-zero excess of 3. In between the two resonant frequencies  $f_1$  and  $f_2$ , the response decreases at a rate of 20 dB/decade, similar to a 1<sup>st</sup>-order system. The influence of the cavity volume is clearly confined to one of the peaks in the actuator response. For both cases, as the cavity volume shrinks to zero, a single low frequency peak near the diaphragm natural frequency is obtained. The second peak progressively moves to higher frequencies as the cavity volume is decreased, and since  $f_H \propto 1/\nabla$  the following limit behavior is observed

$$\begin{cases} \lim_{\nabla \rightarrow 0} (f_1) \rightarrow f_d \\ \lim_{\nabla \rightarrow 0} (f_2) \rightarrow f_H \rightarrow \infty \end{cases} \quad (4-4)$$

### 5.2.2 Experimental Results

This interesting behavior is now experimentally verified. In the experimental investigation described in Section 3, this is referred to as Test 2 in the setup. A nominal synthetic jet device is taken and the cavity volume is systematically decreased to yield four different actuators, with all other components held fixed. The dimensions and test conditions of the devices are listed in Table 3-1. The phase-locked centerline velocity is then acquired at different frequencies using LDV measurements, in the same manner as discussed in Section 3.

Table 5-3: ZNMF device characteristic dimensions used in Test 2

Property:	Case A	Case B	Case C	Case D
Cavity volume $\nabla$ (m <sup>3</sup> )	4.49×10 <sup>-6</sup>	2.42×10 <sup>-6</sup>	1.09×10 <sup>-6</sup>	0.71×10 <sup>-6</sup>
Orifice diameter $d$ (mm)		1.5		
Orifice thickness $h$ (mm)		2.7		
Orifice width $w$ (mm)		11.5		
Diaphragm diameter (mm)		23		
Input sine voltage $V_{ac}$ (V <sub>pp</sub> )		30		
Diaphragm natural frequency $f_d$ (Hz)		2114		
Helmholtz frequency $f_H$ (Hz) *	1275	1738	2586	3221

(\*) computed from Eq. 4-5

The results are plotted in a log-log scale in Figure 5-12 and Figure 5-13 gives a close-up view of the peak locations in a linear plot. Also, Table 5-4 lists the different frequencies of interest. Two sets of frequencies are compared: ones that are experimentally measured, the others that are analytically computed. The frequency

response plot in Figure 5-13 provides  $f_{1,\text{exp}}$  and  $f_{2,\text{exp}}$  the two natural frequencies of the system. For the two test cases that have a cavity wide enough to allow the insertion of a microphone inside (Case A and Case B), the Helmholtz frequency is experimentally determined by a simple “blowing test” (effect of blowing over an open bottle) where the spectra of the microphone is recorded while the actuator is passively excited by blowing air at the orifice lip. Then, analytically  $f_1$  and  $f_2$  are computed solving Eq. 4-2 that only requires the knowledge of the diaphragm and cavity acoustic compliances and  $f_d$  and  $f_H$ . Here,  $f_H$  is calculated from its acoustical definition, i.e.,

$$f_H = \frac{1}{2\pi} c_0 \sqrt{\frac{S_n}{(h+h_0)V}}, \quad (4-5)$$

where  $h_0 = 0.96\sqrt{S_n}$  is the orifice effective length for an arbitrary aperture. Note also that in this experimental setup, the largest dimension of the device is the cavity height  $H$  equals to 26.8mm. The frequency limit under which Eqs. 4-3 and 4-5 are still valid corresponds to about  $kH < 1$ , or  $H/\lambda < 1/6$ . In terms of frequency, this means that the LEM assumption in these test cases is only valid for frequencies  $f < 2200\text{Hz}$ , i.e. about up to the natural frequency of the diaphragm. And clearly, as seen in Table 5-4, this assumption is violated for the 2 smallest cavities, hence the discrepancy between the experimental and analytical  $f_1$  and  $f_2$ .

Table 5-4: Effect of the cavity volume decrease on the ZNMF actuator frequency response for Cases A, B, C, and D.

$f_d = 2114 \text{ (Hz)}$	<i>from experiments</i>			<i>from analytical equations</i>		
	$f_H \text{ (Hz)}$	$f_1 \text{ (Hz)}$	$f_2 \text{ (Hz)}$	$f_H \text{ (Hz)}$	$f_1 \text{ (Hz)}$	$f_2 \text{ (Hz)}$
Case A	1272	1200	2100	1275	1253	2152
Case B	1732	1600	2000	1738	1651	2226*
Case C	N/A	1700	2400	2586*	1972	2774*
Case D	N/A	1700	2600	3221*	2014	3383*

\* LEM assumption no longer valid:  $f_{\text{lim,LEM}} \approx 2200\text{Hz}$

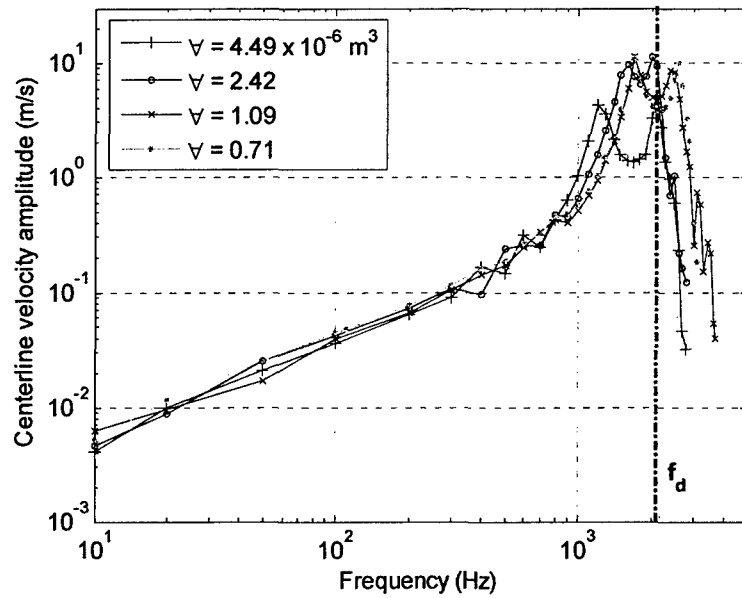


Figure 5-12: Experimental log-log frequency response plot of a ZNMF actuator as the cavity volume is decreased for a constant input voltage.

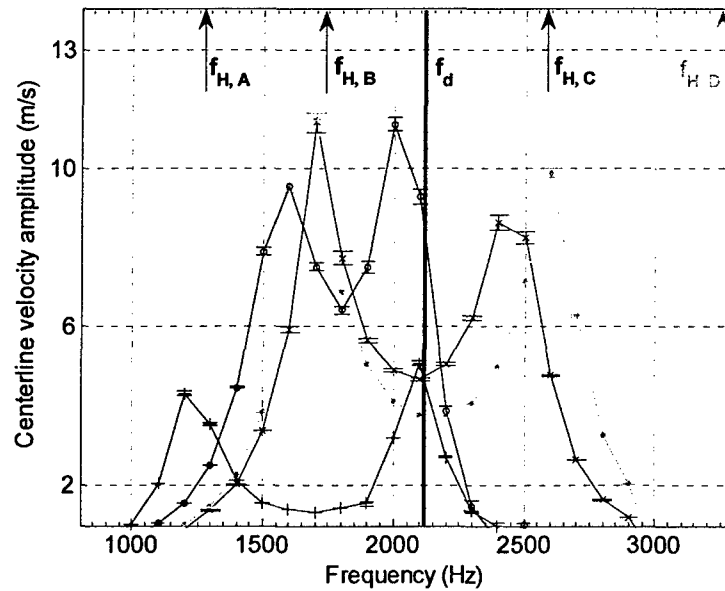


Figure 5-13: Close-up view of the peak locations in the experimental actuator frequency response as the cavity volume is decreased for a constant input voltage. The arrows point to the analytically determined Helmholtz frequency  $f_H$  for each case. (+) Case A:  $V = 4.49 \times 10^{-6} \text{ m}^3$ , (O) Case B:  $V = 2.42 \times 10^{-6} \text{ m}^3$ , (X) Case C:  $V = 1.09 \times 10^{-6} \text{ m}^3$ , (\*) Case D:  $V = 0.71 \times 10^{-6} \text{ m}^3$ .

An identical behavior seen in the lumped element model applied above for the two examples is seen in the results. First the overall dynamic response is still characterized by a +20 dB/decade rise at the low frequencies and -60 dB/decade roll off for the high frequencies. Also, the system response exhibits two frequency peaks. Figure 5-13 shows a close-up view of the peak locations, where the arrows indicate the Helmholtz frequency location given by Eq. 4-5. As the cavity volume decreases,  $f_H$  increases while  $f_d$  remains constant. Also, if  $f_H/f_d < 1$ ,  $f_H$  is easily distinguished from  $f_d$  (as in Case A or Case B), and the actual peak frequencies  $f_1$  and  $f_2$  are close to  $f_H$  and  $f_d$ . However, when  $f_H/f_d \sim 1$ , the experimentally determined peaks  $f_1$  and  $f_2$  tend to move away from  $f_d$  (Case C and Case D). As  $f_H \rightarrow f_d$ ,  $f_1$  and  $f_2$  approach each other. Then as  $f_H$  exceeds  $f_d$ , they separate again, and eventually  $f_1$  tends to  $f_d$ . Then, as the cavity volume is further decreased,  $f_2$  and the Helmholtz frequency move toward higher frequencies, while  $f_1$  tends to  $f_d$ , as in Case D. Notice also how the frequency response is unaffected by the cavity size -hence compressibility effects- for frequencies smaller than  $f_H$  of Case A, as seen in Figure 5-12. This suggests that there exists a threshold limit below which the actuator response is independent of the Helmholtz frequency, or for  $f/f_H < 0.5$ .

To further confirm this trend experimentally, a smaller cavity size would have been ideal, but physical constraints in the actuator configuration prevented it; Case D already has the smallest feasible cavity. Nonetheless, the experimental results validate the lumped element model analysis presented above, where a similar change in the frequency response of a ZNMF actuator occurs due to the cavity volume variation, hence affecting the Helmholtz frequency peak location, as described by Eq. 4-4.

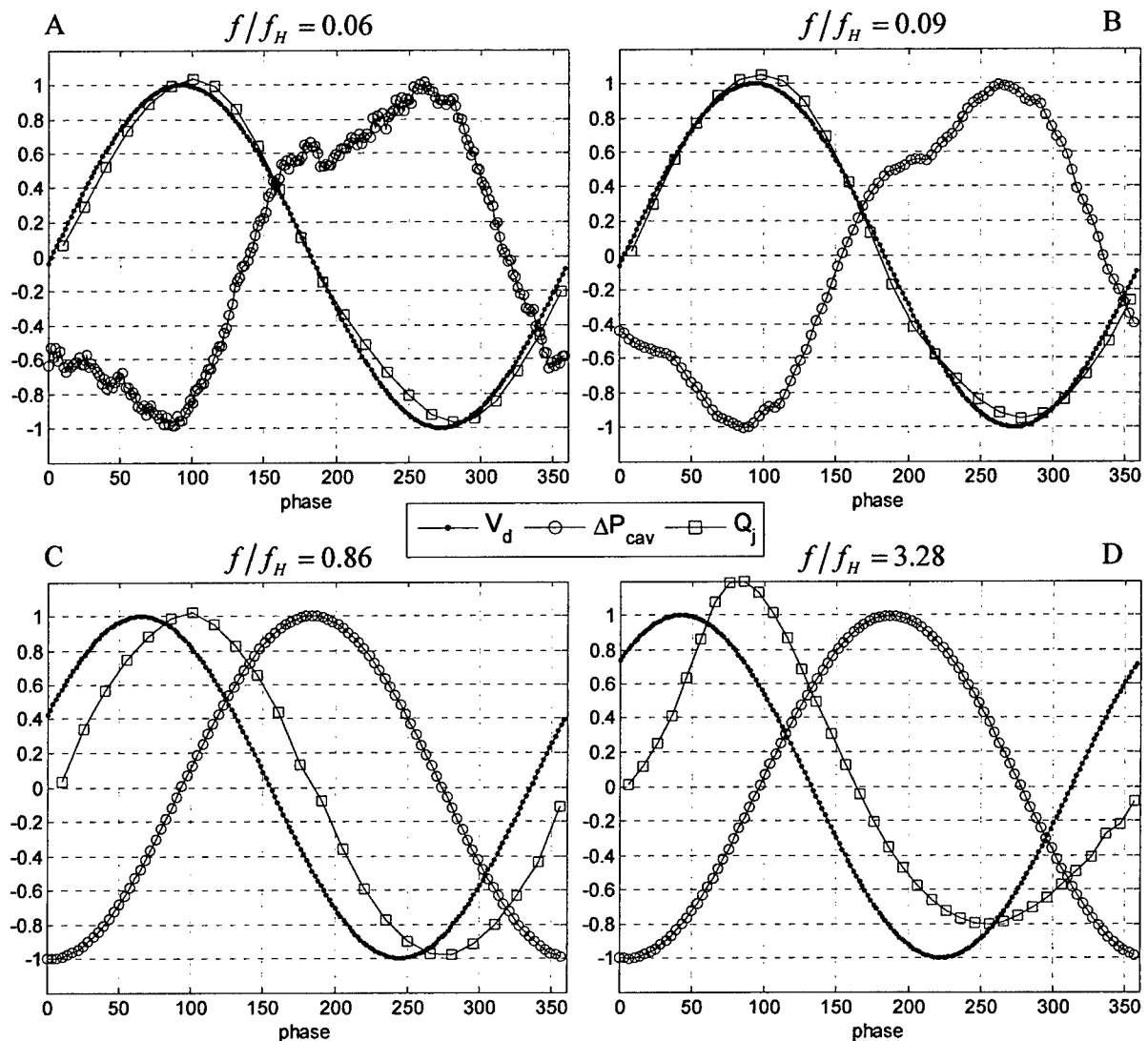


Figure 5-14: Normalized quantities vs. phase of the jet volume rate, cavity pressure and centerline driver velocity. A) Case 20:  $Re=102$ ,  $S=7$ . B) Case 70:  $Re=50$ ,  $S=4$ . C) Case 46:  $Re=109$ ,  $S=53$ . D) Case 65:  $Re=269$ ,  $S=17$ .

Actually, the results from Test 1 described in Section 3 where the pressure fluctuations are recorded inside the cavity can also give additional proof in the above analysis. This is shown in Figure 5-14 where the normalized jet volume flow rate, cavity pressure and driver centerline velocity are plotted phase-locked for four different  $f/f_H$  ratios. Notice that in these plots the small error bars are omitted for better illustration. For cases actuated at a frequency away from the Helmholtz frequency, as seen in Figure 5-14A and Figure 5-14B, the volume flow rate and centerline driver velocity are nearly in phase, indicating that the flow is incompressible. In contrast, for cases of driver frequencies close to or greater than  $f_H$  as in Figure 5-14C and Figure 5-14D, the orifice

volume flow rate is not in phase with the driver velocity, ostensibly due to compressibility effects in the cavity. If the flow in the cavity is incompressible, it has the effect of not delaying the time signals.

The driver-to-Helmholtz frequency ratio  $f/f_H$  is thus the key parameter in this analysis. Recall from Eq. 4-1 and Eq. 4-3 that a small cavity volume with a large Helmholtz frequency is equivalent to having an incompressible cavity. Therefore, if the actuation frequency of the ZNMF actuator is well below its Helmholtz frequency, the flow within the cavity of the device can be treated as incompressible, whereas if the actuator is excited near its Helmholtz frequency or above some critical frequency  $f/f_H > 0.5$ , certainly the flow inside the cavity is compressible, which then has to be consistently considered for modeling purposes. This is an important result that can be summarized by stating that

$$\begin{cases} \frac{f}{f_H} < 0.5 & \Rightarrow \text{incompressible cavity} \\ \text{otherwise} & \Rightarrow \text{compressible cavity} \end{cases} \quad (4-6)$$

This criterion should be taken into account for numerical simulations and design considerations.

### 5.3 Driver, Cavity, and Orifice Volume Velocities

The previous analysis shows the impact of the actuation to Helmholtz frequency ratio  $f/f_H$  on the frequency response of a ZNMF actuator in quiescent air that results in a criterion for the cavity incompressibility limit. However, more results can be extracted from this experimental investigation in terms of the actuator response magnitude. As suggested from Figure 5-12, the variation in amplitude of the jet velocity is a direct function of the Helmholtz frequency. To have a first estimate of these variations, the dimensionless linear transfer function derived in Section 2 for a generic driver and orifice (see Eq. 1-18) that gives a scaling argument for  $Q_j/Q_d$  is considered and reproduced below:

$$\frac{Q_j}{Q_d} = \frac{Q_j(\omega)}{j\omega\Delta V} \approx \frac{1}{\left[1 - \left(\frac{\omega}{\omega_H}\right)^2\right] + j\left[\frac{1}{S}\left(\frac{\omega}{\omega_H}\right)\right]^2}. \quad (4-7)$$

Recall that this expression used Eq. (4-3) to define the Helmholtz frequency, hence neglecting the radiation mass that results in an effective length. Also, Eq. 4-7 was derived assuming a *linear* model, neglecting any nonlinear resistance terms. Yet this expression is still valid for scaling arguments. Eq. 4-7 shows that the system is expected to be governed by the driver response, and when  $f \sim f_d$  (the actuation frequency matches the natural frequency of the driver)  $Q_j/Q_d$  is a 2<sup>nd</sup> order system that is a function of  $f/f_H$  and  $S$ . In the incompressible limit, as seen from the previous section, this is equivalent to  $\forall \rightarrow 0$  or  $f_H \rightarrow \infty$ . And while  $f/f_H \ll 1$ , the actuator output  $Q_j/Q_d$  tends to 1; i.e. the jet flow rate is directly proportional to the driver performance.



On the other hand, in the compressible case,  $C_{ac}$  is finite (i.e. the gas in the cavity has an acoustic compliance and can be compressed). Hence,  $f_H$  is finite and, near the cavity resonance ( $f \sim f_H$ ), the actuator output amplitude  $Q_j$  is expected to be larger than that of the driver volume flow rate  $Q_d$  ( $Q_j \gg Q_d$ ) and to be out of phase; the system produces a larger amplitude with higher Stokes number.

Once again, experimental results are used to validate this analytical analysis. First, Test 2 in the experimental setup (Cases A, B, C, and D) is considered. In addition to the centerline velocities acquired in a frequency sweep at a single input voltage, jet velocity profiles have been acquired at selected frequencies to compute  $Q_j$  and  $\overline{Q_j}$ , and the diaphragm flow rate  $Q_d$  has also been recorded at each frequency. Notice that in this analysis the time averaged  $\overline{Q_j}$  is employed, which is related to the jet volume flow rate amplitude  $Q_j$  by

$$\overline{Q_j} = \frac{\pi}{2} Q_j \quad (4-8)$$

for a sinusoidal signal.. But since only an order of magnitude -or scaling- analysis is performed here, the overhead bar is dropped for convenience. The reader is referred to the data processing section in Section 3 for a clear definition on how these different quantities are defined and computed.

Figure 5-15 plots the ratio between the input flow rate  $Q_d$  and the output flow rate  $Q_j$  of the ZNMF actuator as a function of the driver to Helmholtz frequency  $f/f_H$ , for these four experimental cases where the cavity volume is systematically decreased. The response predicted by the linear transfer function in Eq. 4-7 is clearly seen here, where at low frequency  $Q_j \sim Q_d$ , then around  $f = f_H$ ,  $Q_j \gg Q_d$  and finally at  $f \gg f_H$ ,  $Q_j < Q_d$ . However, in these cases it has been shown that the two dominant frequency peaks  $f_1$  and  $f_2$  tend to overlap (see discussion above), and that the Helmholtz frequency  $f_H$  overpredicts the peak location (see Table 5-4, the LEM assumption being no longer valid for the high frequency cases). Therefore, Figure 5-15B plots again the ratio of the driver to jet volume flow rate but as a function of  $f/f_1$  for Case A and Case B (where  $f_H < f_d$ ), and as a function of  $f/f_2$  for Cases C and D where  $f_H > f_d$ . This shows the similar observed trend but with the data more collapsed. Note that there is still some scatter since the experimentally determined peaks  $f_1$  and  $f_2$  have a resolution of 100 Hz only.

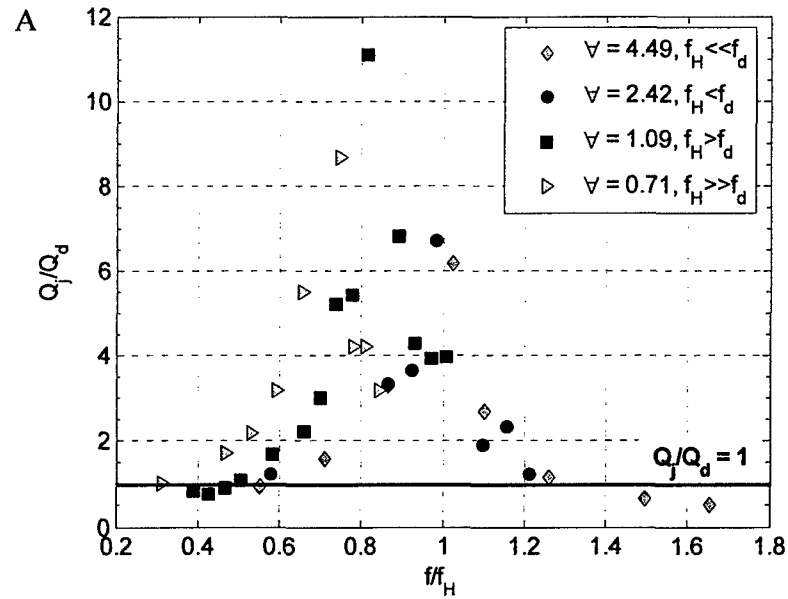


Figure 5-15: Experimental results of the ratio of the driver to the jet volume velocity function of dimensionless frequency as the cavity volume decreases. A) Function of  $f/f_H$ . B) Function of  $f/f_1$  for  $V = 4.49 \times 10^{-6} m^3$  and  $V = 2.42 \times 10^{-6} m^3$ , and function of  $f/f_2$  for  $V = 1.09 \times 10^{-6} m^3$  and  $V = 0.71 \times 10^{-6} m^3$ .

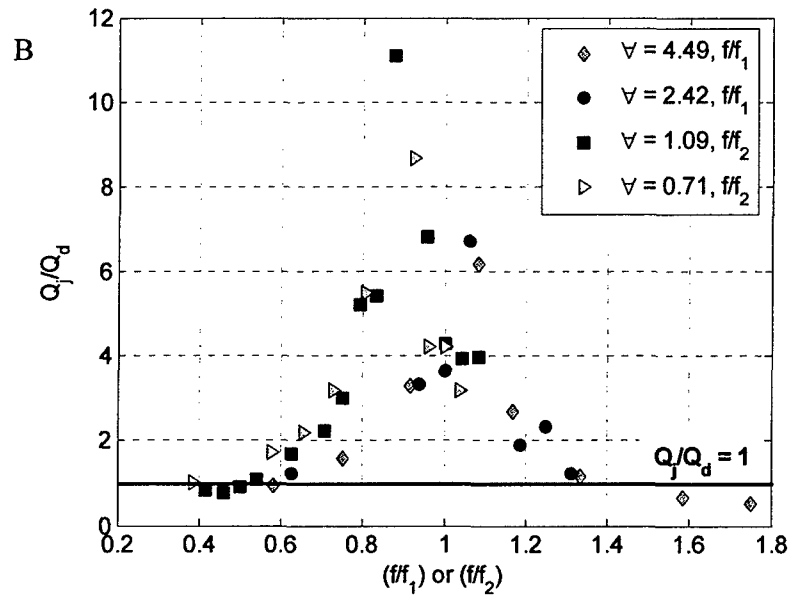


Figure 5-15: Continued.

To confirm these results, the test cases coming from Test 1, ranging from Case 41 to Case 72, are also used where the driver volume velocity is compared to the jet volume flow rate. Figure 5-16A shows the variation in the ratio of the two quantities as a

function of  $f/f_H$  where the symbols are grouped by Stokes number. Figure 5-16B is identical except that  $Q_j/Q_d$  is plotted for different Reynolds numbers. First, note that  $Q_j/Q_d$  is close to unity when  $f < f_H$ , then is greater than unity near  $f/f_H \approx 1$ , and is much less than unity for  $f \gg f_H$ . This is exactly what is seen in Figure 5-15 which was for a fixed input voltage. With reference to Eq. 4-7, the Stokes number dependence can be seen in Figure 5-16A where  $Q_j/Q_d$  is at a maximum for high Stokes number near  $f/f_H \approx 1$ . Also, Figure 5-16B shows that an increase in Reynolds number results in a decrease in the ratio  $Q_j/Q_d$  near  $f/f_H \approx 1$ . This is due to the nonlinear damping terms present in the orifice that are proportional (in part, see Section 5 for more details) to the Reynolds number and decrease the overall response near resonance. Again, since Eq. 4-7 is a linear transfer function, this Reynolds number dependence cannot be seen.

Another way to interpret these results is in terms of the volume velocity continuity equation coming from the LEM circuit representation of a flow divider described in Section 2 and reproduced in Figure 5-17, where

$$Q_d = Q_c + Q_j, \quad (4-9)$$

the driver volume velocity being split into the cavity and the orifice branches. Recall that the  $Q$ 's are represented via phasors as complex variables. In view of the above results, the role of the cavity in this flow divider depends on the value of the cavity impedance that, as shown above, is related to the Helmholtz frequency. In the limit when the cavity acoustic impedance  $C_{ac}$  tends to zero or for  $f/f_H \ll 1$ , the impedance  $Z_{ac} = 1/j\omega C_{ac}$  takes high values and then discourages the flow from going into its branch, which therefore minimizes the cavity volume velocity  $Q_c$  since  $Z_{ac} = \Delta P_c / Q_c$ . This is the case when the cavity can be assumed to be incompressible and yields  $Q_j \sim Q_d$ , as seen in the previous figures. However when the cavity acoustic impedance  $Z_{ac}$  takes finite values, some non-negligible flow enters the cavity branch in Figure 5-17, and in this case where the cavity is clearly compressible two different scenarios can take place, whether the actuator is driven near cavity resonance or not. At resonance, the reactance of the complex impedance in the loop formed with the cavity and the orifice branches is identically zero and the flow is purely resistive. This case then allows  $Q_j$  to be greater than  $Q_d$  via an acoustic lever arm. At frequencies away from resonance –and/or for really large cavities– the acoustic impedance of the cavity goes to zero, thus letting the cavity volume velocity  $Q_c$  be non-negligible when compared to the other  $Q$ 's, thus yielding a small output flow rate  $Q_j$  compared to the input  $Q_d$ . Further consideration on this matter will be to experimentally compute the cavity volume flow rate. But this is a non-trivial problem because of the inherent complex nature of the quantity to measure, and is the subject of future work.

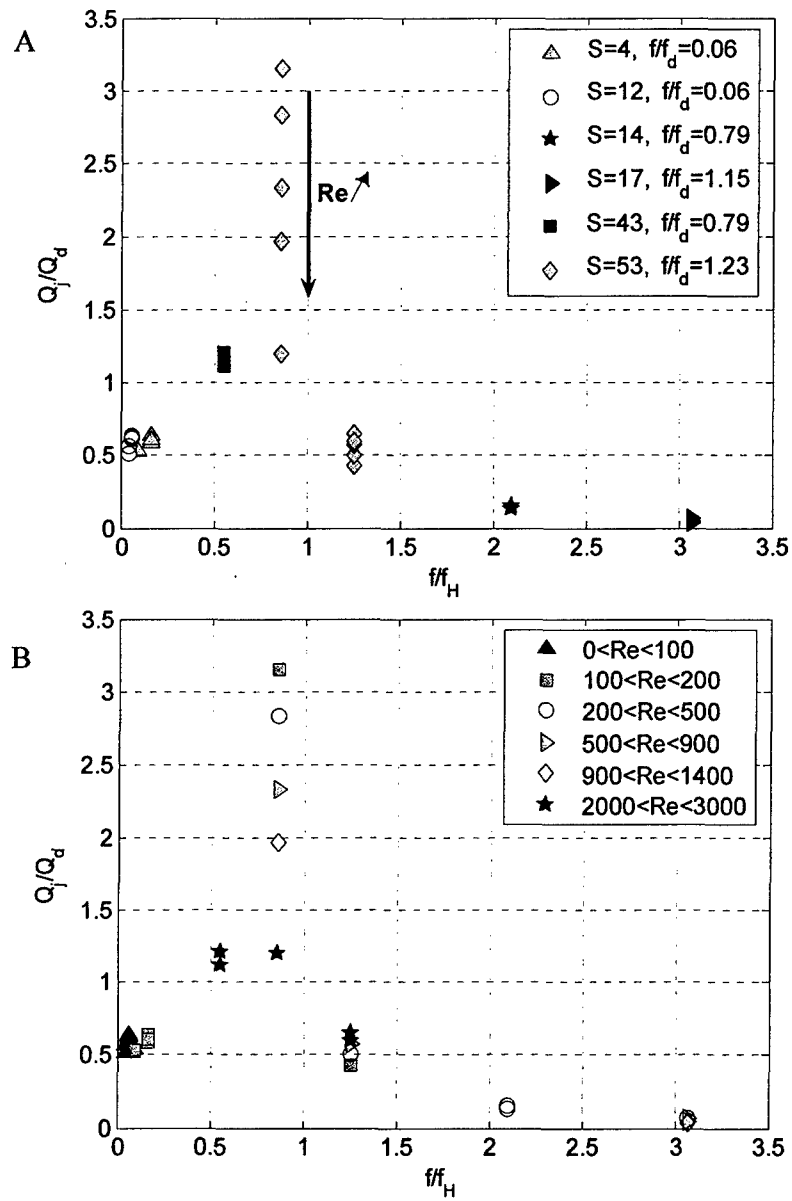


Figure 5-16: Experimental jet to driver volume flow rate versus actuation to Helmholtz frequency. A) Function of Stokes number. B) Function of Reynolds number.

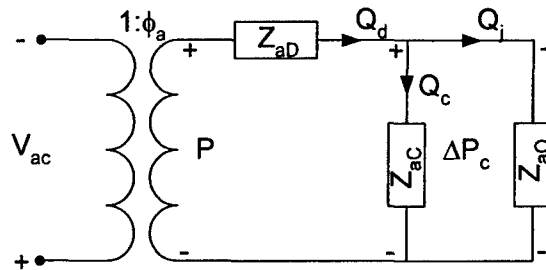


Figure 5-17: Current divider representation of a piezoelectric-driven ZNMF actuator.

Similarly, another important aspect of this flow divider representation is in the conservation of power through the different branches of the circuit in Figure 5-17. Power is defined as the multiplication of an “effort” variable and a “flow” variable. Practically, it is rather difficult to experimentally estimate the power delivered to the driver, and especially in the cavity. Nonetheless, the lumped element model should provide reasonable estimates of the power, and it is shown in Figure 5-18, where again Case 1 from Gallas et al. (2003a) has been used for illustration purposes. In LEM, the governing equations are written in conjugate power variable form by assuming sinusoidal steady state operating conditions. Ideally, the piezoelectric diaphragm actuator driver is modeled as a lossless transformer, which has an input power defined by

$$Pw_d = Q_d \cdot P, \quad (4-10)$$

where  $P$  is related to the piezoelectric diaphragm via the two-port element model by

$$P = \phi_a \cdot V_{ac}. \quad (4-11)$$

The power in the cavity branch is given by

$$Pw_c = Q_c \cdot \Delta P_c, \quad (4-12)$$

and at the orifice exit the power takes the form

$$Pw_j = Q_j \cdot \Delta P_c. \quad (4-13)$$

For the power to be conserved in the circuit, the following identity should hold at any frequency,

$$Pw_j + Pw_c = Pw_d, \quad (4-14)$$

and this is plotted in Figure 5-18 where the real and imaginary part of the power is shown as a function of frequency, taking the parameters from Case 1 (Gallas et al. 2003a).

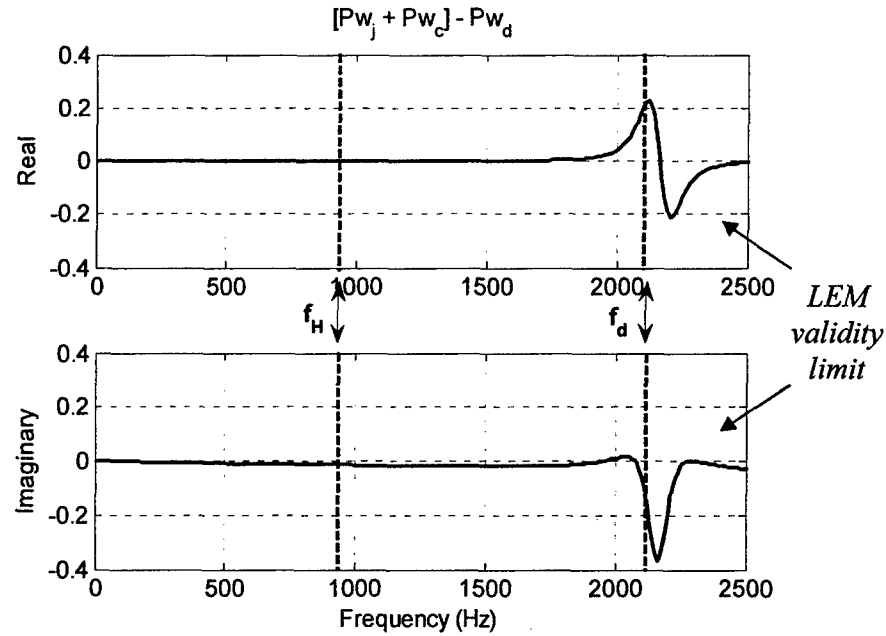


Figure 5-18: Frequency response of the power conservation in a ZNMF actuator from the lumped element model circuit representation for Case 1 (Gallas et al. 2003a).

Note that the power is in fact conserved at all frequencies, especially at cavity resonance when  $f = f_H$ . However, at the mechanical resonance,  $f = f_d$ , a jump is observed which is primarily due to the fact that the piezoelectric diaphragm is modeled as a lossless transformer that is valid only up to its natural frequency, and beyond this frequency, the main assumption of LEM fails.

To summarize this section, it has been found that the cavity plays an important role in the actuator response, in terms of geometric parameters and operating frequency. More particularly, it was found that the pressure inside the cavity may not be equal to the pressure across the orifice, as the LEM assumes it, at least quantitatively in terms of amplitude. Therefore, care must be taken when using the experimental cavity pressure.

Next, the linear dimensionless transfer function developed from LEM has been experimentally validated and can be used as a starting guess in a design tool. It is shown that the cavity can either have a passive role by not affecting the device output, or can greatly enhance the actuator performance. This is a function of the driver-to-Helmholtz frequency as well as the Stokes and Reynolds numbers, and for piezoelectric-driven devices the diaphragm frequency may have a non-negligible impact when  $f_d$  is close to  $f_H$ . More interestingly, large output can be expected ( $Q_j \gg Q_d$ ) at the cavity resonance but only at low forcing level, the nonlinear orifice resistance tending then to decrease the output as the input amplitude increases. This says that the optimal response is not simply given by just maximizing the actuator input. A tradeoff between the cavity design and actuation amplitude must be made, depending on the desired output to be achieved. Notice also that this analysis has been made for a piezoelectric-diaphragm driver. Obviously, using an electromagnetic driver will remove the dimensionless frequency  $f/f_d$ , but the above results still hold and Eq. 4-7 can still be applied since the driver

dynamics are confined in the LHS. Nevertheless, the major impact of this analysis is that by operating near  $f_H$ , the device produces greater output flow rates than the driver due to the acoustic resonance. An added benefit is that the driver is not operated at mechanical resonance where the device may have less tolerance to failure.

## 6. Reduced-Order Model of Isolated ZNMF Actuator

In this section, the lumped element model of an isolated ZNMF actuator presented in Section 2 is refined based on an investigation of the orifice flow physics. More precisely, the orifice impedance model is improved to account for geometric and flow parameter dependence. This refined model stems from a control volume analysis of the unsteady orifice flow. The results from the experimental setup presented in Section 3, along with the discussion on the orifice and cavity flow physics given in Section 4 and Section 5, are used to construct a scaling law of the pressure loss across the orifice, which is found to be essentially a function of the product of the Strouhal number and the orifice aspect ratio  $h/d$ . This improved lumped element model is then compared along with the existing previous version (Gallas et al. 2003a) to some experimental test cases.

### 6.1 Orifice Pressure Drop

In the existing lumped element model of an isolated ZNMF actuator presented in Section 2, the major limitation is found in the expression of the nonlinear acoustic orifice resistance that is directly related to the loss coefficient  $K_d$  such that,

$$R_{ao,nl} = \frac{0.5\rho K_d Q_j}{S_n^2}. \quad (5-1)$$

A primary goal of this effort is to provide a physical understanding of the orifice flow behavior, along with a more accurate expression for the coefficient  $K_d$  in terms of dimensionless geometric and flow parameters, i.e., in terms of the orifice aspect ratio  $h/d$ , Reynolds number  $Re$ , and Strouhal number  $St$ . Note that in the existing version of the lumped element model, the coefficient  $K_d$  is set to unity (McCormick 2000; Gallas et al. 2003a).

In this section, a control volume analysis of the unsteady pressure-driven oscillatory pipe flow is presented. Figure 6-1 shows a schematic of the control volume with the coordinate definitions. The governing equations are first derived to obtain an expression of the pressure drop coefficient across the orifice. Then, the analytical results are validated via available numerical simulations, which are also used to examine the relative importance of each term in the governing equation for the orifice pressure drop.

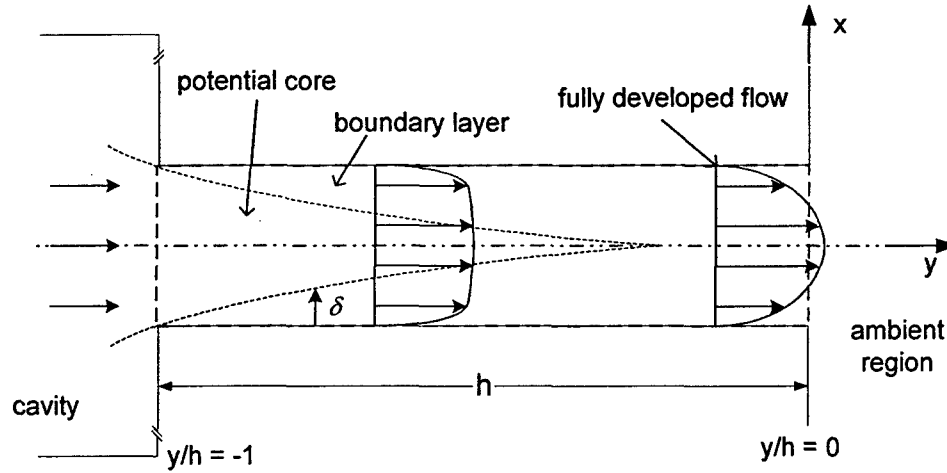


Figure 6-1: Control volume for an unsteady laminar incompressible flow in a circular orifice, from  $y/h = -1$  to  $y/h = 0$ .

### 6.1.1 Control Volume Analysis

Assuming an unsteady, incompressible, laminar flow and a nondeformable control volume, as shown in Figure 6-1, the continuity equation becomes

$$0 = \frac{\partial}{\partial t} \int_{CV} \rho dV + \int_{CS} \rho \vec{V} \cdot d\vec{A} = \int_{CS} \vec{V} \cdot d\vec{A}, \quad (5-2)$$

or simply  $Q_{inlet} = Q_{exit}$ . Since the  $y$  location of the outflow boundary is arbitrary, it

directly follows that  $Q \neq Q(y)$  or  $Q = Q(t)$ . Similarly, the  $y$ -momentum equation

becomes

$$\sum F_y = \frac{\partial}{\partial t} \int_{CV} \rho v dV + \int_{CS} v \rho \vec{V} \cdot d\vec{A}, \quad (5-3)$$

or, for an axisymmetric orifice,

$$(p_0 - p_y) S_n - \int_0^y [\tau(y) + \tau_{FD} - \tau_{FD}] 2\pi \left( \frac{d}{2} \right) dy = \frac{\partial}{\partial t} \int_{CV} \rho v dV + \int_{CS} v \rho \vec{V} \cdot d\vec{A}, \quad (5-4)$$

where the subscript 'FD' signifies 'fully developed,'  $\tau$  is the wall shear stress, and  $S_n = \pi (d/2)^2$  is the circular orifice area. Since density is assumed to be constant, the volume integral can be expressed as follows



$$(p_0 - p_y)S_n - 2\pi \frac{d}{2} \int_0^y [\tau(y) - \tau_{FD}] dy - 2\pi \frac{d}{2} \tau_{FD} y = \rho \left[ \underbrace{\frac{\partial}{\partial t} \int_0^y \int_0^{d/2} v 2\pi x dx dy}_{Q = \text{const}} + \int_0^{d/2} (v_y^2 - v_0^2) 2\pi x dx \right]. \quad (5-5)$$

Since the volume flow rate is independent of the location  $y$  inside the orifice,  $Q \neq Q(y)$ ,

$$(p_0 - p_y)S_n - 2\pi \frac{d}{2} \int_0^y [\tau(y) - \tau_{FD}] dy - 2\pi \frac{d}{2} \tau_{FD} y = \rho \left[ y \frac{\partial Q}{\partial t} + \int_0^{d/2} (u_y^2 - u_0^2) 2\pi x dx \right]. \quad (5-6)$$

Then, assuming that the jet volume flow rate is sinusoidal,  $Q = Q_j \sin(\omega t)$ , and using again the time- and spatial- averaged exit velocity during the expulsion stroke  $\bar{V}_j$  as the characteristic velocity, i.e.,

$$\begin{aligned} \bar{V}_j &= \frac{1}{S_n} \frac{\omega}{\pi} \int_0^{\pi/\omega} \underbrace{\int_0^{d/2} v_y 2\pi x dx dt}_Q = \frac{1}{S_n} \frac{\omega}{\pi} \int_0^{\pi/\omega} Q_j \sin(\omega t) dt \\ &= \frac{Q_j}{S_n} \frac{\omega}{\pi} \frac{2}{\omega} = \frac{Q_j}{S_n} \frac{2}{\pi} = \hat{V}_j \frac{2}{\pi}. \end{aligned} \quad (5-7)$$

Next, the integral momentum equation can be written in nondimensional form as

$$\left( \frac{p_0 - p_y}{\frac{1}{2} \rho \bar{V}_j^2} \right) - \int_0^{y/d} \frac{4(\tau - \tau_{FD})}{\rho \bar{V}_j^2} d \left( \frac{y}{d/2} \right) - 2 \frac{\tau_{FD}}{0.5 \rho \bar{V}_j^2} \frac{y}{d/2} = y \pi \frac{\omega}{V_j} \cos(\omega t) + 4 \int_0^1 \left( \frac{v_y^2 - v_0^2}{\bar{V}_j^2} \right) \frac{x}{d/2} d \left( \frac{x}{d/2} \right). \quad (5-8)$$

By using the definition of the Strouhal number  $St = \omega d / \bar{V}_j$ , and the skin friction coefficient  $C_f = \tau / 0.5 \rho \bar{V}_j^2$ , and defining the normalized pressure drop across the orifice by

$$\Delta c_p = \frac{p_0 - p_y}{0.5 \rho \bar{V}_j^2}, \quad (5-9)$$

Eq. 5-8 can then be rewritten as

$$\Delta c_p = \underbrace{4 \int_0^{y/d} (C_f - C_{f,FD}) d \left( \frac{y}{d} \right)}_I + \underbrace{C_{f,FD} \frac{4y}{d}}_{II} + \underbrace{\frac{y}{d} \pi St \cos(\omega t)}_{III} + \underbrace{4 \int_0^1 \left( \frac{v_y^2 - v_0^2}{\bar{V}_j^2} \right) \frac{x}{d/2} d \left( \frac{x}{d/2} \right)}_{IV}. \quad (5-10)$$

Eq. 5-10 shows that the pressure drop across the orifice is comprised of four terms:

- I* = excess shear contribution to the pressure drop
- II* = fully-developed shear contribution
- III* = unsteady inertia term (= 0 if flow is steady)
- IV* = nonlinear unsteady pressure drop to accelerate the flow (convective term)

Notice that the first two terms (*I* and *II*) can be recombined to yield the total skin friction coefficient integral,  $4 \int_0^{y/d} C_f d(y/d)$ , in the pressure drop expression.

It should be pointed out that this analysis is derived for an isentropic flow, and that since only the continuity and momentum equations are used, no assumptions are taken for the heat transfer. From the energy equation, a simple scaling analysis for the pipe flow shows that the viscous and thermal boundary layer are of the same order of magnitude assuming a Prandtl number (ratio of viscous to thermal diffusivity) of unity for air. However, since no significant heat source is present, the thermal effect are neglected in this analysis. Notice that Choudhari et al. (1999) performed a theoretical analysis (confirmed with numerical simulations) on the influence of the viscothermal effect on flow through the orifice of Helmholtz resonators. They showed that the thermal effect can be neglected for such flows.

Next, before examining the physics behind the expression for the orifice pressure drop, one can examine each term in Eq. 5-10 from a numerical simulation to validate this theoretical analysis and evaluate their relative importance.

#### 6.1.2 Validation through Numerical Results

Once again, the 2D numerical simulations from the George Washington University are used to evaluate the analytical expression for the orifice pressure drop derived above. Three test cases are employed and are referred to as Case 1 ( $S = 25$ ,  $St = 2.38$ ,  $h/d = 1$ , no jet is formed), Case 2 ( $S = 25$ ,  $St = 2.38$ ,  $h/d = 2$ , no jet is formed), and Case 3 ( $S = 10$ ,  $St = 0.38$ ,  $h/d = 0.68$ , a jet is formed) in the test matrix shown in Table 2-3. Figure 6-2 shows the variations during one cycle of each of the terms in Eq. 5-10, for Case 1, Case 2, and Case 3 (Figure 6-2A, Figure 6-2B, and Figure 6-2C, respectively). Actually, the terms *I* and *II* in Eq. 5-10 have been recombined together to remove the explicit fully-developed part and to yield only the total wall shear stress contribution, since the fully-developed region may not be well defined in these test cases (see discussion in Section 4). Note that the pressure has been averaged across the orifice cross section, and again zero-phase corresponds to the onset of the jet volume velocity expulsion stroke. Also, Eq. 5-10 is derived for a circular orifice, and because the numerical simulations are carried out for a 2D slot, it has been adjusted accordingly. Recall also the relationship between the Strouhal number  $St$ , orifice aspect ratio  $h/d$ , and the stroke length (or particle displacement)  $L_0$  via,

$$St \cdot \frac{h}{d} = \pi \frac{h}{L_0}. \quad (5-11)$$

The three numerical cases examined, while not exhaustive, include low and high stroke length cases and should therefore be representative of the general case.

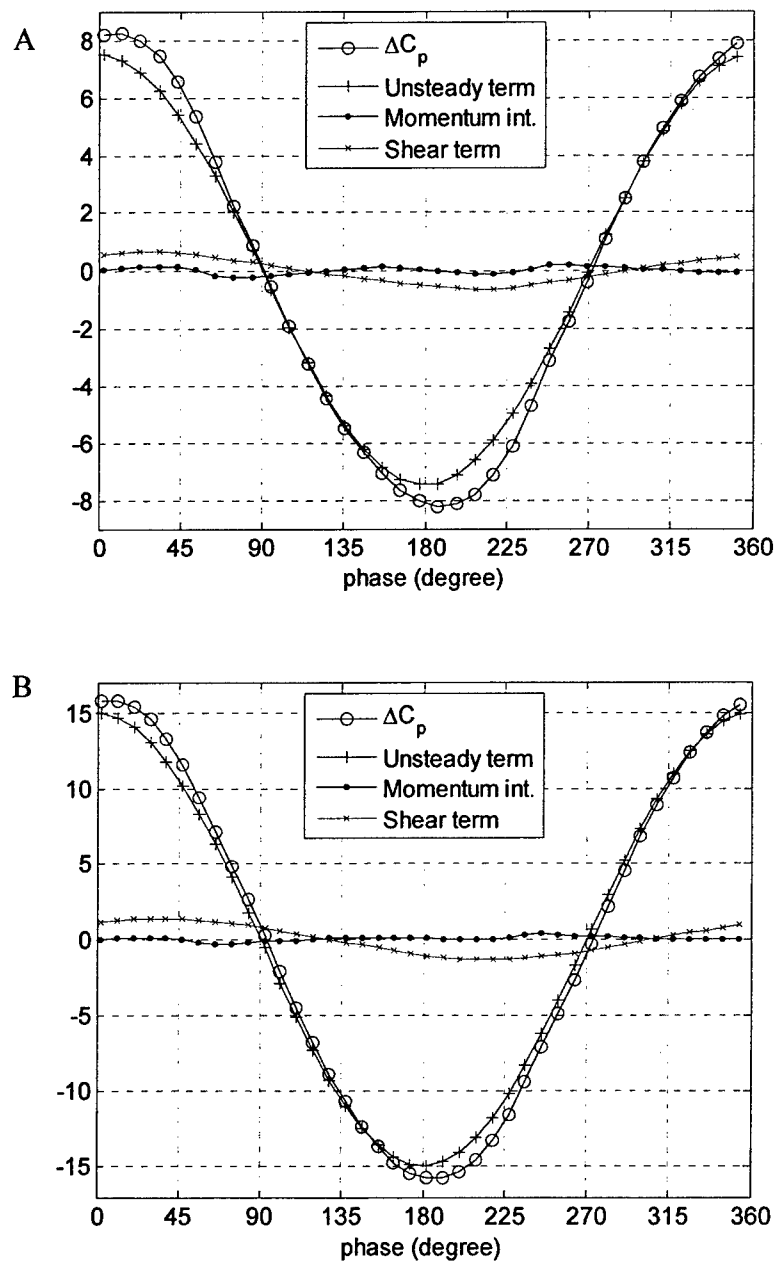


Figure 6-2: Numerical results for the contribution of each term in the integral momentum equation as a function of phase angle during a cycle. A) Case 1:  $h/d = 1, St = 2.38, Re = 262, S = 25$ . B) Case 2:  $h/d = 2, St = 2.38, Re = 262, S = 25$ . C) Case 3:  $h/d = 0.68, St = 0.38, Re = 262, S = 10$ .

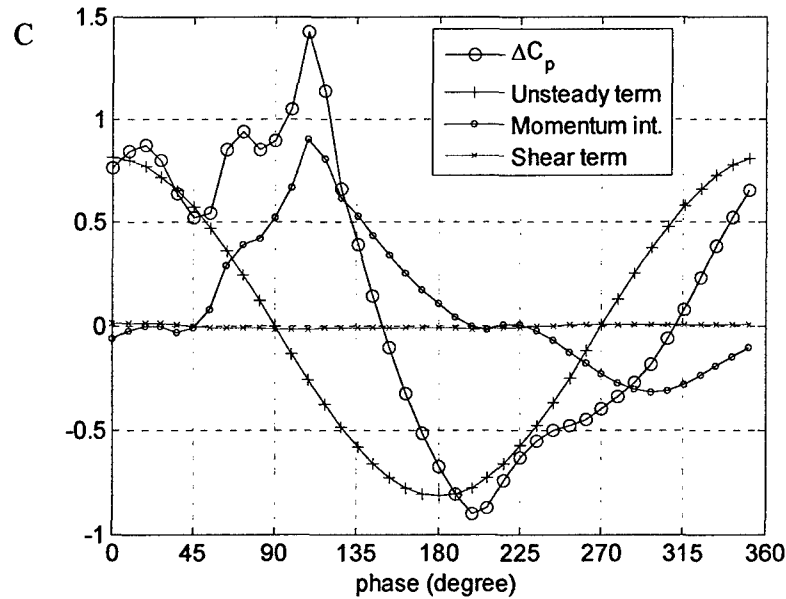


Figure 6-2: Continued.

Clearly, it can be seen that the unsteady inertia term – that is directly proportional to the Strouhal number – is by far the most important contribution in the pressure drop in the orifice, which is not surprising since the two first cases have a large Strouhal number. The momentum integral (or convective) and friction coefficient integral terms seem quite small but actually should not be completely neglected since they contribute in the balance of the pressure drop, especially for the low Strouhal number Case 3. Notice also how the pressure drop is shifted by almost  $90^\circ$  (referenced to the volume velocity) which is primarily due to the unsteady term, but also by the shear stress contribution, the momentum integral term being in phase with the jet volume flow rate. However, it should be noted that the results for Case 3 ( $Re = 262$ ,  $S = 10$ ,  $St = 0.38$ ,  $h/d = 0.68$ ), even though shown here in Figure 6-2C, should be regarded with caution as some non-negligible residuals may be present in the computed pressure drop that may be due to grid/time resolution for extracting the shear stress component and velocity momentum integral (private communication with Dr. Mittal, 2005). Nonetheless, the results for the orifice pressure drop magnitude are still used, as seen later.

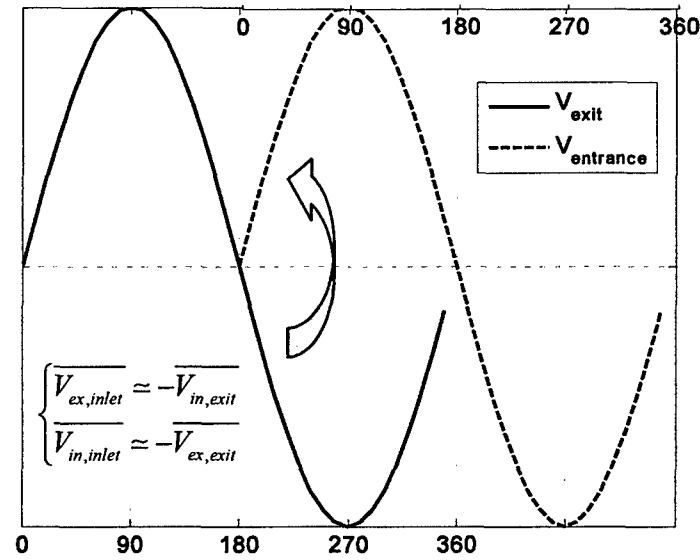


Figure 6-3: Definition of the approximation of the orifice entrance velocity from the orifice exit velocity.

Next, the goal is to extend this analysis to practical experimental results. However, there are no such results available for the velocity profiles at the orifice inlet adjacent to the cavity or for the friction coefficient along the orifice wall. What are known are the time-dependant velocity profiles at the orifice exit (to ambient) and pressure oscillations inside the cavity. However, it was shown in Section 4 that, for a symmetric orifice, the velocity at the exit can be used to estimate the velocity at the inlet, with a  $180^\circ$  phase shift: the flow sees the entrance of the orifice as its exit during the other half of the cycle, and vice versa, as shown in Figure 6-3.

This approximation for the entrance velocity is further verified via Case 1, Case 2, and Case 3. The normalized momentum integral of the exit and inlet velocities, defined by  $\int_1 \frac{v_0^2}{V_j^2} d\left(\frac{x}{d/2}\right)$  and  $\int_1 \frac{v_{y=h}^2}{V_j^2} d\left(\frac{x}{d/2}\right)$  are plotted in Figure 6-4A and Figure 6-4B, and

Figure 6-4C, respectively for Case 1, Case 2, and Case 3, during one cycle along with the approximated momentum integral of the inlet velocity. As can be seen, the result for the approximated inlet velocity is in fair agreement with the actual entrance velocity, although for the large stroke length case (Case 3) the inlet velocity is slightly overpredicted by the approximated one but only during the ingestion stroke. It should be emphasized that this is only valid for a symmetric orifice.

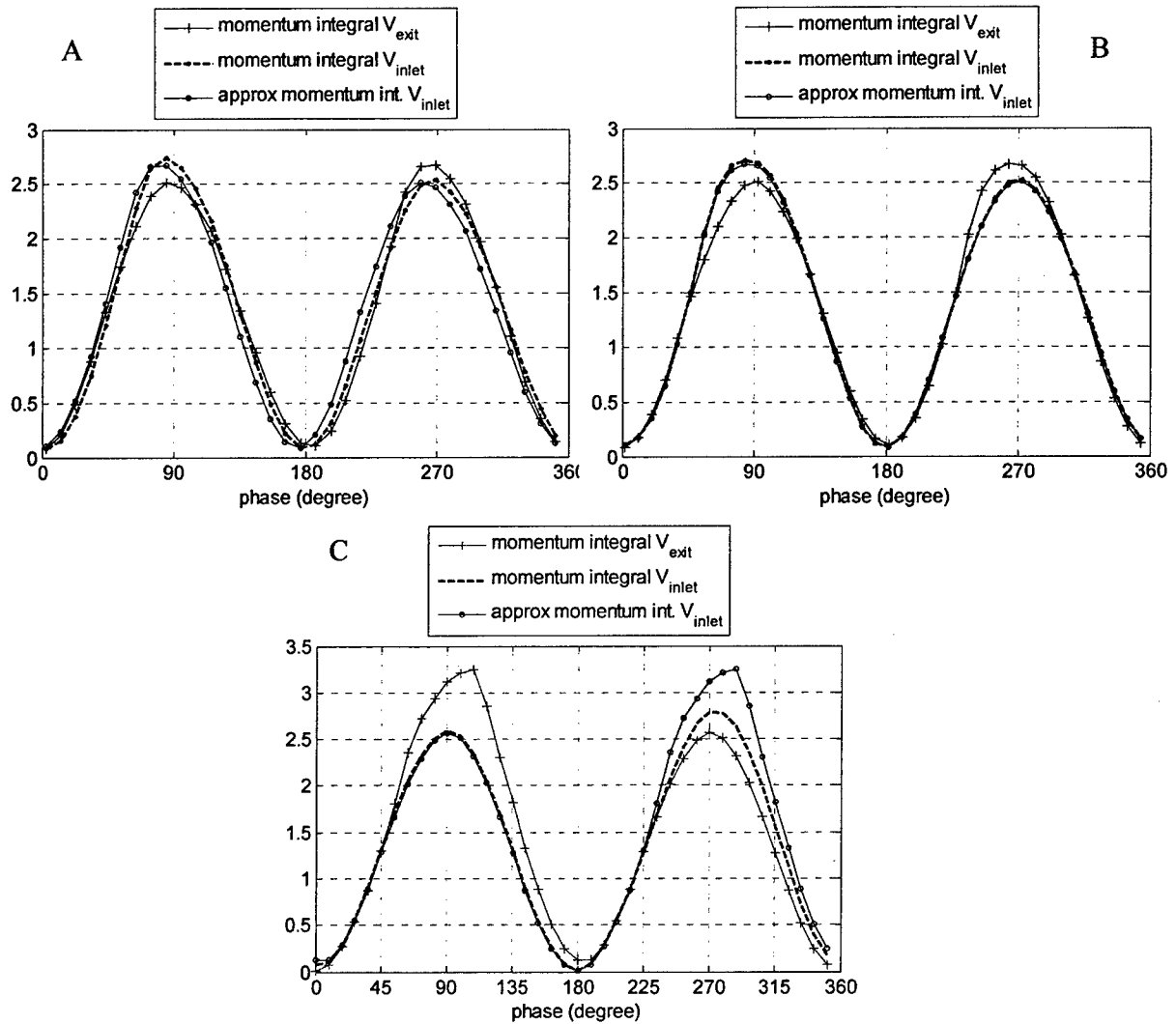


Figure 6-4: Momentum integral of the exit and inlet velocities normalized by  $\overline{V_j}^2$  and comparing with the actual and approximated entrance velocity. A) Case 1:  $h/d = 1$ ,  $St = 2.38$ ,  $Re = 262$ ,  $S = 25$ . B) Case 2:  $h/d = 2$ ,  $St = 2.38$ ,  $Re = 262$ ,  $S = 25$ . C) Case 3:  $h/d = 0.68$ ,  $St = 0.38$ ,  $Re = 262$ ,  $S = 10$ .

Finally, the sum of the source terms in Eq. 5-10 that balance the pressure drop  $\Delta c_p$  are plotted as a function of time for the first two numerical test cases (as noted above, Case 3 is not shown here). Results from using both the actual and approximate entrance velocity are also shown in Figure 6-5. Clearly, the CFD results confirm the validity of Eq. 5-10. Therefore, Eq. 5-10 can be used with confidence to compute the pressure drop across the orifice, and the orifice entrance velocity can also be computed from the orifice exit velocity in the experimental results, and the corresponding time- and spatial-averaged velocity can be defined as

$$\begin{cases} \overline{V_{ex,inlet}} \approx -\overline{V_{in,exit}} \\ \overline{V_{in,inlet}} \approx -\overline{V_{ex,exit}} \end{cases} \quad (5-12)$$

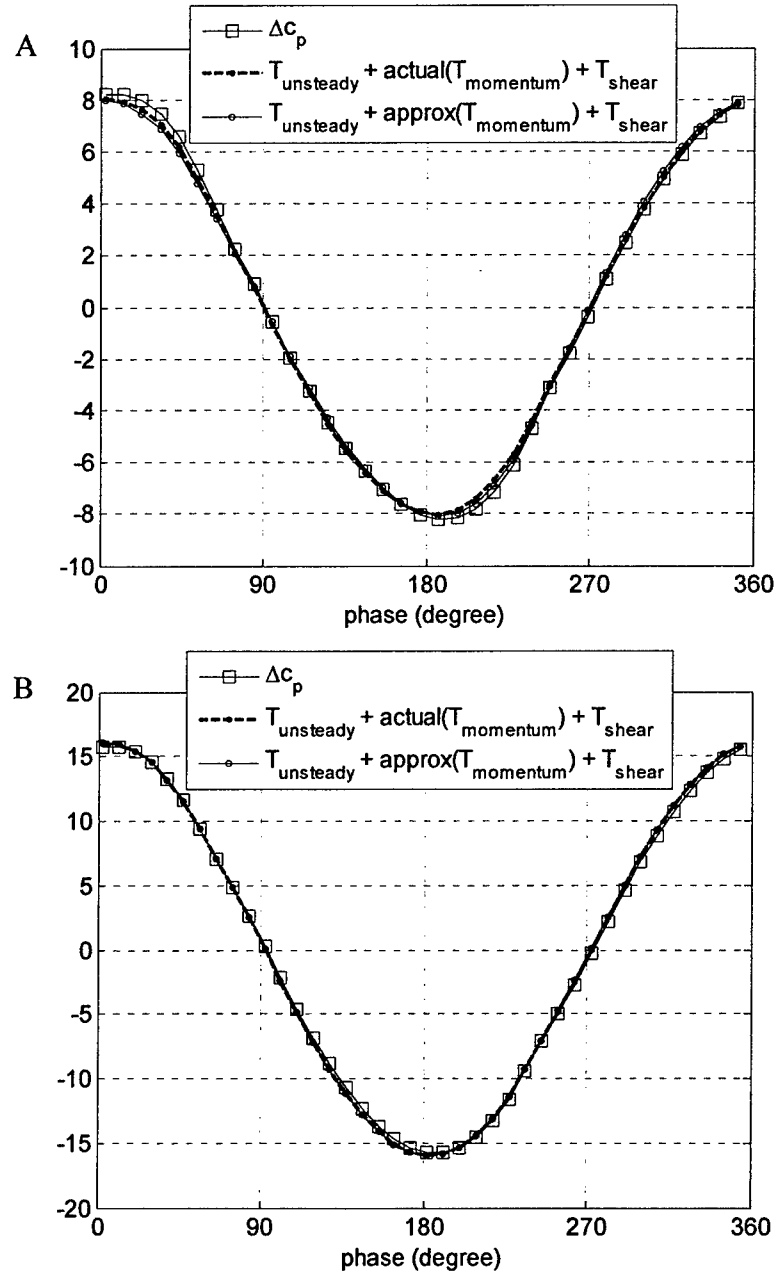


Figure 6-5: Total momentum integral equation during one cycle, showing the results using the actual and approximated entrance velocity. A) Case 1:  $h/d = 1$ ,  $St = 2.38$ ,  $Re = 262$ ,  $S = 25$ . B) Case 2:  $h/d = 2$ ,  $St = 2.38$ ,  $Re = 262$ ,  $S = 25$ .

### 6.1.3 Discussion: Orifice Flow Physics

Now that Eq. 5-10 has been validated via numerical simulations, it is worthwhile to examine the physics behind each term that compose Eq. 5-10, as discussed below.

$I$  = excess shear contribution to the pressure drop

This is a *linear* contribution to the pressure drop. It corresponds to the excess shear needed to reach a fully developed state (in which the time-dependent velocity profile is invariant along the length of the orifice). In particular, it corresponds to the viscous effect in a starting orifice flow and is expected to have both dissipative (resistance) and inertial (mass) components since it will affect the magnitude and phase of the pressure drop. This is in accordance with the discussion provided on the velocity profiles shown in Section 4 in Figure 4-182, Figure 4-193, and Figure 4-204 for Case 1, Case 2, and Case 3, respectively. However, as seen from the numerical results (Figure 6-2), this term appears to be negligible for the low and large Strouhal number cases examined. It is therefore neglected in the rest of this analysis.

$II$  = fully developed shear contribution to the pressure drop

This is again a *linear* contribution to the pressure drop. In fact, the friction coefficient term comes from viscous effects at the orifice walls that are linear by nature. In the case of a fully developed, steady orifice flow, the corresponding pressure loss can be written as

$$\Delta P = 4 \frac{h}{d} C_{f,FD} \frac{1}{2} \rho \bar{V}_j^2, \quad (5-13)$$

or, since  $C_{f,FD} = 16/\text{Re}_{\hat{V}_j} = 16/(\hat{V}_j d/\nu)$  and  $\hat{V}_j = \bar{V}_j$  for a steady pipe flow (White 1991), it directly follows that

$$\Delta P = \frac{4h}{d} \frac{16}{\bar{V}_j d/\nu} \frac{1}{2} \rho \bar{V}_j^2 = \frac{32\mu h \bar{V}_j}{d^2}, \quad (5-14)$$

which can be recast in terms of an acoustic impedance

$$Z_{aO} = \frac{\Delta P}{Q_j} = \frac{128\mu h}{\pi d^4} = \frac{8\mu h}{\pi (d/2)^4} = R_{aO,lin}. \quad (5-15)$$

This is exactly the linear acoustic resistance  $R_{aO,lin}$  of the orifice due to viscous effect derived previously in Section 2. Hence, the shear term  $II$  in Eq. 5-10 corresponds to the viscous linear resistance in the existing lumped element model. As a validation, the numerical data from Case 1 and Case 2 are again used. In Figure 6-6A and Figure 6-6B the total shear stress contribution (terms  $I$  and  $II$ ) from the numerical data for Case 1 and Case 2, respectively, are compared with the corresponding acoustic linear resistance  $R_{aO,lin}$  that actually only models term  $II$ . Clearly, the magnitude of the fully developed contribution (term  $II$ ) is dominant, while the main effect of the excess shear is believed to



add a small phase lag in the signal. This result provides confidence in the assumption of neglecting the excess shear contribution, i.e. term *I*.

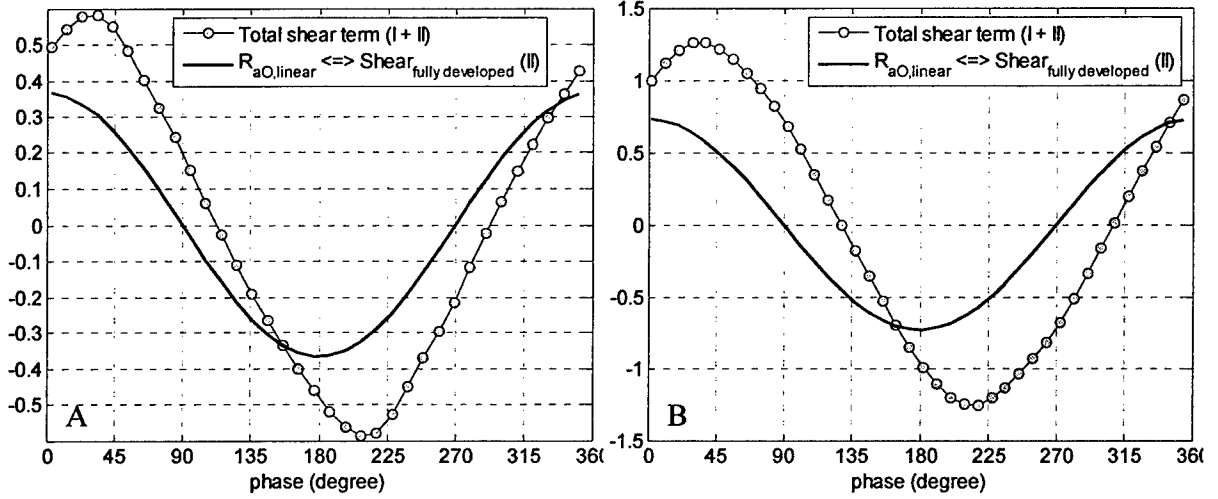


Figure 6-6: Numerical results of the total shear stress term versus corresponding lumped linear resistance during one cycle. A) Case 1:  $h/d = 1$ ,  $St = 2.38$ ,  $Re = 262$ ,  $S = 25$ . B) Case 2:  $h/d = 2$ ,  $St = 2.38$ ,  $Re = 262$ ,  $S = 25$ .

### III = unsteady inertia term

This is again a *linear* contribution to the orifice pressure drop, with a  $90^\circ$  phase shift referenced to the volume flow rate (or velocity). In a similar manner as above, the unsteady term contribution can be rewritten such that

$$\Delta P = \pi \frac{h}{d} St \frac{1}{2} \rho \bar{V}_j^2, \quad (5-16)$$

or in terms of an acoustic impedance,

$$Z_{ao} = \frac{\Delta P}{Q_j} = \frac{\pi \frac{h}{d} \frac{\omega d}{V_j} \frac{1}{2} \rho \bar{V}_j^2}{\frac{\pi}{2} \bar{V}_j S_n} = \frac{\omega \rho h}{S_n} = \omega \frac{3}{4} \frac{4 \rho h}{3 S_n} = \omega \frac{3}{4} M_{aN}, \quad (5-17)$$

where  $M_{aN}$  is the linear acoustic mass of the orifice associated with the fully developed pipe flow. Therefore, the unsteady inertia term is equivalent to a mass (or inertia) in the orifice. Notice that Eq. 5-17 is derived for a circular orifice and that in the case of a 2D slot the multiplicative constant is equal to  $5/6$  instead of  $3/4$ .

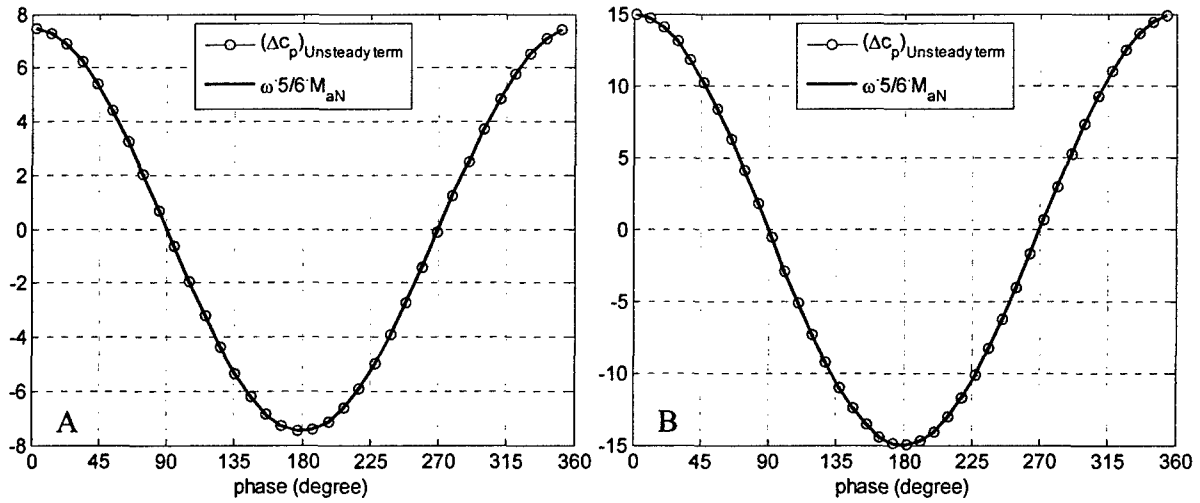


Figure 6-7: Numerical results of the unsteady term versus corresponding lumped linear reactance during one cycle. A) Case 1:  $h/d = 1$ ,  $St = 2.38$ ,  $Re = 262$ ,  $S = 25$ . B) Case 2:  $h/d = 2$ ,  $St = 2.38$ ,  $Re = 262$ ,  $S = 25$ .

Again, the CFD data are compared with the corresponding linear lumped parameter  $M_{aN}$ , as shown in Figure 6-7A and Figure 6-7B for Case 1 and Case 2, respectively. This term along with the skin friction integral (term  $I$ , which is also frequency dependant when the flow is not steady) are the sources of the reactance term in the linear acoustic total orifice impedance model  $Z_{aO} = R_{aO} + j\omega M_{aO}$ .

#### **$IV$ = momentum integral term**

The momentum integral that comes from the convective term is the *nonlinear* term that is the source of the distortion in the orifice pressure loss signal. As a simple example, if the flow is steady and if the location  $y$  is chosen such that the flow is fully developed, then the velocity is given by

$$v_y(x) = 2\widehat{V}_j \left( 1 - \frac{x^2}{(d/2)^2} \right) = \pi \overline{V}_j \left( 1 - \frac{x^2}{(d/2)^2} \right), \quad (5-18)$$

and, by assuming a uniform velocity profile at the orifice inlet, the last integral (term  $IV$  in Eq. 5-10) would be simply  $2/3$ , exactly that found for the case of steady flow in the inlet of ducts derived in White (1991, p. 291). However, in the general case, this term is both resistive and reactive i.e., it has a magnitude and a phase component, as shown from the numerical results of Case 1 and Case 2 in Figure 6-8A and Figure 6-8B, respectively. The magnitude of this nonlinear term is clearly non-negligible at low  $St \cdot h/d$  (or high dimensionless stroke length  $L_0/h$ ) as seen in Figure 6-2. Also, as shown in Figure 6-8, the momentum integral clearly exhibits a  $3\omega$  component. This suggests that the nonlinear term  $IV$  cannot be only modeled by a nonlinear resistor, but should also have a reactance component.

In this regard, one can use a zero-memory “square-law with sign” model in the momentum integral expression (Bendat 1998), which is defined by

$$Y = X|X|, \quad (5-19)$$

where the output  $Y$  would correspond to the output pressure drop and the input  $X$  is the spatial averaged velocity at any location  $y$  inside the orifice. It can be easily shown (see Bendat (1998) who performed a similar derivation but for an input white noise) that by assuming the input  $X$  as a sine wave given by

$$X(t) = A \sin(\omega t + \phi), \quad (5-20)$$

where  $A$  is the magnitude and the phase  $(-\pi \leq \phi \leq \pi)$  is uniformly distributed, and by minimizing the mean square estimate, then this square-law with sign model can be successfully approximated by a cubic polynomial  $\tilde{Y}$  of the form

$$\tilde{Y} = X|X| \cong \frac{16A}{15\pi} X + \frac{32}{15\pi A} X^3. \quad (5-21)$$

Notice that the ratio between the two polynomial coefficients is equal to  $2/A^2$ , which is over the inverse of the power in the input sine wave. Substituting Eq. 5-20 in Eq. 5-21, the output of the zero-memory square-law with sign nonlinear model takes the form

$$\tilde{Y}(t) = \frac{8A^2}{3\pi} \left[ \sin(\omega t + \phi) - \frac{1}{5} \sin(3\omega t + 3\phi) \right]. \quad (5-22)$$

The square law with sign produces a cubic nonlinearity. The nonlinear system redistributes energy to the fundamental ( $\omega$ ) and to the 2<sup>nd</sup> harmonic ( $3\omega$ ). Notice also the relative magnitude between the two contributions in Eq. 5-22 such that it looks like the nonlinear contribution is small while the linear contribution is large. This principal feature of the model can clearly be seen in the numerical results shown in Figure 6-8. How to correlate this square-law with sign model with the momentum integral (term  $IV$  in Eq. 5-10) is investigated in the next section.

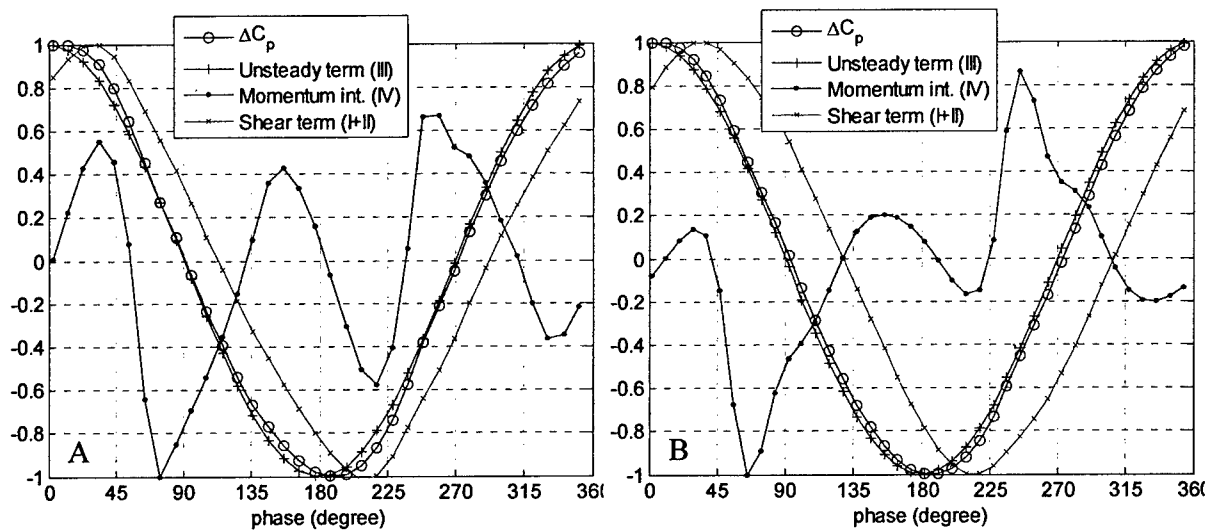


Figure 6-8: Numerical results of the normalized terms in the integral momentum equation as a function of phase angle during a cycle. A) Case 1:  $h/d = 1$ ,  $St = 2.38$ ,  $Re = 262$ ,  $S = 25$ . B) Case 2:  $h/d = 2$ ,  $St = 2.38$ ,  $Re = 262$ ,  $S = 25$ . Each term has been normalized by its respective magnitude.

In summary, a physical explanation has been given of each of the term that composes the equation of the orifice pressure drop given by Eq. 5-10. Each term was related to its lumped element counterpart. It was found that the excess shear contribution from the starting flow (term *I*) can be neglected in comparison to the magnitude of the other terms, the fully developed shear stress component (term *II*) is equivalent to the linear acoustic resistance from LEM, and the unsteady inertia term (term *III*) corresponds to the acoustic linear orifice reactance. Finally, the momentum integral (term *IV*) is the only nonlinear contribution to the pressure drop and can be represented by a nonlinear system having both a resistive ( $R_{aO,nl}$ ) and a reactive ( $M_{aO,nl}$ ) part. Therefore, if one is able to find a correlation for this nonlinear term (term *IV*) as a function of the governing dimensionless parameters, then it can be implemented into the existing low-order lumped model. These findings are shown schematically in Figure 6-9, where a physical parallel is provided between each of the terms in the acoustic orifice impedance of a ZNMF actuator and the control volume analysis described above.

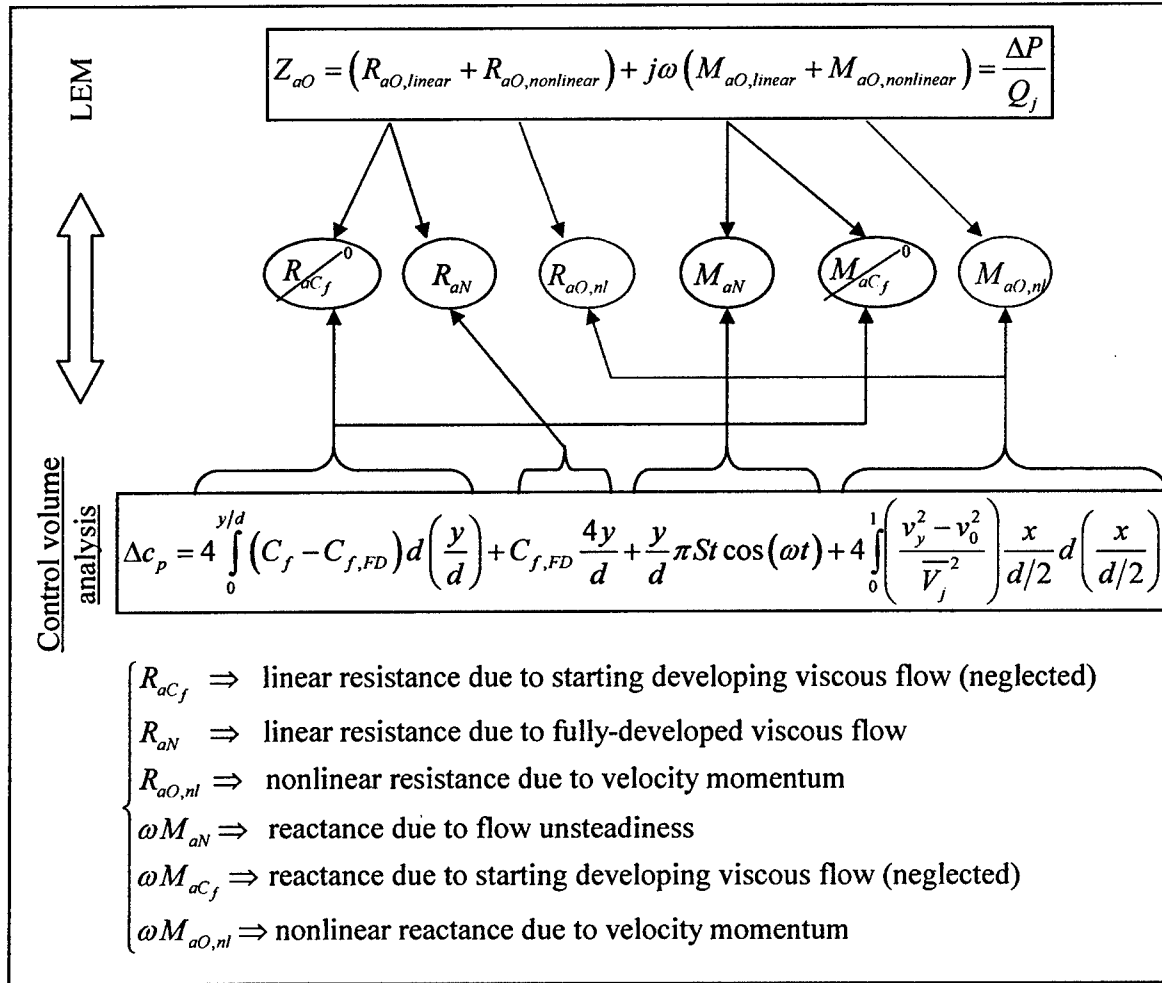


Figure 6-9: Comparison between lumped elements from the orifice impedance and analytical terms from the control volume analysis.

## 6.1.4 Development of Approximate Scaling Laws

### 6.1.4.1 Experimental results

Now that an analytical expression of the pressure drop across the orifice has been derived and validated, the experimental data presented in Section 3 and used throughout this report are used to develop scaling laws of the orifice pressure drop coefficient, to improve the existing lumped element model. In Section 4, the experimentally determined orifice pressure loss coefficient has already been plotted versus the Strouhal number as well and the nondimensional stroke length  $St h/d = \pi h/L_0$ . However, large scatter in the pressure data were noted, since it was assumed that the pressure inside the cavity is equivalent to the pressure drop across the orifice. This is not always a valid assumption, as discussed in the first part of Section 5. Therefore, the RHS of Eq. 5-10 is now used explicitly to compute the orifice pressure drop  $\Delta c_p$ . Notice however that the shear stress contribution is neglected in this experimentally-based investigation, simply because no such information is available and also since, as discussed above, the CFD results suggest

that this term is indeed negligible. Likewise, as validated in the previous section, the entrance velocity is approximated by the exit velocity via Eq. 5-12 to compute the velocity momentum integral (term  $IV$  in Eq. 5-10).

Figure 6-10 shows the experimental results of the total orifice pressure drop coefficient for different Stokes number and as a function of  $St \cdot h/d$ . The  $\Delta c_p$  is computed from the control volume analysis (using the RHS of Eq. 5-10 less the shear term). However, the  $\Delta c_p$  measured from the cavity pressure data using Microphone 1 or Microphone 2 is also shown only for illustration purposes. In addition to the experimental results, the results for the numerical simulations used above are included. The experimental results using the theoretical control volume analysis show good collapse of the data over the whole range of interest. This is especially true even at high  $St \cdot h/d$  (or low dimensional stroke length by recalling that  $St \cdot h/d = \pi \cdot h/L_0$ ) where the orifice pressure drop linearly increases with  $St \cdot h/d$ . This is in accordance with the fact that the unsteady term in Eq. 5-10 is a function of  $St \cdot h/d$  and was shown to be the dominant term. However, at lower values ( $St \cdot h/d < 1$ ), the collapse in the data is less pronounced since for such low Strouhal numbers the nonlinear term becomes significant due to jet formation, as confirmed from the CFD data and shown previously in Gallas et al. (2004). In this scenario at low  $St \cdot h/d$ , the orifice flow may be seen as quasi-steady and/or as a starting flow due to the large stroke length; hence the pressure drop should asymptote to the solution of steady pipe flow, which is mainly a function of geometry and Reynolds number. Notice also that the case of low  $St \cdot h/d$  may also be due to a very thin orifice design, similar to a perforate, for which the orifice flow is always in a developing state.

On the other hand, the scatter in the data using the experimental cavity pressure is made evident when joining the corresponding data from Mic 1 to Mic 2 to estimate the uncertainty in the pressure data. Although the orifice pressure drop is overestimated for certain experimental data cases when using the cavity pressure information, given the large uncertainty in the pressure drop data, the overall trend is well-defined over the intermediate-to-high range of  $St \cdot h/d$ , while the lower range shows an asymptotic behavior to a constant value. In any case, the two distinct regions are well defined. At low dimensionless stroke length, the flow is clearly unsteady, while for high dimensionless stroke length the flow is quasi-steady, as delimited by the dotted line in Figure 6-10, which corresponds to  $St \cdot h/d = 0.62$ , or  $L_0/h = 5$ .

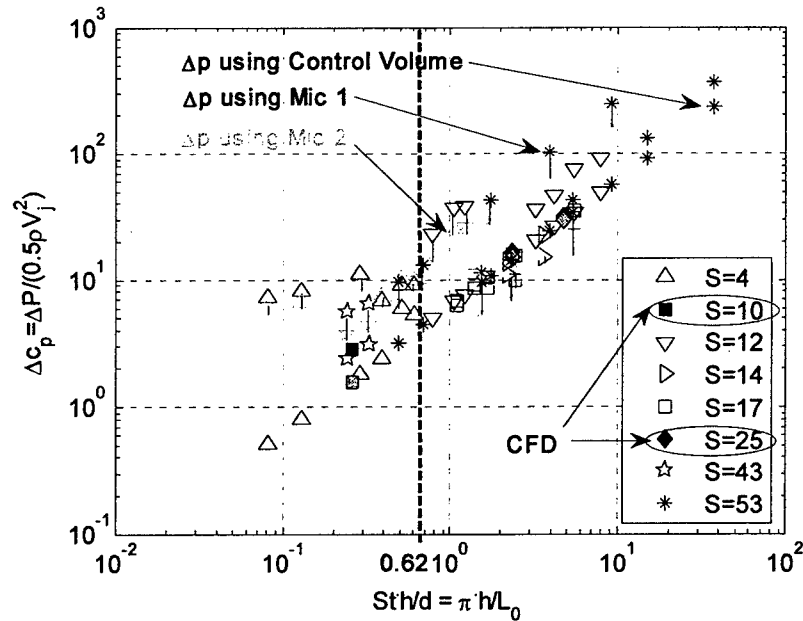


Figure 6-10: Experimental results of the orifice pressure drop normalized by the dynamic pressure based on averaged velocity  $\bar{V}_j$  versus  $St \cdot h/d$  for different Stokes numbers. The pressure drop is computed using either the control volume analysis (terms *III* and *IV*) or the experimental cavity pressure (Mic 1 and Mic 2).

Next, each term in Eq. 5-10 - less term *I* that is neglected - is also plotted versus the dimensionless stroke length  $St \cdot h/d$  using the experimental data. Practically, the nonlinear momentum integral (term *IV*) is computed from the exit velocity profile and using the approximation discussed above to compute the orifice entrance velocity (recall the equivalence with the nonlinear acoustic resistance  $R_{aO,nl}$  and mass  $M_{aO,nl}$ ). The unsteady inertia component (term *III*) is directly computed via its definition (equivalent to the acoustic mass  $M_{aN}$ ). Then, the fully developed friction coefficient contribution (term *II*) is also computed from its definition (recall the equivalence with the linear acoustic resistance  $R_{aN}$ ). The experimental results for these three terms are shown in Figure 6-11.

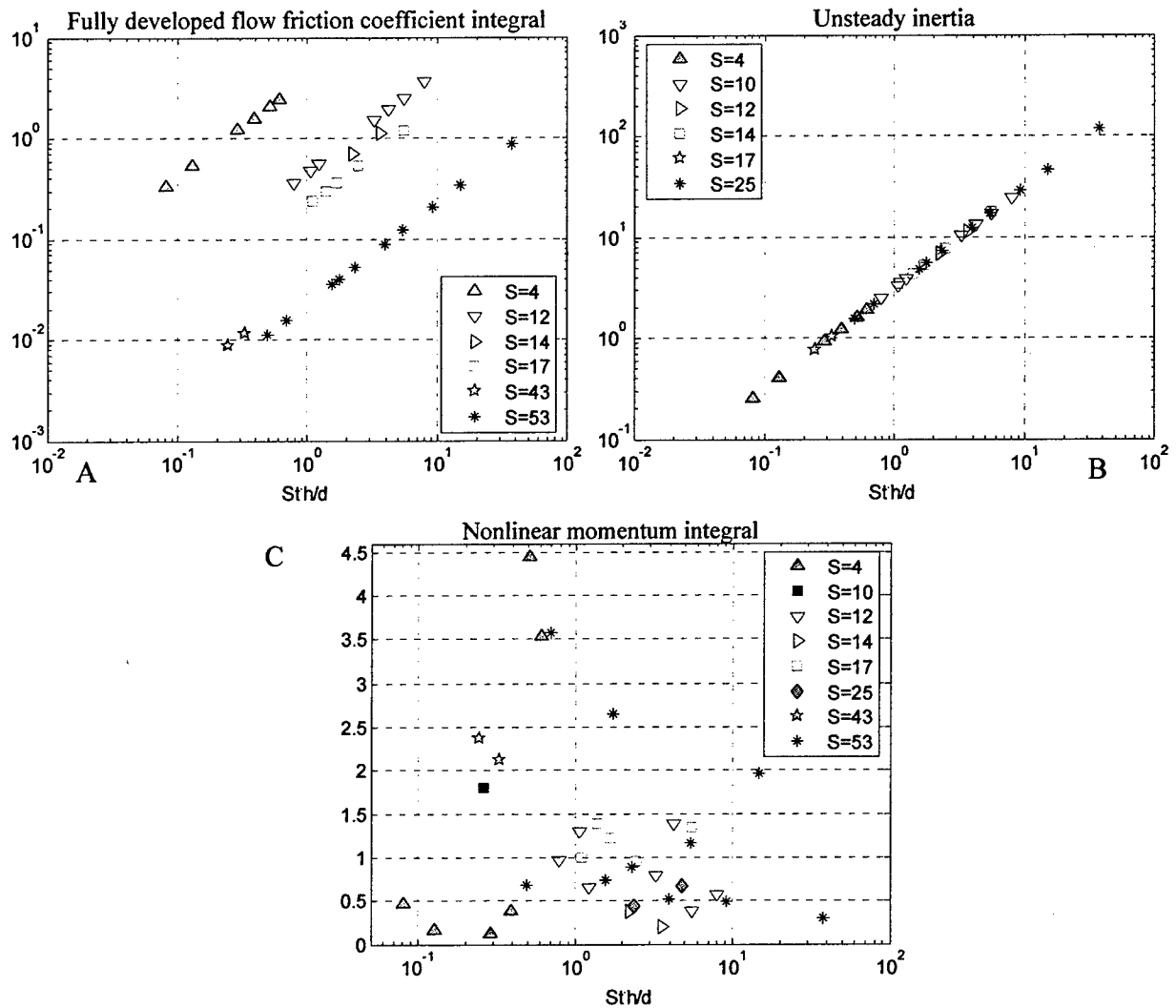


Figure 6-11: Experimental results of each term contributing in the orifice pressure drop coefficient vs.  $St \cdot h/d$ . A) Term II: friction coefficient integral due to fully developed flow. B) Term III: unsteady inertia. C) Term IV: nonlinear momentum integral from convective term.

First of all, the contribution of the friction coefficient integral from the fully developed pipe flow that corresponds to the linear acoustic resistance in the LEM is shown in Figure 6-11A. Not surprisingly, it has a rather small effect overall and linearly increases with  $St \cdot h/d$ . Note that the data will collapse if one plots it as a function of  $(h/d)/Re$  (recall that  $St = S^2/Re$ ). Then, shown in Figure 6-11B, is the contribution of the unsteady inertia effects that varies linearly with  $St \cdot h/d$ , and which is clearly the dominant feature in the total orifice pressure loss, especially for  $St \cdot h/d > 0.62$ . Figure 6-11C shows next the variations of the nonlinear momentum integral as a function of the dimensionless stroke length. It can first be noted that the data seem scattered and that no



obvious trend can be discerned. Notice also that the data oscillate around a value of unity, which is the assumed value for the nonlinear loss coefficient  $K_d$  in the existing lumped model. Finally, Figure 6-12 shows the relative magnitudes of each term in the pressure loss equation for the intermediate to low  $St \cdot h/d$  cases. It confirms that the nonlinear term is only really significant for low values of  $St \cdot h/d < 3$ , where above this value the unsteady inertia term (term III) dominates and takes on a value greater than 10 (see Figure 6-11C), while term IV never exceeds 2 (and is usually less than that).

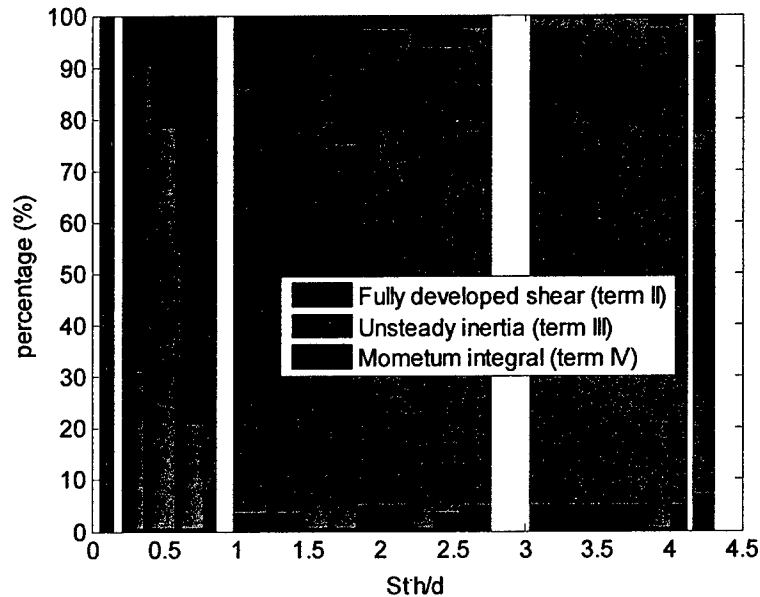


Figure 6-12: Experimental results of the relative magnitude of each term contributing in the orifice pressure drop coefficient vs. intermediate to low  $St \cdot h/d$ .

Therefore, based on these experimental results from the control volume analysis, the next step to be undertaken is to obtain a correlation of the nonlinear term in the pressure drop expression, which is ultimately to be related to the nonlinear coefficient  $K_d$  from the LEM defined in previous sections. The other terms in Eq. 5-10 are already defined, as shown in Figure 6-9. Then the scaling law will be implemented in the existing lumped model from Gallas et al. (2003a) to yield a refined model.

#### 6.1.4.2 Nonlinear pressure loss correlation

In the previous section, it was shown that the nonlinear part of the pressure loss coefficient can be successfully approximated by a square-law with sign model, which has both magnitude and phase information. The experimental results are then used to find a correlation for the magnitude. However, it is difficult to obtain accurate phase information at the present time. Since we are primarily interested in the magnitude of the actuator output, we will concentrate on the nonlinear resistance component. Applications that require accurate phase information (e.g., feedback flow control models) will ultimately require this aspect to be addressed.

As shown in Figure 6-11C, there is no such obvious correlation for the magnitude from the data over the entire range of  $St \cdot h/d$ . However, as noted earlier, two regions of operation can be distinguished from each other. A quasi-steady flow for high

dimensionless stroke length ( $L_0/h > 5$ ) and unsteady flow for intermediate to lower  $L_0/h$ .

In the former case where the nonlinear term  $IV$  is important, a different functional form should be envisaged from known steady pipe flow solutions that usually rely on the orifice geometry and flow Reynolds number. For instance, when studying flows in the inlet of ducts, White (1991, p. 291) describes a correlation of the pressure drop in the entrance of a duct for a laminar steady flow as a function of  $(y/d)/Re$ . Also, another common approach employed is from orifice flow meters. There, from pipe theory (Melling 1973; White 1979), the steady pipe flow dump loss coefficient for a generalized nozzle is given by

$$K_d = \left( \sqrt{1 - \beta^4} / C_D \right)^{-2}, \quad (5-23)$$

with  $\beta = d/D$  is the ratio of the exit to the entrance orifice diameter, and where  $C_D$  is the discharge coefficient that takes the form

$$C_D = 0.9975 - 6.53(\beta/Re)^{0.5} \quad (5-24)$$

for high Reynolds number  $Re$ . The problem however resides in the facts that Eq. 5-23 is based on a beveled-type of orifice, and that it is valid only for high Reynolds number ( $Re > 10^4$ ).

Here, a similar approach is used to correlate the quasi-steady cases. This is shown in Figure 6-13 where the experimentally determined nonlinear loss  $(\Delta c_p)_{\text{nonlinear}}$  is plotted against the Reynolds number  $Re$  in Figure 6-13A and against  $(h/d)/Re$  in Figure 6-13B. In these plots, the circled data are the ones of interest since they occur at a low  $St \cdot h/d$  i.e.,  $St \cdot h/d < 0.62$  or  $L_0/h > 5$ . Note that a distinction has been made on the orifice aspect ratio  $h/d$  (small  $h/d$  are in red symbols, intermediate  $h/d$  are in green, and large  $h/d$  are in blue). Once again, the 3 numerical test cases have been added to the figures for completeness. An estimate can then be found for the low  $St \cdot h/d$  range in terms of  $(h/d)/Re$ , as shown by the regression line in Figure 6-13B. The two outliers in Figure 6-13B are Case 60 ( $S = 4$ ,  $h/d = 5$ ,  $Re = 132$ ,  $St = 0.12$ ) and Case 61 ( $S = 4$ ,  $h/d = 5$ ,  $Re = 157$ ,  $St = 0.10$ ).

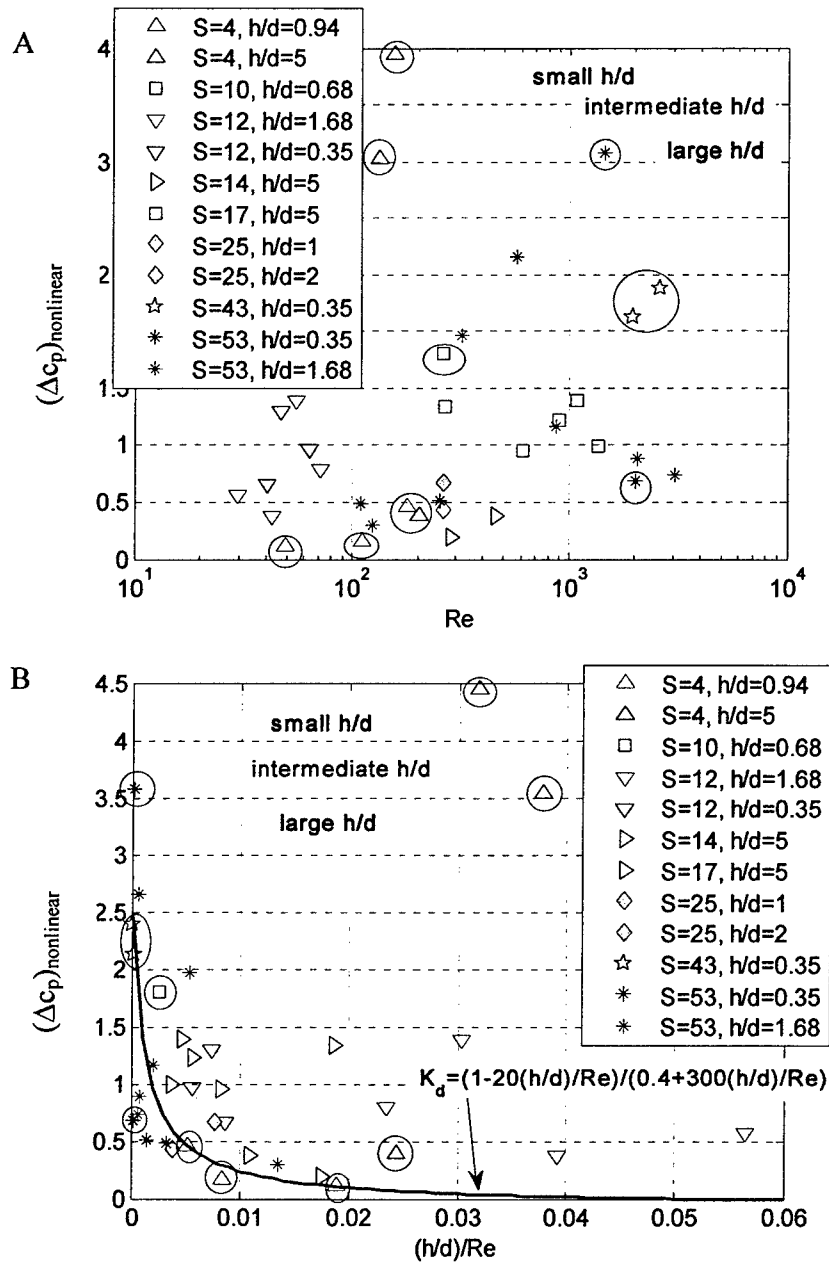


Figure 6-13: Experimental results for the nonlinear pressure loss coefficient for different Stokes number and orifice aspect ratio. A) Versus Reynolds number  $Re$ . B) Versus  $(h/d)/Re$ . The circled data correspond to  $L_0/h > 5$ .

On the other hand, for the case of intermediate to high  $St \cdot h/d$ , one can find a crude correlation as a function of  $St \cdot h/d$ , as shown in Figure 6-14, that should be able to represent the principal variations in the nonlinear part of the orifice pressure loss. Once again, the 3 numerical test cases have been added to the figure for completeness. The

two outliers in Figure 6-14 are Case 48 ( $S = 53$ ,  $h/d = 0.35$ ,  $Re = 571$ ,  $St = 4.96$ ) and Case 56 ( $S = 53$ ,  $h/d = 1.68$ ,  $Re = 318$ ,  $St = 8.79$ ).

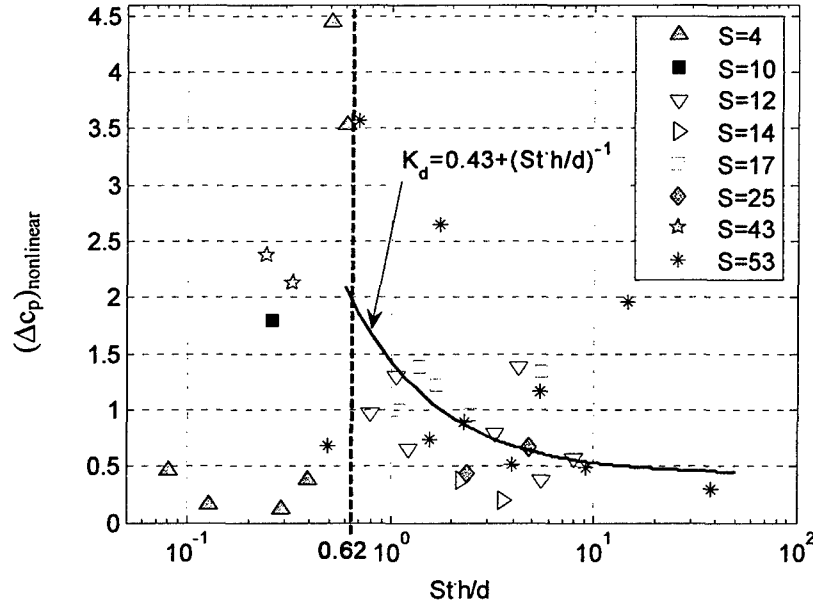


Figure 6-14: Nonlinear term of the pressure loss across the orifice as a function of  $St \cdot h/d$  from experimental data. The straight line shows a curve fit to the data in the intermediate to high  $St \cdot h/d$  range.

Therefore, based on these simple regressions performed on the data, a rough correlation on the amplitude of the nonlinear pressure loss coefficient can be obtained as a function of  $St \cdot h/d$ . At low values of  $St \cdot h/d$ , the nonlinear coefficient varies with  $(h/d)/Re$ , while for intermediate to high values, the nonlinear pressure drop coefficient is a function of  $St \cdot h/d$ . Thus, the following scaling law of the amplitude of the dimensionless orifice pressure loss is proposed

$$\begin{cases} |\Delta c_{p, nl}| = \frac{1 - 20 \left( \frac{h/d}{Re} \right)}{0.4 + 300 \left( \frac{h/d}{Re} \right)} & \text{for } St \cdot \frac{h}{d} < 0.62 \text{ or } \frac{L_0}{h} > 5 \\ |\Delta c_{p, nl}| = 0.43 + \left( St \cdot \frac{h}{d} \right)^{-1} & \text{for } St \cdot \frac{h}{d} \geq 0.62 \text{ or } \frac{L_0}{h} \leq 5 \end{cases} \quad (5-25)$$

Notice that these scaling laws are not optimal since they do not overlap at  $St \cdot h/d = 0.62$ . Although for high  $St \cdot h/d$  it seems accurate, the functional form for the scaling law for low  $St \cdot h/d$  can be greatly refined from an extended available database.

Then, based on this development of a scaling law for the nondimensional pressure loss inside the orifice of an isolated ZNMF actuator, the next logical step is to implement

it into the existing reduced-order lumped element model. This is described in the following section.

## 6.2 Refined Lumped Element Model

### 6.2.1 Implementation

The lumped element model presented in Section 2 has been derived from the hypothesis of fully developed pipe or channel flow. The acoustic impedance of the orifice, which is the component to be improved, is defined as a complex quantity that has both a resistance and a reactance term (Gallas et al. 2003a),

$$Z_{aO} = R_{aO,lin} + R_{aO,nl} + j\omega M_{aO}, \quad (5-26)$$

where  $R_{aO,lin}$  and  $M_{aO}$  are, respectively, the linear acoustic resistance and mass (i.e., reactance) terms from the exact solution for steady fully-developed pipe flow. The nonlinear acoustic resistance,  $R_{aO,nl}$ , is defined as

$$R_{aO,nl} = \frac{0.5K_d\rho Q_j}{S_n^2}, \quad (5-27)$$

where  $K_d$  is the dimensionless orifice loss coefficient that is assumed to be unity (McCormick 2000) in the existing version of the lumped element model.

From the previous analysis using a control volume, the correspondence between the lumped elements and the pressure drop terms was shown in Figure 6-9. All terms were appropriately modeled via lumped elements except for the nonlinear term that is the focus of this effort and that has both a resistance and a reactance. From the scaling law developed next, only the magnitude was successfully correlated with the main nondimensional geometric and flow parameters, not the phase. The magnitude and phase of the nonlinear term are related to the resistance and mass in the LEM impedance analogy via the following relationships. Since the acoustic impedance is defined as

$$Z_{aO} = R_{aO} + j\omega M_{aO} = \frac{\Delta P}{Q_j}, \quad (5-28)$$

and that the orifice pressure drop is

$$\Delta c_p = \frac{\Delta P}{0.5\rho\bar{V}_j^2}, \quad (5-29)$$

then, the correspondence between LEM and the control volume analysis is given by

$$Z_{aO} = \frac{\Delta P}{Q_j} = \left( \frac{\rho\bar{V}_j}{\pi S_n} \right) \Delta c_p. \quad (5-30)$$

However, the nonlinear pressure drop from the momentum integral was shown to be accurately modeled via a square-law with sign model (see Eq. 5-22). So accounting only for the *nonlinear* part, Eq. 5-30 becomes

$$\begin{aligned} Z_{aO,nl} &= R_{aO,nl} + j\omega M_{aO,nl} = \left( \frac{\rho \bar{V}_j}{\pi S_n} \right) \Delta c_{p,nl} \\ &= |A_{nl}| \cdot \left\{ e^{j(\omega t + \angle A_{nl})} - \frac{1}{5} e^{j(3\omega t + \angle A_{nl})} \right\} \end{aligned} \quad (5-31)$$

where  $A_{nl} = (\rho \bar{V}_j / \pi S_n) \Delta c_{p,nl}$ . Notice also that the relationship between the dimensionless orifice loss coefficient  $K_d$  defined in Eq. 5-27 and the *nonlinear* part of  $\Delta c_p$  defined in Eq. 5-29 is such as

$$K_d = \left( \frac{2}{\pi} \right)^2 \Delta c_{p,nl}. \quad (5-32)$$

Hence, the parameters introduced in Eq. 5-31 are related to each other via,

$$\begin{cases} |A_{nl}|^2 = (R_{aO,nl})^2 + (\omega M_{aO,nl})^2 \\ \angle A_{nl} = \cot \left( \frac{\omega M_{aO,nl}}{R_{aO,nl}} \right) \end{cases} \quad (5-33)$$

The problem resides in the fact that, even though a scaling law was developed for the nonlinear magnitude  $|A_{nl}|$ , insufficient information is available to model the nonlinear phase component  $\angle A_{nl}$ . Hence the system of equation Eq. 5-33 cannot be solved for both  $R_{aO,nl}$  and  $M_{aO,nl}$ . Nonetheless, as a first pass, the phase lag from the nonlinear term is neglected, so that the scaling law developed above in Eq. 5-25 for  $|\Delta c_{p,nl}|$  is directly implemented into the total orifice acoustic impedance  $Z_{aO}$  through the refined nonlinear acoustic resistance  $R_{aO,nl}$  via Eqs. 5-31 and 5-32.

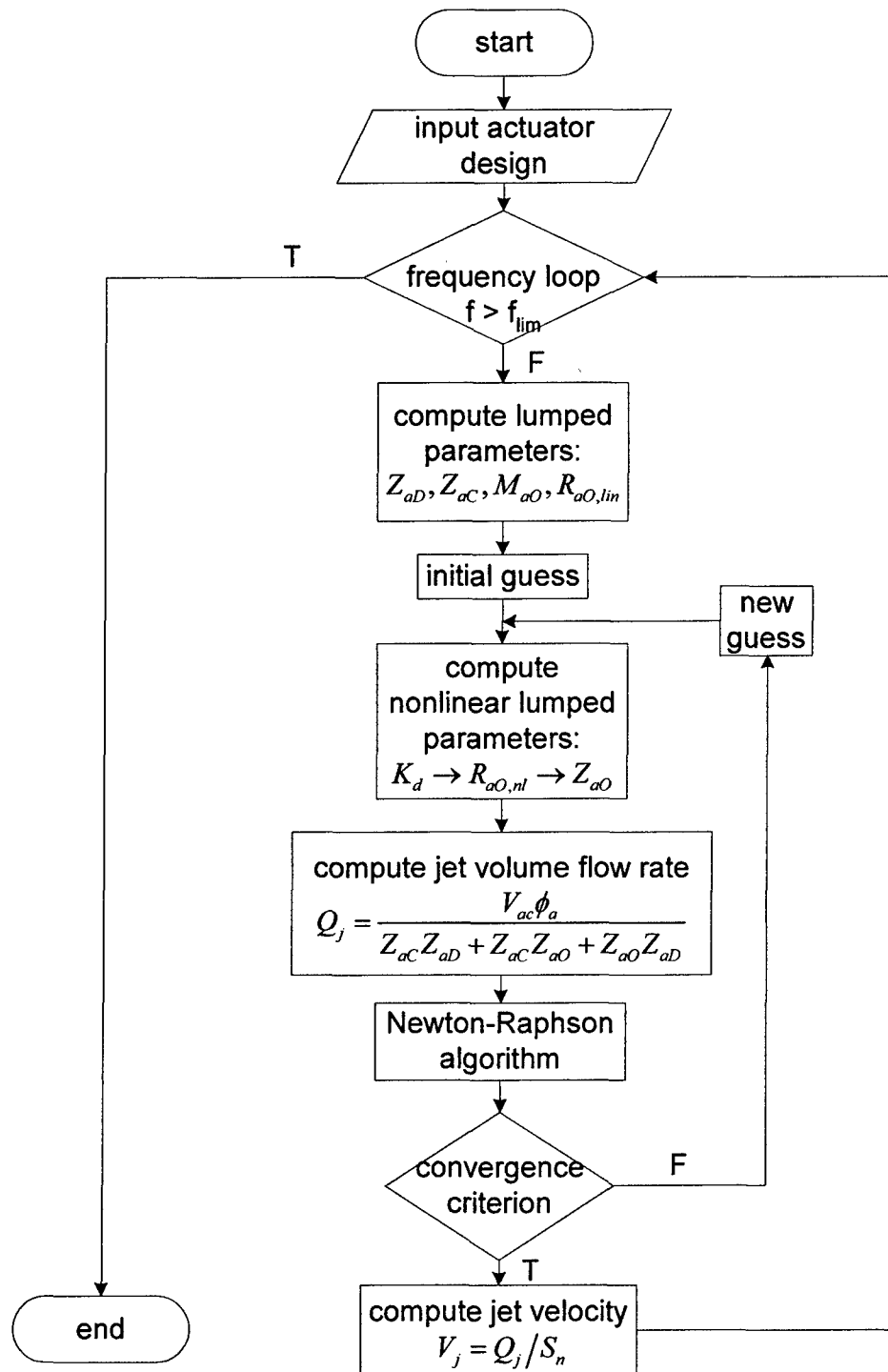


Figure 6-15: Implementation of the refined LEM technique to compute the jet exit velocity frequency response of an isolated ZNMF actuator.

### 6.2.2 Comparison with Experimental Data

The problem being now closed, the refined lumped element model can now be implemented and compared to experimental data. Notice that  $K_d$  is now a function of the output flow, so it should be implemented in an iterative converging loop. Also, LEM provides a frequency response of the actuator output (strictly speaking, it is an impulse response since the system is nonlinear). The actual sequence to compute the jet exit velocity using the refined LEM technique is depicted in the flowchart shown in Figure 6-15. The nonlinear terms in the orifice acoustic impedance are computed via a Newton-Raphson algorithm.

Next, the refined low-order model is implemented and compared with available frequency response experimental data. The two test cases that were used to validate the first version of the lumped model in Gallas et al. (2003) are again utilized for comparison. These two cases are already shown in Section 2, and the reader is referred to Gallas et al. (2003a) for the details of the experimental setup and actuator configuration. In Figure 6-16 and Figure 6-17, the impulse response of the jet exit velocity acquired at the centerline of the orifice is compared with the two lumped element models: the “previous LEM” corresponds to the model developed in Gallas et al. (2003a), and the “refined LEM” corresponds to the refined model developed in this section. Each model prediction is applied to Case I and Case II, as shown in Figure 6-16A and Figure 6-17A, respectively. Notice that here the only empirical factor – the diaphragm damping coefficient  $\zeta_D$  – has been adjusted so that the refined model matches the peak magnitude at the frequency governed by the diaphragm natural frequency.

Before discussing the results, it should be pointed out that the experimental data are for the *centerline* velocity  $V_{CL}(t)$  of the ZNMF device. The lumped element model gives a prediction of the jet volume flow rate amplitude (or spatial-averaged exit velocity  $\widehat{V}_j(t)$ ) which is like a “bulk” velocity. And as seen in Section 4, there is no simple relationship between  $\widehat{V}_j(t)$  and  $V_{CL}(t)$  (see Figure 4-10) for the test cases considered in this study. Therefore, in order to represent this uncertainty, the two minima from the theoretical ratio  $\widehat{V}_j/V_{CL}$  for a fully developed pipe flow, are bounding the refined LEM prediction, as seen in Figure 6-16A and Figure 6-17A.



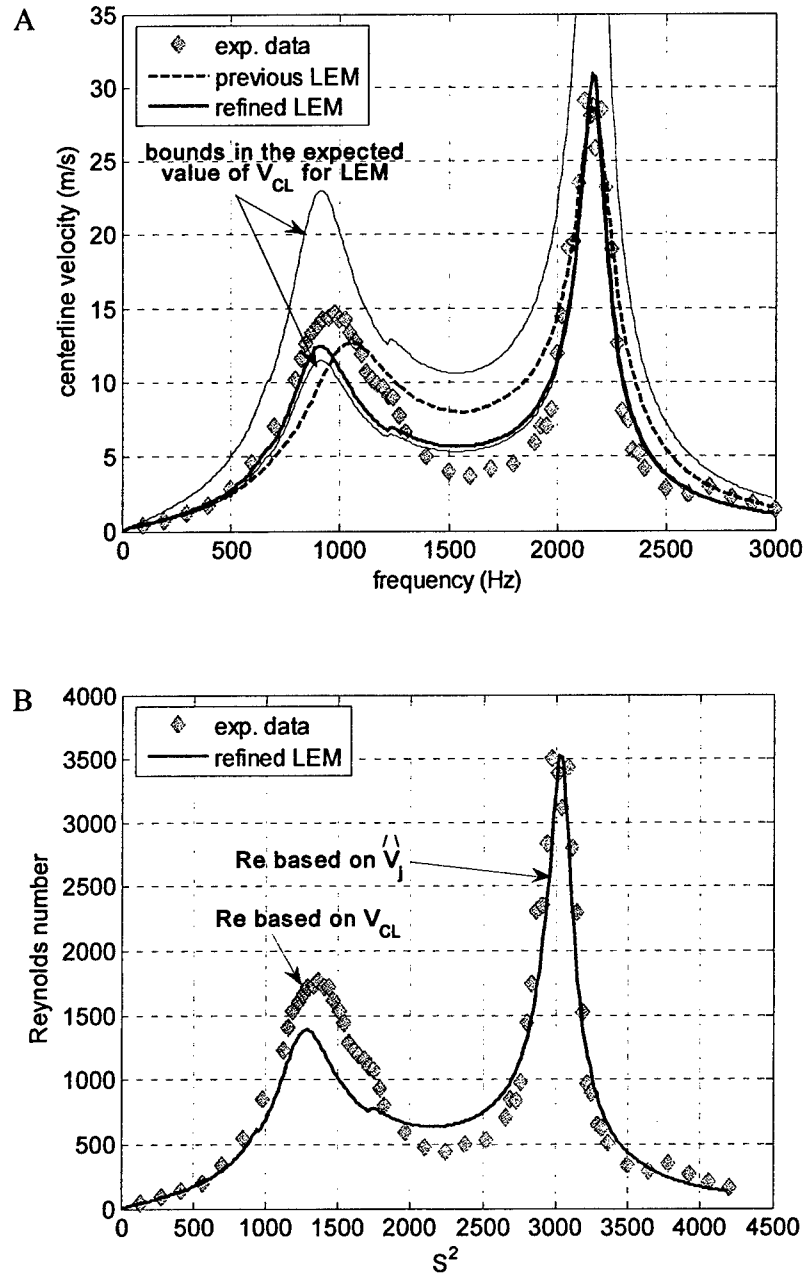


Figure 6-16: Comparison between the experimental data and the prediction of the refined and previous LEM of the impulse response of the jet exit centerline velocity. A) Centerline velocity versus frequency, where the LEM prediction is bounded by the minima of the theoretical ratio  $\hat{V}_j/V_{CL}$ . B) Jet Reynolds number versus  $S^2$ . C) Nonlinear pressure loss coefficient versus  $S^2$ . Actuator design corresponds to Case I from Gallas et al. (2003a).

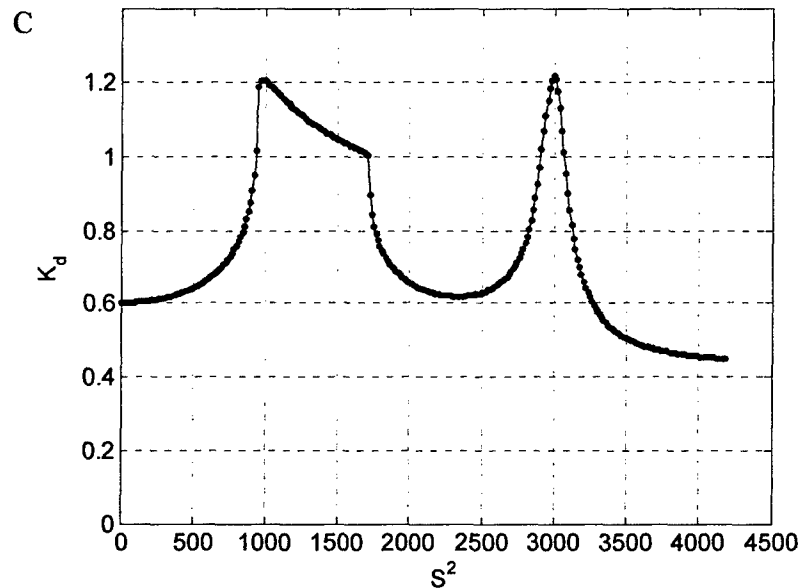


Figure 6-16: Continued.

Similarly, the Reynolds number based either on  $V_{cl}$  for the experimental data or  $\hat{V}_j$  for the LEM prediction is plotted versus the Stokes number squared, as shown in Figure 6-16B and Figure 6-17B. And finally, Figure 6-16C and Figure 6-17C show the corresponding nonlinear orifice pressure loss is plotted versus  $S^2$  for Case I and Case II, respectively.

Clearly, the main effect of the refined nonlinear orifice loss is to provide a slightly better prediction on the overall frequency response. For instance in Case I (Figure 6-16A), the peak near the Helmholtz frequency (first peak in the frequency response) is still overdamped by this new resistance, although the trough between the two resonance peaks and the response in the high frequencies are in better agreement with the experimental data. It is believed that the nonlinear mass information that is still missing in the model is a possible explanation for the residual discrepancy seen. In Case II (Figure 6-17A), the refined model tends to match closely the experimental data, and over the entire frequency range – the peak in the experimental results near 1200 Hz corresponds to a harmonic of the piezoelectric diaphragm resonance frequency, which the lumped model does not account for. In this case the damping of the Helmholtz resonance peak, occurring around 450 Hz, is well predicted. Notice also the jump in  $K_d$  seen in Figure 6-17B around 1050 Hz that is due to the discontinuity between the two scaling laws (Eq. 5-25) at  $St \cdot h/d = 0.62$ .

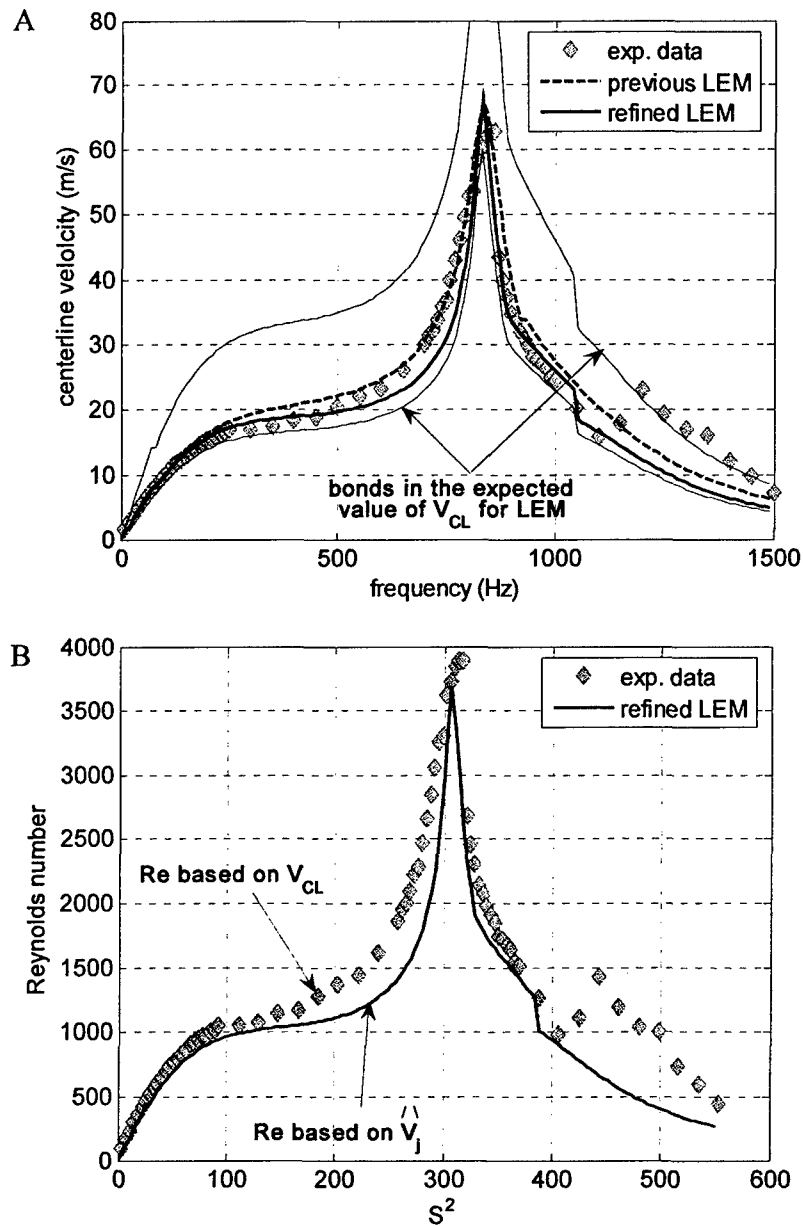


Figure 6-17: Comparison between the experimental data and the prediction of the refined and previous LEM of the impulse response of the jet exit centerline velocity. A) Centerline velocity versus frequency, where the LEM prediction is bounded by the minima of the theoretical ratio  $\widehat{V}_j/V_{CL}$ . B) Jet Reynolds number versus  $S^2$ . C) Nonlinear pressure loss coefficient versus  $S^2$ . Actuator design corresponds to Case II from Gallas et al. (2003a).

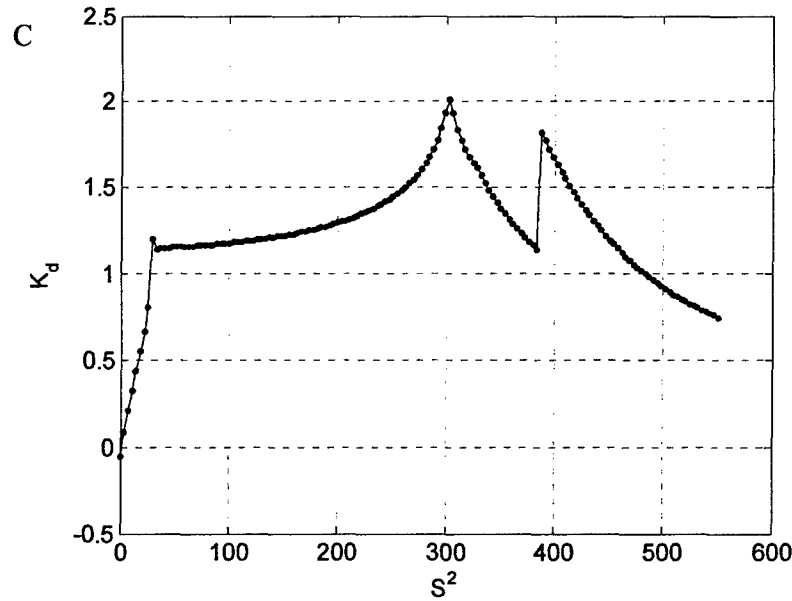


Figure 6-17: Continued.

However, this refined lumped element model fails in predicting some ZNMF actuator configurations, as shown in Figure 6-18. Although the uncertainty in the centerline velocity may explain some of the discrepancy, there are yet some deficiencies in the current lumped model. Some possible explanations would be first on the lack in the nonlinear mass that is non negligible for low  $St \cdot h/d$ , which corresponds to the frequencies above 300 Hz in Figure 6-18B. Similarly, it was shown that, in the time-domain, the nonlinear term includes the generation of  $3\omega$  terms given a forcing at  $\omega$ . While this is true in a time-domain, it may not be exactly similar in the frequency domain method employed above. The amplitude does match for the frequency domain, but the phase information is incorrect, which affects the impedance prediction via Eq. 5-33. This is further investigated next.

The above analysis is performed on the frequency response of the actuator output. However, as outlined in Section 2, the LEM technique can be easily implemented in the time domain to then provide the time signals of the jet exit volume flow rate at a single frequency of operation. Subsequently it can be easily compared with some of the experimental test cases listed in Table 2-3.

The equation of motion in the time domain of an isolated ZNMF actuator has been previously derived in Section 2 that is reproduced here for convenience

$$M_{ao}\ddot{y}_j + \frac{0.5K_d\rho}{S_n} \dot{y}_j |\dot{y}_j| + R_{ao} \dot{y}_j + \frac{1}{C_{ac}} y_j = \frac{S_d}{C_{ac}S_n} W_0 \sin(\omega t). \quad (5-34)$$

In the previous lumped model  $K_d$  was set to unity, so the second term in the LHS of Eq. 5-34 is a constant. However,  $K_d$  is now a function of either  $St \cdot h/d$  or  $(h/d)/Re$  via Eq. 5-25, so that the equation of motion should be rearranged accordingly.

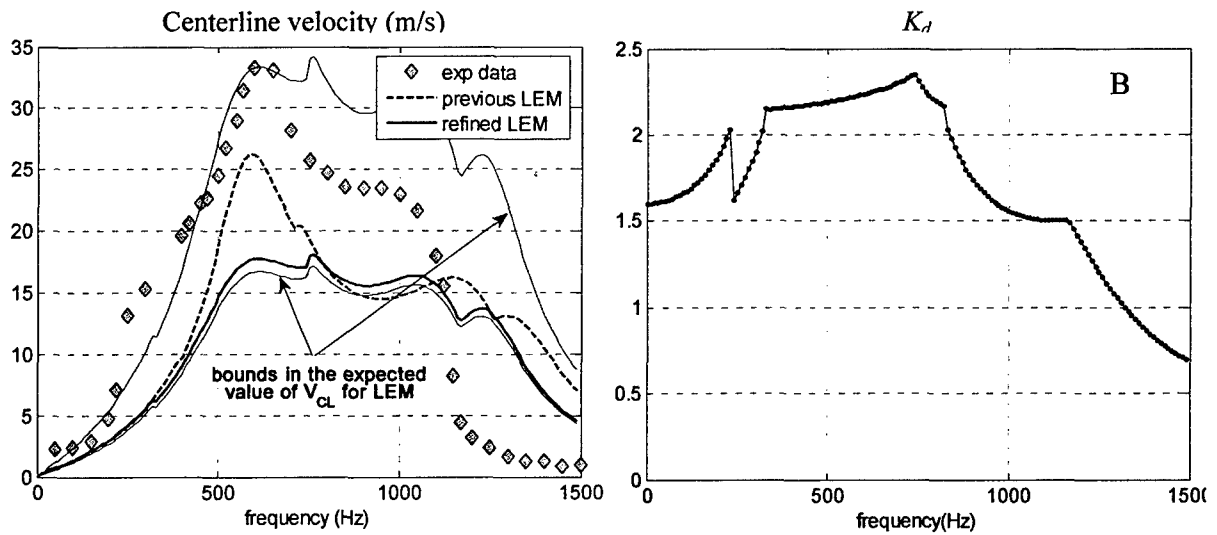


Figure 6-18: Comparison between the experimental data and the prediction of the refined and previous LEM of the impulse response of the jet exit centerline velocity. A) Centerline velocity, where the refined LEM prediction is bounded by the minima of the theoretical ratio  $\widehat{V}_j/V_{CL}$ . B) Nonlinear pressure loss coefficient  $K_d$ . Actuator design is from Gallas (2002) and is similar to Cases 41 to 50 ( $h/d = 0.35$ ).

Then, the nonlinear ODE (Eq. 5-34) that describes the motion of the fluid particle at the orifice is numerically integrated using a 4<sup>th</sup> order Runge-Kutta algorithm with zero initial conditions for the particle displacement and velocity, as outlined in Section 2, until a steady state is reached. The results of the jet volume velocity at the orifice exit are compared with two experimental test cases, namely Case 29 and Case 41, which are shown in Figure 6-19A and Figure 6-19B, respectively. Again, note that zero phase corresponds to the onset of the expulsion stroke. While the magnitude of the jet volume flow rate is clearly well predicted by the refined model, especially for Case 41 (Figure 6-19B), the distortion seen in Case 29 (Figure 6-19A) is not captured by the low-order model that remains nearly sinusoidal. The distortions in the signal are presumably due to the phase distortions that are not completely accounted for in this refined model. Note that at this particular frequency the frequency domain method described above gives a similar value for the jet volume flow rate amplitude.

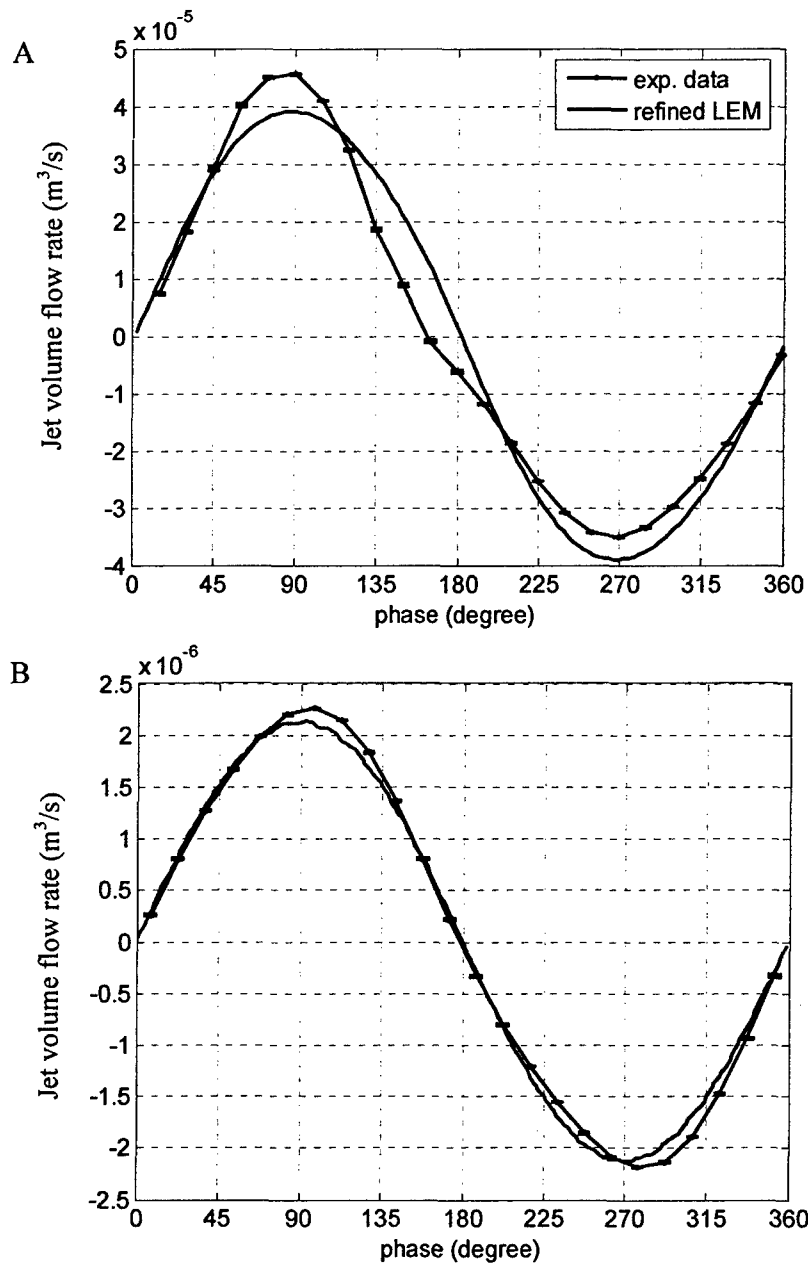


Figure 6-19: Comparison between the refined LEM prediction and experimental data of the time signals of the jet volume flow rate. A) Case 29:  $S = 34$ ,  $Re = 1131$ ,  $St = 1.1$ ,  $h/d = 0.95$ . B) Case 41:  $S = 12$ ,  $Re = 40.6$ ,  $St = 3.49$ ,  $h/d = 0.35$ .

In conclusion, a refined lumped element model as been presented to predict the response of an isolated ZNMF actuator. The model builds on a control volume analysis of the unsteady orifice flow to yield an expression of the dimensionless pressure drop across the orifice as a function of the Reynolds number  $Re$ , Strouhal number  $St$  and orifice aspect ratio  $h/d$ . The model was validated via numerical simulations, and then a scaling law of the orifice pressure loss was developed based on experimental data. Next, the refined pressure loss coefficient was implemented into the existing low-dimensional

lumped element model that predicts the actuator output. The new model was then compared with some experimental test cases in both the frequency and time domain. This refined model is able to reasonably predict the magnitude of the jet velocity. Notice however that this model can be applicable to any type of ZNMF devices, meaning the driver and cavity of the actuator are well modeled, the only refinement made being for the orifice flow. And as seen in Section 4, it exhibits a rich and complex dynamics behavior that the refined model developed above is in essence able to capture, while still lacking in the details. Clearly, the reduced-order model as presented in this section will greatly benefit from a larger available high quality database, both numerically and experimentally.

## 7. Zero-Net Mass-Flux Actuator Interacting with an External Boundary Layer

This section is dedicated to the interaction of a ZNMF actuator with an external boundary layer, in particular with a laminar, flat-plate, zero pressure gradient (ZPG) boundary layer. First, a qualitative discussion is provided concerning grazing flow interaction effects. This discussion is based on the numerical simulations performed by Rampugoon (2001) for the case of a ZNMF device interacting with a Blasius laminar boundary layer and also on studies of other applications such as acoustic liners. Next, the nondimensional analysis performed in Section 2 for the case of an actuator issuing into ambient air is extended to include the grazing flow interaction effects. Based on these results, two approaches to develop reduced-order models are proposed and discussed. One model builds on the lumped element modeling technique that was previously applied to an isolated device and leverages the semi-empirical models developed in the acoustic liner community for grazing flow past Helmholtz resonators. Next, two scaling laws for the exit velocity profile behavior are developed that are based on available computational data. Each model is developed and discussed, and the effects of several key parameters are investigated.

### 7.1 On the Influence of Grazing Flow

As mentioned in Section 1, most applications of ZNMF devices involve an external boundary layer. Intuitively, the performance of a ZNMF actuator will be strongly affected by some key grazing flow parameters that need to be identified. Rampugoon (2001) performed an interesting parametric study on the influence of the Reynolds number based on the boundary layer thickness  $Re_\delta$ , the orifice aspect ratio  $h/d$ , and the jet orifice Reynolds number  $Re = \bar{V}_j d / \nu$ , for a ZNMF device interacting with a Blasius boundary layer. As shown in Figure 7-1, if the jet Reynolds number  $Re$  is small compared with that of the boundary layer, for a constant ratio  $\delta/d = 2$ , the vortex formation process at the orifice neck is completely disturbed by the grazing boundary layer. In particular, the counterclockwise (CCW) rotation vortex that usually develops on the upstream lip of the slot in quiescent flow cases is quickly cancelled out by the clockwise (CW) vorticity in the grazing boundary layer, while a distinct clockwise rotating vortex is observed to form, although it rapidly diffuses as it convects downstream. However, as the jet Reynolds number  $Re$  increases, both vortices of opposite sign vorticity generated at the slot are immediately convected downstream due to the grazing boundary layer and are confined inside the boundary layer. Furthermore,

due to vorticity cross-annihilation (Morton 1984), the CCW vortex rapidly diminishes in strength such that further downstream only the CW vortex is visible. Notice that these simulations are two-dimensional, and that actually there are not really two distinct vortices but a closed vortex loop.



Figure 7-1: Spanwise vorticity plots for three cases where the jet Reynolds number  $Re$  is increased. A)  $Re = 63$ . B)  $Re = 125$ . C)  $Re = 250$ . With  $Re_\delta = 254$ ,  $h/d = 1$ , and  $S = 10$ . (Reproduced with permission from Rampugoon 2001).

By increasing the jet Reynolds number, the vortices now completely penetrate through the boundary layer and emerge into the freestream flow, which is primarily due to the relatively high jet momentum. In each cycle, one vortex pairs with a counter-rotating vortex of the previous cycle and this vortex pair propels itself in the vertical direction through self-induction while being continuously swept downstream due to the external flow. However, in an actual separation control application, it is unlikely that such a scenario of complete disruption of the boundary layer will be possible (due to actuator strength limitations) or even desirable. Similarly in another case study, Rampugoon (2001) looked at the effect of the orifice aspect ratio  $h/d$  and found no significant difference in the initial development of the vortex structures, although it yielded slightly different vortex dynamics further downstream.

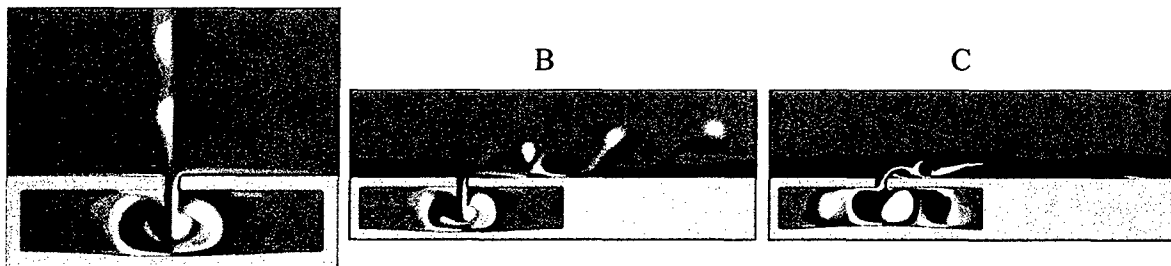


Figure 7-2: Spanwise vorticity plots for three cases where the boundary layer Reynolds number  $Re_\delta$  is increased. A)  $Re_\delta = 0$ . B)  $Re_\delta = 400$ . C)  $Re_\delta = 1200$ . With  $Re = 250$ ,  $h/d = 1$ , and  $S = 10$ . (Reproduced with permission from Rampugoon 2001).

Similarly, the Reynolds number based on the BL thickness  $Re_\delta$  was systematically varied while holding all other parameters fixed. In this case, it was found that as  $Re_\delta$  increases, the vortex structures generated at the orifice lip are quickly swept away and convected downstream, but can still penetrate through the BL thickness. When such vortex structures are large enough to directly entrain freestream fluid into the boundary layer, this entrainment becomes an important feature since in an adverse pressure gradient situation, the resulting boundary layer is more resistant to separation. Figure 7-2



shows spanwise vorticity plots for three cases in which the boundary layer Reynolds number  $Re_\delta$  is gradually increased from 0 to 1200.

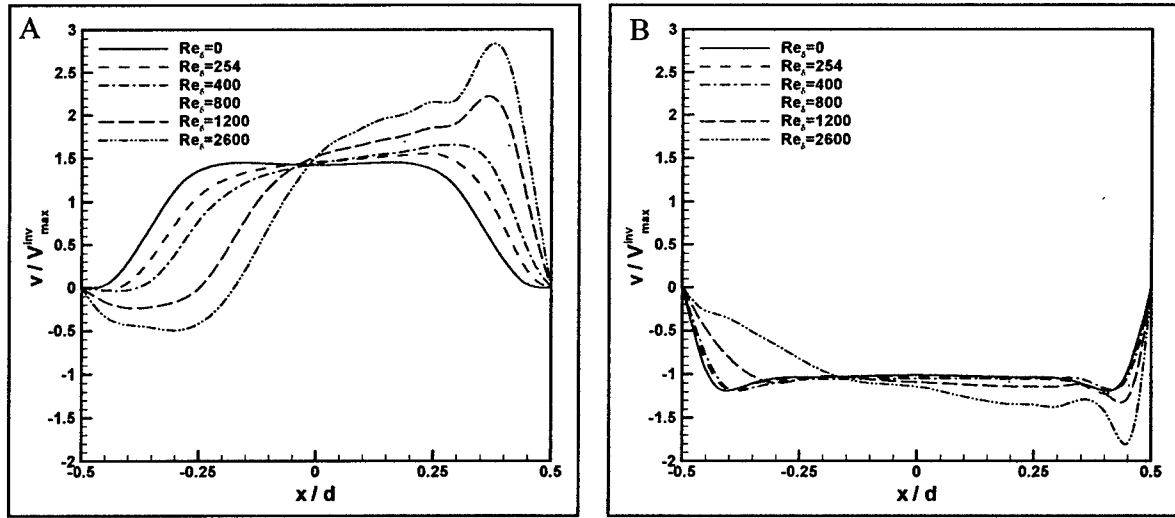


Figure 7-3: Comparison of the jet exit velocity profile with increasing  $Re_\delta$  from 0 to 2600, with  $Re = 250$ ,  $h/d = 1$ , and  $S = 10$ . A) Expulsion profiles. B) Ingestion profiles. (Reproduced with permission from Rampugoon 2001).

Next, Figure 7-3 shows the impact of  $Re_\delta$  on the exit velocity profile of the jet. It is clear that the jet profile in the case of quiescent flow,  $Re_\delta = 0$ , is significantly different from the case where there is an external boundary layer,  $Re_\delta \neq 0$ . In the case of an external boundary layer, the jet velocity profile may not be characterized by just one parameter, such as the conventional momentum coefficient  $C_\mu$  (defined below in Eq. 6-1), that is commonly employed in active flow control studies using ZNMF devices (Greenblatt and Wygnanski 2000; Yehoshua and Seifert 2003). In particular, the jet velocity profile is increasingly skewed in the flow direction as the Reynolds number of the boundary layer  $Re_\delta$  increases; this has a direct effect on the flux of momentum, vorticity, and energy from the slot. Therefore, from the point of view of parameterization of the jet velocity profile, the skewness appears to be an important parameter that should be considered, and is introduced in the next section. Similarly, it was shown (Utturkar et al. 2002) that the momentum coefficient differs during the ingestion versus the expulsion portion of the stroke and both are different from the ambient case.

The above discussion permits one to gain significant insight on the influence of several key dimensionless parameters on the overall behavior of a ZNMF actuator interacting with an external boundary layer. However, Rampugoon's study was limited to the special case of a Blasius boundary layer, which is an incompressible, laminar, zero pressure gradient boundary layer over a flat plate. Hence, a further discussion is provided below based on the work performed on flow past Helmholtz resonators over a wider range of flow conditions.

As previously discussed in Section 1, research involving flow-induced resonators has been mainly triggered by the desire to suppress oscillations, such as those occurring for example on automobile sunroofs (Elder 1978; Meissner 1987), or in sound absorbing

devices, such as mufflers (Sullivan 1979) or acoustic liners in engine nacelles (Malmay et al. 2001). Others have also suggested that an array of Helmholtz resonators driven by a grazing flow can modify a turbulent boundary layer (Flynn et al. 1990). Even though these flow-induced resonators are *passive*, as compared to *active* ZNMF actuators, their major findings are of interest and warrant a discussion. It should also be noted that the key parameter that has been widely used by researchers to quantify the interaction between the acoustic field and the grazing flow at the orifice exit is the specific acoustic impedance of the treated surface. Conveniently, this is similar to that of our previous research for isolated ZNMF actuators in using LEM.

Choudhari et al. (1999) performed an interesting study by comparing their numerical simulation results of flow past a Helmholtz resonator to published experimental data. Three different configurations for the resonator were studied, as listed in Table 7-1. The two-dimensional or axisymmetric laminar compressible Navier-Stokes equations were solved using an-house, node-based finite volume Cartesian grid solver. When applicable, a turbulent model was used based on the one-equation Spalart-Allmaras model (Spalart and Allmaras 1992). The reader is referred to their paper for a discussion of the numerical scheme that was employed. Although not reproduced here, the numerical simulations compared well, both qualitatively and quantitatively, with the experimental data from Hersh and Walker (1995) and Melling (1973).

Table 7-1: List of configurations used for impedance tube simulations used in Choudhari et al. (1999).

Reference	Orifice diameter (or width) $d(mm)$	Thickness to diameter ratio $h/d$	Open area ratio $\sigma(\%)$	Acoustic amplitude SPL(dB)	Cavity height $H(mm)$	Freq. $f(Hz)$
Hersh & Walker (1995) <i>Single circular orifice</i>	9.52	1.33	3.5	95 $\rightarrow$ 126	22.23**	250-600
Melling (1973) <i>Perforate 153 A/00</i>	1.27	0.5	7.5	114 $\rightarrow$ 162*	25.4 = $\lambda/4$	3400
LaRC (1998-1999) <i>Slot</i> <i>Perforate</i>	2.54	1	5	linear	76.2	566
	2.54	2.5	5	114 $\rightarrow$ 148*	76.2 = $\lambda/4$	1139

\* Free space SPL

\*\* Tuned for  $f = 500 Hz$

As previously discussed in Section 4, although incomplete in terms of essential dimensionless parameters, two different regimes were identified in terms of the sound pressure level (SPL): one for low-amplitude that is termed "linear" and one for high acoustic amplitude it is nonlinear. The computation from Choudhari et al. (1999) showed that in the linear regime, the fully-developed unsteady pipe flow theory applied to perforates with an  $O(1)$  aspect ratio  $h/d$  gave reasonable estimates, although the flow near the orifice edges is dominated by the rapid acceleration around the corners. Also, they were able to show that the dissipation occurring in the orifice is mainly due to

viscous effects rather than thermal dissipation. In the nonlinear regime, clear distortion in the probe signals (pressure fluctuation, orifice velocity) are present as already shown in the first part of Section 5 in Figure 5-9. When a laminar boundary layer interacts with the liner surface, as shown in Figure 7-4, the inflow part of the cycle exhibits a narrower “vena contracta” than for the outflow phase. This supports the hypothesis reported in earlier experimental studies (e.g., Budoff and Zorumski 1971) that, in the presence of grazing flow, the resistance to blowing into the flow is significantly less than the resistance to suction from the stream. Physically, this is equivalent in comparing the expulsion phase from a “quiescent medium” inside the resonator to the ingestion phase that directly interacts with a grazing flow. Such a result is relevant and should be taken into account when modeling a ZNMF actuator.

Therefore, from the study of previous work performed in aerodynamics as well as in aeroacoustics, some main features of the interaction of a grazing flow with a Helmholtz resonator and/or a ZNMF actuator can be extracted that yield more insight into the flow physics of such complex interaction behavior. In this regard, a nondimensional analysis is first described below, followed by the development of physics-based reduced-order models.

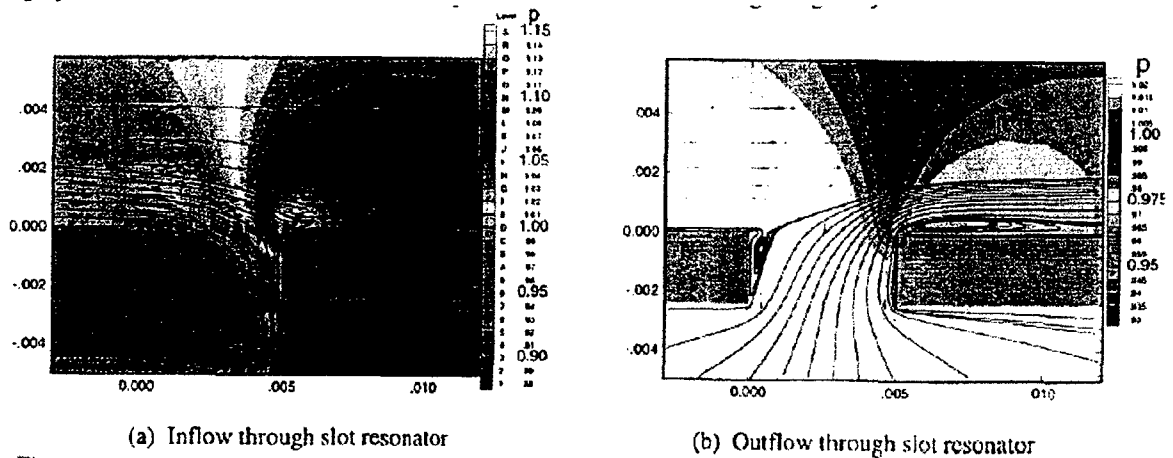


Figure 7-4: Pressure contours and streamlines for mean A) inflow, and B) outflow through a resonator in the presence of grazing flow (laminar boundary layer at  $Re_\delta = 3120$ ,  $\delta/d \approx 1$ ,  $h/d \approx 0.5$ , and average inflow/outflow velocity  $\approx 10\%$  of grazing velocity). (Reproduced with permission from Choudhari et al. 1999)

## 7.2 Dimensional Analysis

In Section 2, the actuator output parameters of interest were identified and defined from the time- and spatial-averaged jet velocity  $\bar{V}_j$  during the expulsion portion of a cycle defined in Eq. 1-4. Examples of such quantities are the jet Reynolds number  $Re$ , or amplitude of the jet output volume flow rate  $Q_j$ . Another quantity of interest in the case of a grazing boundary layer is the oscillatory momentum coefficient. In the presence of a grazing boundary layer, to quantify the addition of momentum by the actuator and

following the definition suggested by Greenblatt and Wygnanski (2000), the total (mean plus oscillatory) momentum coefficient of the periodic excitation is defined as the ratio of the momentum flux of the jet to the freestream dynamic pressure times a reference area. For a 2-D slot,

$$C_\mu = \frac{\rho_j \overline{u_{rms}^2} S_n}{1/2 \rho_\infty U_\infty^2 S_{ref}}, \quad (6-1)$$

where the subscript  $j$  refers to the jet,  $S_n = d \times w$  is the slot area,  $S_{ref} = L \times w$  is a reference area with  $L$  being any relevant length scale of either the airfoil model or the grazing BL (chord length  $c$ , boundary layer momentum thickness  $\theta$ , displacement thickness  $\delta^*$ , etc.). Notice that since no net mass is injected from the jet to the exterior medium (indeed, the jet is “synthesized” from the working ambient fluid), and if the turbulent boundary layer is assumed incompressible along with the flow through the orifice, then no significant density variations are expected, neither in the incoming boundary layer nor in the jet orifice. Therefore the fluid density of the jet can be considered as the same as the ambient fluid, i.e.  $\rho_j \cong \rho_\infty$ . Similarly, even though the jet velocity contains both mean and oscillatory components, here only the oscillatory part of  $C_\mu$  is retained since the mean component is identically zero for a zero-net mass flux device. Thus, for incompressible flow and after time-averaging, the momentum coefficient is defined as

$$C_\mu = \frac{2 \overline{u_{rms}^2} d}{U_\infty^2 \theta}, \quad (6-2)$$

where  $\overline{u_{rms}^2}$  is the mean square value of the oscillatory jet velocity normal component, and the boundary layer momentum thickness  $\theta$  is chosen as the relevant local boundary layer length scale. Based on the experimental results on the orifice flow described in Section 4, a clear distinction between the ejection and the ingestion part of the cycle exists. Thus, the momentum coefficient defined in Eq. 6-2 can be rewritten such as

$$C_\mu = C_{\mu,ex} + C_{\mu,in}, \quad (6-3)$$

where the subscripts “ $ex$ ” and “ $in$ ” refer to, respectively, the expulsion and ingestion portions of the cycle.

Yet other parameters, such as energy or vorticity flux, etc. might also play an important role in determining the effect of the jet on the boundary layer, not limiting ourselves to the momentum coefficient as in previous studies (Amitay et al. 1999; Seifert and Pack 1999; Yehoshua and Seifert 2003). In this current work, a more general approach to characterizing the jet behavior via successive moments of the jet velocity profile is thus advocated, following Rampugoon (2001). The  $n^{\text{th}}$  moment of the jet is defined as  $C_{\phi_{12}}^n = \langle V_j^n \rangle_{\phi_{12}}$ , where  $V_j$  is the jet velocity normalized by a suitable velocity

scale (e.g., freestream velocity) and  $\langle \cdot \rangle_{\phi_2}$  represents an integral over the jet exit plane and a phase average of  $V_j^n$  over a phase interval from  $\phi_1$  to  $\phi_2$ . This leads to the following expression

$$C_{\phi_2}^n = \frac{1}{\phi_2 - \phi_1} \frac{1}{S_n} \int_{S_n} \int_{\phi_1}^{\phi_2} [V_j(t, x)]^n d\phi dS_n. \quad (6-4)$$

Note the similarity with the definition of the jet velocity  $\bar{V}_j$  given by Eq. 1-4 previously defined, where one period of the cycle and the phase interval are related by  $T = \phi_2 - \phi_1$ , and the normalized jet velocity is related by

$$V_j(t, x) = \frac{v_j(t, x)}{U_\infty}, \quad (6-5)$$

if one takes, for instance, the freestream velocity  $U_\infty$  as a suitable velocity scale.

As observed from the discussion above, preliminary simulations (Rampungoon 2001; Mittal et al. 2001) indicate that the jet velocity profile is significantly different during the ingestion and expulsion phases in the presence of an external boundary layer. Defining the moments separately for the ingestion and expulsion phases, they are denoted by  $C_{in}^n$  and  $C_{ex}^n$ , respectively. Furthermore, it should be noted that this type of characterization is not simply for mathematical convenience, since these moments have direct physical significance. For example,  $C_{in}^1 + C_{ex}^1$  corresponds to the jet mass flux (which is identically equal to zero for a ZNMF device). The mean normalized jet velocity during the expulsion phase is  $C_{ex}^1$ . Furthermore,  $C_{in}^2 + C_{ex}^2$  corresponds to the normalized momentum flux of the jet, while  $C_{in}^3 + C_{ex}^3$  represents the jet kinetic energy flux. Finally, for  $n \rightarrow \infty$ ,  $(C_{ex}^n)^{1/n}$  corresponds to the normalized maximum jet exit velocity.

In addition to the moments, the skewness or asymmetry of the velocity profile about the center of the orifice is found to be useful (see Rampugoon 2001) and can be estimated as

$$X_{\phi_2} = \frac{1}{\phi_2 - \phi_1} \frac{1}{d/2} \int_0^{d/2} \int_{\phi_1}^{\phi_2} [V_j(\phi, x) - V_j(\phi, -x)] d\phi dx. \quad (6-6)$$

Assuming the external boundary layer to be flowing in the positive  $x$  direction, if  $X_{\phi_2} > 0$  the jet velocity profile is skewed towards the positive  $x$ , i.e. the jet has higher velocity in the downstream portion of the orifice than in its upstream part, while for  $X_{\phi_2} < 0$  the trend is inversed. If  $X_{\phi_2} = 0$ , the jet velocity profile is symmetric about the orifice center in an average sense, which would, for example, correspond to the no-grazing flow or ambient case. Similarly, the flux of vorticity can be defined as (Didden 1979),

$$\Omega_v = \frac{1}{d/2} \int_0^{d/2} \int_{\phi_1}^{\phi_2} \xi_z v_j(\phi, x) d\phi dx, \quad (6-7)$$

where  $\xi_z = [\nabla \times \vec{V}_j]_z$  is the vorticity component of interest.

Building on the dimensional analysis carried out in Section 2, the dependence of the moments and skewness can be written in terms of nondimensional parameters using the Buckingham-Pi theorem.

$$\left. \begin{matrix} C_{\phi_2}^n \\ X_{\phi_2} \end{matrix} \right\} = fn \left( \underbrace{\frac{\omega}{\omega_H}, \frac{h}{d}, \frac{w}{d}, \frac{\omega}{\omega_d}, \frac{\Delta V}{d^3}}_{\text{device}}, \underbrace{S, Re_\theta, \frac{\theta}{d}, H, M_\infty, \beta, C_f, \frac{\theta}{R}}_{\text{grazing BL}} \right). \quad (6-8)$$

By comparison with Eq. (2.19), the new terms are all due to the grazing BL. The physical significance of these new terms in the RHS of Eq. 6-8 is now described; refer back to Eq. 1-10 and accompanying text for an explanation of the isolated device parameters.

- $Re_\theta$  is the Reynolds number based on the local BL momentum thickness, the ratio of the inertial to viscous forces in the BL.
- $\theta/d$  is the ratio of local momentum thickness to slot width.
- $H = \delta^*/\theta$  is the local BL shape factor.
- $M_\infty = U_\infty/c_0$  is the freestream Mach number, the measure of the compressibility of the incoming crossflow.
- $\beta = \delta^*/\tau_w (dP/dx)$  is the Clauser equilibrium dimensionless pressure gradient parameter, relating the pressure force to the inertial force in the BL, where  $\tau_w$  is the local wall shear stress.
- $C_f = \tau_w/0.5\rho_\infty U_\infty^2$  is the skin friction coefficient, the ratio of the friction velocity squared to the freestream velocity squared.
- $\theta/R$  is the ratio of the local momentum thickness to the surface of curvature.

Notice that the parameters based on the BL momentum thickness have been selected versus the BL thickness or displacement thickness, by analogy with the LEM-based low dimensional models developed in this report. Also, it is fairly obvious that the parameter space for this configuration is extremely large and some judicious choices have to be made to simplify the parametric space. For instance, in the case of a ZNMF actuator interacting with an incompressible, zero pressure gradient laminar boundary layer (i.e., a Blasius boundary layer), the functional form of Eq. 6-8 takes the form

$$\left. \begin{matrix} C_{\phi_2}^n \\ X_{\phi_2} \end{matrix} \right\}_{\text{Blasius}} = fn \left( \frac{\omega}{\omega_H}, \frac{h}{d}, \frac{w}{d}, \frac{\omega}{\omega_d}, \frac{\Delta \nabla}{d^3}, S, \text{Re}_\theta, \frac{\theta}{d} \right), \quad (6-9)$$

which is the situation for which the low-order models described next are restricted to.

### 7.3 Reduced-Order Models

From the discussion provided in the previous sections, two approaches can be sought to characterize the interaction of a ZNMF actuator with an external boundary layer. One approach is an extension of the lumped element model to account for the grazing flow on the orifice impedance. However, this method does not provide any details regarding the velocity profile. A second approach is thus to develop a scaling law of the velocity profile at the orifice exit and its integral parameters that will represent the local interaction of the ZNMF actuator with the incoming grazing boundary layer. Both of these are discussed below.

#### 7.3.1 Lumped Element Modeling-Based Semi-Empirical Model of the External Boundary Layer

##### 7.3.1.1 Definition

As a first model, the LEM technique previously introduced, described, and validated for a ZNMF actuator exhausting into still air is extended to include the effect of a grazing boundary layer. Figure 7-5 shows a typical LEM equivalent circuit representation of a generic ZNMF device interacting with a grazing boundary layer, where the parameters are specified in the acoustic domain (as denoted by the first letter *a* in the subscript). The boundary layer impedance is introduced in series with the orifice impedance, since they share the same volume flow rate  $Q_j$ , the ZNMF actuator exhausting into the grazing boundary layer.

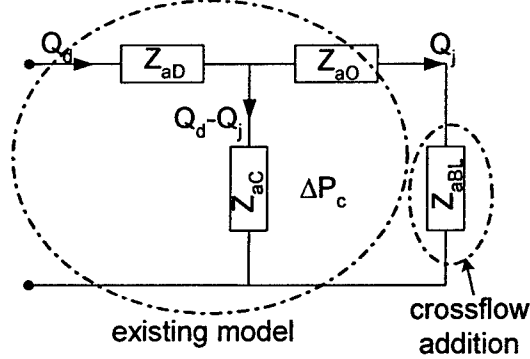


Figure 7-5: LEM equivalent circuit representation of a generic ZNMF device interacting with a grazing boundary layer.

For clarification, each component of the equivalent circuit shown in Figure 7-5 is briefly summarized below. First, the acoustic driver impedance  $Z_{ad}$  is inherently dependant on the dynamics of the utilized driver, although the volumetric flow rate  $Q_d$  that it generates can be generalized to be equal to

$$Q_d = j\omega\Delta\nabla = j\omega S_d W_0 \sin(\omega t). \quad (6-10)$$

The acoustic impedance of the cavity is modeled as an acoustic compliance

$$Z_{ac} = \frac{\Delta P_c}{Q_d - Q_j} = \frac{1}{j\omega C_{ac}}, \quad (6-11)$$

where the cavity acoustic compliance is given by

$$C_{ac} = \frac{V}{\rho c_0^2}. \quad (6-12)$$

Then, the acoustic impedance of the orifice is defined by (see previous Section for details)

$$Z_{ao} = R_{ao,lin} + R_{ao,nl} + j\omega M_{ao}, \quad (6-13)$$

where the linear acoustic resistance  $R_{ao,lin}$  corresponds to the viscous losses in the orifice and is set to be

$$R_{ao,lin} = R_{aN}, \quad (6-14)$$

which takes a different functional form depending on the orifice geometry as described in Section 2. As discussed in Section 2 and in great detail in Section 6, the nonlinear acoustic resistance  $R_{ao,nl}$  represents the nonlinear losses due to the momentum integral and is given by

$$R_{ao,nl} = \frac{0.5\rho K_d Q_j}{S_n^2}, \quad (6-15)$$

where  $K_d$  is the nonlinear pressure drop coefficient that is a function of the orifice shape, Stokes number and jet Reynolds number (see Section 6 for details). Finally, the acoustic orifice mass  $M_{ao}$  groups the effect of the mass loading (or inertia effect)  $M_{aN}$  and that of the acoustic radiation mass  $M_{aRad}$ , such that

$$M_{ao} = M_{aN} + M_{aRad}, \quad (6-16)$$

where again each quantity is a function of the orifice geometry.

The new term is the acoustic boundary layer impedance, which takes the form

$$Z_{aBL} = R_{aBL} + jX_{aBL}, \quad (6-17)$$

where the acoustic resistance  $R_{aBL}$  and reactance  $X_{aBL}$  will be defined further below. The total acoustic impedance of the orifice, including the grazing boundary layer effect is then defined by



$$Z_{aO,t} = Z_{aO} + Z_{aBL} = \frac{\Delta P_c}{Q_j} \quad (6-18)$$

where the boundary layer impedance is in series with the isolated orifice impedance since they share a common flow. Note that in the ZNMF actuator lumped element model, the pressure inside the cavity  $\Delta P_c$  is equal to the pressure drop across the orifice (see discussion on the pressure field in Section 5). Also, the radiation impedance of the orifice is modeled as a circular (rectangular) piston in an infinite baffle for an axisymmetric (rectangular) orifice, and only the mass contribution is taken into account, since at low wavenumbers,  $kd$ , the radiation resistance term is almost negligible (Blackstock 2000, p. 459).

The goal here is to find an analytical expression for the acoustic grazing boundary layer impedance  $Z_{aBL}$  that will capture the main contributions of the grazing boundary layer, i.e. increase the resistance of the orifice and reduce the effective mass oscillating in the orifice. From the dimensionless analysis carried out in Section 2 and in the previous section, a large parameter space has been revealed that should be sampled.

Based on acoustic liner literature, the so-called NASA Langley ZKTL (Betts 2000) is first implemented in the application of a ZNMF device to extract a simple analytical expression. Specifically, the impedance model is derived from the boundary conditions used in the ZKTL impedance model, which finds its origins in the work done by Hersh and Walker (1979), Heidelberg et al. (1980) for the resistance part, and by Rice (1971) and Motsinger and Kraft (1991) for the reactance part of the impedance. With slight modifications and rearrangements discussed below, the model is extended to the present problem to yield the following impedance model in the acoustic domain

$$R_{aBL} = \frac{\rho c_0}{S_n} \frac{M_\infty}{\left(2 + 1.256 \delta/d\right)}, \quad (6-19)$$

for the acoustic resistance part and

$$X_{aBL} = \frac{\rho c_0}{S_n} \frac{1}{C_D} \frac{0.85kd}{1 + 305M_\infty^3}, \quad (6-20)$$

to characterize the acoustic reactance of the grazing impedance. The quantity  $\rho c_0/S_n$  corresponds to the characteristic acoustic impedance of the medium and is used for normalization to express the results in the acoustic domain,  $C_D$  is the orifice discharge coefficient that has been previously introduced, and  $h_0 = 0.96\sqrt{S_n}$  is an orifice end correction. Notice that the original expressions are functions of the porosity factor. However, the resistance part was originally derived from first principles for a single orifice (Hersh and Walker 1979) and then extended to an array of independent orifices (hence perforated plate) via the simple relation

$$Z_{0, \text{perforate}} = \frac{Z_{0, \text{single orifice}}}{\sigma}, \quad (6-21)$$

where the porosity is defined by

$$\sigma = \frac{N_{\text{holes}} \times (\text{hole area})}{\text{total area}}, \quad (6-22)$$

and  $N_{\text{holes}}$  is the number of holes in the perforate. Eq. 6-21 is applicable when assuming that the orifices are not too close to each other in order to alleviate any interactions between them. Ingard (1953) states that the resonators can be treated independently of each other if the distance between the orifices is greater than half of the acoustic wavelength. This statement can be related to the discussion in Section 4 on the influence of the dimensionless stroke length. The porosity factor in the resistance expression can then be disregarded to yield Eq. 6-19. Similarly, the end correction  $0.85[1 - 0.7\sqrt{\sigma}]d$  in the reactance expression is found from Ingard (1953) when perforate plates are used and should be compared with the single orifice end correction  $0.85d$  for a circular orifice. Thus, the acoustic reactance due to the grazing flow effect takes the form of Eq. 6-20.

It is worthwhile to note that the boundary layer model in its present form is primarily a function of the grazing flow Mach number  $M_\infty$ , the ratio between the orifice diameter and the acoustic wavelength  $kd = 2\pi d/\lambda$ , and the ratio of the boundary layer thickness to the orifice diameter  $\delta/d$ , the latter mainly limiting the resistance contribution. Also, the orifice effect is represented by the discharge coefficient  $C_D$  in the reactance expression. Furthermore, it is sometimes useful to denote the specific reactance in terms of the effective length  $h_0$ , such that

$$X_0 = \rho\omega h_0. \quad (6-23)$$

From Eq. 6-20 and Eq. 6-23, it can be seen that when the specific reactance is normalized by the orifice area, it yields the reactance expression in the acoustic domain. The effect of the grazing boundary layer tends to decrease the "no crossflow" orifice effective length  $h_0 = 0.96\sqrt{S_n}$  by the quantity  $C_D(1 + 305M_\infty^3)$ , which is a function of the orifice shape, flow parameters, and freestream Mach number.

Before directly implementing this grazing boundary layer impedance into the full lumped element model of a ZNMF actuator and observing its effect on the device behavior, the model is compared to previous data for flow past Helmholtz resonators in order to validate it.

### 7.3.1.2 Boundary layer impedance implementation in Helmholtz resonators

A large variation in operating conditions for a range of applications is considered. However, in the process of gathering suitable data to compare the impedance model presented above, two main difficulties appeared:

- First, proper documentation of the experimental setup and operating conditions (especially the grazing BL) is often deficient. Therefore, some available experimental databases were not used because one or more variable definitions were lacking.
- Second, since practical applications of acoustic liners often deal with a thin face sheet perforate, the orifice ratio  $h/d$  is usually much less than unity. As seen from the results of modeling of a ZNMF actuator in a quiescent medium, this can yield complex orifice flow patterns and thus represents a limiting case of  $h/d \rightarrow 0$  in the impedance model.

Nonetheless, two datasets from two different publications were found to suit our purpose. The first database comes from the extensive experimental study performed by Hersh and Walker (1979). Only the thick orifice investigation is used here in order to fulfill the model assumption of  $h/d \geq 1$ . The two-microphone impedance test data is summarized herein for the five orifice resonator configurations described in Table 7-2. The complete dataset can be found in Hersh and Walker (1979). It is basically an effort divider, as shown in Figure 7-6.

Table 7-2: Experimental operating conditions from Hersh and Walker (1979).

Resonator model	$D_c (mm)$	$H (mm)$	$d (mm)$	$h (mm)$	$h/d$
1	31.75	12.7	1.78	0.51	0.28
2	"	"	"	1.01	0.57
3	"	"	"	1.03	1.14
4	"	"	"	4.06	2.28
5	"	"	"	8.13	4.56
	$\bar{\sigma} = d^2/D_c^2$	$f (Hz)$	$T_\infty (K)$	$P_\infty (kPa)$	$\delta/d$
1	0.003	552	292.04	101.93	4.8
2	"	530	295.93	101.83	"
3	"	414	292.04	100.07	"
4	"	333	297.04	101.93	"
5	"	255	296.48	101.93	"

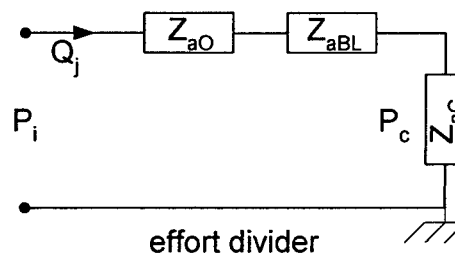


Figure 7-6: Schematic of an effort divider diagram for a Helmholtz resonator.

The data is presented for different values of incident pressure  $P_i$  and grazing flow velocity  $U_\infty$  in terms of the total resonator area-averaged specific resistance and reactance normalized by the specific medium impedance, respectively  $R_0/\rho c_0$  and  $X_0/\rho c_0$ . The resistance and reactance were computed by measuring the amplitude of the incident  $P_i$  and cavity  $P_c$  sound waves, and also by measuring the phase difference between the incident sound field and the cavity sound field  $\phi_{ic}$ . These values are substituted into Eqs. 6-24 and 6-26 given below, respectively, for the resistance and reactance

$$\frac{R_0}{\rho c_0} = \bar{\sigma} \left[ 10^{\frac{\text{SPL}(i) - \text{SPL}(c)}{20}} \right] \frac{\sin \phi_{ic}}{\sin(\omega H/c_0)}, \quad (6-24)$$

following the effort divider depicted in Figure 7-6,

$$\frac{R_0}{\rho c_0} = \text{Re} \left\{ Z_{nC} \left( \frac{P_c}{P_i} \right)^{-1} \right\} = \text{Re} \left\{ Z_{nC} \left( \frac{Z_{aC}}{Z_{aO} + Z_{aBL} + Z_{aC}} \right)^{-1} \right\}, \quad (6-25)$$

and

$$\frac{X_0}{\rho c_0} = \bar{\sigma} \left[ 10^{\frac{\text{SPL}(i) - \text{SPL}(c)}{20}} \right] \frac{\cos \phi_{ic}}{\sin(\omega H/c_0)}, \quad (6-26)$$

where  $\text{SPL}(i) - \text{SPL}(c)$  represents the sound pressure level difference (in dB) between the incident sound field and the cavity sound field,  $H$  is the cavity depth of the resonator,  $\bar{\sigma} = S_n/S_c$  is an averaged area (ratio of the orifice-to-cavity cross sectional area), and  $Z_{nC}$  is the area-averaged normalized acoustic cavity impedance such that

$$Z_{nC} = Z_{aC} \left( \frac{S_n}{\rho c_0} \right) \bar{\sigma}, \quad (6-27)$$

$S_n/\rho c_0$  being the characteristic impedance of the medium in the acoustic domain.

For each resonator tested, the frequency was adjusted to achieve resonance at  $P_i = 70 \text{ dB}$  and  $U_\infty = 0$ , by seeking the frequency for which the phase difference between the incident and cavity sound pressure fields were  $90^\circ$ . The results presented hereafter are from the five orifice models as listed in Table 7-2. The normalized area-averaged impedance, defined by  $\zeta = \theta + j\chi$  for a single orifice, as a function of the grazing flow Mach number are plotted in Figure 7-7A to Figure 7-7E. Specifically, the total specific resistance  $R_0$  of the resonator is normalized by the characteristic impedance of the

medium  $\rho c_0$ , and the cavity reactance is subtracted from the total resonator reactance such that

$$\frac{X_0}{\rho c_0} = \frac{X_{0o,t}}{\rho c_0} + \frac{X_{0c}}{\rho c_0} = \frac{X_{0o,t}}{\rho c_0} - \bar{\sigma} \cot\left(\frac{\omega H}{c_0}\right), \quad (6-28)$$

where  $X_{0o}$  is the specific orifice reactance that includes the inertia effect and the BL contribution,

$$\frac{X_{0c}}{\rho c_0} = -\bar{\sigma} \cot(kH) \quad (6-29)$$

is the normalized specific reactance of the cavity, and  $k = \omega/c_0$  is the wavenumber. Notice that Eq. 6-29 is similar to the definition of the acoustic cavity impedance  $Z_{ac}$  given by Eqs. 6-11 and 6-12, since for  $kH \ll 1$  the Maclaurin series expansion of the cotangent function can be truncated to its first term, such that

$$\frac{X_{0c}}{\rho c_0} = -\bar{\sigma} \cot(kH) = -\bar{\sigma} \left( kH + \frac{k^3 H^3}{3} - \dots \right)^{-1} \approx -\bar{\sigma} \frac{c_0}{\omega H}, \quad (6-30)$$

and the normalized acoustic cavity impedance is given by

$$\frac{Z_{ac} S_n}{\rho c_0} = \frac{\rho c_0^2}{j\omega \nabla} \left( \frac{S_n}{\rho c_0} \right) = \frac{c_0}{j\omega H S_c} S_n = \frac{c_0}{j\omega H} \bar{\sigma} = j \frac{X_{0c}}{\rho c_0}, \quad (6-31)$$

where  $S_c = \nabla/H$  is the cross sectional area of the cavity.

Clearly, the resistance is well captured, although the experimental data suggest a nonlinear increase with the grazing flow Mach number. The resistance tends to not vary for very low Mach numbers but increases after a threshold in the Mach number is reached, and this is true for all models with different orifice aspect ratio  $h/d$ . It also appears that the effect of the incident pressure is primarily felt for low Mach numbers and tends to saturate for higher values.

With regards to the reactance, the data are consistently overpredicted by the model and start in the positive axis for the no flow condition, but the trend of a nearly constant value with a slight decrease for higher Mach numbers is well captured. Also, the reactance model is insensitive to the incident pressure amplitude. Note that although no information was provided in Hersh and Walker (1979) about the grazing flow boundary layer for the different Mach number tested, it was assumed that the boundary layer thickness was held constant from the nominal case such that  $\delta = 7.62 \text{ mm}$  for all tests.

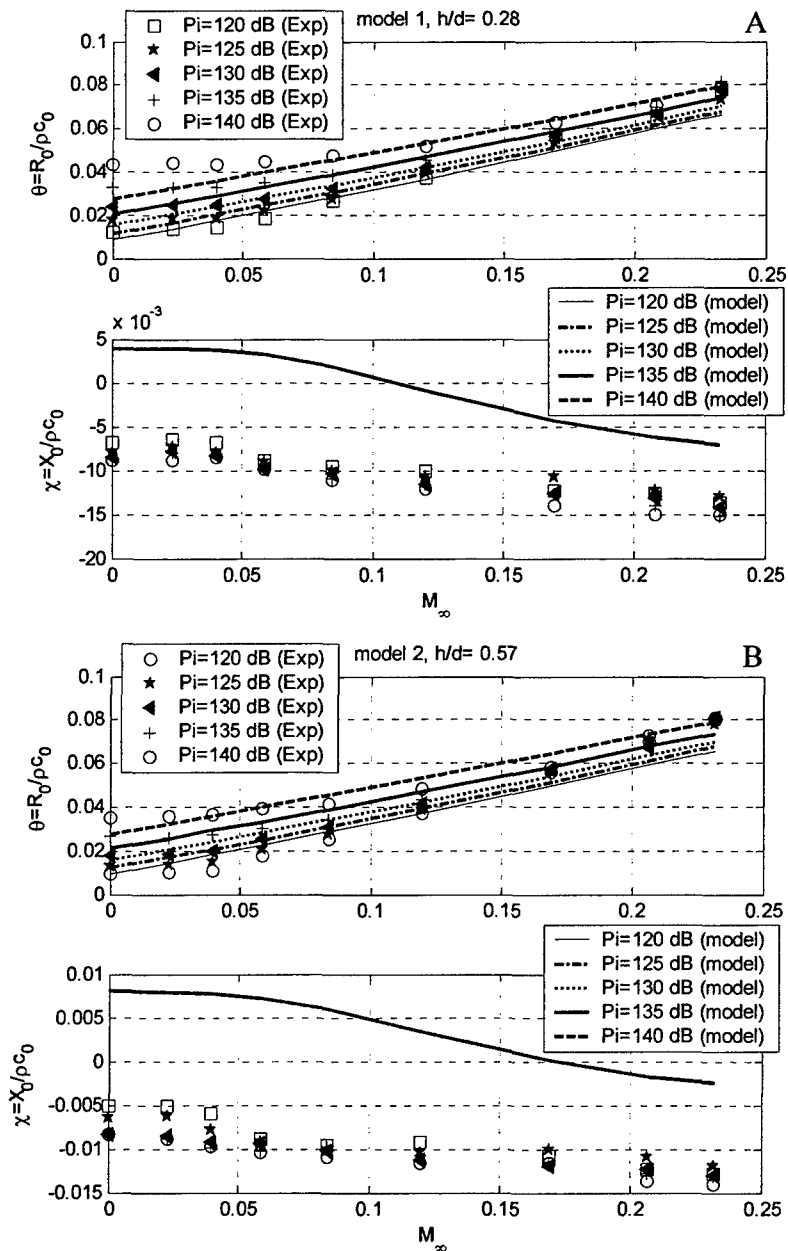


Figure 7-7: Comparison between BL impedance model and experiments from Hersh and Walker (1979) as a function of Mach number for different SPL. The Helmholtz resonators refer to Table 7-2: A) Resonator model 1. B) Resonator model 2. C) Resonator model 3. D) Resonator model 4. E) Resonator model 5.

C

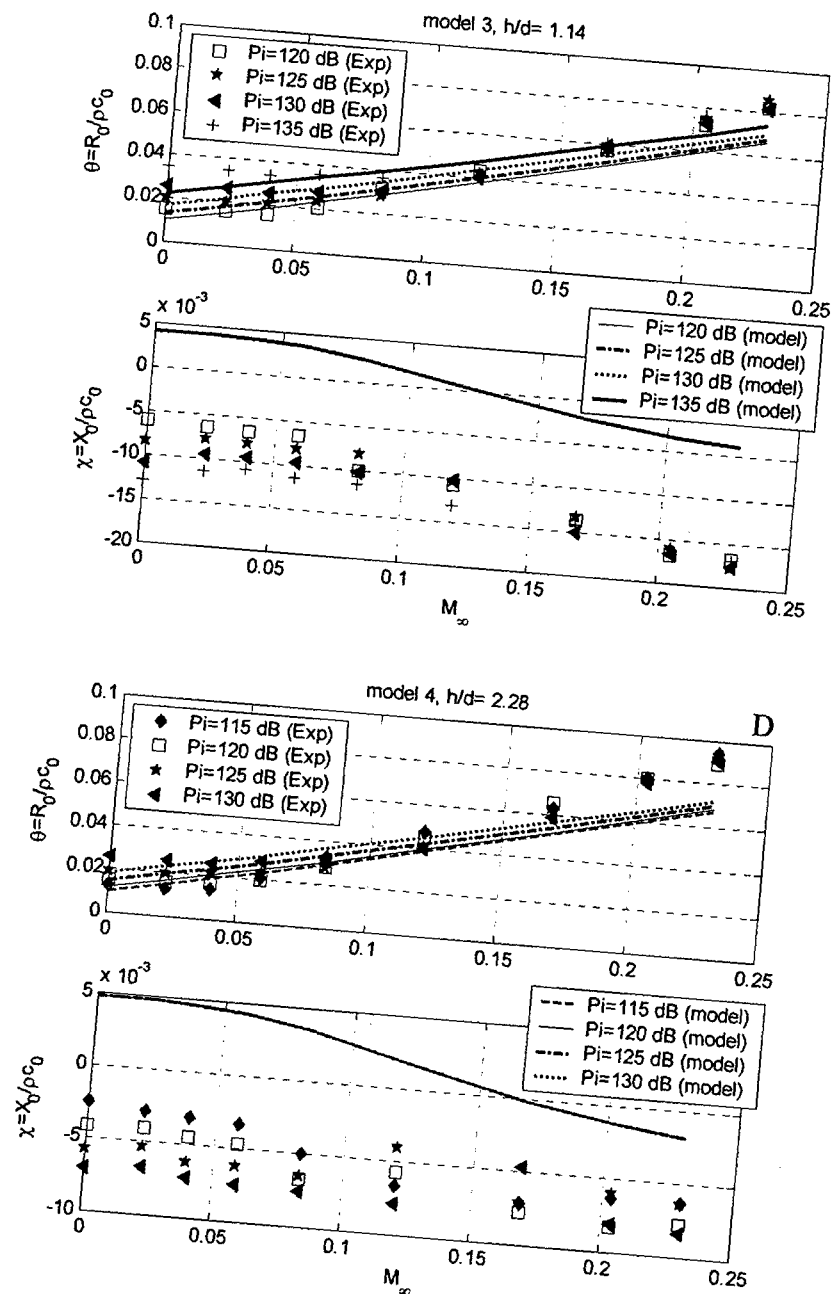


Figure 7-7: Continued.

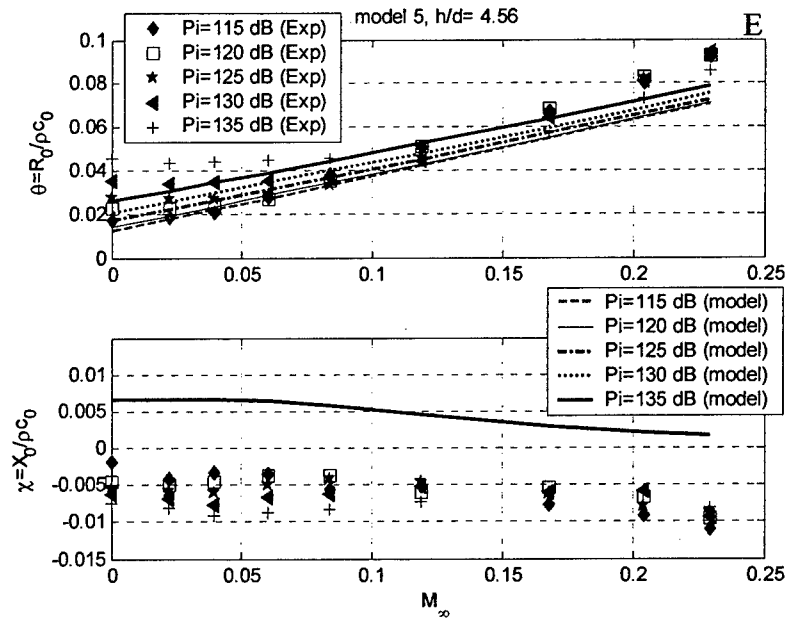


Figure 7-7: Continued.

Another suitable experimental dataset is that of Jing et al. (2001). Their set up is shown in Figure 7-8, and Table 7-3 summarizes the test conditions and device geometry. A grazing flow of Mach number varying from 0 to 0.15 was introduced through a square-section wind tunnel of internal width 120.0 mm. A boundary layer survey was performed using a Pitot-static tube and they show that the profile agrees with the well-known one-seventh order power law for a turbulent boundary layer. The amplitudes of the sound pressures measured by the two microphone method and their phase difference were then utilized to compute the acoustic impedance of the tested sample in a similar manner as presented above.

Table 7-3: Experimental operating conditions from Jing et al. (2001).

$d$ (mm)	$h$ (mm)	$D_c$ (mm)	$H$ (mm)	$\sigma$ (%)	$f$ (Hz)	$\delta$ (mm)
3	2	32	150	2.94	200	30



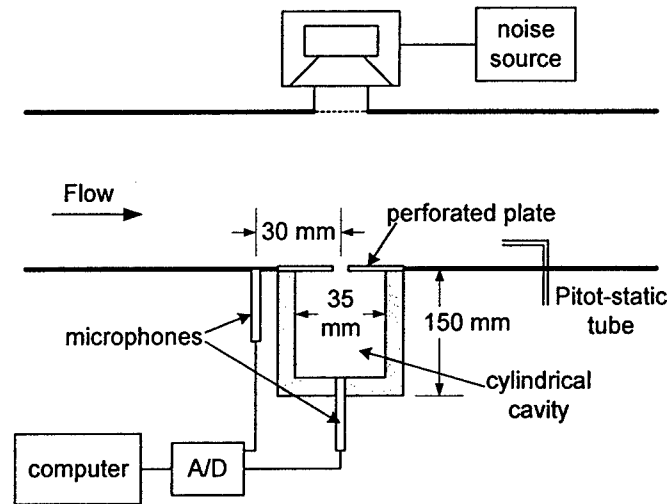


Figure 7-8: Experimental setup used in Jing et al. (2001). (Arranged from Jing et al. 2001)

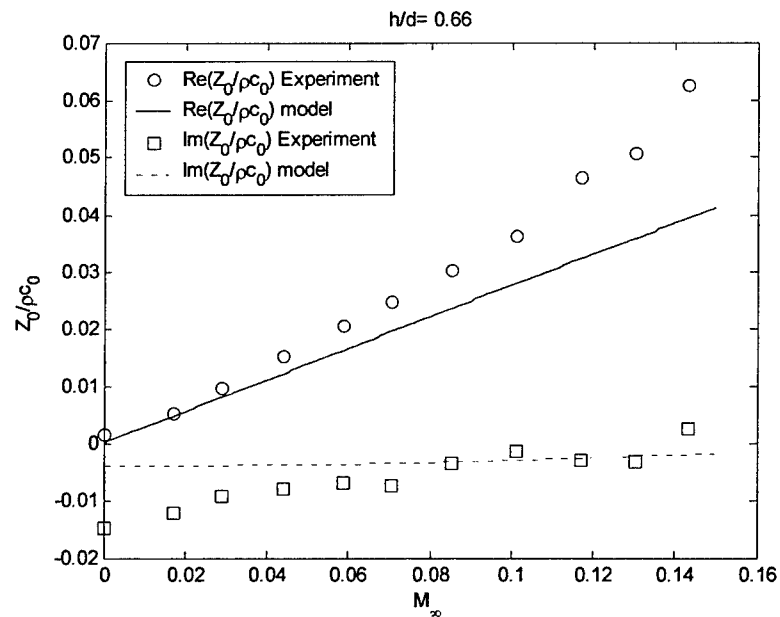


Figure 7-9: Comparison between model and experiments from Jing et al. (2001). The resonator design refers to Table 7-3.

Figure 7-9 compares the present model with the experimental data from Jing et al. (2001), where the normalized impedance is plotted as a function of the grazing flow Mach number. As in the previous example, the resistance model agrees with the experimental data for low Mach numbers, while the overall reactance trend is captured as well (nearly constant value as the Mach number increases). However, the resistance data do not follow the same trend as in the previous example, since no plateau in the resistance curve is observed in the low Mach number region for the data from Jing et al. (2001).

It should be pointed out, however, that all these experimental data should be regarded with some skepticism. They rely on the two microphone impedance technique (Dean 1974) and no uncertainty estimates are provided. Also, good reactance data are more difficult to obtain than resistance data, since the method principally relies on the phase difference knowledge which, for instance, can be systematically altered by instrumentation equipment data acquisition hardware and hydrodynamic effects in the cavity. Also, the data were usually acquired when the device was operating near resonance, when the radiated sound pattern can clearly extend to several orifice diameters away from the resonator (typically, at resonance a Helmholtz resonator scattering cross sectional area scales with the wavelength squared), hence resulting in a different acoustic mass near the orifice exit. Proper placement of the microphone near the orifice is therefore of great importance in order to retrieve the correct mass due to the end correction. As generally concluded by the acoustic liner community, more accurate calculations of the variation of the resonator resistance and reactance could only be made if more flow details in the vicinity of the orifice are known.

Nevertheless, it should be emphasized that the goal of this exercise was not to validate the grazing flow impedance model via available experimental data, since at the present time no one has been able to accomplish this goal. The validation of low-order models for flow past Helmholtz resonators is not the focus of this research. However, the above discussion improves our understanding of the BL impedance model in its present form and gives us some confidence in its use, while keeping in mind its limitations and shortcomings.

#### **7.3.1.3 Boundary layer impedance implementation in ZNMF actuator**

In order to fully appreciate the effect of the key parameters present in the BL impedance model, such as the Mach number  $M_\infty$ , the boundary layer thickness to orifice length ratio  $\delta/d$ , or  $kd$ , on the frequency response of a ZNMF actuator, the synthetic jet design used in the NASA Langley workshop (CFDVal 2004) and denoted as Case 1 is modeled and employed. In a similar way, the actuator designed by Gallas et al. (2003a) and referred therein as Case 1 is also used, since the two resonant peaks that characterize their dynamic behavior are reversed. In particular, in Case 1 (CFDVal 2004) the first peak is due to the natural frequency of the diaphragm while the second one is governed by the Helmholtz frequency of the resonator, while the opposite is true in Case 1 from Gallas et al. (2003a). The first peak is dictated by the Helmholtz frequency while the second peak corresponds to the piezoelectric-diaphragm natural frequency. The reader is referred to the discussion in Section 5 on the cavity compressibility effect, where a similar comparison between these two cases has already been performed; this discussion gives a clear definition of the different governing frequencies of the system and their respective effects.

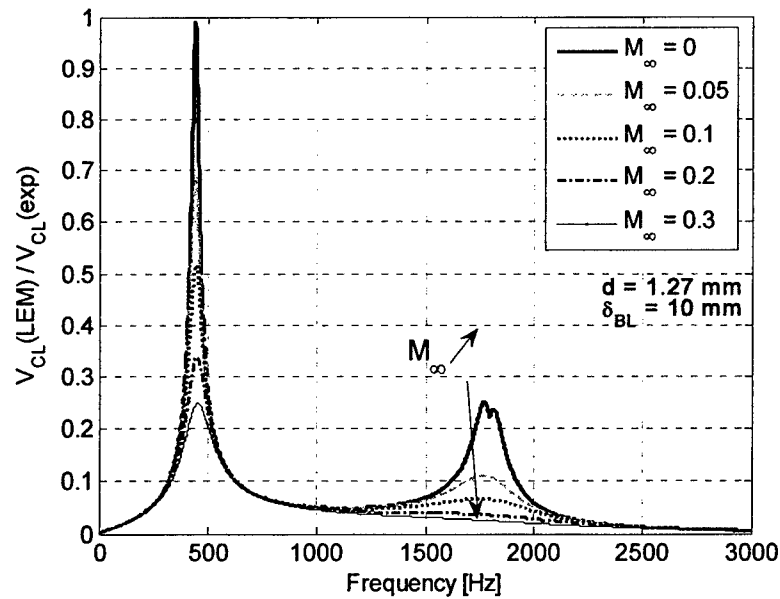


Figure 7-10: Effect of the freestream Mach number on the frequency response of the ZNMF design from Case 1 (CFDVal 2004) using the refined LEM. The centerline velocity is normalized by the experimental data at the actuation frequency.

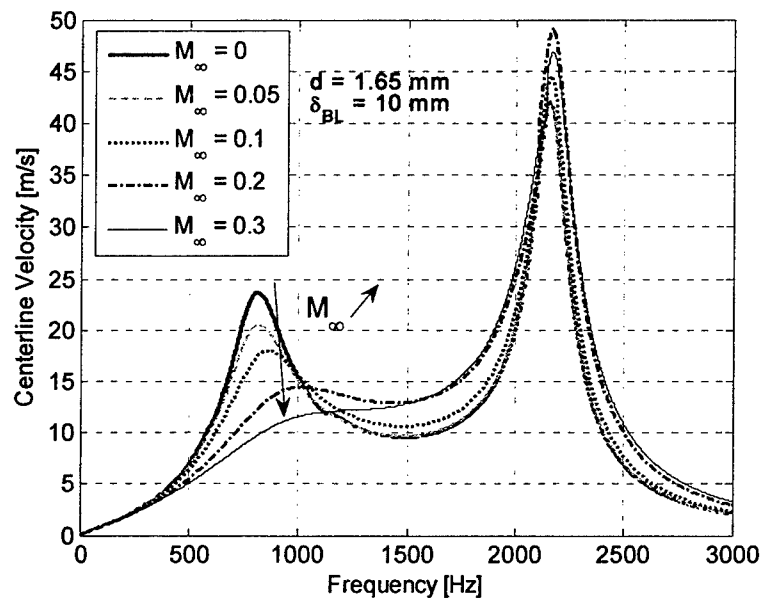


Figure 7-11: Effect of the freestream Mach number on the frequency response of the ZNMF design from Case 1 (Gallas et al. 2003a).

Figure 7-10 shows the effect of varying the freestream Mach number  $M_\infty$  on the centerline velocity of the actuator versus frequency for the Case 1 (CFDVal 2004) design,

while Figure 7-11 is for the Case 1 (Gallas et al. 2003a) design. The incoming grazing flow is assumed to be characterized by a boundary layer  $\delta = 10\text{ mm}$  and a freestream Mach number ranging from 0 to 0.3.

Clearly, the effect of the freestream Mach number is principally experienced at the Helmholtz frequency peak, while a global decrease in magnitude is still seen over the entire frequency range due to the increase in the total orifice resistance. Recalling the definition of the Helmholtz frequency, the shift in frequency of the peak is explained by the modification of the acoustic mass by the boundary layer or, more specifically, by the decrease of the effective orifice length  $h_0$ . Since  $M_{aBL}$  and  $M_{aO}$  are weak functions of the grazing flow parameters (only  $M_\infty$ ), the Helmholtz frequency that strongly depends of the acoustic masses in the system will therefore be only slightly affected by the external BL. Hence, the cavity compressibility criterion described in Section 5 should not be greatly affected and can be generalized to a ZNMF actuator with an external boundary layer. Also, letting the ratio  $\delta/d$  vary will affect the overall magnitude of the device response since it is present in the acoustic BL resistance expression, although it will not affect the location of the frequency peaks since the acoustic BL mass expression does not contain the ratio  $\delta/d$ .

### 7.3.2 Velocity Profile Scaling Laws

Despite the power of LEM that resides in its simplicity and reasonable estimate (typically within  $\pm 20\%$ ) achieved with minimal effort, it unfortunately does not provide any information on the profile or shape of the jet exit velocity which is also strongly phase dependant as seen in Section 4. In this regard, a low-dimensional model or description of the jet velocity shape is needed, i.e. a parameterization of the profile in terms of the key parameters that capture the important dynamic and kinematic features of the orifice flow, as well as scaling laws that relate these parameters to the other flow variables. In the first section of this section, it is proposed that the successive moments and skewness of the jet velocity profile can be useful in characterizing ZNMF actuators. However, dimensional analysis revealed a large parameter space (see Eq. 6-8). To be applicable, some restrictions need to be employed since a candidate jet profile should be low dimensional and also capable of reasonably matching the observed and measured jet profile characteristics. Therefore, as a first step, a Blasius boundary layer is assumed to characterize the incoming grazing flow that reduces the parameter space to

$$\left. \begin{matrix} C_{\phi_2}^n \\ X_{\phi_2} \end{matrix} \right\} = f\left( \frac{\omega}{\omega_H}, \frac{h}{d}, \frac{w}{d}, \frac{\omega}{\omega_d}, \frac{\Delta V}{d^3}, S, \text{Re}_\theta, \frac{\theta}{d} \right). \quad (6-32)$$

Two approaches are described next that yield two different scaling laws of a ZNMF actuator issuing into a grazing boundary layer. One focuses on fitting the velocity profile  $v(x,t)$  at the actuator exit, while the other one employs a model based on the local integral parameters of the actuator, such as the successive moments  $C_{\phi_2}^n$  and skewness  $X_{\phi_2}$ , as shown in Figure 7-12.

Table 7-4: Tests cases from numerical simulations used in the development of the velocity profiles scaling laws

Case	$h/d$	$\theta/d$	$S$	$Re_j$	$Re_\theta$	$\bar{V}_j/U_\infty$	$W/d$	$H/d$	$W_0/d$
I	1	0.266	20	188	133	0.375	3	1.5	0.393
II	1	0.266	20	281	133	0.563	3	1.5	0.393
III	1	0.266	20	375	133	0.75	3	1.5	0.393
IV	1	0.133	20	188	133	0.188	3	1.5	0.393
V	1	0.399	20	62	133	0.188	3	1.5	0.393
VI	1	0.532	20	47	133	0.188	3	1.5	0.393
VII	1	0.266	20	24	33	0.188	3	1.5	0.393
VIII	1	0.266	20	47	66	0.188	3	1.5	0.393
IX	1	0.266	20	188	266	0.188	3	1.5	0.393
X	1	0.266	5	94	133	0.188	3	1.5	0.393
XI	1	0.266	10	94	133	0.188	3	1.5	0.393
XII*	1	0.266	20	94	133	0.188	4	1.5	0.393
XIII	1	0.266	50	94	133	0.188	3	1.5	0.393

\* Nominal / Test case

To develop these scaling laws, numerical simulations from the George Washington University, courtesy of Prof. Mittal, are again used in a joint effort. The 2D numerical simulations are employed to construct the test matrix given in Table 7-4. It consists of 13 cases, all based on a nominal flow condition (Case XII), 4 flow parameters being systematically varied around the nominal case. In Cases I to III, the ratio  $\bar{V}_j/U_\infty$  is varied from about 0.2 to 0.75. Case IV to Case VI vary  $\theta/d$ , whereas in Cases VII to IX the jet Reynolds number is varied. Finally the Stokes number is varied in Cases X to XIII.

The velocity profile scaling laws are next detailed. For both approaches, the idea is to first assume a candidate jet velocity profile and, based on the test matrix comprised of CFD simulation results (summarized in Table 7-4), the candidate jet velocity profile is refined, and a regression analysis is then performed to yield a scaling law that predicts either the velocity profile or the integral parameters as a function of the main dimensionless numbers. The candidate profile is adapted from Rampugoon (2001) who performed a similar study on modeling the velocity profile of ZNMF actuator exhausting in an external crossflow (his motivation was to try to match the integral parameters of his test cases). He assumed a candidate velocity profile of the form

$$V_j(\bar{x}, t) = |T(\bar{x})| \sin(\omega t), \quad (6-33)$$

where  $\bar{x} = 2x/d$  is the normalized spatial coordinate across the orifice. However, his chosen profile  $T(\bar{x})$  was just a parabolic-type profile of steady channel flow. Here, this

work is extended to a more general approach, where the choice of  $T(\bar{x})$  is motivated by the results of the investigation outlined in Section 4 on the 2D slot flow physics of a ZNMF actuator in a quiescent medium. It takes the form

$$T(\bar{x}) = \left\{ 1 - \frac{\cosh(\bar{x} S/2 \sqrt{-j})}{\cosh(S/2 \sqrt{-j})} \right\}, \quad (6-34)$$

which satisfies the no-slip condition at the orifice walls and is already Stokes-number dependant in accordance with pressure-driven oscillatory flow in a channel (White 1991). Each scaling law is now detailed.

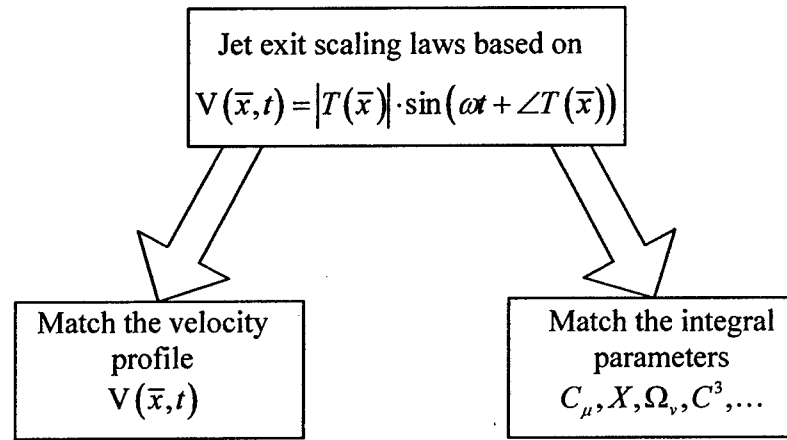


Figure 7-12: Schematic of the two approaches used to develop the scaling laws from the jet exit velocity profile.

### 7.3.2.1 Scaling law based on the jet exit velocity profile

This approach focuses on the shape of the velocity profile at the actuator orifice exit, as a function of the phase angle. The methodology to develop a scaling law is summarized in Figure 7-13 and is comprised of 5 steps.

In the first step, a candidate velocity profile is chosen, as detailed above. Next, since the velocity profile is sinusoidal in nature, it can be simply decomposed by a dc component – equivalent to an average – plus a magnitude and phase angle components, such that

$$V_{decomp}(\bar{x}, t) = V_{dc}(\bar{x}) + V_{mag}(\bar{x}) \cdot \sin(\omega t + V_{arg}(\bar{x})). \quad (6-35)$$

Then, based on the candidate jet velocity profile  $T(\bar{x}, t)$ , the local average (dc), magnitude, and phase angle are extracted from the CFD results, and a nonlinear least-squares curve fit is performed to yield a corrected candidate velocity profile,  $T_{mod}(\bar{x}, t)$  for each component.

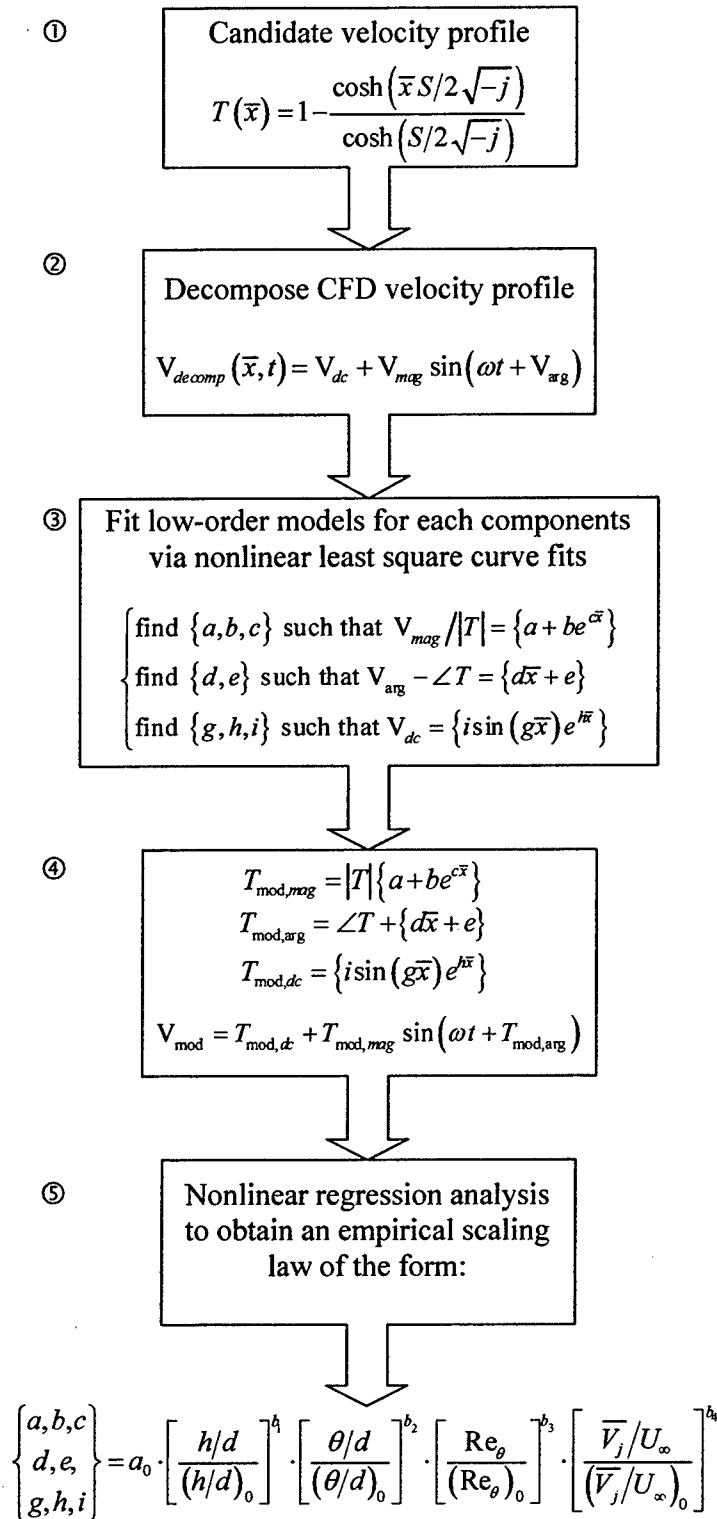


Figure 7-13: Methodology for the development of the velocity profile based scaling law.

The results are shown in Figure 7-14, Figure 7-15, Figure 7-16, Figure 7-17, Figure 7-18, Figure 7-19, and Figure 7-20 for Case I, Case III, Case V, Case VII, Case IX, Case XI, and Case XIII, respectively; Table 7-5 summarizes the value that all 8 coefficients take for each test case. For each figure, the comparison between the candidate velocity profile  $T(\bar{x}, t)$ , decomposed into its magnitude  $|T|$  and argument  $\angle T$ , is compared with the equivalent model ( $T_{\text{mod}, \text{mag}}$  and  $T_{\text{mod}, \text{arg}}$ , respectively) and the CFD data. The choice of the three models, namely

$$\begin{cases} T_{\text{mod}, \text{mag}} = |T| \{a + b e^{c\bar{x}}\} \\ T_{\text{mod}, \text{arg}} = \angle T + \{d\bar{x} + e\} \\ T_{\text{mod}, \text{dc}} = \{i \sin(g\bar{x}) e^{h\bar{x}}\} \end{cases} \quad (6-36)$$

is motivated so that it yields the "best fit" for all cases studied. For instance, the ratio of the amplitudes,  $V_{\text{mag}}/|T|$ , has usually large gradients near the edge of the orifice but remains quite "flat" in the center. Similarly, it is found that the phase difference  $V_{\text{arg}} - \angle T$  varies linearly over the slot depth. Finally, notice that the dc value of the decomposed velocity profile, which can be thought of as the velocity average across the orifice, is usually an order of magnitude less than the amplitude value and has a sinusoidal-type shape. Although not perfect, the modeled profiles are in agreement with the CFD data.



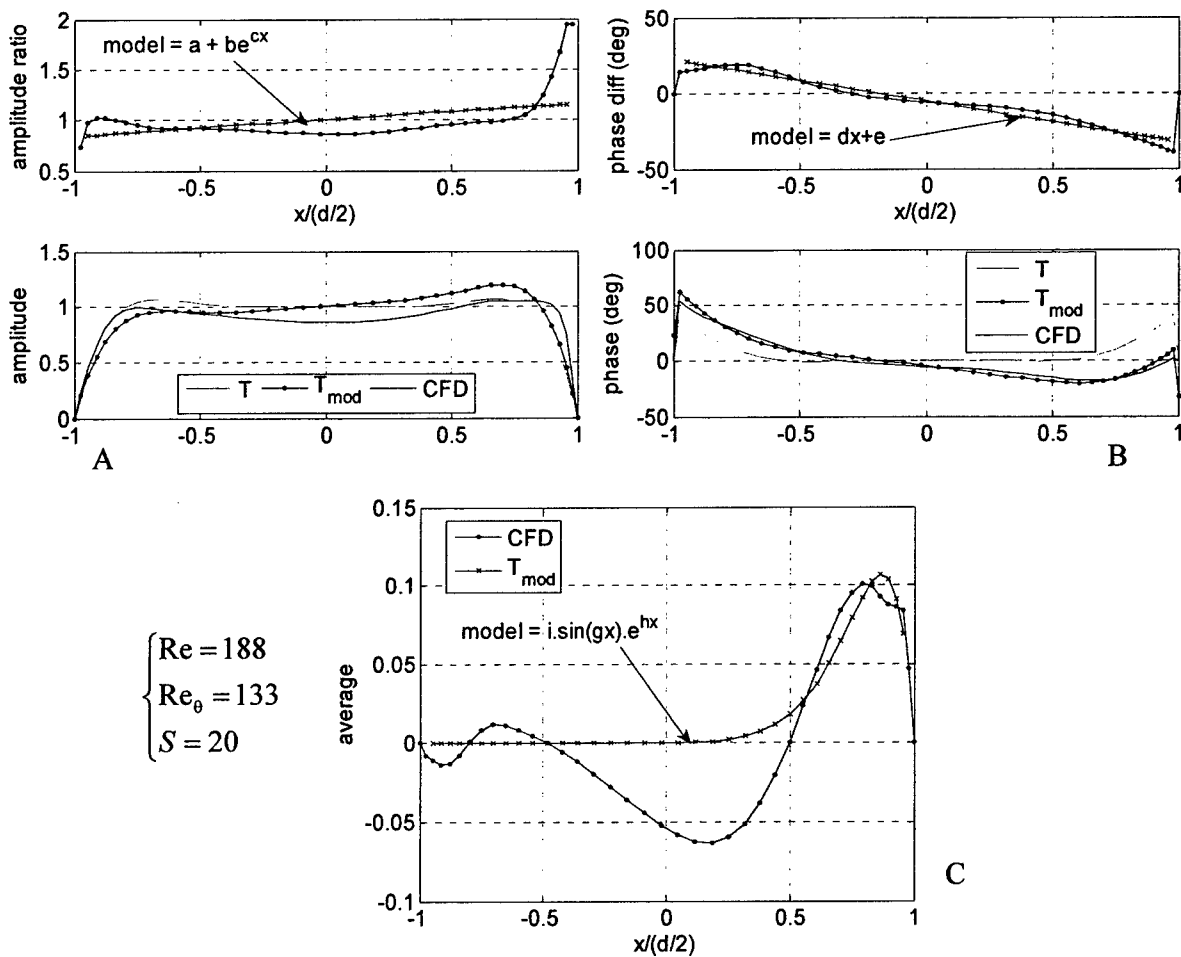


Figure 7-14: Nonlinear least square curve fit on the decomposed jet velocity profile for Case I. A) Amplitude. B) Phase angle. C) dc components. The blue curves are for the components of the candidate profile  $T(\bar{x}, t)$ ; the green curves are for the components of the modeled profile  $T_{mod}(\bar{x}, t)$ ; the red curves are the CFD results.

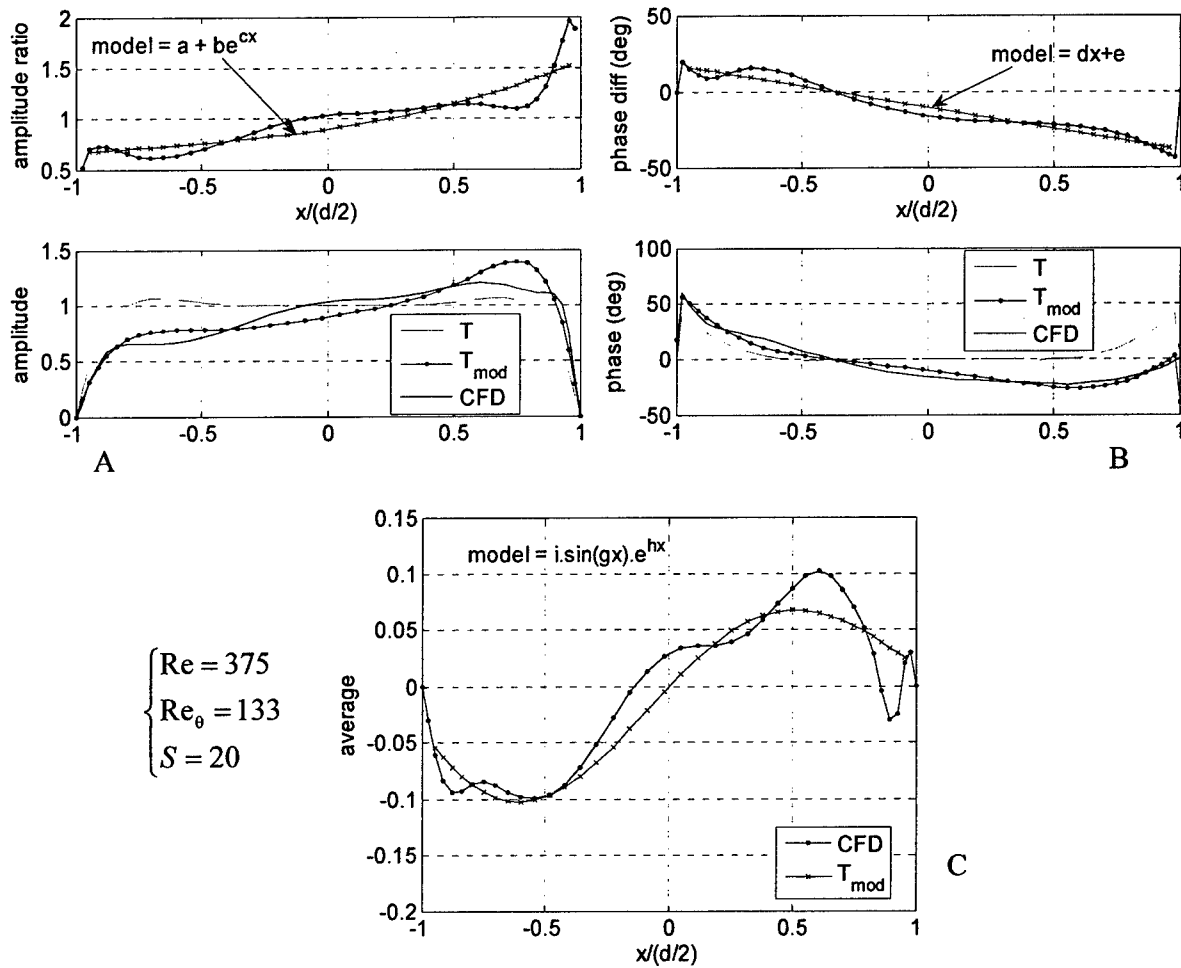


Figure 7-15: Nonlinear least square curve fit on the decomposed jet velocity profile for Case III. A) Amplitude. B) Phase angle. C) dc components. The blue curves are for the components of the candidate profile  $T(\bar{x}, t)$ ; the green curves are for the components of the modeled profile  $T_{\text{mod}}(\bar{x}, t)$ ; the red curves are the CFD results.

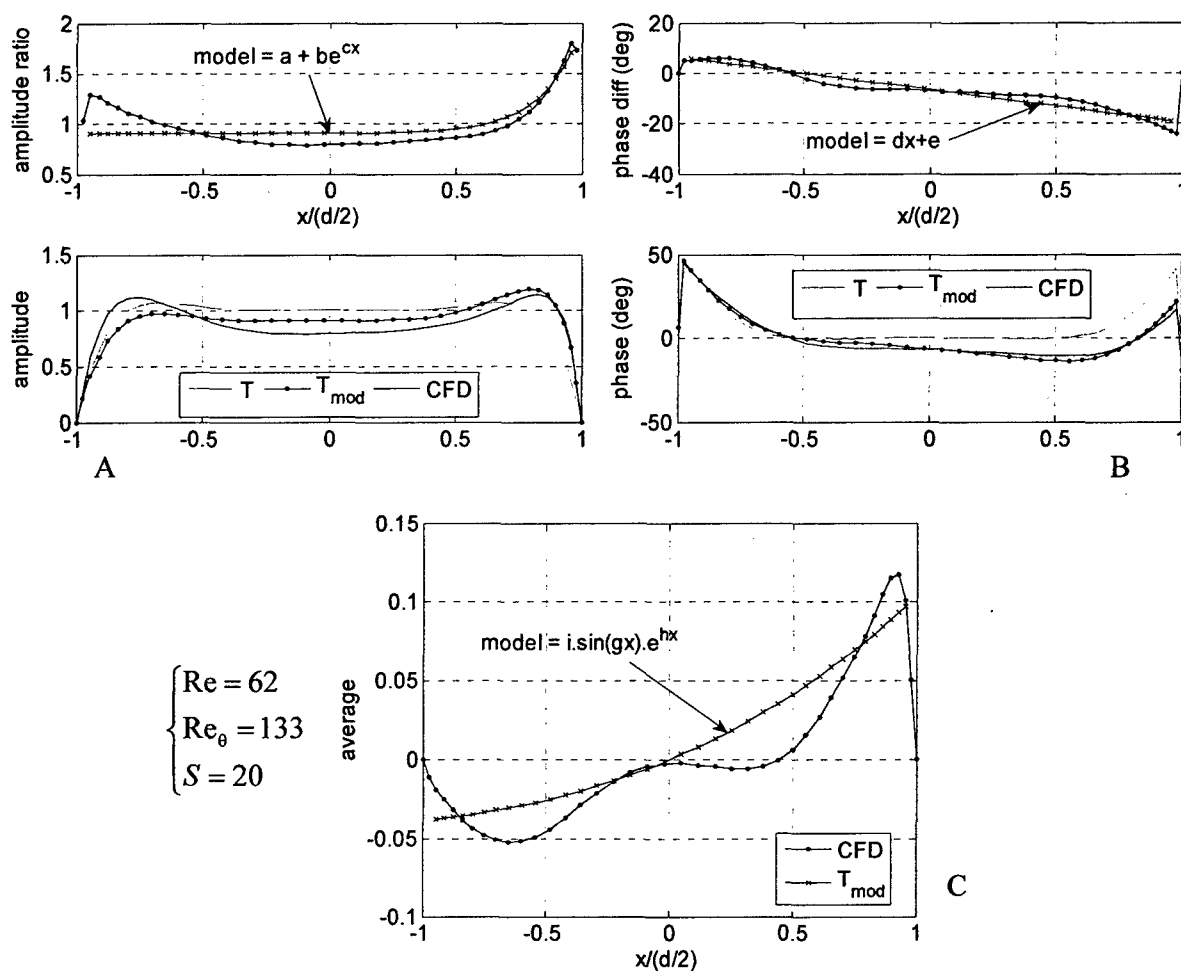


Figure 7-16: Nonlinear least square curve fit on the decomposed jet velocity profile for Case V. A) Amplitude. B) Phase angle. C) dc components. The blue curves are for the components of the candidate profile  $T(\bar{x}, t)$ ; the green curves are for the components of the modeled profile  $T_{\text{mod}}(\bar{x}, t)$ ; the red curves are the CFD results.

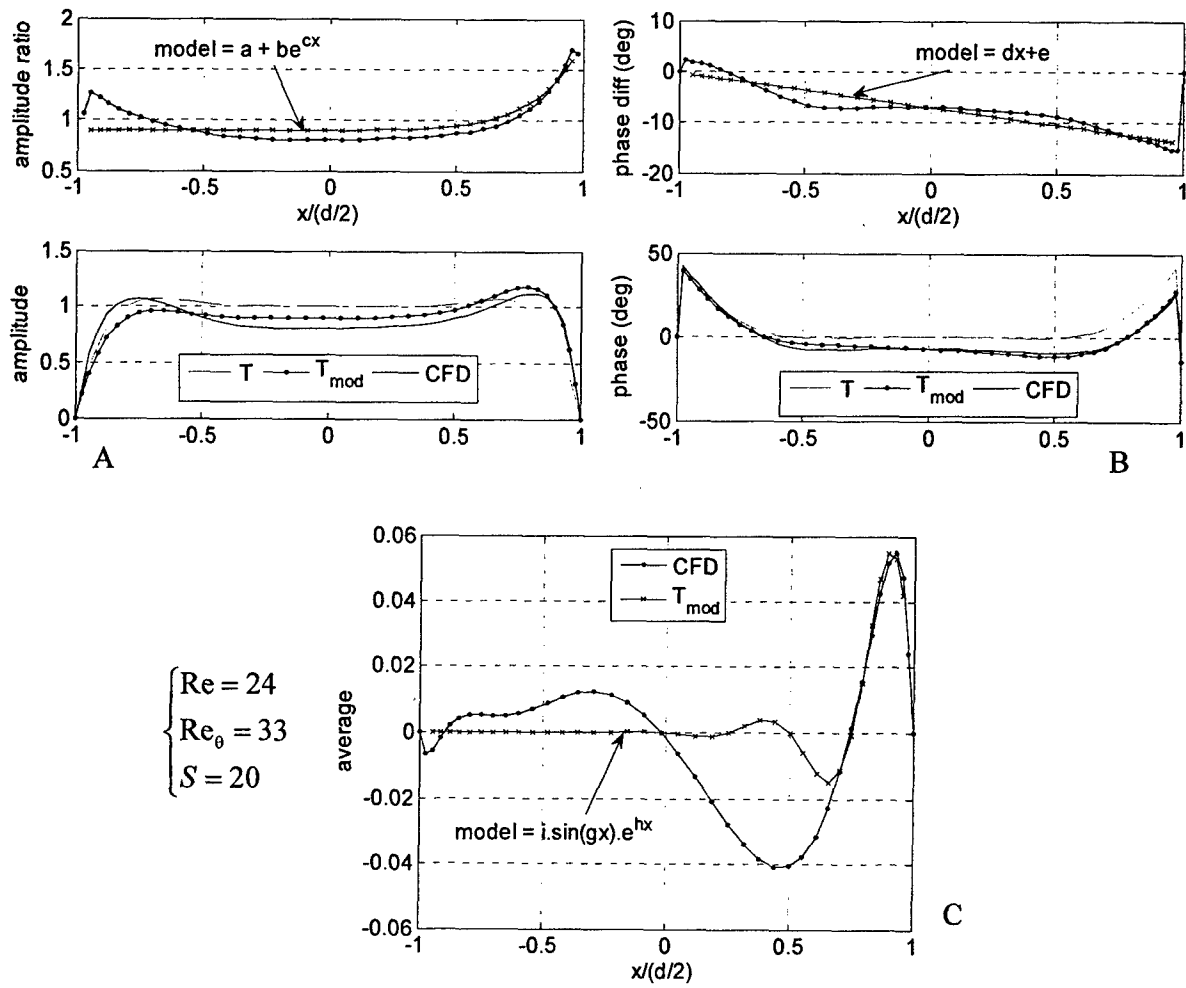


Figure 7-17: Nonlinear least square curve fit on the decomposed jet velocity profile for Case VII. A) Amplitude. B) Phase angle. C) dc components. The blue curves are for the components of the candidate profile  $T(\bar{x}, t)$ ; the green curves are for the components of the modeled profile  $T_{\text{mod}}(\bar{x}, t)$ ; the red curves are the CFD results.

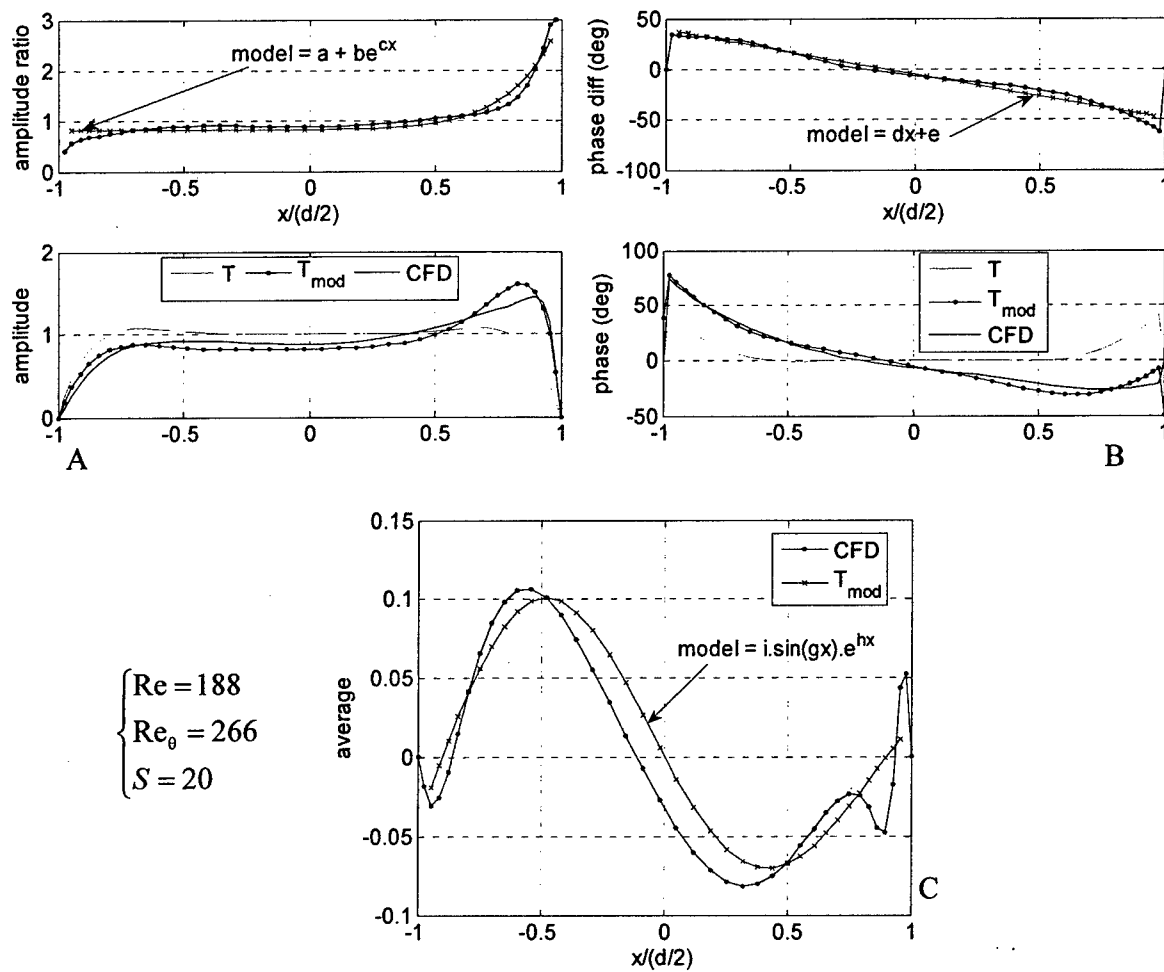


Figure 7-18: Nonlinear least square curve fit on the decomposed jet velocity profile for Case IX. A) Amplitude. B) Phase angle. C) dc components. The blue curves are for the components of the candidate profile  $T(\bar{x}, t)$ ; the green curves are for the components of the modeled profile  $T_{\text{mod}}(\bar{x}, t)$ ; the red curves are the CFD results.

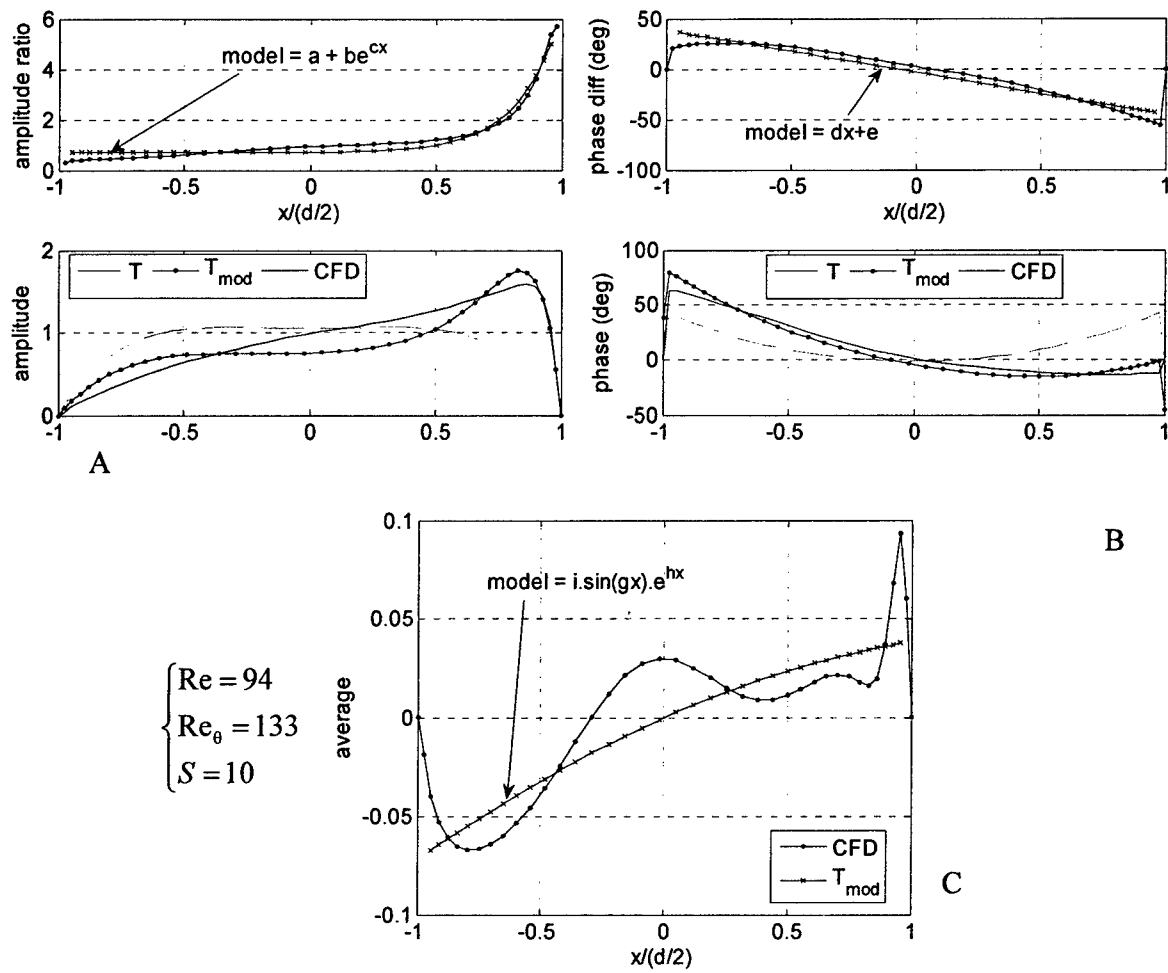


Figure 7-19: Nonlinear least square curve fit on the decomposed jet velocity profile for Case XI. A) Amplitude. B) Phase angle. C) dc components. The blue curves are for the components of the candidate profile  $T(\bar{x}, t)$ ; the green curves are for the components of the modeled profile  $T_{\text{mod}}(\bar{x}, t)$ ; the red curves are the CFD results.

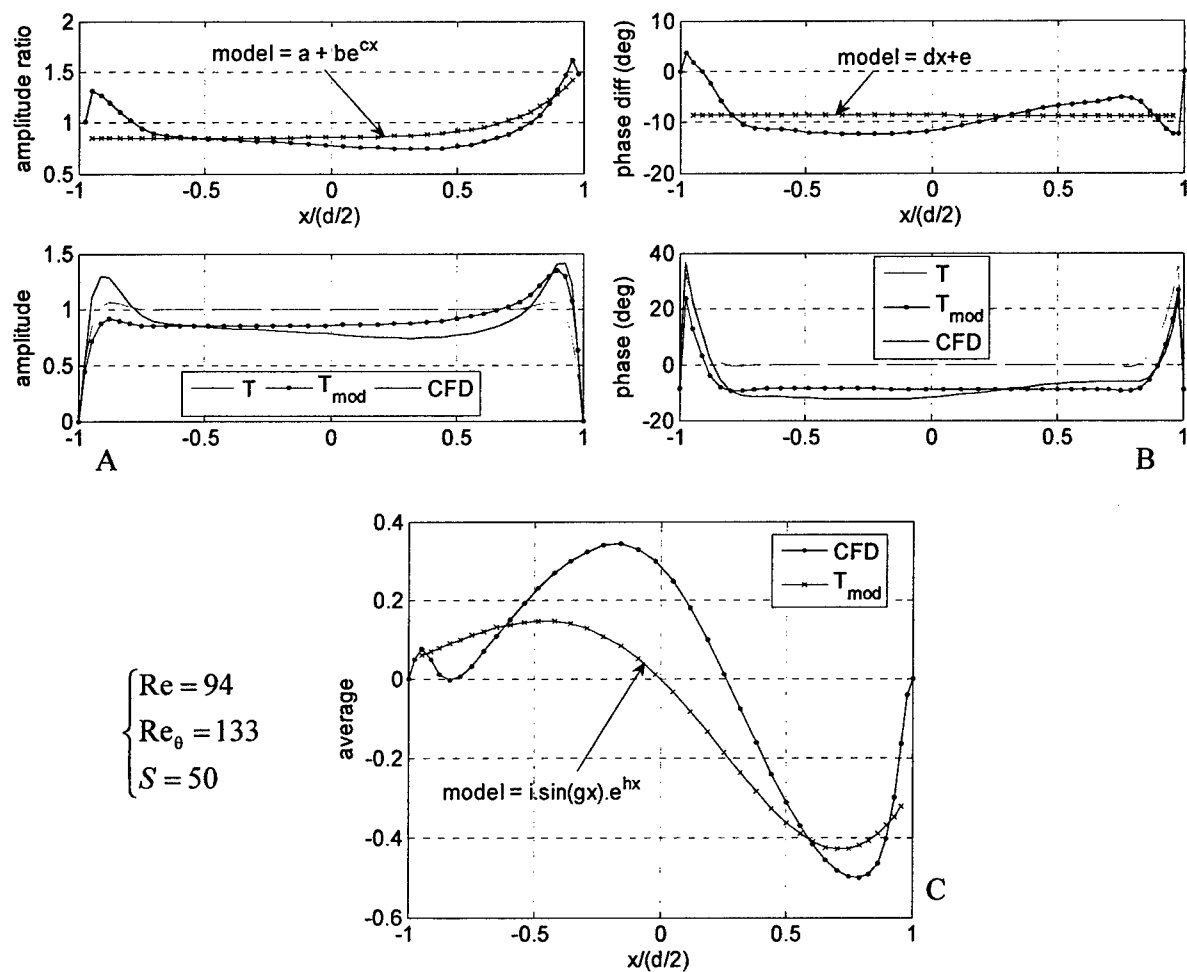


Figure 7-20: Nonlinear least square curve fit on the decomposed jet velocity profile for Case XIII. A) Amplitude. B) Phase angle. C) dc components. The blue curves are for the components of the candidate profile  $T(\bar{x}, t)$ ; the green curves are for the components of the modeled profile  $T_{\text{mod}}(\bar{x}, t)$ ; the red curves are the CFD results.

Table 7-5: Coefficients of the nonlinear least square fits on the decomposed jet velocity profile

Case	<i>a</i>	<i>b</i>	<i>c</i>	<i>d</i>	<i>e</i>	<i>g</i>	<i>h</i>	<i>i</i>
I	2.46	-1.45	0.11	-27.57	-5.18	-3.15	7.29	-5.10 <sup>-5</sup>
II	2.71	-1.66	0.13	-25.97	-11.82	-1.29	-1.28	-0.05
III	0.56	0.34	1.09	-28.13	-10.44	-2.82	-0.37	-0.08
IV	0.38	1.33	0.52	-59.83	6.71	-3.12	0.22	0.11
V	0.91	0.002	6.48	-12.91	-6.49	-0.43	0.49	-0.15
VI	0.90	0.003	5.67	-6.70	-6.42	4.89	1.39	-0.02
VII	0.89	0.003	5.69	-6.82	-7.08	-12.56	5.18	5.10 <sup>-5</sup>
VIII	0.90	0.002	6.01	-13.02	-5.63	-3.12	10.78	-2.10 <sup>-5</sup>
IX	0.81	0.01	5.40	-43.95	-5.03	-3.49	-0.40	0.084
X	0.68	0.01	6.80	-13.06	-23.61	-1.61	-0.16	-0.05
XI	0.70	0.02	5.81	-41.91	-3.32	-0.61	-0.311	-0.09
XII	0.93	0.002	6.09	-33.17	-5.69	-0.32	1.34	-0.18
XIII	0.85	0.006	4.82	-0.07	-8.69	-2.65	0.89	0.24

Next, the 4<sup>th</sup> step shown in Figure 7-13 consists of recombining each component of the modeled profile developed above, such that the final modeled velocity profile takes the form

$$V_{\text{mod}}(\bar{x}, t) = T_{\text{mod},dc}(\bar{x}) + T_{\text{mod},mag}(\bar{x}) \cdot \sin(\omega t + T_{\text{mod},arg}(\bar{x})), \quad (6-37)$$

and is a function of the 8 parameters  $\{a, b, c, d, e, g, h, i\}$ . Notice that Eq. 6-37 is time and spatial dependant and that it needs at least these 8 parameters to represent it. Figure 7-21 compares the velocity profiles at the orifice exit from the CFD results, the decomposition of the velocity  $V_{\text{decomp}}$  defined in Eq. 6-35, and the modeled velocity profile  $V_{\text{mod}}$  defined by Eq. 6-37. First of all, it can be seen that the velocity profile decomposition in terms of a dc term plus a sinusoidal time variation is a good approximation of the velocity profile at the orifice exit from the CFD results for all cases studied. Similarly, following the discussion above, the overall modeled profiles tend to be in agreement with the CFD data, and again at each instant in time during a cycle (although only four phase angles have been shown in Figure 7-21 for clarity). Clearly, the choice of the candidate velocity profile that is Stokes number dependent is able to capture the Richardson effect (overshoot near the orifice edge) that is present in all cases. Notice also how different can the velocity profiles be among the test cases considered, and still this 8-parameters candidate velocity profile model is capable of representing a large variety of velocity profiles, some being completely skewed, others nearly symmetric. Thus, based on this finding, the next step in developing a scaling law can be taken and is described next.



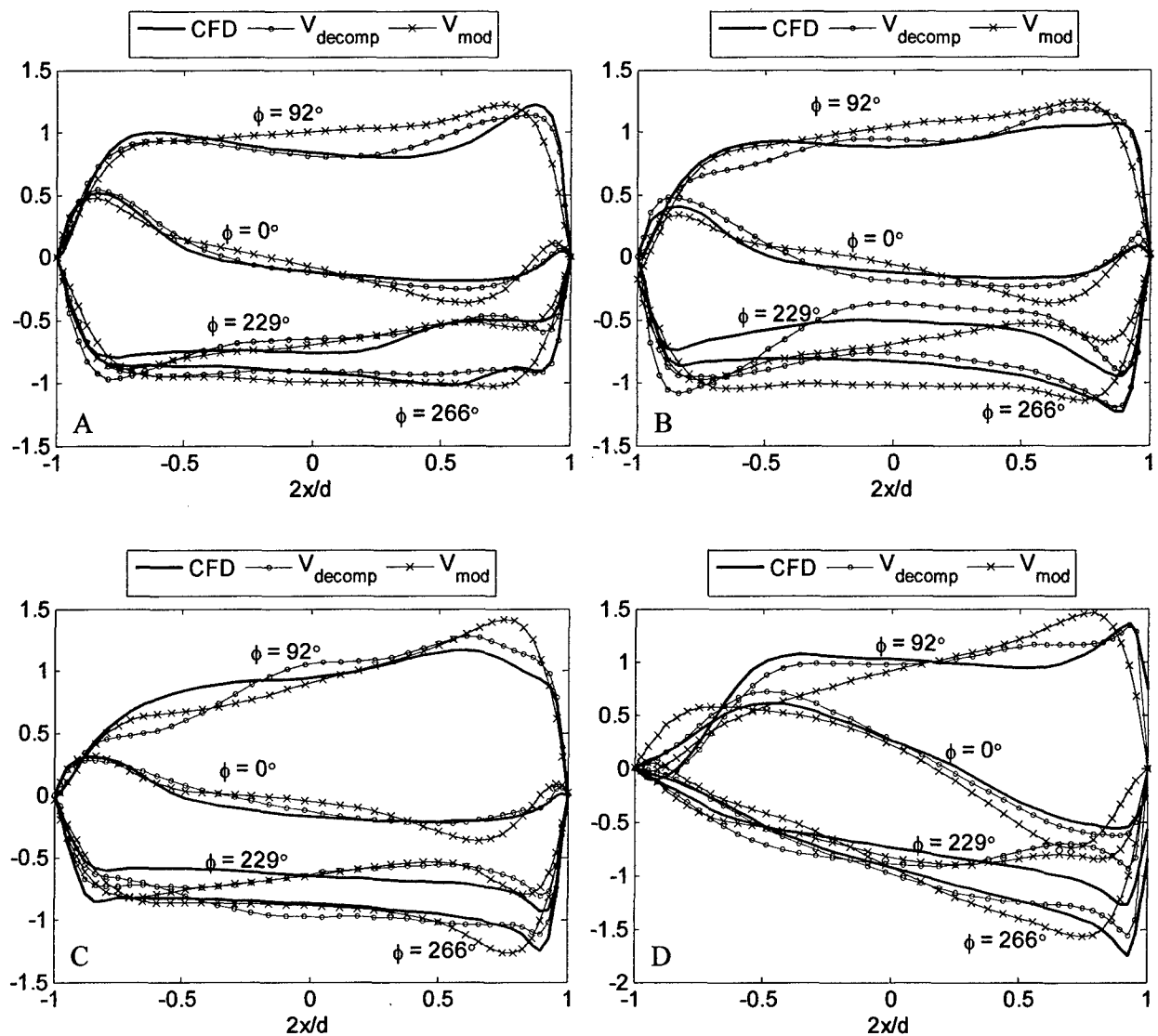


Figure 7-21: Comparison between CFD velocity profile, decomposed jet velocity profile, and modeled velocity profile, at the orifice exit, for four phase angles during a cycle. A) Case I. B) Case II. C) Case III. D) Case IV. E) Case V. F) Case VI. G) Case VII. H) Case VIII. I) Case IX. J) Case X. K) Case XI. L) Case XIII. The velocity in the vertical abscise is normalized by  $U_\infty$ .

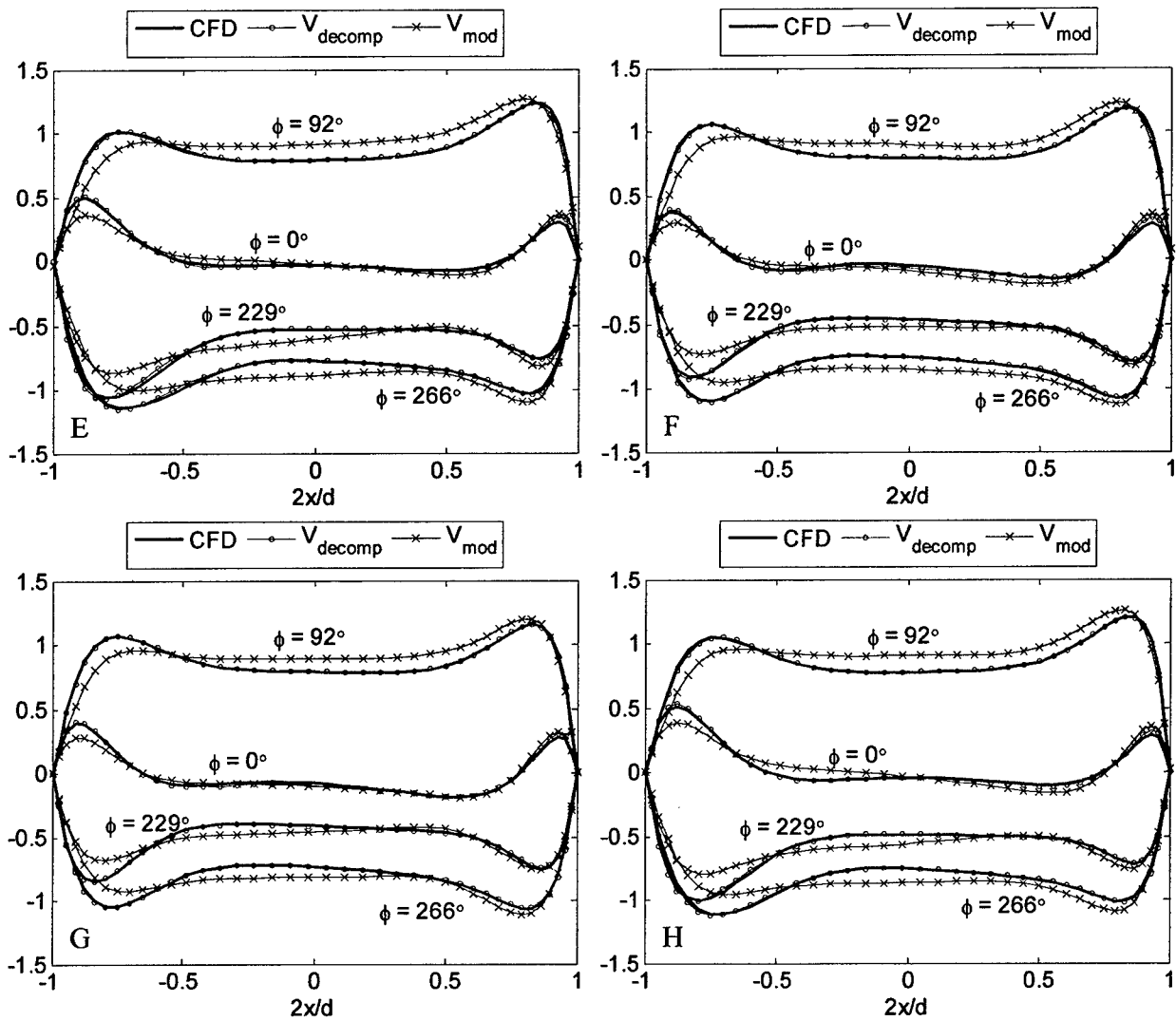


Figure 7-21: Continued.

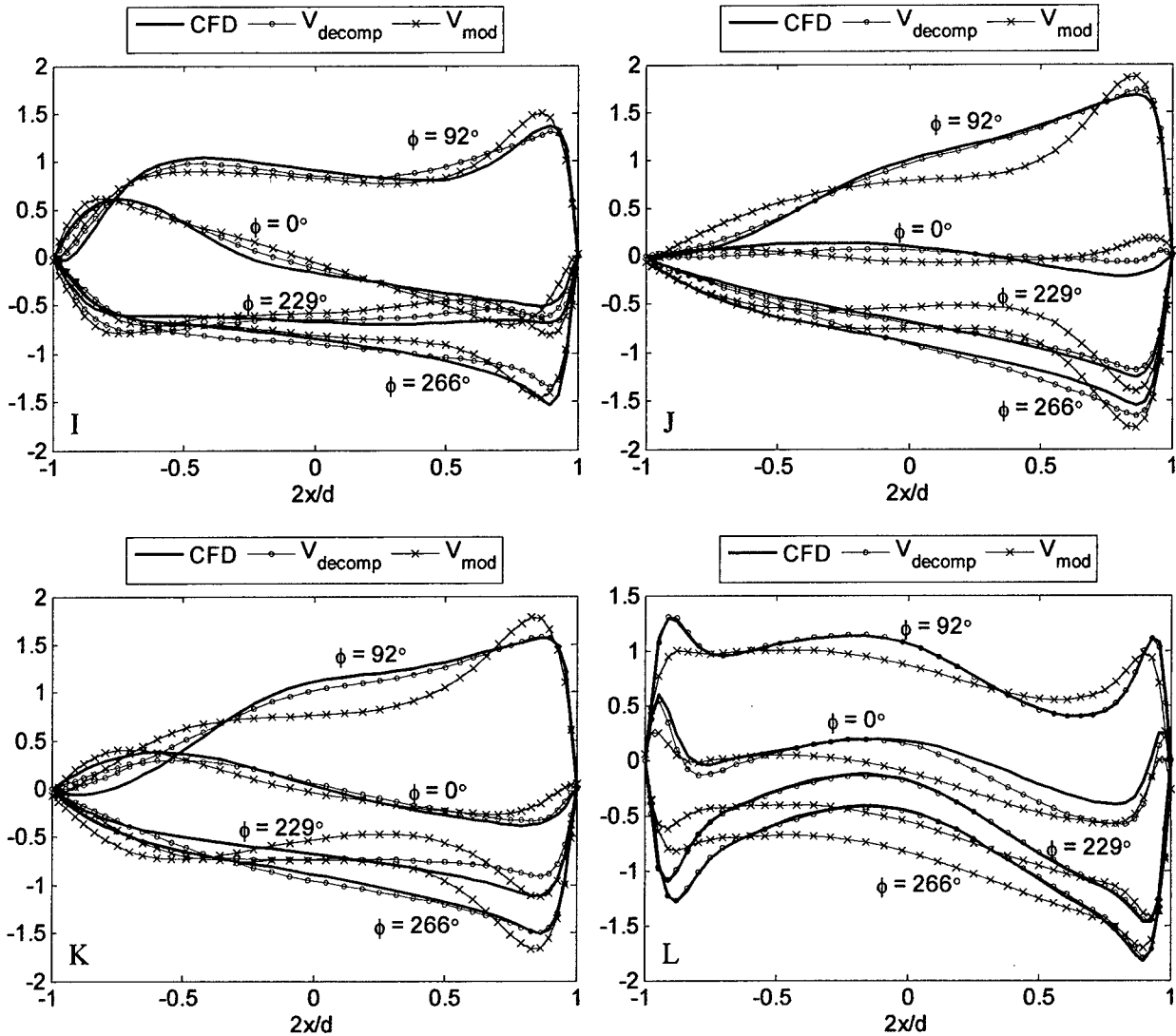


Figure 7-21: Continued.

As shown in Figure 7-13, the next logical step is to extract a scaling law relating the computed values of the parameters  $\{a, b, c, d, e, g, h, i\}$  to the dimensionless flow parameters. Because the relationship among the involved parameters and the target values, i.e. the family set  $\{a, b, c, d, e, g, h, i\}$ , is nonlinear as can be seen by inspection, a nonlinear regression technique is sought for deriving an empirical scaling law, which can be implemented in any available commercial statistical calculation software such as SPSS (Statistical Analysis System). Taking into account the effect of the most important parameters, such as the orifice aspect ratio  $h/d$ , the Stokes number  $S$  (already present in the functional form of the velocity profile), the BL momentum thickness to orifice diameter  $\theta/d$ , the BL Reynolds number  $Re_\theta$  and the nominal jet-to-freestream velocity ratio  $\bar{V}_j/U_\infty$ , an empirical scaling law for the 8 coefficients of the modeled velocity

profile in Eq. 6-37 can be obtained by the regression analysis. The chosen target function takes the general form

$$\begin{Bmatrix} a, b, c \\ d, e, \\ g, h, i \end{Bmatrix} = a_0 \cdot \left[ \frac{h/d}{(h/d)_0} \right]^{b_1} \cdot \left[ \frac{\theta/d}{(\theta/d)_0} \right]^{b_2} \cdot \left[ \frac{\text{Re}_\theta}{(\text{Re}_\theta)_0} \right]^{b_3} \cdot \left[ \frac{\bar{V}_j/U_\infty}{(\bar{V}_j/U_\infty)_0} \right]^{b_4}, \quad (6-38)$$

where  $a_0$  and  $\{b_i\}$  are the regression coefficients (with  $i=1,2,3,4$ ). Here,  $a_0$  is the respective "nominal" value of  $a, b, c, d, e, g, h$ , or  $i$ , while the  $b$ 's are the exponent of each nondimensional term.

These regression coefficients are determined by the nonlinear regression analysis with the data provided in Table 7-5, i.e. for 12 cases since the test case (Case XII) is left out of this regression analysis for verification purposes. The results are given in Table 7-6 where  $R^2$  is the correlation coefficient. Before commenting on these results, it should be pointed out that this problem is clearly over-parameterized, i.e., the family set contains 8 parameters for only 12 numerical cases to do the regression analysis. Therefore, the next steps are explained only for illustration purposes.

Table 7-6: Results from the nonlinear regression analysis for the velocity profile based scaling law

	$R^2$	$a_0$	$b_1$	$b_2$	$b_3$	$b_4$
$a$	0.225	0.903	1.0	0.276	-0.0182	0.490
$b$	0.102	-0.123	1.0	1.028	0.300	1.161
$c$	0.786	4.983	1.0	0.533	-0.0969	-4.402
$d$	0.730	-20.70	1.0	-1.526	1.046	0.238
$e$	0.122	-6.182	1.0	0.668	-0.085	0.405
$g$	0.163	0.010	1.0	-3.502	3.078	-11.02
$h$	0.303	$8 \times 10^{-10}$	1.0	32.43	-0.0375	-0.576
$i$	0.267	1.772	1.0	0.087	-1.008	-0.329

First of all, notice the small correlation coefficients  $R^2$  for all parameters but  $c$  and  $d$ , far from unity, indicative of the poor confidence level in the corresponding regression coefficients. Clearly, such low correlation coefficients indicate a sub-optimal regression form. One way to increase the  $R^2$  values is to increase the test matrix, by more covering the parametric space used here. Keeping in mind the poor level of confidence in these parameters, it is still worthwhile to examine the relative values of the coefficients  $a_0$  and  $b_i$ ,  $a_0$  being representative of the importance of the parameter  $a$  to  $i$ . It can be seen from the parameter  $a$  that the dc part of the profile (parameters  $g, h$ , and  $i$ ) does not have a significant influence on the overall profile, compared with  $d$  and  $e$  from the phase angle or  $a, b$  and  $c$  from the magnitude. Next, the constant value for the coefficient  $b_1$  is due to the fact that the ratio  $h/d$  has not been varied in the test cases used in this analysis, as

shown in Table 7-4. Finally, at this stage it is quite difficult to draw firm conclusions concerning the other coefficients  $b_2$ ,  $b_3$ , and  $b_4$ , with such low associated  $R^2$  values.

Nonetheless, for verification purposes the test case (Case XII) is used to evaluate the velocity profile based scaling law. The results are shown in Figure 7-22 where the numerical data are plotted along with the scaling law of the velocity profile obtained by applying the results in Table 7-6 into the modeled profile defined in Eq. 6-37. Only four phase angles  $\{0; \pi; 5\pi/4; 3\pi/2\}$  are plotted for clarity. Clearly, the proposed scaling law fails to accurately predict the actual velocity profile. Although the velocity is in agreement near the upstream edge of the orifice, it is clearly over-predicted near the downstream orifice edge. This should mainly come from the functional form chosen for the magnitude term  $T_{\text{mod}, \text{mag}} = |T| \{a + be^{c\bar{x}}\}$  which has really poor associated regression coefficients  $R^2$ . Recall however that this all analysis has been performed on only 12 cases, which is a modest but valuable start in view of the results presented in this section. It is clearly not enough if one considers the wide parameter space to span and the strongly coupled interactions between each dimensionless parameter.

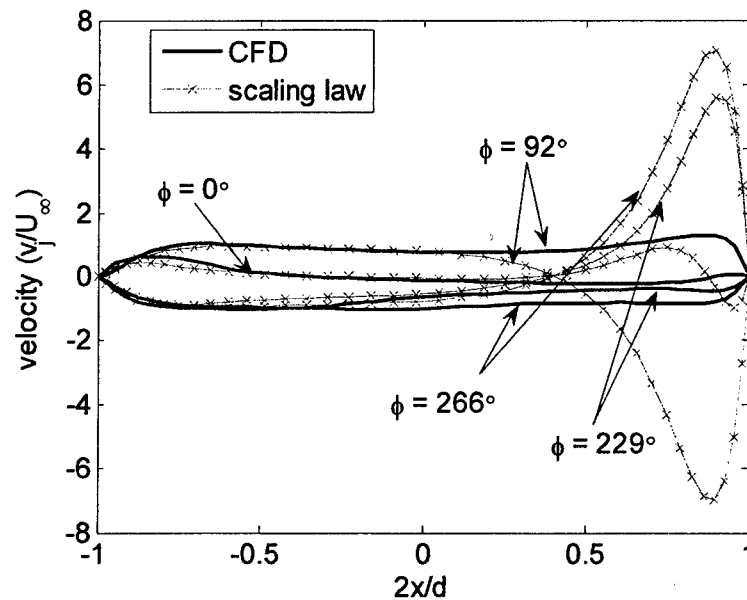


Figure 7-22: Test case comparison between CFD data and the scaling law based on the velocity profile at four phase angles during a cycle. Case XII:  $S = 20$ ,  $Re = 94$ ,  $\theta/d = 0.26$ ,  $Re_\theta = 133$ .

### 7.3.2.2 Scaling law based on the jet exit integral parameters

The first scaling law previously presented is using the spatial velocity profile at the orifice exit, but disregards the integral parameters (momentum coefficient, skewness, vorticity flux,...). Another approach - presented next - is to base the scaling law on these integral parameters, regardless of the actual velocity profile. The methodology of this approach is outlined in Figure 7-23. First, a candidate velocity profile is chosen, in a similar fashion as already explained above. Because of the zero-net mass flux nature of the device, the dc or average component of the velocity should be identically zero in a

time average sense. Hence, the candidate profile is refined such that the new low-order model for the velocity profile takes the form

$$V_{\text{mod}}(\bar{x}, t) = V_{\text{mag}}(\bar{x}) \cdot \sin(\omega t + V_{\text{arg}}(\bar{x})), \quad (6-39)$$

where the magnitude and argument of the velocity are defined by

$$\begin{cases} V_{\text{mag}}(\bar{x}) = (a\bar{x}^2 + b\bar{x} + c) \cdot |T(\bar{x})| \\ V_{\text{arg}}(\bar{x}) = (b\bar{x} + c) \cdot \angle T(\bar{x}) \end{cases} \quad (6-40)$$

Notice that  $V_{\text{mod}}(\bar{x}, t)$  is a low-parameterized model since it is only function of 3 parameters:  $a$ ,  $b$ , and  $c$ . Again, this functional form is motivated by the results of the investigation outlined in Section 4 on the 2D slot flow physics of a ZNMF actuator in a quiescent medium. But since only the integral parameters are of interest in here, the shape of the velocity profile is not considered as crucial and thus does not have a more complex functional form as seen in the previous scaling law.

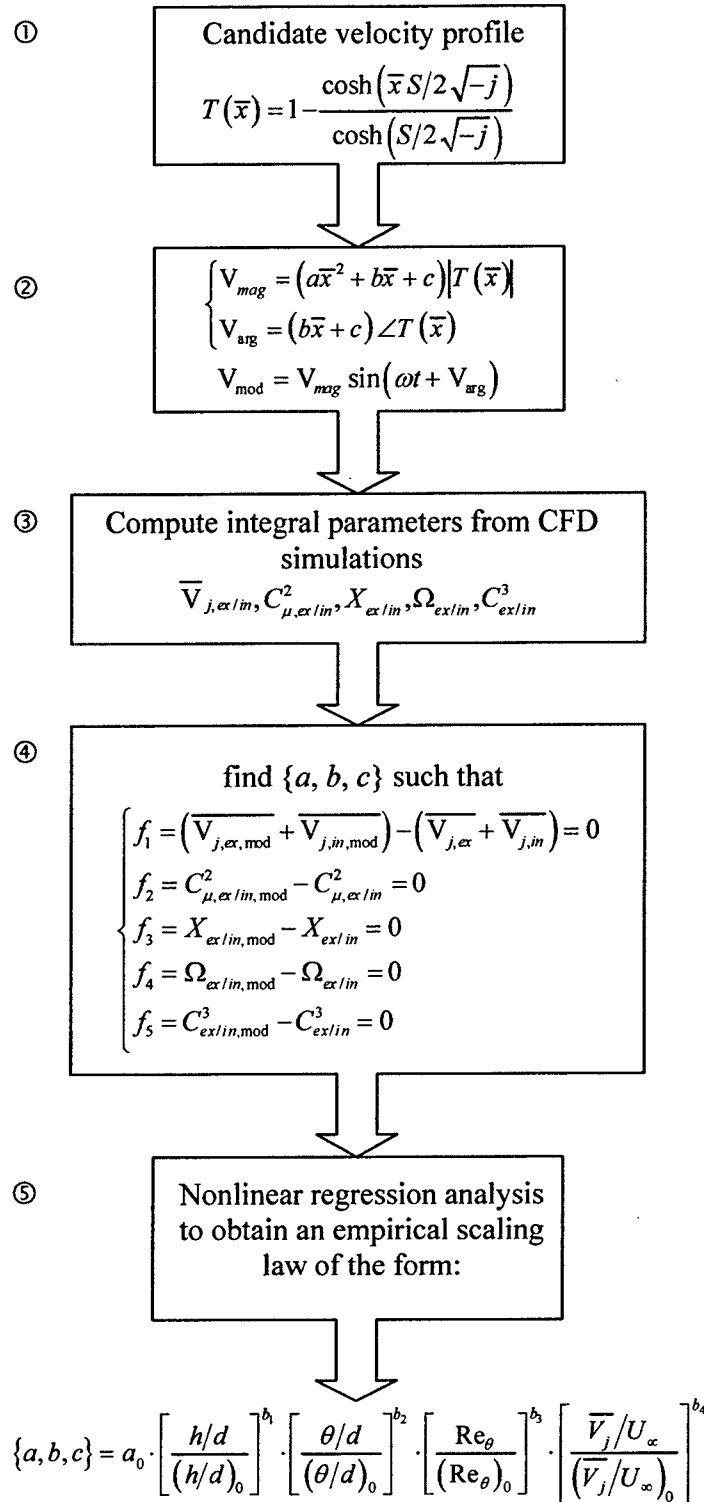


Figure 7-23: Methodology for the development of the integral parameters based scaling law.

The requirements of this model profile are:

1. zero-net mass flux (identically satisfied by the assumed functional form)
2. match momentum coefficient

$$C_\mu = \frac{1}{2\pi} \frac{1}{\theta/d} \int_0^{2\pi} \int_{-1}^1 V(x, \phi)^2 d\left(\frac{x}{d/2}\right) d\phi \quad (6-41)$$

3. match skewness coefficient

$$X = \frac{1}{2\pi} \int_0^{2\pi} \int_{-1}^1 [V(x, \phi) - V(-x, \phi)] d\left(\frac{x}{d/2}\right) d\phi \quad (6-42)$$

4. match vorticity flux

$$\Omega_v = \int_0^{2\pi} \int_{-1}^1 \left(-\frac{d}{dx} v(x, \phi)\right) \cdot v(x, \phi) d\left(\frac{x}{d/2}\right) d\phi = \int_0^{2\pi} \frac{1}{2} v(0, \phi)^2 d\phi \quad (6-43)$$

5. match jet kinetic energy flux

$$C^3 = \frac{1}{2\pi} \frac{1}{\theta/d} \int_0^{2\pi} \int_{-1}^1 V(x, \phi)^3 d\left(\frac{x}{d/2}\right) d\phi \quad (6-44)$$

Recall that  $V(x, \phi) = v(x, \phi)/U_\infty$  is the normalized velocity and that Eqs. 6-41, 6-42, 6-43, and 6-44 are derived for a 2D slot orifice geometry. Also, the vorticity flux should be nondimensionalized with, for instance, the quantity  $\bar{V}_j d$ .

As outlined in Figure 7-23, the procedure is thus to compute these integral parameters from the CFD data of the test cases tabulated in Table 7-4, and then to solve for the coefficients  $a$ ,  $b$ , and  $c$  from the modeled velocity profile (Eq. 6-39) to match them. This yields a system of 5 equations and 3 unknowns to solve, that can be written as

$$\text{find } \{a, b, c\} \text{ such that } \begin{cases} f_1 = (\overline{V_{j,ex,mod}} + \overline{V_{j,in,mod}}) - (\overline{V_{j,ex}} + \overline{V_{j,in}}) = 0 \\ f_2 = C_{\mu,ex/in,mod}^2 - C_{\mu,ex/in}^2 = 0 \\ f_3 = X_{ex/in,mod} - X_{ex/in} = 0 \\ f_4 = \Omega_{v,ex/in,mod} - \Omega_{v,ex/in} = 0 \\ f_5 = C_{ex/in,mod}^3 - C_{ex/in}^3 = 0 \end{cases} \quad (6-45)$$

Eq. 6-45 is clearly an over-determined system, with more equations than unknowns. Recall also that the suffix 'ex' and 'in' stand for 'expulsion' and 'ingestion'. So one can actually compute the equations  $f_2, f_3, f_4$ , or  $f_5$  for either the expulsion part or the ingestion part of the cycle, which can add the number of equations up to 9.



Therefore, some choices have to be made to reduce the number of equations in Eq. 6-45. First of all,  $f_1$  can be removed since it insures the zero-net mass flux criterion, which is automatically satisfied by the assumed functional form (Eqs. 6-39 and 6-40). Then, the momentum flux can be recast to account for both the expulsion and ingestion parts, and only the expulsion parts of the skewness coefficient and normalized vorticity flux are retained. The new nonlinear system to be solved can then be written as

$$\text{find } \{a, b, c\} \text{ such that } \begin{cases} f_1 = (C_{\mu,ex,mod}^2 + C_{\mu,in,mod}^2) - (C_{\mu,ex}^2 + C_{\mu,in}^2) = 0 \\ f_2 = X_{ex,mod} - X_{ex} = 0 \\ f_3 = \Omega_{v,ex,mod}/\overline{V}_j d - \Omega_{v,ex}/\overline{V}_j d = 0 \end{cases} \quad (6-46)$$

These 3 coefficients are numerically obtained via the Matlab function FSOLVE. The results are summarized in Table 7-7 showing the results for the 3 parameters  $a$ ,  $b$ , and  $c$ , along with the corresponding equations  $f_1$ ,  $f_2$ , and  $f_3$  from Eq. 6-46. Also, Table 7-8 shows the resulting integral parameters computed from the CFD data and the low-order model. Clearly, the candidate velocity profile is able to accurately predict the integral parameters when compared with the CFD data for the expulsion and ingestion parts of the cycle. It should be noted that even by choosing different functions in the nonlinear system of equations in Eq 6-46 - for instance by choosing the jet kinetic energy flux, or skewness coefficient and vorticity flux during the ingestion part of the cycle - the results presented in Table 7-7 and Table 7-8 do not notably vary. Then, based on these computed parameters  $a$ ,  $b$  and  $c$ , the next step in constructing a scaling law for the velocity profiles can be pursued.

Table 7-7: Results for the parameters  $a$ ,  $b$  and  $c$  from the nonlinear system

Case	$a$	$b$	$c$	$f_1$	$f_2$	$f_3$
I	-1.111	0.065	0.508	$3.06 \times 10^{-12}$	$1.84 \times 10^{-15}$	$-5.13 \times 10^{-12}$
II	-1.748	0.179	0.777	$3.17 \times 10^{-11}$	$-7.81 \times 10^{-15}$	$1.72 \times 10^{-11}$
III	-2.701	0.367	1.052	$1.06 \times 10^{-8}$	$1.01 \times 10^{-10}$	$-2.75 \times 10^{-9}$
IV	-0.758	0.064	0.242	$7.71 \times 10^{-14}$	$5.93 \times 10^{-16}$	$6.59 \times 10^{-12}$
V	-0.649	0.034	0.224	$1.57 \times 10^{-10}$	$3.95 \times 10^{-13}$	$1.80 \times 10^{-10}$
VI	-0.647	0.024	0.221	$1.01 \times 10^{-10}$	$2.04 \times 10^{-13}$	$2.12 \times 10^{-9}$
VII	-0.646	0.019	0.222	$7.05 \times 10^{-11}$	$1.34 \times 10^{-13}$	$1.45 \times 10^{-9}$
VIII	-0.645	0.030	0.223	$8.31 \times 10^{-8}$	$2.28 \times 10^{-10}$	$-6.09 \times 10^{-10}$
IX	-0.709	0.039	0.240	$9.04 \times 10^{-12}$	$3.26 \times 10^{-14}$	$1.56 \times 10^{-10}$
X	-1.002	0.212	0.243	$1.29 \times 10^{-7}$	$1.39 \times 10^{-9}$	$-2.41 \times 10^{-8}$
XI	-0.849	0.133	0.233	$7.91 \times 10^{-9}$	$6.49 \times 10^{-11}$	$1.15 \times 10^{-8}$
XII*	-0.673	0.037	0.236	$3.74 \times 10^{-10}$	$1.01 \times 10^{-12}$	$3.76 \times 10^{-10}$
XIII	-0.614	-0.069	0.209	$4.58 \times 10^{-11}$	$3.25 \times 10^{-14}$	$7.97 \times 10^{-10}$

\* Test case

Noting that  $a$ ,  $b$  and  $c$  are themselves functions of the dimensionless flow parameters defined in Eq. 6-32, the next logical step is to extract a scaling law relating the computed values of the parameters  $\{a,b,c\}$  to the flow parameters. As already mentioned in the previous section, since the relationship among the involved parameters and the target values, i.e. the family set  $\{a,b,c\}$ , is nonlinear, a nonlinear regression technique is sought for deriving an empirical scaling law, which can be implemented in any available commercial statistical calculation software such as SPSS (Statistical Analysis System).

Table 7-8: Integral parameters results

Case	$C_\mu$		$C_{\mu,mod}$		$X$		$X_{mod}$	
	ex	in	ex	in	ex	in	ex	in
I	0.114	0.106	0.110	0.110	0.017	-0.008	0.017	-0.017
II	0.281	0.258	0.257	0.282	0.069	-0.031	0.069	-0.076
III	0.662	0.441	0.538	0.565	0.171	-0.069	0.171	-0.179
IV	0.037	0.034	0.037	0.035	0.027	-0.061	0.027	-0.026
V	0.027	0.027	0.0267	0.027	0.010	0.004	0.010	-0.010
VI	0.025	0.026	0.025	0.026	0.004	-0.003	0.004	-0.004
VII	0.025	0.026	0.026	0.026	0.001	-0.006	0.001	-0.001
VIII	0.025	0.026	0.025	0.027	0.007	0.001	0.007	-0.008
IX	0.031	0.031	0.029	0.032	0.011	-0.038	0.011	-0.012
X	0.035	0.031	0.033	0.033	0.072	-0.056	0.072	-0.072
XI	0.035	0.030	0.033	0.033	0.055	-0.047	0.055	-0.055
XII*	0.029	0.028	0.028	0.028	0.011	0.008	0.011	-0.011
XIII	0.028	0.034	0.029	0.033	-0.051	-0.049	-0.051	0.056

Case	$\Omega_v/\sqrt{V_j d}$		$\Omega_{v,mod}/\sqrt{V_j d}$		$C^3$		$C_{mod}^3$	
	ex	in	ex	in	ex	in	ex	in
I	0.856	1.252	0.856	0.856	0.049	-0.042	0.033	-0.033
II	1.384	1.053	1.384	1.375	0.173	-0.156	0.109	-0.122
III	2.328	1.183	2.328	2.325	0.705	-0.352	0.201	-0.212
IV	1.514	1.221	1.514	1.516	0.009	-0.009	-0.0001	0.0001
V	0.846	0.864	0.846	0.846	0.005	-0.005	0.001	-0.001
VI	0.908	0.922	0.908	0.907	0.005	-0.005	0.001	-0.001
VII	0.890	0.934	0.890	0.890	0.005	-0.005	0.001	-0.001
VIII	0.858	0.895	0.858	0.857	0.005	-0.005	0.001	-0.001
IX	1.057	1.238	1.057	1.053	0.007	-0.008	0.001	-0.001
X	1.429	1.201	1.429	1.429	0.010	-0.008	0.002	-0.002
XI	1.612	1.244	1.612	1.612	0.0010	-0.007	0.001	-0.001
XII*	0.834	1.267	0.834	0.834	0.006	-0.006	0.001	-0.001
XIII	1.771	0.337	1.770	1.764	0.006	-0.009	-0.002	0.002

\* Test case

Taking into account the effect of the most important parameters, such as the orifice aspect ratio  $h/d$ , the Stokes number  $S$  (already present in the functional form of the velocity profile), the BL momentum thickness to orifice diameter  $\theta/d$ , the BL Reynolds

number  $Re_\theta$  and the jet to freestream velocity ratio  $\bar{V}_j/U_\infty$ , an empirical scaling law for the coefficients  $\{a, b, c\}$  of the modeled velocity profile in Eq. 6-39 can be obtained by the nonlinear regression analysis. The chosen target function takes the general form

$$\{a, b, c\} = a_0 \cdot \left[ \frac{h/d}{(h/d)_0} \right]^{b_1} \cdot \left[ \frac{\theta/d}{(\theta/d)_0} \right]^{b_2} \cdot \left[ \frac{Re_\theta}{(Re_\theta)_0} \right]^{b_3} \cdot \left[ \frac{\bar{V}_j/U_\infty}{(\bar{V}_j/U_\infty)_0} \right]^{b_4} \quad (6-47)$$

where  $a_0$  and  $\{b_i\}$  are the regression coefficients (with  $i=1,2,3,4$ ). Again,  $a_0$  is the respective "nominal" value of  $a$ ,  $b$ , or  $c$ , while the  $b$ 's are the exponent of each nondimensional term. These regression coefficients are determined by the nonlinear regression analysis with the data provided in Table 7-7, i.e. for 12 cases since the test case (Case XII) is left out of this regression analysis for verification purposes. The results are given in Table 7-9 where  $R^2$  is the correlation coefficient.

Table 7-9: Results from the nonlinear regression analysis for the integral parameters based velocity profile

	$R^2$	$a_0$	$b_1$	$b_2$	$b_3$	$b_4$
$a$	<b>0.945</b>	<b>-0.698</b>	<b>1.0</b>	<b>-0.124</b>	<b>0.059</b>	<b>0.928</b>
$b$	<b>0.625</b>	<b>0.042</b>	<b>1.0</b>	<b>-0.620</b>	<b>0.291</b>	<b>1.494</b>
$c$	<b>0.999</b>	<b>0.232</b>	<b>1.0</b>	<b>-0.068</b>	<b>0.041</b>	<b>1.093</b>

Recall that the parameters  $a$ ,  $b$ , and  $c$  are the coefficient of the quadratic term in front of the amplitude of the modeled velocity, and that the same  $b$  and  $c$  parameters are the coefficients for the linear term in front of the argument of the modeled velocity profile. First of all, notice the large correlation coefficients  $R^2$  for the  $a$  and  $c$  parameters, close to unity, indicative of the good confidence level in the corresponding regression coefficients. On the other hand, although acceptable, the correlation coefficients for the  $b$  parameters indicate that the assumed regression form is sub-optimal.

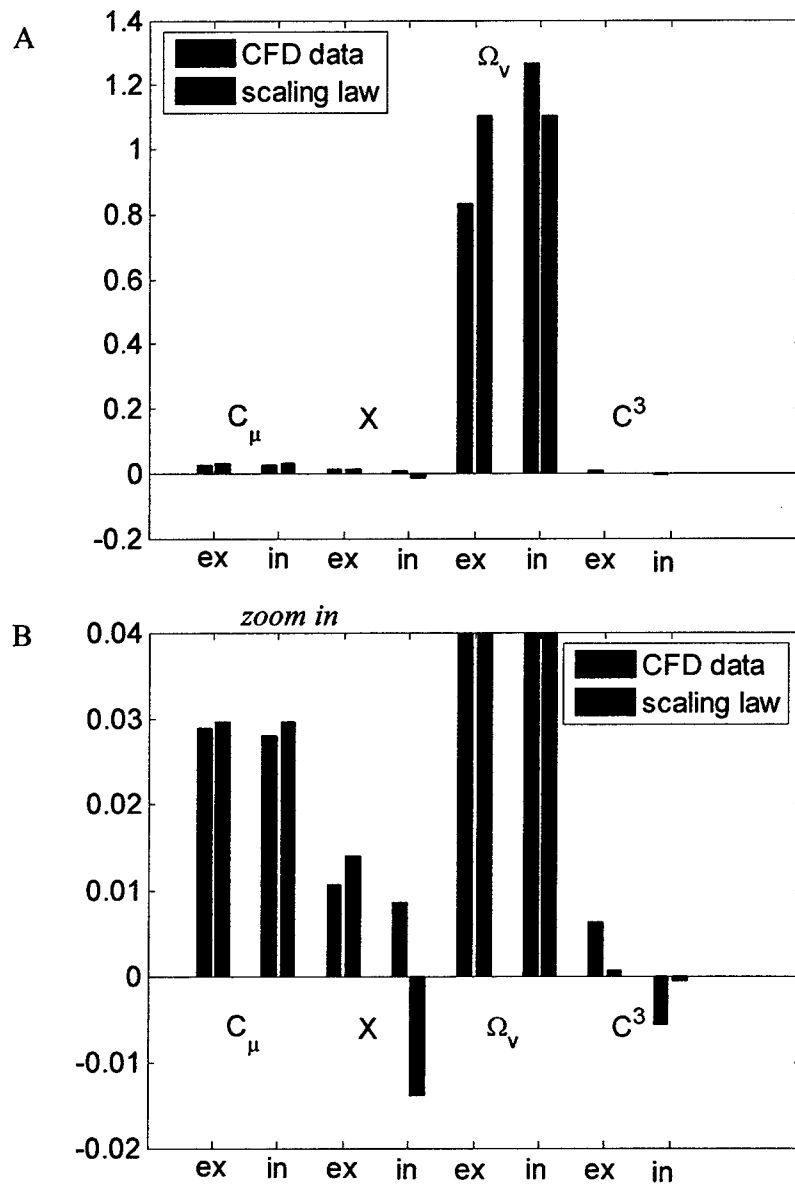


Figure 7-24: Comparison between the results of the integral parameters from the scaling law and the CFD data for the test case. Case XII:  $S = 20$ ,  $Re = 94$ ,  $\theta/d = 0.26$ ,  $Re_\theta = 133$ . A) Full view. B) Close-up view.

Consider next the relative values of the coefficients  $a_0$  and  $b_i$ ,  $a_0$  being representative of the importance of the parameter  $a$ ,  $b$  or  $c$ . It can be seen that the parameter  $a$  does have the most significant influence on the overall profile, especially compared with  $b$ . Next, the constant value for the coefficient  $b_1$  is due to the fact that the ratio  $h/d$  has not been varied in the test cases used in this analysis, as shown in Table 7-4. The coefficient  $b_2$  weights the momentum thickness influence, which clearly has a dominant influence on the parameter  $b$ , although one has to be cautious with respect to the associated correlation coefficient, and a minor influence on the parameter  $c$ . Similarly, the Reynolds number associated with the boundary layer mainly influences the

parameter  $b$  of the profile, which shows that the skewness of the velocity profile is strongly dependant on the momentum of the incoming boundary layer. Finally, it can be seen that the ratio of the jet-to-freestream velocity equally weights all velocity profile parameters.

Next, the test case (Case XII) is used to evaluate the scaling law. The results are shown in Figure 7-24 where the integral parameters from the numerical data are plotted along with those from the scaling law of the velocity profile obtained by applying the results shown in Table 7-9. Clearly, the scaling law in its present form is globally able to provide reasonable estimates of the principal integral parameters, for both the expulsion and the ingestion part of the cycle. More particularly, the momentum coefficient  $C_\mu$  predicted by the scaling law closely matches the numerical data. However, the ingestion part is poorly represented in terms of the skewness  $X$ . This can be explained by the low correlation coefficient associated with the parameter  $b$ . As for the vorticity flux  $\Omega_v$ , the scaling law predicts an equal value for both the expulsion and the ingestion part, which is not quite true as seen from the CFD data. Finally, the jet kinetic energy flux  $C^3$ , although only shown here for verification purposes since it does not enter in the system of equations to be solved, is under-estimated by the scaling law. Recall however that this all analysis has been performed on only 12 cases, which is a modest but valuable start in view of the results presented in this section. It is clearly not enough if one considers the wide parameter space to span and the strongly coupled interactions between each dimensionless parameter.

### 7.3.2.3 Validation and Application

The next step in developing these scaling laws of a ZNMF actuator interacting with a grazing boundary layer is to first validate them, and then apply them in practical applications. Here, a road map is presented to achieve such a goal.

First of all, in order to be valid the two scaling laws developed above need to be refined based on a larger database, especially the scaling law that is based on the velocity profile and for whom the nonlinear regression analysis gives unsatisfactory regression coefficients  $R^2$ . Next, the scaling laws must be implemented in practical cases. Recall that one goal in developing such reduced-order models is to use them in a numerical simulation as a boundary condition in lieu of resolving the local flow details near the actuator. This is illustrated in Figure 7-25, where the concept is to use the results of the scaling law presented above and set it as the boundary condition for a simple application (e.g. flow over a flat plate). Then, the numerical results for the full computational domain (flow over the airfoil plus the whole ZNMF actuator) are compared with the numerical results where the actuator is only modeled as a time-dependant boundary condition at the orifice exit. Computed flow parameters at specific locations are probed - i.e., right at the orifice edge to see the local flow region, and farther downstream for the global flow region - to check the correspondence between the two simulations.

Once this validation of the current scaling law presented above in the previous sections has been accomplished, the model can be extended to include more dimensionless parameters, such as pressure gradient, surface curvature, etc., hence to be extended to more general flow conditions (e.g., flow past an airfoil). This requires a more important test matrix of available numerical simulations.

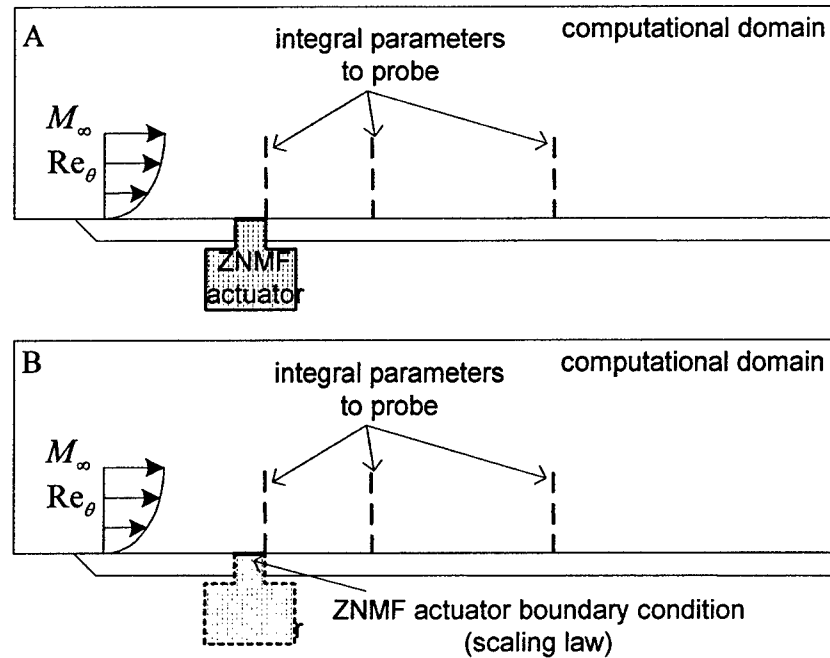


Figure 7-25: Example of a practical application of the ZNMF actuator reduced-order model in a numerical simulation of flow past a flat plate. A) Computational domain is flow over the plate + actuator. B) Computational domain is flow over the plate only.

Finally, the next logical step to be undertaken would be to compute the impedance  $Z_{aBL}$  (see Eq. 6-17) from the scaling law based jet exit velocity profiles. This impedance is then to be compared with the results from the extension of the low-dimensional lumped elements that include a boundary layer impedance from the Helmholtz resonator analogy. Such a comparison will help in validating both approaches, as well as refining the LEM-based reduced-order model. However, the scaling law must first be sufficiently accurate before taking this next step.

To conclude this section, the interaction of a ZNMF actuator with an external boundary layer has been investigated in great detail, starting from a physical description of the different interactions and the effects on the local velocity profile, and then followed by a dimensional analysis used to extract the governing parameters. Since the parameter space is extremely large, as a first step a variation in some of the dimensionless numbers have been neglected, such as the surface curvature and shape factor.

Next, two reduced-order models have been presented. The first one is an extension of the LEM detailed in the previous sections for a ZNMF actuator in quiescent flow, where the effects of an external boundary layer have been added to the model. This model is based on the work done in the acoustic liner community and looks promising, although it is only a function of few flow parameters ( $kd$ ,  $C_d$ ,  $\delta/d$ , and  $M_\infty$ ). A logical extension to this model would be to include the jet-to-freestream velocity ratio  $\bar{V}_j/U_\infty$ , a

boundary layer Reynolds number, such as  $Re_\theta$ , and the BL integral parameter  $\theta/d$  instead of  $\delta/d$ .

The second low-dimensional model is based on a regression analysis on available numerical data that provides the jet velocity profile as a function of 5 dimensionless parameters ( $S$ ,  $h/d$ ,  $\theta/d$ ,  $Re_\theta$ , and  $\bar{V}_j/U_\infty$ ). Two scaling laws are developed, one based on the jet velocity profile at the orifice exit, the other one on the integral parameters of the local flow at the orifice exit. The results are encouraging, but more test cases are needed to ensure a better validation of the results due to the nonlinear relationship between the correlation coefficients and also due to the large parameter space. Finally, a discussion is provided on the next steps that have to be taken in order to fully appreciate the usefulness of such reduced-order models of a ZNMF actuator interacting with a grazing boundary layer.

## 8. Conclusions and Future Work

This section summarizes the work presented in this report. Concluding remarks are provided along with suggestions for future research.

### 8.1 Conclusions

The dynamics governing the behavior of zero net mass flux (ZNMF) actuators interacting with and without an external flow have been presented and discussed, and physics-based low-order models have been developed and compared with an extensive database from numerical simulations and experimental results. The objective was to facilitate the physical understanding and to provide tools to aid in the analysis and development of tools for sizing, design and deployment of ZNMF actuators in flow control applications.

From the standpoint of an isolated ZNMF actuator issuing into a quiescent medium, a dimensional analysis highlighted identified the key dimensionless parameters. An extensive experimental setup, along with some available numerical simulations, has permitted us to gain a physical understanding on the rich and complex behavior of ZNMF actuators. The results of the numerical simulations and experiments both revealed that care must be exercised concerning modeling the flow physics of the device. Based on these findings, a refined reduced-order, lumped model was successfully developed to predict the performance of candidate devices and was shown to be in reasonable agreement with experimental frequency response data.

In terms of interacting with an external flow, a dimensional analysis revealed additional relevant flow parameters, and the interaction mechanism was qualitatively discussed. An acoustic impedance model of the grazing boundary layer influence based on the NASA ZKTL model (Betts 2000) was then evaluated and implemented in the original lumped element model described in Gallas et al. (2003a). Its validation must await a future investigation. Next, two scaling laws were developed for the time-dependent jet velocity profile of a ZNMF actuator interacting with an external Blasius boundary layer. Although the preliminary results seem promising, further work is still required.

The main achievements of this work are summarized below.

- Orifice flow physics (Sections 4 and 5)

The rich and complex orifice flow field of an isolated ZNMF actuator has been thoroughly investigated using numerical and experimental results, both in terms of the velocity and pressure fields. The straight orifice exit velocity profile is primarily a function of Strouhal number  $St$  (or, alternatively, the dimensionless particle stroke length), Reynolds number  $Re$ , and orifice aspect ratio  $h/d$ .

- Actuator design (Sections 2, 4, and 5)

An analytical criterion has been developed on the incompressibility assumption of the cavity, based on the actuation-to-Helmholtz frequency ratio  $f/f_H$ . This is especially relevant for computational studies that seek to model the flow inside the cavity.

A simple linear dimensionless transfer function relating the jet-to-driver volume flow rate is developed, regardless of the driver dynamics. It can be used as a starting point as a design tool. It is found that by operating near acoustic resonance, the device can produce greater output flow rates than the driver, hence revealing an “acoustic” lever arm that can be leveraged in practical applications where actuation authority is critical. An added benefit is that the driver is not operated at mechanical resonance where the device may have less tolerance to failure.

The sources of nonlinearities present in a ZNMF actuator have been systematically investigated. Nonlinearities from the driver arise due to the driving-transducer dynamics and depend on the type of driver used (piezoelectric, electromagnetic ...). Nonlinearities from large cavity pressure fluctuations can arise due to a departure from the isentropic speed of sound assumption, but this effect was found to be negligible for the test conditions considered in this study. Finally, appropriately modeling the nonlinearities from the orifice is the main focus of the current reduced-order models.

- Reduced-order model of an isolated ZNMF actuator (Section 6)

Based on a control volume analysis for an unsteady orifice flow, a refined physics-based, low-order model of the actuator orifice has been successfully developed that accounts for the nonlinear losses in the orifice that are a function of geometric (orifice aspect ratio  $h/d$ ) and flow parameters (Strouhal  $St$  and Reynolds  $Re$  numbers). Two distinct flow regimes are identified. The first one is for high dimensionless stroke length where the flow can be considered as quasi-steady and where nonlinear effects may dominate the orifice pressure drop. Another regime occurs at intermediate to low stroke length where the pressure losses are clearly dominated by the flow unsteadiness. The refined lumped element model builds on two approximate scaling laws that have been developed for these two flow regimes.

- Reduced-order models of a ZNMF actuator interacting with a grazing boundary layer (Section 7)

Reduced-order models of a ZNMF actuator interacting with a grazing Blasius boundary layer have been developed. One model is based on the orifice acoustic impedance and leverages the work done in the acoustic liner community. Two others are based on scaling laws for the exit velocity profile: one using the velocity profile information, the other one using the integral parameters of the jet exit velocity. While promising, these models need further validation. These models can be used to provide



approximate, time-dependent boundary conditions for ZNMF actuators based on computed upstream dimensionless parameters of the flow. This approach frees up computational resources otherwise required to resolve the local details of the actuator flow to instead resolve the “global” effects of the actuators on the flow.

## **8.2 Recommendations for Future Research**

The physics-based low-order models presented and developed in this report can always be refined and will certainly benefit from a larger high quality database, both numerically and experimentally. This database should cover a wide range of flow parameters such as Strouhal and Reynolds number (hence Stokes number) and geometric parameters such as the orifice aspect ratio. The following points indicate some directions for future work that are envisioned to enhance and complete the present physical understanding of ZNMF actuator behavior and to improve the low-order models developed in this report. The reader is referred to Gallas (2005) for further details.

- **Need for extracting specific quantities** – numerical simulations over a wide range of Strouhal numbers, Reynolds numbers, and orifice aspect ratios to extract the time-dependent (1) velocity profiles at the orifice entrance and exit, (2) pressure drop across the orifice, and (3) wall shear stress along the orifice.
- **Proper Orthogonal Decomposition (POD)** – a technique which defines modes that contain the most kinetic energy, POD is an additional low-order modeling technique that can be implemented for ZNMF devices
- **Boundary layer impedance characterization** - if the orifice dimensions are judiciously chosen such that the flow inside the orifice is well behaved and has a validated model, it will then be possible to isolate the BL impedance for analysis, thereby extracting a low-order model to be implemented as a design tool.
- **MEMS scale implementation** – an interesting analysis will be to investigate the effect of scaling the results found in this report for the meso-scale down to the MEMS scale, and to examine the corresponding effects with the intrinsic limitations.
- **Design synthesis problem** – the designer seeks to achieve a desired frequency response function. Due to the nonlinear nature of the system, the design objective can be approximated by a linear transfer function that is valid at a particular driving voltage. A key challenge here is that the end user must be able to translate desirable actuator characteristics into quantitative design goals.

## 9. List of References

- Amitay, M., and Glezer, A., "Role of Actuation Frequency in Controlled Flow Reattachment over a Stalled Airfoil," *AIAA Journal*, Vol. 40, No. 2, February 2002.
- Amitay, M., Honohan, A., Trautman, M., and Glezer, A., "Modification of the Aerodynamic Characteristics of Bluff Bodies using Fluidic Actuators," AIAA Paper 97-2004, 1997.
- Amitay, M., Kibens, V., Parekh, D., and Glezer, A., "The Dynamics of Flow Reattachment over a Thick Airfoil Controlled by Synthetic Jet Actuators," AIAA Paper 99-1001, 1999.
- Amitay, M., Pitt, D., Kibens, V., Parekh, D., and Glezer, A., "Control of Internal Flow Separation using Synthetic Jet Actuators," AIAA Paper 2000-0903, 2000.
- Amitay, M., Smith, B.L., and Glezer, A., "Aerodynamic Flow Control using Synthetic Jet Technology," AIAA Paper 98-0208, 1998.
- Bauer, A.B., "Impedance Theory and Measurements on Porous Acoustic Liners," *Journal of Aircraft*, Vol. 14, pp 720-728, 1977.
- Bendat, J.S., *Nonlinear Systems Techniques and Applications*, John Wiley & Sons, Inc., New York, NY, pp. 71-76, 1998.
- Béra, J.C., Michard, M., Grosjean, N., and Comte-Bellot, G., "Flow Analysis of Two-dimensional Pulsed Jets by Particle Image Velocimetry," *Experiments in Fluids*, Vol. 31, pp. 519-532, 2001.
- Béra, J.C., and Sunyach, M., "Control of Boundary Layer Separation by Jet Oscillation," AIAA Paper 98-2373, 1998.
- Betts, J.F., "Experiments and Impedance Modeling of Liners Including the Effect of Bias Flow," PhD Dissertation, Department of Mechanical Engineering, Virginia Polytechnic Institute and State University, Hampton, Va, 2000.
- Blackstock, D.T., *Fundamentals of Physical Acoustics*, John Wiley & Sons, Inc., New York, NY, 2000.
- Bridges, A., and Smith, D.R., "The Influence of Orifice Orientation on the Interaction of Synthetic Jet with a Turbulent Boundary Layer," AIAA Paper 2001-2774, 2001.
- Buckingham, E., "On Physically Similar Systems; Illustrations of the Use of Dimensional Equations," *Physical Review Series II*, Vol. 4, No. 4, pp. 345-376, 1914.
- Budoff, M., and Zorumski, W.E., "Flow Resistance of Perforated Plates in Tangential Flow," NASA TM X-2361, 1971.

- Campbell, J.S., Black, W.Z., Glezer, A. and Hartley, J.G., "Thermal Management of a Laptop Computer with Synthetic Air Microjets," Intersociety Conference on Therm. Phenomenon, IEEE, pp. 43-50, 1998.
- Cater, J., and Soria, J., "The Evolution of Round Zero-Net-Mass Flux Jets," *Journal of Fluid Mechanics*, Vol. 472, pp. 167-200, 2002.
- Chandrasekaran, V., Sankar, B.V., Cattafesta, L., Nishida, T., and Sheplak, M., "An Analytical Model for Thermoelastic Actuation of Composite Diaphragms," 12th International Conference on Solid-State Sensors and Actuators, Boston, MA, June 2003.
- Chen, Y., Liang, S., Aung, K., Glezer, A., and Jagoda, J., "Enhanced Mixing in a Simulated Combustor Using Synthetic Jet Actuators," AIAA Paper 99-0449, 1999.
- Choudhari, M., Khorrami, M.D., and Edwards, J.R., "Computational Study of Micro Fluid Mechanics of Duct Acoustic Treatment," AIAA Paper 99-1851, 1999.
- Crook, A., Sadri, A.M. and Wood, N.J., "The Development and Implementation of Synthetic Jets for the Control of Separated Flow," AIAA Paper 99-3176, 1999.
- Crook, A. and Wood, N.J., "Measurements and Visualizations of Synthetic Jets," AIAA 2001-0145, 2001.
- Cummings, A., "The Effects of Grazing Turbulent Pipe-Flow on the Impedance of an Orifice," *Acustica*, Vol. 61, pp. 233-242, 1986.
- Davis, S.A. and Glezer, A., "Mixing Control of Fuel Jets Using Synthetic Jet Technology: Velocity Field Measurement," AIAA Paper 99-0447, 1999.
- Dean, P.D., "An In-Situ Method of Wall Acoustic Impedance Measurements in Flow Ducts," *Journal of Sound and Vibration*, Vol. 34, pp. 97-130, May 1974.
- Déquand, S., Luo, X., Willems, J., and Hirschberg, A., "Helmholtz-Like Resonator Self-Sustained Oscillations, Part 1: Acoustical Measurements and Analytical Models," *AIAA Journal*, Vol. 41, No. 3, pp. 408-415, 2003.
- Didden, N., "On the Formation of Vortex Rings: Rolling up and Production of Circulation," *Journal of Applied Mathematics and Physics*, Vol. 30, pp. 101-116, 1979.
- Elder, S.A., "Self-Excited Depth-Mode Resonance for a Wall-Mounted Cavity in Turbulent Flow," *Journal of the Acoustical Society of America*, Vol. 64, pp. 877-890, 1978.
- Eldredge, R., and Bons, J.P., "Active Control of a Separating Boundary Layer with Steady Vortex Generating Jets – Detailed Flow Measurements," AIAA Paper 2004-751, 2004.

- Fargie, D., and Martin, B.W., "Developing Laminar Flow in a Pipe of Circular Cross-Section," *Proceedings of the Royal Society of London, Series A*, Vol. 321, pp. 461-476, 1971.
- Fisher, F.A., *Fundamentals of Electroacoustics*, Interscience Publishers, Inc., New York, NY, Section III and XI, 1955.
- Flynn, K.P., Panton, R.L., and Bogard, D.G., "Effect of Helmholtz Resonators on Boundary-Layer turbulence," *AIAA Journal*, Vol. 28, No. 11, pp. 1857-1858, November 1990.
- Gallas, Q., "On the Modeling and Design of Zero-Net Mass-Flux Actuators," Ph.D. Dissertation, Department of Mechanical & Aerospace Engineering, University of Florida, Gainesville, FL, 2005.
- Gallas, Q., "Lumped Element Modeling of Piezoelectric-Driven Synthetic Jet Actuators for Active Flow Control," M.S. Thesis, Department of Mechanical and Aerospace Engineering, University of Florida, Gainesville, FL, 2002.
- Gallas, Q., Holman, R., Nishida, T., Carroll, B., Sheplak, M., and Cattafesta, L., "Lumped Element Modeling of Piezoelectric-Driven Synthetic Jet Actuators," *AIAA Journal*, Vol. 41, No. 2, pp. 240-247, February 2003a.
- Gallas, Q., Holman, R., Raju, R., Mittal, R., Sheplak, M., Cattafesta, L., "Low Dimensional Modeling of Zero-Net Mass-Flux Actuators," AIAA Paper 2004-2413, 2004.
- Gallas, Q., Wang, G., Papila, M., Sheplak, M., and Cattafesta, L., "Optimization of Synthetic Jet Actuators," AIAA Paper 2003-0635, 2003b.
- Garrison, G.D., "Suppression of Combustion Oscillations with Mechanical Damping Devices," Pratt & Whitney Aircraft Rep. PWA-FR-3299, 1969.
- Ghias, R., Mittal, R., and Lund, T.S., "A Non-Body Conformal Grid Method for Simulation of Compressible Flows with Complex Immersed Boundaries," AIAA Paper 2004-, 2004.
- Glezer, A., "The Formation of Vortex Rings," *Physics of Fluids*, Vol. 31, No. 12, pp. 3532-3552, 1998.
- Glezer, A., and Amitay, M., "Synthetic Jets," *Annual Review of Fluid Mechanics*, Vol. 34, pp. 503-529, 2002.
- Glezer, A., Amitay, M., and Honohan, A.M., "Aspect of Low- and High-Frequency Aerodynamic Flow Control," AIAA Paper 2003-0533, 2003.

- Greenblatt, D., and Wygnanski, I., "Effect of Leading-Edge Curvature on Airfoil Separation Control," *Journal of Aircraft*, Vol. 40, No. 3, pp. 473-481, May-June 2003.
- Greenblatt, D., and Wygnanski, I., "Effect of Leading-Edge Curvature on Separation Control - A Comparison of Two NACA airfoils," AIAA Paper 2002-0411, 2002.
- Greenblatt, D., and Wygnanski, I., "The Control of Flow Separation by Periodic Excitation," *Progress in Aerospace Sciences*, Vol. 36, pp. 487-545, 2000.
- Guarino, J.R. and Manno, V.P., "Characterization of a Laminar Jet Impingement Cooling in Portable Computer Applications," 17<sup>th</sup> IEEE Semi-Therm. Symposium, 2001.
- Guo, D., Kral, L.D., and Cary, A.W., "Numerical Simulation of the Interactions of Adjacent Synthetic Jets," AIAA Paper 2000-2565, 2000.
- He, Y.-Y., Cary, A.W. and Peters, D.A., "Parametric and Dynamic Modeling for Synthetic Jet Control of a Post-Stall Airfoil," AIAA 2001-0733, 2001.
- Heidelberg, L. J., Rice, E. J., and Homyak, L., "Experimental Evaluation of a Spinning-Mode Acoustic Treatment Design Concept for Aircraft Inlets," NASA Technical Paper 1613, 1980.
- Hersh, A.S., and Walker, B.E., "Acoustic Behavior of Helmholtz Resonators: Part I. Nonlinear Model," AIAA Paper 95-0078, 1995.
- Hersh, A.S., and Walker, B.E., "Effect of Grazing Flow on the Acoustic Impedance of Helmholtz Resonators Consisting of Single and Clustered Orifices," NASA CR-3177, 1979.
- Holman, R., "An Experimental Investigation of Flows from Zero-Net Mass Flux Actuators," Ph.D. Dissertation, Department of Mechanical and Aerospace Engineering, University of Florida, Gainesville, FL, 2005.
- Holman, R., Gallas, Q., Carroll, B., and Cattafesta, L., "Interaction of Adjacent synthetic Jets in an Airfoil Separation Control Application," AIAA 2003-3709, 2003.
- Holman, R., Utturkar, Y., Mittal, R., Smith, B.L., and Cattafesta, L., "A Formation Criterion for Synthetic Jets," submitted to *AIAA Journal*.
- Honohan, A.M., "The Interaction of Synthetic Jets with Cross Flow and the Modification of Aerodynamic Surfaces," Ph.D. Dissertation, Department of Mechanical Engineering, Georgia Institute of Technology, Atlanta, GA, 2003.
- Honohan, A.M., Amitay, M., and Glezer, A., "Aerodynamic Control Using Synthetic Jets," AIAA Paper 2000-2401, 2000.

- Howe, M.S., *Acoustics of Fluid-Structure Interactions*, Cambridge University Press, New York, NY, 1998.
- Howe, M.S., "On the Theory of Unsteady Shearing Flow over a Slot," *Philosophical Transactions of the Royal Society of London Series A - Mathematical and Physical Sciences*, Vol. 303, No. 1475, pp. 151-180, 1981a.
- Howe, M.S., "The Influence of Mean Shear on Unsteady Aperture Flow, with Application to Acoustical Diffraction and Self-Sustained Cavity oscillations," *Journal of Fluid Mechanics*, Vol. 109, pp. 125-146, 1981b.
- Ingard, U., "On the Theory and Design of Acoustic Resonators," *Journal of the Acoustical Society of America*, Vol. 25, No 6, pp. 1037-1061, Nov. 1953.
- Ingard, U., and Ising, H., "Acoustic Non-Linearity of an Orifice," *Journal of the Acoustical Society of America*, Vol. 42, No. 1, pp. 6-17, 1967.
- Ingard, U., and Labate, S., "Acoustic Circulation Effects and the Nonlinear Impedance of Orifices," *Journal of the Acoustical Society of America*, Vol. 22, No. 2, pp. 211-218, 1950.
- Innes, D., and Creighton, D., "On a Non-Linear Differential Equation Modeling Helmholtz Resonator Response," *Journal of Sound and Vibration*, Vol. 131, No. 2, pp. 323-330, 1989.
- Jacobson, S.A. and Reynolds, W.C., "An Experimental Investigation towards the Active Control of Turbulent Boundary Layer," Thermosciences Div., Rept TF-64, Stanford, 1995.
- Jing, X., Sun, X., Wu, J., and Meng, K., "Effect of Grazing Flow on the Acoustic Impedance of an Orifice," *AIAA Journal*, Vol. 39, pp. 1478-1484, 2001.
- Jones, M.G., Parrott, T.L., and Watson, W.R., "Comparison of Acoustic Impedance Eduction Techniques for Locally-Reacting Liners," AIAA Paper 2003-3306, 2003.
- Kirby, R., Cummings, A., "The Impedance of Perforated Plates Subjected to Grazing Gas Flow and Backed by Porous Media," *Journal of Sound and Vibration*, Vol. 217, pp. 619-636, 1998.
- Kral, L.D., Donovan, J.F., Cain, A.B., and Cary, A.W., "Numerical Simulation of Synthetic Jet Actuators," AIAA Paper 97-1824, 1997.
- Lee, C.Y., and Goldstein, D.B., "Two-Dimensional Synthetic Jet Simulation," *AIAA Journal*, Vol. 40, No.3, pp. 510-516, March 2002.
- Lee, C.Y., and Goldstein, D.B., "DNS of Microjets for Turbulent Boundary Layer Control," AIAA 2001-1013, 2001.

- Lee, S.-H., and Ih, J.-G., "Empirical Model of the Acoustic Impedance of a Circular Orifice in Grazing Mean Flow," *Journal of the Acoustical Society of America*, Vol. 114, No. 1, pp. 98-113, 2003.
- Lighthill, Sir J., "Acoustic Streaming," *Journal of Sound and Vibration*, Vol. 61, pp. 391-418, 1978.
- Liu, J, and Long, L.N, "Direct Aeroacoustic and Aerodynamic Simulation of Multi-Hole Engine Liners," AIAA Aeroacoustic Meeting, 1998.
- Lumley, J.L., "The Structure of Inhomogeneous Turbulent Flows," in *Atmospheric Turbulence and Radio Wave Propagation*, A.M. Yaglon & V.I. Tatarski eds., pp. 166-178, Nauka, Moskow, 1967.
- Madou, M., *Fundamentals of Microfabrication*, CRC Press, New York, NY, 1997.
- Mallison, S.G., Kwok, C.Y., and Reizes, J.A., "Numerical Simulation of Micro-fabricated Zero Mass-Flux Jet Actuator," *Sensors and Actuators*, Vol. 105, pp. 229-236, 2003.
- Mallison, S.G., Reizes, J.A., Hong, G., and Westbury, P.S., "Analysis of Hot-Wire Anemometry Data Obtained in a Synthetic Jet Flow," *Experimental Thermal and Fluid Science*, Vol. 28, pp. 265-272, 2004.
- Malmay, C., Carbonne, S., Aurégan, Y., and Pagneux, V., "Acoustic Impedance Measurement with Grazing Flow," AIAA Paper 2001-2193, 2001.
- Margalit, S., Greenblatt, D., Seifert, A., and Wygnanski, I., "Active Flow Control of a Delta Wing at High Incidence using Segmented Piezoelectric Actuators," AIAA Paper, 2002-3270, 2002.
- Mast, T.D., and Pierce, A.D., "Describing-Function Theory for Flow Excitation of Resonators," *Journal of the Acoustical Society of America*, Vol. 97, No. 1, pp. 163-172, 1995.
- McCormick, D.C., "Boundary Layer Separation Control with Directed Synthetic Jets," AIAA Paper, 2000-0519, 2000.
- Meissner, M., "Excitation of Helmholtz resonator by Grazing Air Flow," *Journal of Sound and Vibration*, Vol. 256, No. 2, pp. 382-388, 2002.
- Meissner, M., "Self-Sustained Deep Cavity Oscillations Induced by Grazing Flow," *Acustica*, Vol. 62, pp. 220-228, 1987.
- Melling, T.H, "The Acoustic Impedance of Perforates at Medium and High Sound Pressure Levels," *Journal of Sound and Vibration*, Vol. 29, pp. 1-69, 1973.

- Merhaut, J., *Theory of Electroacoustics*, McGraw-Hill, Inc., New York, NY, Section 6, 1981.
- Milanovic, I. M., and Zaman, K.B.M.Q., "Synthetic Jets in Cross-Flow," *AIAA Journal*, in press.
- Mittal, R., and Rampugoon, P., "On the Virtual Aeroshaping Effect of Synthetic Jets," *Physics of Fluids*, Vol. 14, No. 4, pp. 1533-1536, 2002.
- Mittal, R., Rampugoon, P., and Udaykumar, H.S., "Interaction of a Synthetic Jet with a Flat Plate Boundary Layer," AIAA Paper 2001-2773, 2001.
- Morton, B.R., "The Generation and Decay of Vorticity," *Geophys. Astrophys. Fluid Dynamics*, Vol. 28, pp.277-308, 1984.
- Motsinger, R.E., and Kraft, R.E., "Design and Performance of Duct Acoustic Treatment," in *Aeroacoustics of Flight Vehicles: Theory and Practice*, Section 14, Volume 2, NASA Reference Publication 1258 ed, pp.176-189, August 1991.
- Najjar, F.M., and Mittal, R., "Simulations of Complex Flows and Fluid-Structure Interaction Problems on Fixed Cartesian Grids," FEDSM 2003-45577, 2003.
- National Aeronautics and Space Administration CFDVal, "CFD Validation of Synthetic Jets and Turbulent Separation Control," NASA Langley Research Center Workshop, Williamsburg, VA, March 29-31, 2004.
- National Instruments, "LabView Measurements Manual," National Instruments Corporation, Austin, TX, 2000.
- Nelson, P.A., Halliwell, N.A., and Doak, P.E., "Fluid Dynamics of a Flow Excited Resonance, Part II: Flow Acoustic Interaction," *Journal of Sound and Vibration*, Vol. 91, No. 3, 1983, pp.375-402, 1983.
- Nelson, P.A., Halliwell, N.A., and Doak, P.E., "Fluid Dynamics of a Flow Excited Resonance, Part I: Experiment," *Journal of Sound and Vibration*, Vol. 78, No. 1, pp. 15-38, 1981.
- Orkwis, P.D., and Filz, C., "Characterization of Dual Two-Dimensional Synthetic Jets in Cross Flow at Low Mach number," *AIAA Journal*, in press.
- Ozyörük, Y., and Long, L.N., "Time-Domain Calculation of Sound Propagation in Lined Ducts with Sheared Flows," *AIAA Journal*, Vol. 38, No. 5, pp. 768-773, May 2000.
- Pack, L.G., and Seifert, A., "Periodic Excitation for Jet Vectoring and Enhanced Spreading," AIAA Paper 99-0672, 1999.
- Park, S-H., Lee, I., and Sung, H.J., "Effect of Local Forcing on a Turbulent Boundary Layer," *Experiments in Fluids*, Vol. 31, No. 4, pp. 384-393, 2001.



- Parrott, T.L., and Jones, M.G., "Parallel-Element Liner Impedances for Improved Absorption of Broadband Sound in Ducts," *Journal of Noise Control Eng.*, Vol. 43, No. 6, pp. 183-195, 1995.
- Prasad, S., Horowitz, S., Gallas, Q., Sankar, B., Cattafesta, L., and Sheplak, M., "Two-Port Electroacoustic Model of an Axisymmetric Piezoelectric Composite Plate," AIAA Paper 2002-1365, 2002.
- Raju, R., Mittal, R., Gallas, Q., and Cattafesta, L., "Scaling of Vorticity Flux and Entrance Length Effects in Zero-Net Mass Flux Devices," AIAA Paper 2005-xxxx, 2005.
- Rampunggoon, P., "Interaction of a Synthetic Jet with a Flat-Plate Boundary Layer," Ph.D. Dissertation, Department of Mechanical Engineering, University of Florida, Gainesville, FL, 2001.
- Rao, K.N., and Munjal, M.L., "Experimental Evaluation of Impedance of Perforate with Grazing Flow," *Journal of Sound and Vibration*, Vol. 108, pp 283-295, 1986.
- Rathnasingham, R. and Breuer, K.S., "Coupled Fluid-Structural Characteristics of Actuators for Flow Control," *AIAA Journal*, Vol. 35, No. 5, 1997.
- Ravi, B.R., Mittal, R., and Najjar, F.M., "Study of 3-Dimensional Synthetic Jet Flowfields Using Direct Numerical Simulation," AIAA Paper 2004-0091, 2004.
- Rediniotis, O.K., Ko, J. and Kurdila A.J., "Reduced Order Nonlinear Navier-Stokes Models for Synthetic Jets," *Journal of Fluids Engineering*, Vol. 124, No. 2, pp. 433-443, 2002.
- Rice, E.J., "A Theoretical Study of the Acoustic Impedance of Orifices in the Presence of a Steady Grazing Flow," NASA TM X-71903, 1976.
- Rice, E.J., "A Model for the Acoustic Impedance of a Perforate Plate Liner with Multiple Frequency Excitation," NASA TM X-67950, 1971.
- Ritchie, B.D. and Seitzman, J.M., "Controlled Fuel-Air Mixing Using a Synthetic Jet Array," AIAA Paper 2000-3465, 2000.
- Rizzetta, D.P., Visbal, M.R., and Stanek, M.J., "Numerical Investigation of Synthetic-Jet Flow Fields," *AIAA Journal*, Vol. 37, No. 8, pp. 919-927, 1999.
- Ronneberger, D., "The Acoustical Impedance of Holes in the Wall of Flow Ducts," *Journal of Sound and Vibration*, Vol. 24, No. 1, pp. 133-150, 1972.
- Rossi, M., *Acoustics and Electroacoustics*, Artech House, Norwood, MA, pp. 245-373, 1988.

- Schultz, T., Cattafesta, L., Nishida, T., and Sheplak, M., "Uncertainty Analysis of the Two-Microphone Method for Acoustic Impedance Testing," Submitted to *Journal of Sound and Vibration*.
- Seifert, A., Bachar, T., Koss, D., Shepshelovich, M. and Wygnanski, I., "Oscillatory Blowing: A Tool to Delay Boundary-Layer Separation," *AIAA Journal*, Vol. 31, No. 11, pp. 2052-2060, 1993.
- Seifert, A., Darabi, A., and Wygnanski, I., "Delay of Airfoil Stall by Periodic Excitation," *Journal of Aircraft*, Vol. 33, pp. 691-698, 1996.
- Seifert, A. and Pack, L.G., "Sweep and Compressibility Effects on Active Separation Control at High Reynolds Numbers," AIAA Paper 2000-0410, 2000a.
- Seifert, A., and Pack, L.G., "Separation Control at Flight Reynolds Numbers – Lessons Learned and Future Directions," AIAA Paper 2000-2542, 2000b.
- Seifert, A. and Pack, L.G., "Oscillatory Control of Separation at High Reynolds Numbers," *AIAA Journal*, Vol. 37, No. 9, 1999.
- Senturia, S. D., *Microsystem Design*, Kluwer Academic Publishers, 2001.
- Shuster, J.M., and Smith, D.R., "A Study of the Formation and Scaling of a Synthetic Jet," AIAA Paper 2004-0090, 2004.
- Sirovich, L., "Turbulence and the Dynamics of Coherent Structures," *Quarterly of Applied Mathematics*, Vol. XLV, No. 3, pp. 561-590, 1987.
- Smith, B.L., and Glezer, A., "Jet Vectoring using Synthetic Jets," *Journal of Fluid Mechanics*, Vol. 458, pp.1-24, 2002.
- Smith, B.L. and Glezer, A., "The Formation and Evolution of Synthetic Jets," *Physics of Fluids*, Vol. 10, No. 9, pp. 2281-2297, 1998.
- Smith, B.L. and Glezer, A., "Vectoring and Small-Scale Motions Effected in Free Shear Flows Using Synthetic Jet Actuators," AIAA Paper 97-0213, 1997.
- Smith, B.L., and Swift, G.W., "A comparison Between Synthetic Jets and Continuous Jets," *Experiments in Fluids*, Vol. 34, pp. 467-472, 2003a.
- Smith, B.L., and Swift, G.W., "Power Dissipation and Time-Averaged Pressure in Oscillating Flow Through a Sudden Area Change," *Journal of the Acoustical Society of America*, Vol. 113, No. 5, pp. 2455-2463, May 2003b.
- Smith, B.L., Trautman, M.A., and Glezer, A., "Controlled Interactions of Adjacent Synthetic Jet Actuators," AIAA Paper 99-0669, 1999.

- Smith, D.R., Amitay, M., Kibens, V., Parekh, D.E., and Glezer, A., "Modification of lifting body aerodynamics using synthetic jet actuators," AIAA Paper 98-0209, 1998.
- Sondergaard, R., Rivir, R.B., and Bons, J.P., "Control of Low-Pressure Turbine Separation Using Vortex-Generator Jets," *Journal of Propulsion and Power*, Vol. 18, No. 4, pp. 889-895, July-August 2002.
- Spalart, P.R., and Alnaras, S.R., "A One-Equation Turbulence Model for Aerodynamics Flows," AIAA Paper 92-0439, 1992.
- Sullivan, J.W., "A Method for Modeling Perforated Tube Muffler Components. II. Application," *Journal of the Acoustical Society of America*, Vol. 69, pp. 779-788, 1979.
- Urzyrnick, F., and Fernholz, H.-H., "Flow-Induced Acoustic Resonators for Separation Control," AIAA Paper 2002-2819, 2002.
- Utturkar, Y., Holman, R., Mittal, R., Carroll, B., Sheplak, M., and Cattafesta, L., "A Jet Formation Criterion for Synthetic Jet Actuators," AIAA Paper 2003-0636, 2003.
- Utturkar, Y., Mittal, R., Rampunggoon, P., and Cattafesta, L., "Sensitivity of Synthetic Jets to the Design of the Jet Cavity," AIAA Paper 2002-0124, 2002.
- Wang, G., Sheplak, M., Cattafesta, L., and Sankar, B.V., "Analysis of Composite Piezoelectric Circular Plate with Initial Stresses for MEMS," International Mechanical Engineering Congress and Exposition, Paper IMECE2002-39328, November 2002.
- Wang, H., and Menon, S., "Fuel-Air Mixing Enhancement by Synthetic Microjets," *AIAA Journal*, Vol. 39, No.12, pp. 2308-2319, 2001.
- Watson, M., Jaworski, A.J., and Wood, N.J., "Contribution to the Understanding of Flow Interactions between Multiple Synthetic Jets," *AIAA Journal*, Vol. 41, No. 4, pp. 747-749, 2003.
- Watson, W.R., Tanner, S.E., and Parrott, T.L., "Optimization Method for Educing Variable-Impedance Liner Properties," *AIAA Journal*, Vol. 36, No. 1, pp. 18-23, January 1998.
- White, F.M., *Viscous Fluid Flow*, McGraw-Hill, Inc., New York, NY, 2<sup>nd</sup> ed., 1991.
- White, F.M., *Fluid Mechanics*, McGraw-Hill, Inc., New York, NY, 1979.
- Wiltse, J.M., and Glezer, A., "Manipulation of Free Shear Flows Using Piezoelectric Actuators," *Journal of Fluid Mechanics*, Vol. 249, pp. 261-285, 1993.

- Wood, N.J., Sadri, A.M., and Crook, A., "Control of Turbulent Flow Separation by Synthetic Jets," AIAA Paper 2000-4331, 2000.
- Wynanski, I., "Boundary Layer and Flow Control by Periodic Addition of Momentum," AIAA Paper 97-2117, 1997.
- Ye, T., Mittal, R., Udaykumar, H.S., and Shyy, W., "An Accurate Cartesian Grid Method for Viscous Incompressible Flows with Complex Immersed Boundaries," *Journal of Computational Physics*, Vol. 156, pp. 209-240, 1999.
- Yehoshua, T., and Seifert, A., "Boundary Condition Effects on Oscillatory Momentum Generators," AIAA Paper 2003-3710, 2003.
- Zang, Y., Street, R.L., and Koseff, J.R., "A non-staggered Grid, Fractional Step Method for Time-Dependent Incompressible Navier-Stokes Equations in Curvilinear Coordinates," *Journal of Computational Physics*, Vol. 114, No. 18, 1994.
- Zwikker, C., and Kosten, C.W., *Sound Absorbing Materials*, Elsevier, Amsterdam, 1949.